Additive Manufacturing of Nickel-based superalloys: a state-of-the-art review on process-structure-defect-property relationship

Amir Mostafaei [a,*], Reza Ghiaasiaan [b,c,*], I-Ting Ho [a], Seth Strayer [d], Kai-Chun Chang [e], Nima Shamsaei [b,c], , Shuai Shao [b,c], Santanu Paul [d], An-Chou Yeh [e], Sammy Tin [d], Albert C. To [d]

[a] Department of Mechanical, Materials and Aerospace Engineering, Illinois Institute of Technology, 10 W 32nd Street, Chicago, IL 60616, USA
[b] Department of Mechanical Engineering, Auburn University, Auburn, AL 36849, USA
[c] National Center for Additive Manufacturing Excellence (NCAME), Auburn University, Auburn, AL 36849, USA
[d] Department of Mechanical Engineering and Material Science, University of Pittsburgh, Pittsburgh, 15261, USA
[e] Materials Science and Engineering Department, National Tsing Hua University, 101, Sec. 2, Kuang-Fu Road, Hsinchu 30013, Taiwan, R. O. C.
[d] Department of Material Science and Engineering, University of Arizona, Tucson, AZ 85721

* Corresponding authors: mostafaei@iit.edu and ghiaasiaan@auburn.edu

Abstract

Fusion-based additive manufacturing (AM) has significantly grown to fabricate Nickel-based superalloys with design freedom across multiple length scales. Several phenomena such as feedstock/energy source/melt pool interactions, solidification and phase transformations occur during fusion-based AM processes of Nickel-based superalloys, which determine the ultimate microstructure and mechanical performance of the built parts. In this review, we elaborate a comprehensive discussion on AM Nickel-based superalloys and influential factors including feedstock characteristics (powder morphology, chemistry, contamination, flowability, recycling) and AM processing (parameters, and powder spreading/wall/balling/spattering effects) on their microstructure (micro-segregation, phases formations and grain structures), defect generation (sub-surface/internal defects, microcracks, surface roughness, and residual stress). Furthermore, the mechanical properties of AM Nickel-based superalloys such as tensile, creep and fatigue at room/elevated temperatures are analyzed in accordance with the initial, and post processing effects. Additionally, the commonly utilized modeling approaches in literature to predict the microstructure and mechanical behavior of these alloys are highlighted. Finally, the current challenges and mitigation approaches for future research are identified considering the gaps in the AM Nickel-based superalloys.

Keywords: Fusion-based additive manufacturing; Nickel-based superalloys; Process-structure-defect-property relationship; Mechanical properties; Computational modeling.

1. **Table of Contents**

1. Introduction

Additive manufacturing (AM) or 3D printing has accrued significant attention from the academia and various industry sectors such as aerospace, automobile, and healthcare for the advantages it offers compared to conventional manufacturing processes. The U.S. AM market size was valued at about $3 billion in 2021 and is projected to expand at a compound annual growth rate of 18.9% from 2022 to 2030 [1]. The assertive research and development in AM and the increasing demand for prototyping applications are expected to drive the growth of the market. For instance, it has allowed engineers to rethink the entire design process for its ability to produce highly complex parts with high levels of design freedom. Structural topology optimization using finite element analysis [2], for example, can be used to lightweight the part via removing material in specific regions such that the components behave more efficiently and with better mechanical properties than a conventional sample [3]. Leveraging the layer-by-layer processing paradigm, this optimization procedure permits fabrication of lattice (cellular) structures with high ratios of strength/stiffness to weight, better energy absorption, and enhanced thermal properties. In this regard, every part fabricated via AM can be uniquely designed for function, such as "conformal coolant" components with complex internal passages and cooling channels. Since AM can print these parts in a single processing step, rather than requiring several manufacturing processes such as casting, machining, and drilling, the mass customization becomes achievable at a lower cost in AM processing [4].

AM also facilitates part integration through its ability to consolidate several parts of an assembly into a single component. This integration offers many advantages, such as reducing the overall weight, manufacturing time, processing steps, cost, and complexity. Besides, it can also optimize the mechanical properties and performance of the final component. For example, the GE integrated fuel nozzle combines a 20-part assembly into a single component consisting of cobalt chrome material; it achieves a 25% weight reduction and is five times more durable than a conventional assembly [5]. Further, AM reduces the buy-to-fly ratio, which is the ratio of input material weight to final part weight. The buy-to-fly ratios for aerospace engines and structural components fabricated via conventional manufacturing processes can be as high as 10:1 and 20:1, respectively. AM can produce these components with a buy-to-fly ratio as low as 1:1 [6]. The reduction in required material by AM processes can lower the cost up to 30 to 50% compared to conventional processes [7]. Additionally, parts can be 3D printed on-demand, reducing inventory requirements and lead-times for critical or replacement components. All these factors significantly streamline the legacy manufacturing process and mitigate environmental impact [4]. Attributed to these merits, the AM technology, as an emerging manufacturing process, has revolutionized the conventional design practices and enable innovation in engineering community. However, there are challenges in AM processing such as repeatability, dimensional tolerance, delamination, powder recycling, defects, microstructural heterogeneity, elemental micro segregation, anisotropic mechanical properties,

and post processing difficulties, etc., all of which are under constant research and standardizations for structural materials and various applications.

The manufacturing has been the main challenge of high performance and high temperature Nickel-based superalloys, because the costly subtractive techniques are required to obtain structurally sound mechanical properties of cast superalloy [8]. For example, the jet engine turbine blade with complex internal cooling channels can be produced using the conventional precision investment casting using either a wax model or a silica-based replica methodology. Additionally, a ceramic mold is required to vacuum cast a large volume of molten metal into the desirable parts, during which the precipitation of γ' precipitates (Ni_3Al) becomes inevitable due to the prolonged and slow solidification process. To reduce the as-cast elemental micro segregation, careful subsequent heat treatment of several hours is needed just below the melting point at ~1300 °C [9]. Additional post processing such as machining are also required for the final complex shape of the component such as intricate turbine blade geometry. Machining of the Nickel-based superalloys such as alloy 718 (Inconel 718 or IN718) is very difficult because of their high hardness and propensity to work harden during the conventional thermomechanical wrought processes, which in turn requiring high cutting forces, resulting in higher work hardening effects [10]. Furthermore, the traditional thermomechanical processing of turbine part manufacturing, for instance, includes investment casting, several post processing such as machining processes, which in turn may result in severe chemical micro-segregation and significant waste/scrappage during the final machining. As a result, only about 10% of the Nickel-based superalloys ends up as finished goods [11].

Since the γ-γ' microstructure in the modern Nickel-based superalloys such as IN718 with excellent weldability due to slow precipitation kinetics [12] is desirable for AM processing. In other words, only AM can allow for designing an alloy containing a high-volume fraction of γ'. Due to the rapid solidification rate during the fusion-based AM processes (i.e., direct energy deposition and powder bed fusion), inhomogeneous grain structures ranging from nanometer to sub-millimeter length scales are generated [13]. These are not otherwise feasible by traditional manufacturing methods [13]. Therefore, a wide range of microstructure and subsequently mechanical behavior are possible in the AM components. For example, a decrease in microcracking in AM Nickel-based superalloy Hastelloy X was observed by increasing the solid solution strengthening elements within the commercial alloy composition range [14]. Furthermore, before printing, AM enables the mixing of different alloy powders, resulting in the manufacture of metal-metal composites with special microstructures that would be difficult to manufacture by other means [15].

Aim of this review - In recent years, several review papers were published in AM of metal alloys and compounds. Debroy et al. [16] presented an overview on AM processes and elaborated various technologies, process-structure-property correlations and their pros and cons on a wide variety of materials. Sanaei et al. [17] addressed the influential microstructural

factors on fatigue performance of AM parts with a focus on generated defects. Recently, Mostafaei et al. [18] published a comprehensive review on the commonly induced defects and anomalies during the powder bed fusion AM processes of different metallic alloying systems such as aluminum, nickel, iron, and titanium based alloys. Although, there are some other review summaries in the literature background on specific Nickel-based superalloy fabricated by specific AM technology [19–24], this article endeavors to provide a more comprehensive and conclusive review summary of fusion-based AM of Nickel-based superalloys, with an emphasis on processing details, microstructures, defects, and mechanical properties, and the "process-structure-defect-properties" relationship. This is partly because for there are limited data available in the literature [25] for other AM technologies such as the non-beam-based ones, e.g., the binder jetting, despite their fast growing rate. Furthermore, simulations and predictions of fusion-based AM Nickel-based superalloys will be highlighted and compared with the experimental data. Finally, challenges, outlook and perspective for future research are provided.

2. Metallurgy of Nickel-based superalloys

In Nickel-based superalloys, different alloying elements are added to improve mechanical properties and stability of microstructural constituent at elevated temperatures. Even regular steels and titanium alloys cannot maintain their room temperature strength at elevated temperatures above 540 °C, where the Iron-Nickel, Nickel- and Cobalt-based alloys become the alternative, which subsequently earned them "*superalloy*" title for their high temperature properties. This is shown in Fig. 1 (a) using schematic stress-rupture behavior where different types of superalloys show different resistivity to high temperature due to their strengthening mechanism and phases. For example, the Fe-Ni-Co-superalloys, the solid solution strengthened alloys, are less temperature resistive compared to the carbide-strengthened Co-based superalloys. Notably, the precipitation-strengthened Fe-Ni-based superalloys show the most effective strengthening mechanism against elevated temperatures due to formation of strengthening precipitates such as the γ' and γ" phases. The iron, nickel and cobalt are the main alloying elements for the superalloys, all of which with face centered cubic (fcc) crystal structures. However, unlike nickel which maintains a single fcc-type crystal structure at all temperature, iron and cobalt are allotropic metallic elements, i.e., both possess two different crystal structures depending on time and solid solutioned alloying elements. They have a body centered cubic (bcc) crystal structure at room temperature which can transform to a fcc structure at elevated temperatures, which can also happen due to presence of other alloying elements such as nickel in their composition as solid solution element. The popular examples for Nickel-based superalloys are the Haynes 282 and IN718, which are basically an extension of stainless-steel alloys [26].

The strengthening mechanism in the Nickel-based superalloys can be attributed to the alloying elements that are selectively included in the austenitic nickel matrix. For instance, Cr,

Fe, Co, Mo, W, Hf, Re, and Ru prefer to exhibit in the γ-grain matrix and contribute to the solid solution strengthening of the Nickel-based superalloys; whereas the other elements such Al, Ti, Nb, and Ta tend to partition and form Ni_3Al (γ') or Ni_3Nb (γ") precipitates with ordered crystal structures (i.e., $L1_2$ or $D0_{22}$, respectively). Other examples are the B, C, and Zr elements that have the tendency to segregate in grain boundaries in form of strengthening solute-clusters or precipitates combined with Ti, Ta, Hf, Cr, and Mo. Fig. 1(b) presents the typical alloying elements exist in Nickel base superalloys are illustrated.

In general, the microstructure of Nickel-based superalloys consists of austenitic (fcc) γ-grain nickel matrix and a range of other secondary phases. Examples are (1) fcc-type carbide phases (i.e., MC, M_6C, $M_{23}C_6$, M_7C_3); (2) the gamma prime (γ') phase, which is a fcc-type $Ni_3(Al,Ti)$ ordered phase; (3) the gamma double prime (γ") phase, which is a body-centered tetragonal (bct) type Ni_3Nb ordered phase; (4) the eta (η) phase, which is a hexagonal closed pack (hcp)-type Ni_3Ti (or $Ni_6TiAlNb$) ordered phase; (5) the delta (δ) phase, which is an orthorhombic Ni_3Nb ordered intermetallic compound [27]. The γ', γ" and η phases are also known as the geometrically closed-packed (gcp) phases [26]. Due to their *ordered* crystal structure, the γ', γ", δ and η phases play an important strengthening role in the Nickel-based superalloys. This is because they require extra energy to get passed by the dislocations. The ordering increases the antiphase boundary (APB) and stacking fault (SF) energies, which in turn increase the strengthening effect of these phase. The strengthening effect of the ordered phases could be ascribed to the fact that certain elements always occupy specific locations in their crystal structures. For instance, in the ordered (fcc) γ'-phase (i.e., $Ni_3(Al, Ti)$), the Nickel atoms always occupy the face centered positions in the cubic crystal structure while the Ti and Al atoms always occupy the corner positions that are shared with eight other neighboring atoms. In contrast, in the *disordered* structures, atoms may occupy any given locations and therefore the presence of each atom is identified by a volume or weight fraction within the known unit cell crystal structure [28]. Fig. 1(c) presents the crystal structures of γ', γ", δ and η phases. It is notable that there are other phases in the microstructure of Nickel-based superalloys which are known to have detrimental effect on their mechanical properties. Examples are (1) sigma (σ) phase with a tetragonal crystal structure (i.e., FeCr, FeCrMo, CrFeMoNi, CrCo and CrNiMo); (2) mu (μ) phase with a Rhombohedral crystal structure (i.e., Co_2W_6 and $(Fe, Co)_7(Mo, W)_6$); and (3) Laves phase with a hexagonal crystal structure (i.e., Fe_2Nb, Fe_2Ti, Fe_2Mo, Co_2Ta, and Co_2Ti). These σ, μ and Laves phases are so known as the topologically close-packed (tcp) phases that mostly likely can form at the interface of γ-matrix and the gcp phases (i.e., γ', γ", δ and η) with an irregularly elongated plate-like or needle-like morphology and less frequently at grain boundary areas [26,29].

Among the separated strengthening mechanisms, γ'- and γ"-precipitates further yield a unique temperature capability to Nickel-based superalloys and Ni-Fe-based superalloys in comparison with the other alloying systems. Owing to the coherency of γ'- and γ"-precipitates

to nickel γ-grain matrix, the order-disorder transition is allowed leading to extremely high volume fraction of such precipitates [30]. Simultaneously, the ordering temperatures of γ'- and γ"-precipitates can reach 1375 ºC and 650 ºC, respectively, without the effects from impurities such as Fe [31]. The thermal stability of precipitates guarantees their ability to pin the dislocations in pairs by forming an anti-phase boundary (APB) and Kear-Wilsdorf (KW) locks at elevated temperatures, thus improving the mechanical performance of Nickel-based superalloys including yield strength, creep resistance, and fatigue strength [32]. The increasing strength attributed to the γ'- and γ"-precipitates, however, also restricts the formability and weldability of superalloys (directly linked to the Ti + Al content) [33]. With increasing γ'-fraction, the solvus temperature of γ'-precipitates is expected to increase, and mechanically forming the superalloy parts can be difficult to accomplish in practice as γ'- precipitates cannot be eliminated by heat treatment. Therefore, the compositions of conventional superalloys are required to be compliant with the traditional processing routes such as forging [34] and welding [35], and the geometry of parts will be confined by the molds applied during the processing.

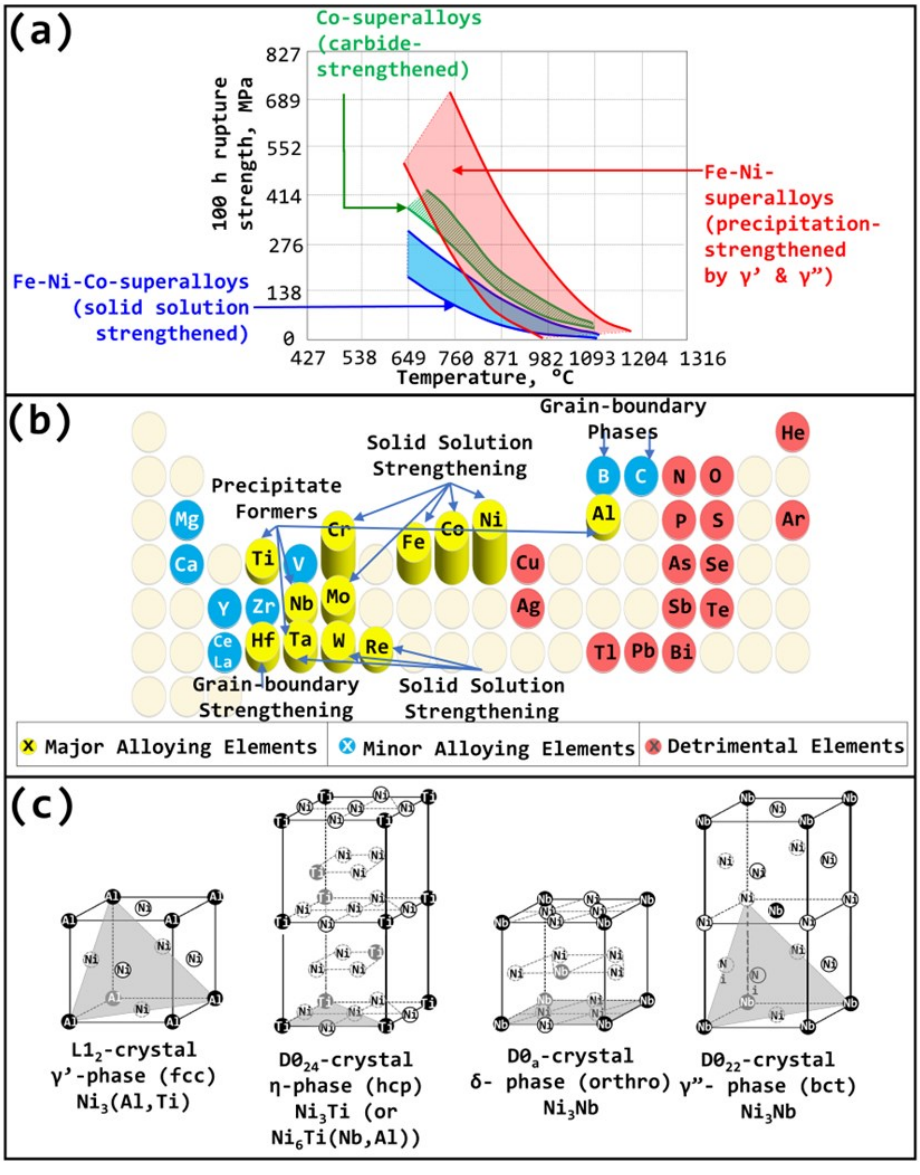

Fig. 1 (a) Typical stress-rupture behavior of three types of superalloy classes, i.e., the iron-nickel-, nickel-, and cobalt-base). Reproduced from [36]. (b) Typical alloying elements exist in the superalloys. Reproduced from [36] (c) Crystal structures of geometrically closed-packed (gcp) phases with ordered crystal structures, i.e., γ', γ", δ and η phases found in the microstructure of superalloys. Note that open hollow circle represents Ni atoms, and the solid black circle represents the M atoms (i.e., Al, Ti, and Nb) in compounds; also, a shaded plane shows the closest packed plane in crystal structure. Reproduced from [28].

3. Fusion-based AM technologies

Typically, different AM processes have been developed based on type of feedstock and layer-by-layer deposition technologies. In metal fusion-based AM processes, feedstock is in form of powder or wire and the binding system is based on the heat source such as laser or electron beam in which metal is fused followed by rapid solidification (rate of 10^4-10^6 K/s). Fig. 2 shows schematic of the most common fusion-based AM processes. In this section and following paragraphs, each of these fusion-based AM technologies are further explained. Currently the fusion-based AM techniques offer the best reproducibility and dimensional accuracy within the other metal AM production methods and, hence, have been well-researched in academia and industry such as medical (titanium, stainless steels, and cobalt-chrome alloys), aerospace and defense (Nickel-based superalloys), and energy (stainless steels and superalloys) [37]. ISO/ASTM 52900:2015 standard [38] has defined the following terminologies for AM technologies:

- Laser beam powder bed fusion (L-PBF): selective laser melting, laser powder bed fusion, direct metal laser sintering, etc.
- Electron beam direct energy deposition (E-DED)
- Electron beam powder feed or powder bed (E-PBF)
- Laser beam directed energy deposition (L-DED): direct laser deposition
- Wire arc additive manufacturing (WAAM): electric arc based additive manufacturing

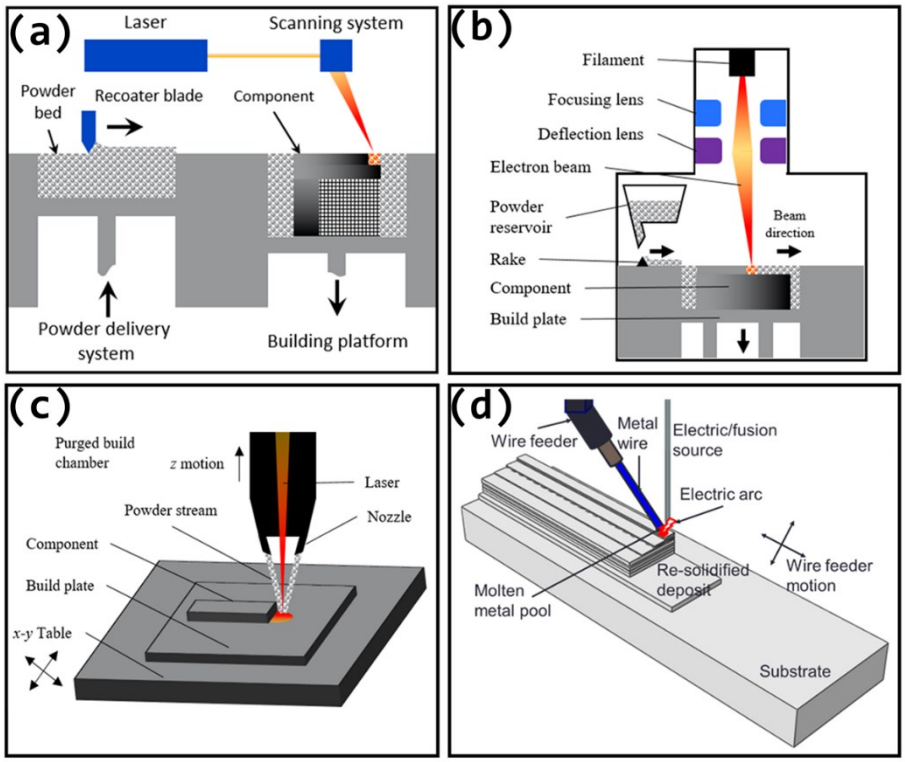

Fig. 2. Schematic of the generic fusion-based AM processes: (a) laser powder bed fusion (L-PBF), reproduced from [39,40]. (b) electron-beam powder bed fusion (E-PBF), reproduced from [41,42]. (c) laser-beam direct energy deposition (DED) and cross-sectional view of laser melting, powder stream, and shield gas application. reproduced from [40]. (d) wire arc additive manufacturing (WAAM).

Laser powder bed fusion - L-PBF employs thermal energy selectively provided by a laser beam to fuse different regions of a powder bed. Fig. 2(a) depicts a schematic of the generic L-PBF process. A recoater blade or cylindrical roller is used to spread a thin (20 – 100 µm [5]) layer of metal powder from a powder reservoir across a build plate. Subsequently, this powder layer is melted and fused with previously deposited layers via a laser beam using a predefined scan strategy determined by a corresponding two-dimensional slice of the desired computer aided design (CAD) model geometry. Upon completion of one layer, the build plate lowers by the prescribed layer thickness, a new layer of powder is deposited, and this process repeats until the final three-dimensional (3D) geometry of the part is fully printed.

Most L-PBF systems use a single 200 W – 1 kW fiber laser as the thermal energy source [5]. The build chamber is typically purged with argon gas to create an inert atmosphere that shields the reactive metal material and purifies the process. The main process parameters include laser power, scan speed, hatch spacing (distance between adjacent scan tracks), and powder layer thickness. As the beam diameter, hatch spacing, and layer thickness are all on the order of µm and the scan speed remains relatively low compared to electron-beam powder bed fusion, this process facilitates the fabrication of nearly fully dense parts with high-resolution features, complex internal passages, and relatively good surface finish. However, this paradigm also limits the deposition rate (5 – 20 cm^3/h [5]) and invokes a high production time, making the process most suitable for the fabrication of small, high-fidelity components [5].

From a design for AM perspective, any overhanging surfaces – such as a cantilever beam – require support material to lower distortion or prevent possible collapse of molten material under the influence of gravity or thermally-induced residual stress [43]. The support structure acts as a mechanical support and heat sink by which heat is dissipated through the solid material beneath it. Since the support structures are temporary and removed by mechanical means in the post processing stage, it usually consists of a lattice structure to reduce manufacturing time and costs. Optimal support structures can be obtained during preprocessing through topology optimization or other numerical methods [5]. This process involves adjusting the orientation or configuration of the support structure to ensure its manufacturability. It can also be applied to lightweight the component itself by removing material in specific regions such that the component behaves more efficiently and with better mechanical properties such as strength and stiffness [44].

Upon completion of the build, the entire build plate will be surrounded by loose powder, which must be removed to comply with health and safety standards. It is especially critical to remove powders in volumes of complex features or internal passages where the particles may remain stubbornly trapped. The powder particles are often capable of being reused to avoid wastage. After support material and loose powder removal, the part may undergo several heat treatments to increase its mechanical integrity and performance. Some of these treatments include shot peening, polishing, machining, and heat treatment, depending on the requirement. Critical components may also require hot isostatic pressing (HIP) to partially close up some of the internal voids (which can be detrimental to the fatigue properties) generated during the thermo-mechanical process [5].

Electron-beam powder bed fusion - E-PBF is another powder-bed-based, layer-by-layer AM technology in which an electron beam (as compared with a laser beam used in L-PBF process), is used to selectively fuse different regions of the powder bed in vacuum chamber. E-PBF offers several advantages, such as higher building rates (up to 80 cm^3/hr. [5]) via faster scanning speeds and increased beam penetration depth. However, it also limits the dimensional control and produces parts with an inferior surface finish [45]. Combined with the higher machine cost and lack of unconstrained build volume, E-PBF has achieved less popularity than other powder-based processes such as L-PBF and direct energy deposition (DED).

Fig. 2(b) shows an illustration of the generic E-PBF process. A hot tungsten filament emits electrons at high speed (60 kV), which are subsequently focused and deflected towards the desired location on the powder bed via electromagnetic lenses. As the electron beam hits the powder bed, the electrons' kinetic energy is converted to thermal energy, which melts the powder particles. The beam current ranges from 1 – 50 mA, resulting in a maximum beam power of about 3 kW. Although, some new machines, to increase their productivity, have

power limits exceeding 6 kW. The beam diameter can be focused down to a minimum of about 0.1 mm [5].

Each layer is scanned in two distinct stages: the preheating stage and the melting stage. During preheating, the defocused electron beam makes several passes over the building area with an approximate velocity of 10 m/s while the beam power gradually increases to ~3 kW. This step is critical, and its purpose is two-fold: one, it maintains a high temperature (up to 1100 °C for Nickel-based superalloys) within the building volume, and two, it sinters the powder particles slightly [44]. Sintering the powder particles is essential to hold them in place and prevent the so-called smoke events, in which the powder particles get spread within the build chamber due to electrostatic repulsions. Note that it is critical to avoid a smoke event since this usually leads to termination of the process [44]. Additionally, maintaining a high temperature within the building volume is useful for reducing residual stress caused by steep thermal gradients. This is especially advantageous for AM of Nickel-based superalloys since they are prone to crack formation due to their high amount of alloying elements [46], and it could also help eliminate the need for heat treatment [5]. Considering the lower residual stress and additional support provided by the slightly sintered powder particles, the density and number of required support structures are lower for E-PBF than L-PBF. Besides, support structures fabricated during E-PBF are mainly used to enhance heat conduction rather than providing structural support [5].

After preheating, the already-sintered powder particles are next melted during the heating stage to form the component. The heating stage uses lower beam velocity (~4 m/s) and melts the powder particles at locations specified by the corresponding two-dimensional slice of the desired CAD model geometry [44]. The entire build chamber is subject to a vacuum (10^{-4} – 10^{-5} mbar) to shield the alloy from ambient gases such as oxygen and nitrogen. Additionally, a small helium pressure of 10^{-3} mbar is applied to further stabilize the process and prevent smoke. The main process parameters include beam power, scan speed, hatch spacing, layer thickness (50 – 200 μm [5]), and preheating temperature. Generally, this process facilitates a welding process driven by heat conduction which would otherwise give rise to deep (keyhole) welding [47].

Laser-beam direct energy deposition **–** In DED technologies, thermal energy is used to selectively melt and fuse feedstock material (in the form of powder or wire) which it is fed coaxially with the laser beam using a set of nozzles. Popular DED technologies include laser engineered net shaping (LENS), direct metal deposition (DMD), laser-aided additive manufacturing (LAAM), wire arc additive manufacturing (WAAM), electron beam freeform fabrication (EB-FFF), among others [5].

Fig. 2(c) depicts a schematic of the generic DED process. A substrate or build plate is first placed on a table capable of *x*-*y* motion. A relatively high powered energy source such as

Nd:YAG or CO_2 laser [48] is then used to fuse powder particles as they are blown through one or several nozzles into the laser beam and finally form the melt pool. A shielding gas such as argon protects the molten metal from oxidation or other chemical reactions. This shielding gas is also applied within the nozzles to deliver the powder particles into the melt pool [48].
DED is especially valuable for its potential to fabricate functionally graded materials and repair and clad damaged parts that are otherwise unable to be repaired via traditional manufacturing techniques. Functionally graded materials, or in-situ alloys, can be achieved by altering the process parameters or raw materials during the building process. DED also provides a higher deposition rate and larger allowable processing window to powder-bed based AM technologies, making it most suitable for the fabrication of large metallic components of medium geometric complexity [49]. The effectiveness of DED in manufacturing large, medium complexity parts can be attributed to unconstrained build volumes and substantially higher deposition rates than alternative approaches such as L-PBF [50].

Wire arc additive manufacturing - WAAM is a wire-based DED technique that melts the wire feedstock and deposits a component preform, layer by layer, using an electric arc as the fusion source. Fig. 2(d) shows the schematic of a WAAM process. Compared to the electron beam and laser AM processes, which are the alternative sources of fusion in DED described in the Standard Guide for DED of Metals in the ASTM F3187-16 standard series [51], the use of an electric arc offers many processing advantages. Additionally, the absence of any shielding gas in WAAM process could eliminate the possibility of any chemical reactions with much less equipment. Also, the existing arc welding systems can be easily upgraded for WAAM processes.

Unlike conventional manufacturing processes such as casting and forging, the WAAM process does not require specific tools, therefore reducing the cycle time for low production volumes [52]. The ability to use wire as feedstock in DED is complementary, providing high-efficiency material deposition eliminating the need for peripheral powder recycling processes [53], reducing health and safety risks, and offering a substantial price reduction compared to powder [54]. Additionally, low capital investment is a crucial benefit of the WAAM process, as the components of a WAAM machine can be obtained from an open-source welding equipment [55]. In contrast to the alternative fusion sources, the non-vacuum processing characteristics make the WAAM process preferable[36].

4. AM of Nickel-based superalloys

4.1. Alloy compatibility

As in welding, the fusion-based AM processed parts experience non-equilibrium solidification process with complex melt flow and extreme thermal history, and multiple iterations of scanning can affect the bonding between the subsequent layers or tracks and promote the phase transformation within the parts [56]. The processability of Nickel-based

superalloys through the fusion-based AM process can hence be estimated using the weldability of Nickel-based superalloys. Generally, the boundary between weldable and non-weldable Nickel-based superalloys depends on the Al and Ti contents within the alloys, as shown in Fig. 3. It is believed that the γ′ precipitates formed by these constituents are responsible for the cracking formation at elevated temperature [57]. The microcrack formation mechanisms of in Nickel-based superalloys during AM fabrication processes will be discussed in section 4.4.1.

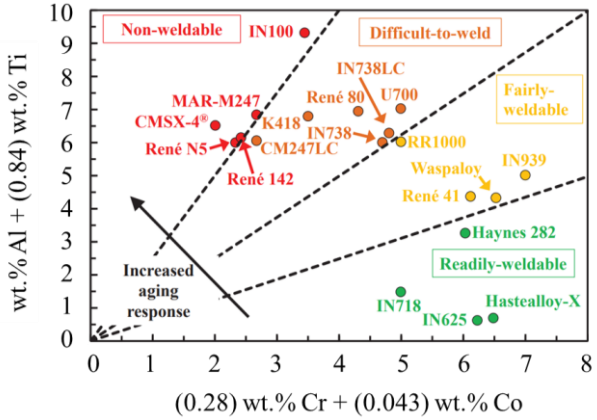

Fig. 3. Relative weldability of various superalloys determined by the compositions of Al/Ti vs. Cr/Co [58].

The selection of Nickel-based superalloys for AM industry will highly remain dependent on their applications. For instance, below is a brief list of Nickel-based superalloys and their common applications. ***IN718*** is mainly used in aircraft engines, high-speed airframe parts, cryogenic tankage, petrochemical applications, nuclear power plants, and cars' turbochargers. ***CMSX-4*** is the second-generation Ni-based superalloy suitable for high-pressure blades of jet engines, helicopter engines, high-pressure turbine shrouds, and gas turbines of power generation. ***Udimet 720*** is commonly used for hot section components such as in gas turbine. ***Waspaloy*** is applicable for jet engines such as cast turbine disks, shafts, low-pressure rings, and seal rings. ***Rene N6*** is basically a single crystal Nickel-based superalloy used for high pressure blades such as those used in military aeroengines. ***IN625*** is a suitable Nickel-based superalloy for nuclear reactors and oceanographic equipment due to its high corrosion resistance as well as the structures in thermal power plants, armoring in aeroengines, and plugs in aeroengines. ***Haynes 242*** is a suitable Nickel-based superalloy for a variety of applications in aircraft and industrial gas turbines. ***MAR-M247*** is commonly used for blades and vanes and integral wheels of helicopter engines and, turbochargers. ***IN738*** is mainly used in gas turbine blades and vanes applications.

4.2. Processing effects

4.2.1. Feedstock

Powder is the most common raw material input for the fused based AM technology. The main advantage of using powder is the industrial supply chain available for metallic

powders[59]. Other advantages of powder feedstock are the feedstock storage, flexibility, and recycling [60]. Varied by the supplier, atomized process by gas or water and plasma rotating electrode process could provide metallic powders with different characteristics (morphology, size distributions, chemistry, etc.) for the fusion-based AM technologies.

Though the major mechanisms of defects formation in AM of Nickel-based superalloys are attributed to unoptimized process parameter, complex chemistry, and residual stress, there are many research articles reported the influence of powder characteristics on the defect formation of AM Nickel-based superalloy components [61]. These characteristics are, but not limited to, powder size, flowability, packing density, shape, chemical composition, and trapped gas inside the powders. The detailed discussions on the effect of powder characteristic on processibility and subsequently on the final product properties are summarized in the following.

Pre-alloyed powders - Due to the complex effect of compositional alloying elements in the Nickel-based superalloys, most of researches still focused on pre-alloyed and atomized commercial alloys such as weldable Nickel-based superalloys including IN718 [62] and IN625 [63] as well as non-weldable ones including CM247LC [64], IN738LC [65], CMSX-4 [66], Mar M-247 [67], Rene 104 [68], and Rene 142 [69]. The γ′-forming elements such as Al, Co, Cr, Ta, and W were found to profoundly increase the viscosity of pre-alloyed powders as compared with that of pure Ni powders [70,71]. As a result, the difficulty to fabricate the pre-alloyed Nickel-based superalloy powders is largely increased. Typically the atomization methodology produces powder size distributions for which less than 10% falls within the size range required for powder based AM techniques [72]. To avoid the waste for developing new alloys for AM with combination of good processibility and mechanical performance, *in-situ alloying* during AM process might be preferable methodology by mixing of different compositional pre-alloyed powders that are homogenized in the melt pool during deposition process.

In-situ alloying can also be significantly beneficial during the DED process due to the larger melt pool area, higher laser powers, and larger area of re-melting, thus, lower solidification rate that is believed to effectively homogenize the chemistry of the mixture liquid [73]. Through the control of powder flow by individual nozzles, the DED process also renders more flexibility to determine the final composition independently, without any concerns of flowability of separate elemental powders. This characteristic also contributes to the capability of creating more homogenized gradient of compositions.

Several studies have been conducted and successfully fabricated NiTi alloy and Ni-Fe-Cr alloys, which were summarized by Mosallanejad et al [74]. It should be noted that, however, fabrication of Nickel-based superalloys via *in-situ alloying* is still challenging due to the alloying elements' different energy absorptivity, melting temperatures, and optical properties that would increase the viscosity while decrease the surface tension of the melt [75]. All of

these can affect the melt pool physics, which in turn would exacerbate the difficulty to achieve the homogeneity in the mixture liquid in the melt pool during solidification. Furthermore, these alloying elements generally have high tendency to segregate to within the inter-dendritic regions or at grain boundaries elevating crack susceptibility during the fusion-based AM processing. Despite the immense potentials of *in-situ alloying*, studies are still required to improve the processibility and homogeneity of Nickel-based superalloys.

Powder characteristics - For the powder bed fusion including L-PBF and E-PBF, the most important characteristics of powders are the flowability and packing density. As the particles are spread by a rack or roller, there are inter-particle forces (Van der Waals forces), gravitational forces, and resistance from moisture against the recoating direction [76]. The particles with poor flowability tend to agglomerate as the resistance against the moving direction is too large and consequently result in non-uniform powder layer and low packing density [77]. Without sufficient packing density, the parts may possess high surface roughness and low relative densities that would significantly undermine the mechanical properties [78]. The packing density of powder also influences the thermal conductivity of powder bed [79] and melt pool kinetics [80] due to the void formation in the bed of powder. Generally, the higher the powder packing density, the higher thermal conductivity of the powder bed. With sufficient rate of heat transfer, powder can be fully melted and reduce the discontinuity of the melt tracks as well as bonding defects leading to better mechanical properties of the final parts [81]. The flowability can be estimated by Hall Flowmeter Funnel [82], Hausner ratio (HR) [83], flow resistance measurement [84], and avalanche angle [85] while packing density can be determined by Gas pycnometry [82] and tapping analysis [82]. Table 1 briefly summarized the characterization methods used for powders in additive manufacturing industry.

Table 1. Characterization methods for powder used in fusion-based AM technology.

Analysis	Method	Description
Size determination	Sieve [82,86]	Not suitable for powder size smaller than 45 μm due agglomeration.
	Light scattering [82,86]	Laser diffraction pattern of powder converted into particle size. Sensitive to powder morphology since it views the powder as a perfect sphere.
	Image analysis [82,86,87]	Microscopy image of powder analyzed to calculate the powder size.
Chemical composition	Inert gas fusion [82,86]	Oxygen, nitrogen, and hydrogen carried by an inert gas from the fusion area. The gas then collected and quantified.
	X-ray Photoelectron Spectroscopy [82,86]	The sample bombarded by X-ray and kinetic energy of ejected K level electrons characterized for element analysis.
	Inductively coupled plasma optical emission spectroscopy/ atomic emission spectroscopy [86]	The sample fed into plasma and convert into free atoms with specific emission spectra, which are quantified using the the intensity of each spectrum.
	Energy Dispersive X-ray Spectroscopy/	The sample surface is excited by electron or X-ray and ejected electron from the inner shell and outer shell of

	X-ray Fluorescence [82]	element are analyzed for element characterization based on the released energy in X-ray.
	Auger Electron Spectroscopy [86]	The machine quantifies excited Auger electron (L level electron).
Flow characteristic	Hall Flowmeter Funnel/ Carney funnel [88]	Powder feedstock flows through the funnel freely. The flow time represents the flowability of powder.
	Flow resistance measurement [84]	The force or the energy which is needed to push the powder flow is recorded and considered as flowability.
	Tap density testing (Hausner Ratio/ Carr index) [83]	The ratio of bulk density (or apparent density) and tapped density of powder is considered as powder flowability.
	Avalanche angle [84]	Certain amount of powder is sealed inside a cylindrical drum and then rotated. The cross-section image of rotating powder is recorded and analyzed between different powder batches.
Density analysis	Hall Flowmeter Funnel/ Carney funnel/ Scott volumeter/ Arnold meter [82]	The powder flows freely and slowly into a small chamber with known volume. The weight of powder filled the chamber is measured and used for apparent density calculation.
	Tapping analysis [82]	The powder is placed inside a graduated glass cylinder and then tapped until no further decrease in the volume. The tapping density of powder is then calculated.
	Gas pycnometry [82]	The pores between particles are filled with gas. The gas volume is calculated and converted into packing density of powder.

Flowability and packing density of powder are determined mainly by the powder size distribution and morphology. Powder with smaller particle size has more surface area, thus, has higher interaction between particles. It was noted that particles with the size smaller than 10 μm could lead to severe agglomeration arising from interparticle forces (typically Van der Waals forces), and degrade the flowability or packing density of powder [77]. Powder size also influences the energy absorption of powder. It is reported that small particles have higher energy absorption due to more surface area exposed to irradiation which in turn increase the scattering of irradiation [89], and therefore will impact the process window of the fusion-based AM processes. Since small particles may adhere to the surface of large particles, a wide range of size distribution of powder with ultra-fine particles usually imparts a poor flowability. Without the satellite particles, on the other hand, a wide range of size distribution of powder provides a better packing density and a better bulk density of AM components since small particles could fill the gap between larger particles [78].

Particle shape - Another powder characteristic which associated with flowability and packing density is particle shape. Spherical powder with smooth surface could prevent friction between particles, improving the flowability and the packing density of the powder feedstock [90]. Each variable was also confirmed by a study investigating the processability of different IN738LC powders processed by L-PBF [65]. As shown in Fig. 4, a good combination of

spherical particles as well as particle size distribution without satellite particles smaller than 10 μm can result in a decent fraction of porosities below 0.5 %. The results also verified that powder fabricated by water atomization possessed the largest fraction of porosity due to its irregular morphology. It was thought that gas atomized powder seemed to perform better than water atomized powder, but there are still limitations to gas atomized powder, such as satellite particles. Although recoating of powder is not required for the DED process, the flowability of powder seemed to impact the bulk densities of final AM component. A recent study on DED processed IN718 has reported that the powder prepared by plasma rotating electrode processing (PREP) exhibited a noticeable improvement on bulk density by 4.39 % when compared to that prepared by gas atomization (GA) under the same powder feed rate and scan conditions [91]. Despite not explicitly explained, it is believed that the better circularity and flowability in PREP powders allowed the enhanced filling efficiency leading to less porosities.

	d_{10} [μm]	d_{50} [μm]	d_{90} [μm]	Span [−]	Apparent density [g/ccm]	Tapped density [g/ccm]	Hausner ratio [−]
a	10	19	34	1.2	4.27	5.16	1.21
b	7	16	32	1.6	2.34	3.57	1.53
c	23	36	49	0.7	4.27	4.98	1.17

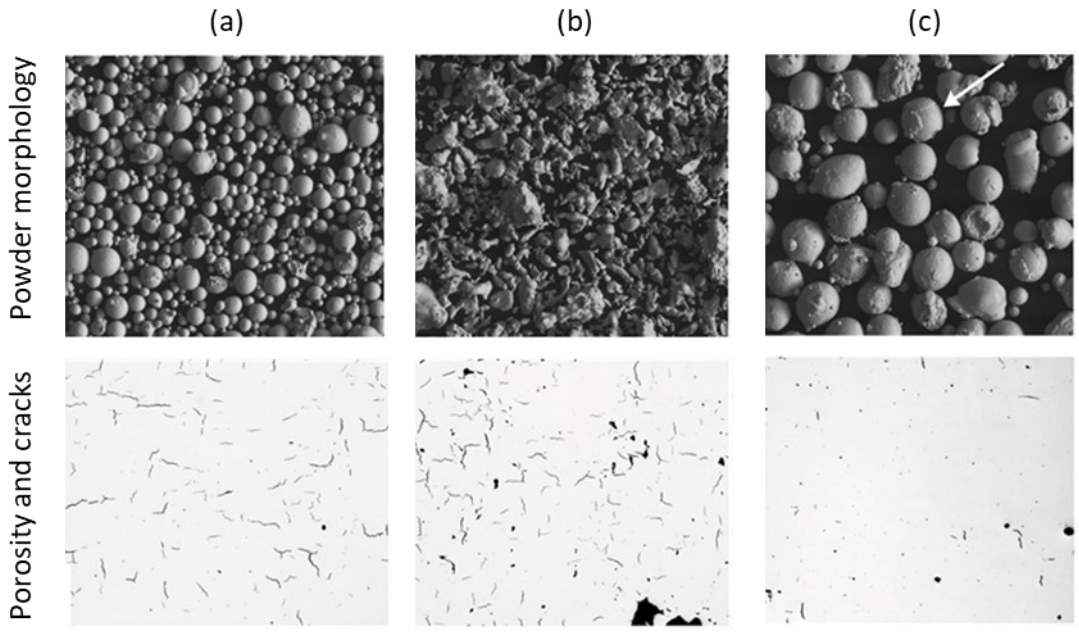

Fig. 4. (Top) Powder characteristics such as size distribution, apparent and tap densities, and Haunser ratio, (middle) scanning electron micrographs of powder, and (bottom) optical images at the cross-section of L-PBF processed Nickel-based alloy indicating porosity and cracking defects [65].

Chemical composition is critical for Nickel-based superalloy and there are essential elements (e.g., Al, Ti, Nb, Ta, V, Cr, Fe, Co, and Mo) to achieve designed properties. It is also well known that trace elements inside Nickel-based superalloy have huge effects on the microstructure and mechanical properties [92]. Among these elements, oxygen content is the most important issues for AM Nickel-based superalloy. Nickel-based superalloy powders have higher oxygen content compared to the wrought or cast ingot [93], thus, the possibility of oxide

inclusions formation in the AM processed Nickel-based superalloy is higher [94]. The excess oxygen could influence the molten pool kinetics [95] leading to severe spattering or balling phenomenon [96] during the fusion-based AM process. The excess oxygen content in powders also degrades the ductility of the final AM processed Nickel-based superalloy components [97].

In addition to the oxygen content, some inert gas or hydrogen could also be entrapped inside the atomized powder [98]. Trapped gas forms bubbles inside the powder which will transfer into melt pool during the fusion-based AM processes. Once the gas bubble does not escape from the melt pool, it will become small pores , thus decreases the density of the final AM components [99].

The other minor elements such as Si, B, P, and C were also reported to affect the AM processability of Nickel-based superalloys. R. Engeli et al. [65] demonstrated that the cracking density of L-PBF processed IN738LC presented a positive correlation with the contents of Si, Ga, and Pb. Similar phenomenon was reported by Tomus et al. [100] in L-PBF processed Hastelloy X in which a low Mn+Si containing alloy showed considerably less cracking than a high Mn+Si containing alloy. In conventional welding, these elements were known to segregate to the grain boundaries, thus, locally decreasing the solidus temperature along the grain boundary areas. According to Tomus et al. [100], the addition of Si up to 1 wt. % can result in a significant decrease in solidus temperature by 33 ^{o}C. These elements (Si, B, P, and C) could potentially be detrimental by forming unfavorable phases such as eutectic or borides [101]. Thus, susceptibility to cracking would undermine the processibility and mechanical properties of the Nickel-based superalloys.

Minor contamination of elements such as C and O enhances the laser absorption in because they are reported to increase the powder-surface roughness. This was validated by the decreasing reflectivity in Nickel-based metal matrix composites (MMC) [102]. It should be noted, however, the deposition of these thermo-resistant particles also degrades the effective thermal conductivity of the powder simultaneously [103]. The cumulative effects of agglomeration of contamination due to the complicated melt pool convection and buoyancy force as well as degraded heat conduction may consequently deteriorate the building efficiency and facilitate defect formation during the fusion-based AM process [104]. The surface modification for metal powders can significantly impact the as-built microstructures and processing window for the optimized scan parameters.

Powder recycling - Since powder characteristics can significantly influence the properties of fusion-based AM components, it is important to thoroughly characterize powders before usage, especially for recycled powders. Spatter, evaporation of elements and oxidation will change the characteristics of recycled powders such as size distribution, flowability, packing density, and chemical composition [105]. The ASTM F3049 standard [82] provides a series of

standard method for metal powder characterization, which are summarized in Table 1.

For powder bed techniques including E-PBF and L-PBF, powder recycling is one of the crucial steps since a small fraction of powders layered on the build plate are melted to manufacture the object. Nevertheless, the heat-affected powders distributing in the periphery of the melted powders may contribute negatively to the recycled powder characteristics due to effects such as oxidation, loss of elements, morphological effects, and size effects leading to variation in mechanical properties [106]. Therefore, sieving is needed to ensure the high-quality powders similar to the virgin powders. However, similar to the Ti-alloys or steels [107], no significant change in mechanical properties was reported in weldable Nickel-base superalloys such as IN718 for recycled powders as compared with virgin powders [108].

The re-melted powder surfaces, spattered particles, and deformed powders that were generated and ejected from the melt pool, however, were found to broaden the particle size distribution in the recycled powder characteristics [109]. Nguyen et al. [110] further reported that the flow rate and the packing density of the recycled IN718 powders were decreased by $1.12s \cdot (50g)^{-1}$ and 0.8 % approximately after 10 cycles. Kong et al. [109] also showed the drop in both ductility and yield strength of AMed IN718 by 8 % and 50 MPa using the recycled powders after 6 cycles due to the change in particle size as compared with those of virgin powders.

Additionally, it was found that the oxygen content in the recycled powders were gradually enhanced with increase in number of recycling. As reported by Rock et al. [111], the oxygen content in the recycled powders can increase by 100 ppm in IN718 powder after 10 times of recycling. Although the un-used particles also slowly gained the oxygen during the building process, the main reason that incrementally mounted up the oxygen content of the recycled powders was found to be the presence of spatter particles, which will be further discussed in next section.

4.2.2. Fabrication

Process parameters - The microstructure, density, and surface quality of the parts processed by fusion-based AM methods are tightly linked to the AM fabrication parameters. Review papers on the process-microstructure relationship have demonstrated that using optimized parameters can effectively suppress the formation of cracks and porosities leading to higher bulk densities in both DED [112] and PBF [113] processes. These parameters include power (laser or electron beam), scan speed, hatch spacing, layer thickness, and laser spot size. For the DED process, powder feed rate would also be considered as an important parameter that defines the minimum track width associated with the hatch spacing and layer thickness. Since parametric studies of AM processes can be complex due to the large amount of process variables involved, combined parameters were also used to design the processing window for Nickel-based superalloys. For example, previous studies have shown that certain measured

responses can be related to a volumetric energy density (VED) (in J/mm^3) defined as VED=P/(V.H.L)x10^6 [114] (where P is power in W, V is scan speed in mm/s, H is hatch spacing in μm, and L is layer thickness in μm).

A study on L-PBF of CM247LC and CMSX486 demonstrated that the cracking density is proportional to the applied energy density [114]. Similar conclusion was also proposed by other studies on PBF processed IN738LC [115] and Hastelloy X [116]. The energy density was also found to correlate with the dynamics of melt pool. Cloots et al. [115] reported that the keyholes were observed in PBF processed IN738LC with relatively high energy densities. The large melt pool dimension due to high energy density induced the micro-humping and overlapping of the adjacent deposits could result in degrading flatness [117]. When processing with comparatively low energy densities, balling phenomenon may occur due to the insufficient flowability of the melt and large tendency to shrinkage, leading to reduced surface area [104,117]. The poor metallurgical bonding also corresponds to decreasing relative density of PBF processed Nickel-based superalloys such as IN718 [117], CM247LC [114], and IN738LC [115]. Since the powder feed rate would determine the size of the deposits in DED process, the coupling of powder feed per unit length and energy density generally dominates porosity and surface quality. The incorporation of feed rate and energy density were widely studied in various superalloys including IN625 [118], IN100 [119], Rene 41 [120], Waspaloy [121], and Hastelloy X [122].

It should be noted that, however, the individual parameters may also impact the resulting properties despite the same VED. Recently, de Leon Nope et al. [123] showed that the most influential processing parameters on porosities are the hatch spacing followed by the power and scan speeds. In particular, the hatch spacings are mainly responsible for the formation of bonding defects whereas the scan speeds dominate the porosities due to the molten pool instabilities (e.g., spherical porosity due to the entrapped gas). The unequal contributions of each processing parameters account for the mismatch of prediction on fraction of porosity and VED. To efficiently and precisely optimize the processing parameters, some studies utilized the computer-aided design and machine learning [81].

The use of different scan strategies can profoundly impact the properties of AM processed Nickel-based superalloys in terms of defect formation, microstructures, and residual strains. Since different scan strategies lead to variations in thermal distribution, the grain structures would vary simultaneously, which are dependent on the direction and magnitude of thermal gradient. The island scanning with rotation of pattern led to more homogeneous grain structures and less texture, showing that a uniform scan strategy may reduce the directionality of thermal gradient that drove the epitaxial growth of the grains (see Fig. 5) [124]. The uniformity of scan strategy was also observed to contribute to the interruption in epitaxial growth of Nickel-based superalloys processed by DED [125]. Likewise, scan strategies with less repetition resulted in less residual strains and thereby the deflection of the builds [126]. The cumulative effects

altered the susceptibility to cracking during the PBF process. Studies have confirmed the repeated scanning and non-uniform scan strategies would significantly mount up the density of cracks especially in non-weldable superalloys such as Rene 104 [127] and CM247LC [128]. The studies clearly revealed the importance to seek for an optimized combination of scan strategy and processing parameters for Nickel-based superalloys processed by fusion-based AM techniques. The underlying mechanisms through which process conditions affect the defect formation (section 3.4), and the subsequent mechanical properties (section 4) as well as the processing optimization (section 6) will be further elucidated.

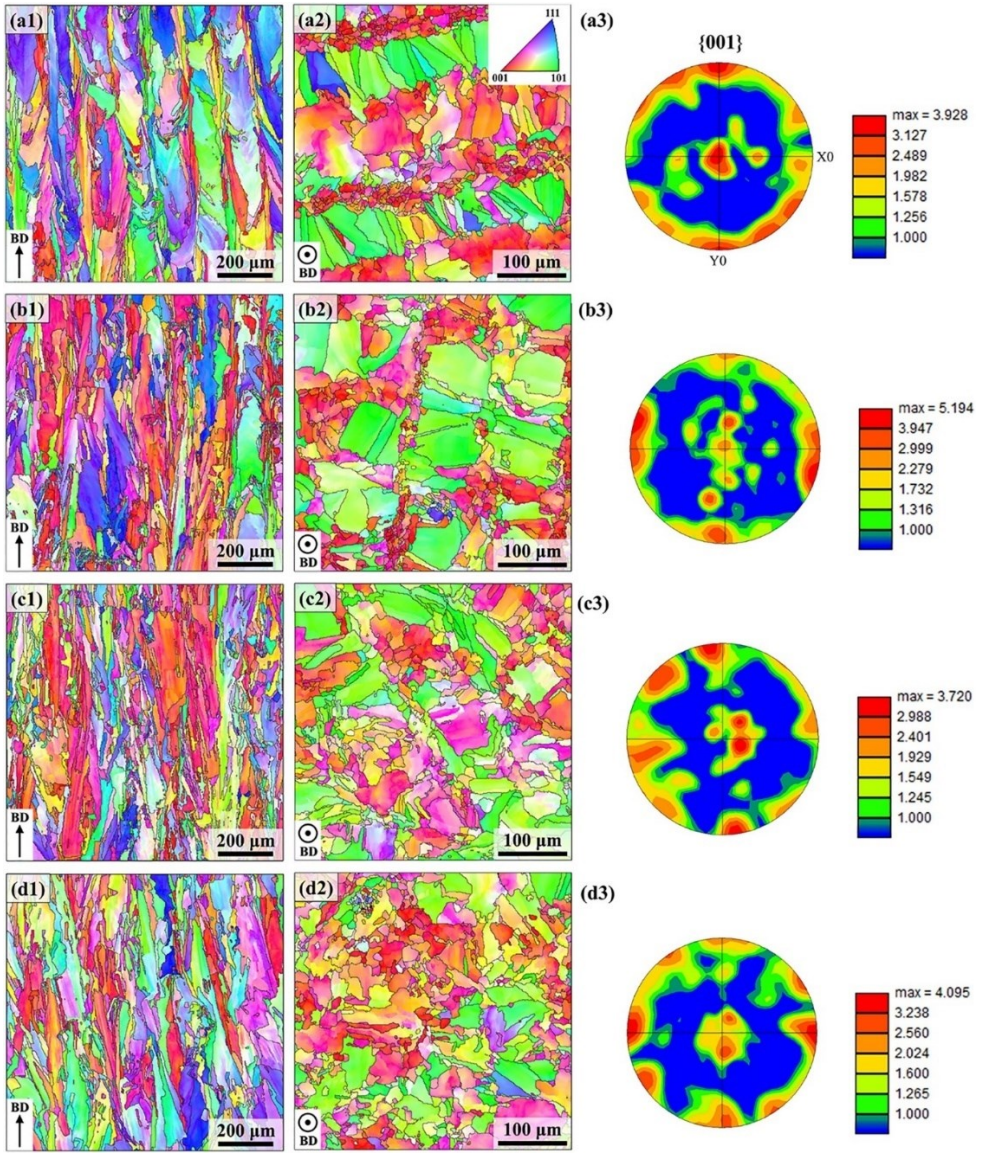

Fig. 5. Electron backscattered diffraction (EBSD) and Inverse Pole Figure (IPF) Z maps showing the grain morphologies of L-PBF processed Hastelloy X using different scan strategies of (a) line scanning without scan rotation, (b) line scanning with scan rotation of 90°, (c) line scanning with scan rotation of 67°, and (d) island scanning with scan rotation of 67°, respectively. Note that the row 1 corresponds to the grain structures with respect to the build direction; row 2 corresponds to the grain structures with respect to the transverse direction; row 3 presents the pole figures for each condition [124].

As in the case of other alloying systems, shielding gas is used in AM processing of Nickel-based superalloys to circumvent the reaction between atmosphere and the powder or melt by

fusion-based techniques. The purpose of using the gas flow is to remove any process by-products such as spatter, condensate, and welding fumes from the path of the laser as well as prevent the formation of detrimental inclusion and porosity. Oxygen is the most influentially detrimental element that facilitates the formation of inclusions and spatters, thus, changes the melt pool physics. Similarly, the reuse of powders exposed to the oxidation environment can lead to drops of various mechanical properties due to the presence of spatter which alters the tendency to form γ'- γ'' precipitates. The PBF build chambers were typically operated under the vacuum or an inert gas (e.g., Ar or N_2) to minimize oxidation both in AM parts and unfused powder [129]. Although the inert gas or vacuum environment are not necessary in DED process, inert shielding gas delivered along with powder flow is still needed to flood the area beyond the melted zone induced by arc or laser to exclude atmospheric gases for forming gas pores or inclusions [50].

However, the atmosphere can interact with the powder bed and melt pool during the AM process. Simulations and experiments have indicated that the atmosphere used for the PBF process significantly impacted the melt pool geometry [130]. As illustrated in Fig. 6, the low-density gases such as He possess faster speed flow than high-density gases under the same pressure and thereby to induce larger dragging force that is proportional to the square of flow velocity. Despite not explicitly understood, the preliminary analysis suggested that the higher flow velocity of gases may induce larger radial flow leading to more pronounced denudation and balling phenomenon. These light inert gases could also potentially raise the cooling rate of the builds fabricated by DED process that is characterized to have comparatively lowing cooling rate due to the generation of large melt pool [50]. As one of the benefits from DED process, multiple shielding gases can be supplied periodically to take the beneficial properties of each shielding gas.

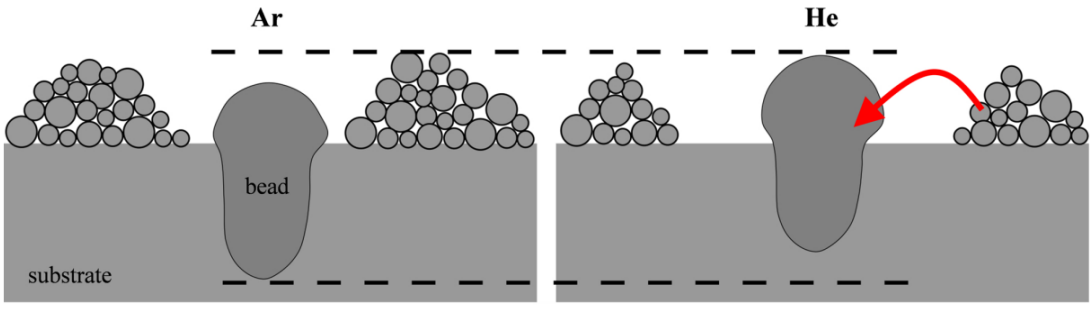

- More denudation under helium gas
- Part of the powder from the denuded areas is incorporated into the bead
- Same global molten surface
- Higher volume above the substrate under helium gas

Fig. 6. Schematic illustration showing the comparison the single bead morphologies in terms of denudation and balling phenomenon under Ar and He atmosphere, respectively [131].

In addition to the flow velocity, the pressure of atmosphere affects melt pool geometry and formation of certain types of defects. Y. Zhao et al. [132] suggested that the L-PBF process

under ambient pressure would cause larger recoil pressure related to the formation of keyhole and surface instability when compared to the E-PBF processed under vacuum condition [132]. The more intense convection and evaporation in L-PBF process account for smaller melted zone induced by faster heat dissipation, while, increasing fraction of porosity. The pressure-dependent defect formation was also confirmed by Calta et al. [133]. The operating environment can profoundly influence the processing window of Nickel-based superalloys processed by fusion-based AM where optimized microstructure and density are achieved.

Wall effect - During powder bed AM processes such as L-PBF and E-PBF, particles are spread as a thin powder layer by a rake (usually a roller, blade, or brush) and then the laser or electron beam perform fusion process. The rake contacts with powders and influences the powder bed condition directly. Chen et al. [134] investigated the interaction between powder particles and the rake during powder spreading through computational modeling. They found when powder particles flow through the gap between the rake and baseplate, some particles located at the surface of powder bed could be removed since the space is not enough for powder particles. Also, there is a net of transient contact force between powder particles, which sometimes develops into a ‘’force-arch”. The force-arch is hard to break, and it could act as a dynamic wall and remove powder. These phenomena were called “wall effect” since the powder is blocked from flowing through the gap just like there is a wall here. Consequently, this creates voids on the powder bed surface and decreases the packing density of powder bed. Nan et al. [135] suggested if the gap is much larger than powder particles, it is less likely that powder could be dragged by the rake, thus, the powder bed has higher density. Fig. 7(a,b) illustrates the “wall effect” and the influence of powder size and gap space. However, it should be mentioned that increasing gap space leads to thicker powder bed, which requires higher energy input for melt formation. Simultaneously, decreasing particle size could degrade the powder flow and packing density. To reach the balance, powder size, gap space and other process parameter should be well controlled during fusion-based AM process.

Powder spreading - In addition to the micro-voids, some macro-flaws of powder bed could be observed during powder bed AM processes, which could lead to instable powder distribution. These flaws transfer into porosity [136] or even severe failure of AM components. They are considered as powder spreading anomalies and related to abnormal behavior between rake, powder bed and as-build AM part. Scime et al. [137] demonstrated different anomalies during the powder spreading and categorized them into six types (Fig. 7(c)). According to the literature and similar work from Foster et al. [138], the rake might strike the “super-elevation” of AM components and hop during powder spreading, causing part failure and unsmooth powder bed. If the rake is damaged by super-elevation or contamination on the powder bed, it could lead to stripes on the powder bed which are parallel to spreading direction.

The “super-elevation” occurs when AM components warp up above the powder layer. Warping is a common defect observed in the overhang structure of AM components without proper support design [139]. Since the powder bed beneath the overhang structure has poor thermal conductivity compared to as-build solid part, the heat from the energy source concentrates at the overhang. This will result in high thermal gradient and shrinking to the overhang structure. Part failure also causes warping and super-elevation because heat cannot dissipate through the failure surface. Rough surface or spatter of AM components with improper fusion parameter also leads to super-elevation and damages the rake during powder spreading [138]. To alleviate issues related to powder spreading using a conventional dispenser (such as blade, roller, brush, etc.), it could be practical to use a non-contact electrostatic powder dispenser.

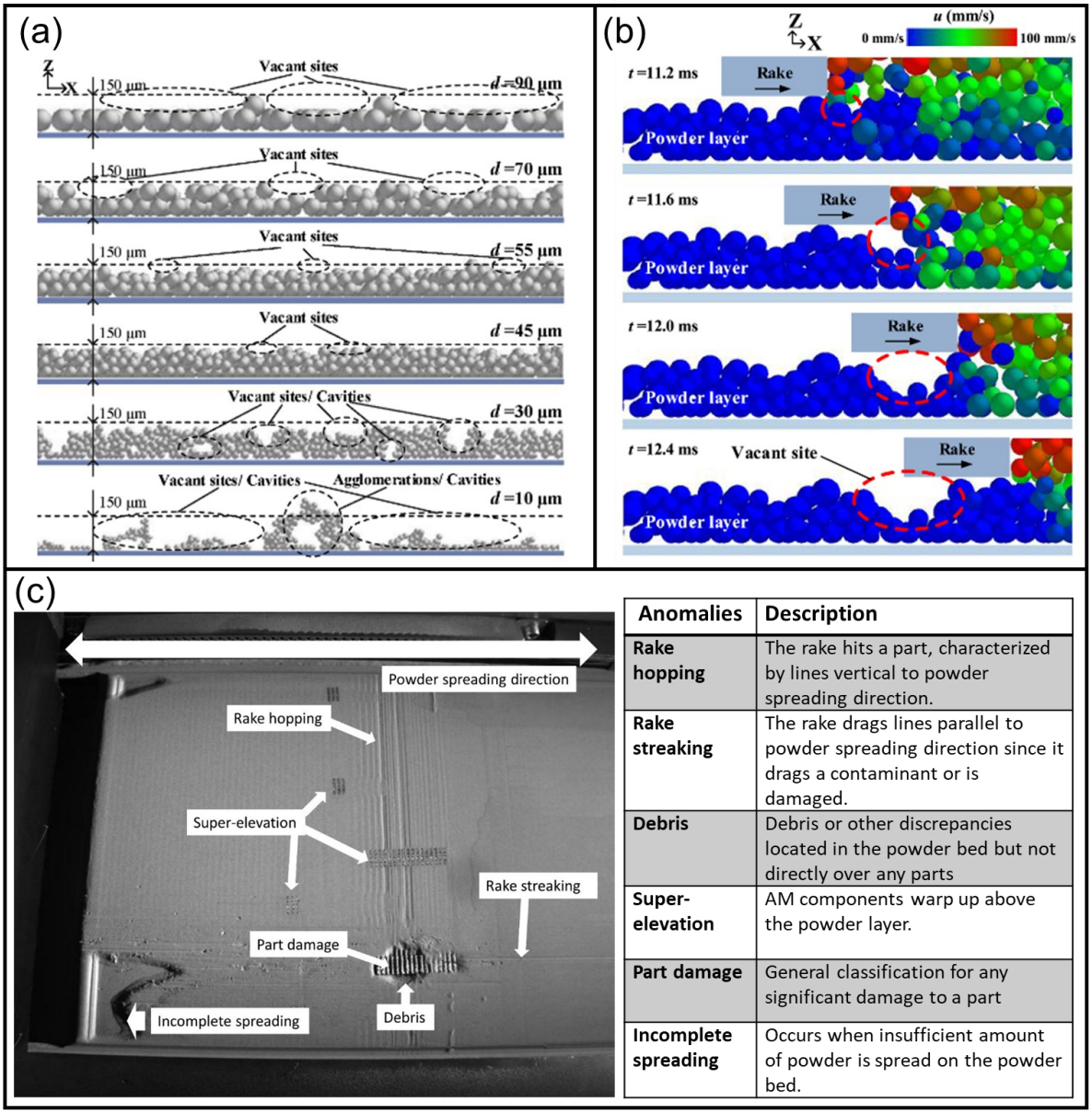

Anomalies	Description
Rake hopping	The rake hits a part, characterized by lines vertical to powder spreading direction.
Rake streaking	The rake drags lines parallel to powder spreading direction since it drags a contaminant or is damaged.
Debris	Debris or other discrepancies located in the powder bed but not directly over any parts
Super-elevation	AM components warp up above the powder layer.
Part damage	General classification for any significant damage to a part
Incomplete spreading	Occurs when insufficient amount of powder is spread on the powder bed.

Fig. 7. The powder spreading dynamic in powder bed fusion AM process. (a) The relationship between particle size and layer thickness in term of powder bed quality and uniform spread powder. (b) The dynamic “wall effect”:

when rake pushes the powder pile, strong contact force between powder drags some particles from the powder layer [134]. (c) The illustration of powder bed anomalies [137].

Spattering **-** Spattering is a common phenomenon observed during fusion-based AM process. When the high energy source fuses the feedstock, welding sparks are ejected from the fusion zone. These sparks then solidify as solid particles and disperse inside the working chamber. Spattering is critical especially to the fusion-based AM process with powder bed because the spatter could attach on the surface of AM components or powder bed in processing, it might cause powder bed anomalies by damaging powder spreading rake [137] or cause LoF if the next layer scanning cannot melt the large particles completely [140].

Gasper et al. [105] have divided the spattering into two categories: (1) the molten material ejected from the molten pool, and (2) the particles entrained by an ambient gas flow or electrostatic force of electron beam [141]. The spatter ejected from the molten pool was demonstrated to be related to the forces induced by Marangoni flow and recoil pressure [142], in which the molten material is pushed to the edge of the molten pool and ejected to the surrounding. On the other hand, the feedstock particles on the powder bed could be entrained by the inert gas flow induced by the vapor jet of molten pool [143]. For electron beam melting, the electron beam not only creates a molten pool but charges the metal particles and substrate. The electrostatic force then triggers the powder jet [141]. If the entrained particles are molten by the energy source, they become “hot ejection spatter”. While some particles are not molten by the energy source and retain their morphology, they are “cold ejection spatter” and has less influence on the process. The vaporized material especially the elements with low vapor pressure also causes nano-particles [107], which attach to the surface of the chamber or the optical lens and are harmful to human health and performance of energy source.

Spatter will be collected with un-melt powder as recycled feedstock after the process. Ejected material from the molten pool solidifies as spherical particles. However, the size of spatter may be different with virgin powder and change the powder size distribution of recycled feedstock [144]. Entrained particles with partial melting could form agglomerates and degrade the aspect ratio of recycled feedstock. As mentioned earlier in section 4.2.1 about powder characteristic, powder morphology will impact the flowability and packing density of recycled feedstock [78]. Furthermore, it was reported that molten spatter could react with oxygen inside the chamber. Nickel-based superalloy usually has elements such as Al, Ti, Cr, and Si to reach the property requirement. These elements interact with oxygen under low oxygen partial pressure based on Ellingham diagram [145]. Gasper et al. [105] reported the oxide film of Al and Ti with the thickness hundreds of nanometers on the surface of spattered particles in L-PBF processed IN 718. They also reported the oxide of Cr and Si on the spattered particles of L-PBF processed Hastelloy X [146]. The oxide film formation might increase the oxygen content of recycled feedstock [97] and provide a source for oxide inclusion formation inside the AM Nickel-based superalloy components. More details about the oxide will be discussed

in section 4.4.1 about inclusion.

Based on the observations for the spattered particles, Fig. 8, oxide spots and films generated by the AM process can be clearly identified, either by liquid ejection or by particle entrainment (Fig. 8c). Despite the subtle change in chemical compositions, slight amount of Al and Ti was characterized reacting with oxygen leading to the formation of Al-rich and/or Ti-rich oxides, acting as heterogeneous nucleation sites for Nb/Ti carbides that further deprive the γ'-forming elements [147]. The increasing density of oxide inclusions was also confirmed by Kong et al. [109], Gasper et al. [105] and Nandwana et al. [107]. The presence of elemental oxygen and/or oxide particles may slightly influence the microstructures and mechanical properties of the built part attributed to the impediments to the movements of dislocations and grain boundaries [148].

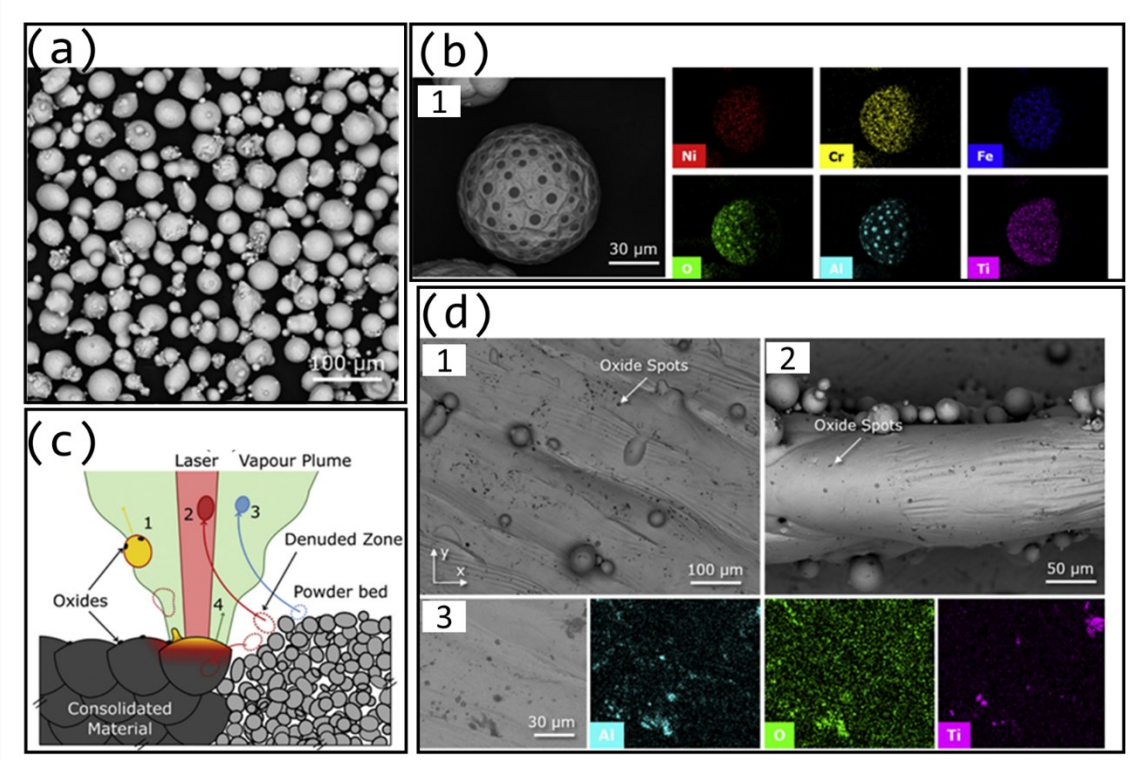

Fig. 8. (a) SEM micrograph of nickel alloy 718. Backscattered electron SEM micrograph and EDS elemental may analysis from (b) a spattered nickel alloy 718 particle, and (d) surface of the L-PBF process IN718 where oxide spots are detected, (c) Schematic illustrating laser-powder interaction and how spattered particles form during PBF process. Reprinted with permission from Ref. [105].

To reduce the influence of spattering, a proper energy input during fusion-based AM process is important since the spattering is associated with kinetic stability of the molten pool [149]. A large energy density causes a deeper keyhole and more vaporized material, which leads to unstable molten pool kinetics. For L-PBF, a gas flow and proper specimen position are suggested to prevent the components from being covered by the spatter [150]. For electron beam melting, a vacuum chamber is shown benefit to stabilize the molten pool with smaller recoil pressure [132]. Also, low beam current and defocus electron beam could avoid the

unexpected powder spreading because of the electrostatic forces [151]. For recycled feedstock, it is suggested to sieve the powders after cycling use to remove agglomerates or huge particles. Composition analysis is also recommended for recycled feedstock [146].

Elemental evaporation - During the fusion-based AM processes, high energy source interacts with molten pool and evaporates the molten material, which causes gas expansion and recoil pressure inside the molten pool [149]. However, the elements of molten material evaporate in different rates since some elements have higher vapor pressure under specific temperature. The selective vaporization cloud cause compositional changes and impact the subsequent properties of the fusion-based AM components. Based on the well-known Langmuir equation [152], the evaporation rate of alloying elements of a molten liquid under low pressure is defined as $J=P/\sqrt{(2\pi MRT)}$ (where J is the vapor flux, P is the partial pressure of the vaporizing element over the liquid, M is the molecular weight of the element, R is the gas constant and T is the specific temperature in k). Though it was reported that the experiment data of AM components has about 5~20% deviation or more between the calculation results [153], the equation still provides a good approach to understand the selective evaporation of alloying elements during fusion-based AM process.

Mukherjee et al. [153] found that for IN625 alloy with fusion-based AM process, the element loss of Cr is about 0.01 wt. %, which is less susceptible to elemental evaporation compared to Ti-6Al-4V or other alloys with high Mn content. Ahsan et al. [154] calculated the mass flow of L-PBF processed IN718 and found that Ni and Cr have the maximum concentration change (~0.2%) under high energy density fusion. A similar result given by Nandwana et al. [107] showed that Cr and Ni have the largest mass flux during E-PBF process. These findings indicated that the element with high vapor pressure and high concentration fraction in Nickel-based superalloy could experience concentration loss while the elements with low vapor pressure will segregate during fusion-based AM process. Also, Gasper et al. [105] and Nadawana et al. [107] found that Ni and Cr had the maximum concentrations in the plume. Panwisawas et al. [155] also showed that Cr and Co have about 1 at% loss after L-PBF process. Although, a compositional variation of about 1~2% does not seem critical for the AM Nickel-based superalloys, extra caution and careful efforts need to be employed to fulfill the alloy standard compositional requirements. It is also important to use extra caution about the powder condition because the spatter with elemental evaporation which could influence the composition of recycled powders and subsequently impact the mechanical properties of the resultant AM components [97].

4.3. Microstructure

AM process optimization includes adjustments of scan parameters and pre-heat temperature. Since no additional procedures are needed, it possesses higher freedom of

adjustment and lower cost when compared to heat treatment. Overall, the process optimization aims to minimize the thermal gradient by (1) decreasing the cooling rate and (2) altering the melt pool volume and partial re-melting volume of the deposited layers or tracks. Pre-heating the substate can effectively reduce the thermal gradient that exists between successive layers by prolonging the cooling time, and thus reducing the residual stress during the solidification. The effectiveness has also been validated for Nickel-based superalloys processed by fusion-based AM [156]. It should be noted, however, the processes such as E-PBF has already used the pre-heated substrate up to 1000 ℃. Although the magnitude of residual stress is lower in E-PBF processed parts compared to other laser-based techniques, other strategies such as adjustments of scan parameters could further reduce the level of residual stress. Nickel-based superalloys fabricated by fusion-based AM techniques generally present the columnar-grained feature with respect to the building direction while equiaxed feature with respect to the transverse direction, and process parameters such as different scan strategies may result in different degrees of non-epitaxial solidification that accounts for variations in texture tendencies. This microstructural morphology has widely been reported in several Nickel-based superalloys processed by L-PBF [157], DED [158], and E-PBF [159].

4.3.1. Grain structure

The forming mechanism by which grains grow within single-track molten pool as well as the overlapping regime between successive tracks or layers is schematically illustrated in Fig. 9 [160]. For Nickel-based superalloys with fcc crystal structure, the formation of columnar grained structure tends to follow the [001] direction due to lower elastic modulus than that along [110] and [111] directions [161]. Driven by the thermal gradient denoted by vector G (in Fig. 9a), the grains with [001] direction would grow preferentially with respect to the melt pool boundaries. Particularly, three kinds of grain growth modes could be activated. In zone A where G_z dominates the vector G (i.e., $G_z \gg G_y$), the columnar grains keep growing along [001] direction under the thermal gradient G. With moving the location away from the center (e.g., zone B), G_y increases to a considerable value which is comparable with G_z, both grains with [010] and [001] direction are growing competitively, leading to the coexistence of columnar grains and equiaxed grains. Eventually, the G_z becomes predominant in the edge of melt pool (i.e., zone C), thus, the grains grow perpendicularly to the building direction. Gu et al. [162] provided a more comprehensive quantitative thermal data for L-PBF processed IN718 using ANSYS analysis. The cooling rate in this study was estimated to be 10^6 K/s at the center of melt pool and decreased when leaving the center; the thermal gradient was found to approach 0 at the center of melt pool and then drastically increased away from the center. According to the criterion proposed by Hunt et al. [163] and modified by Gaumman et al. [164], the large cooling rate and low thermal gradient favor the columnar to equiaxed transition (CET). This is in good agreement with the microstructural change from columnar to equiaxed structure in the

middle of melt pool.

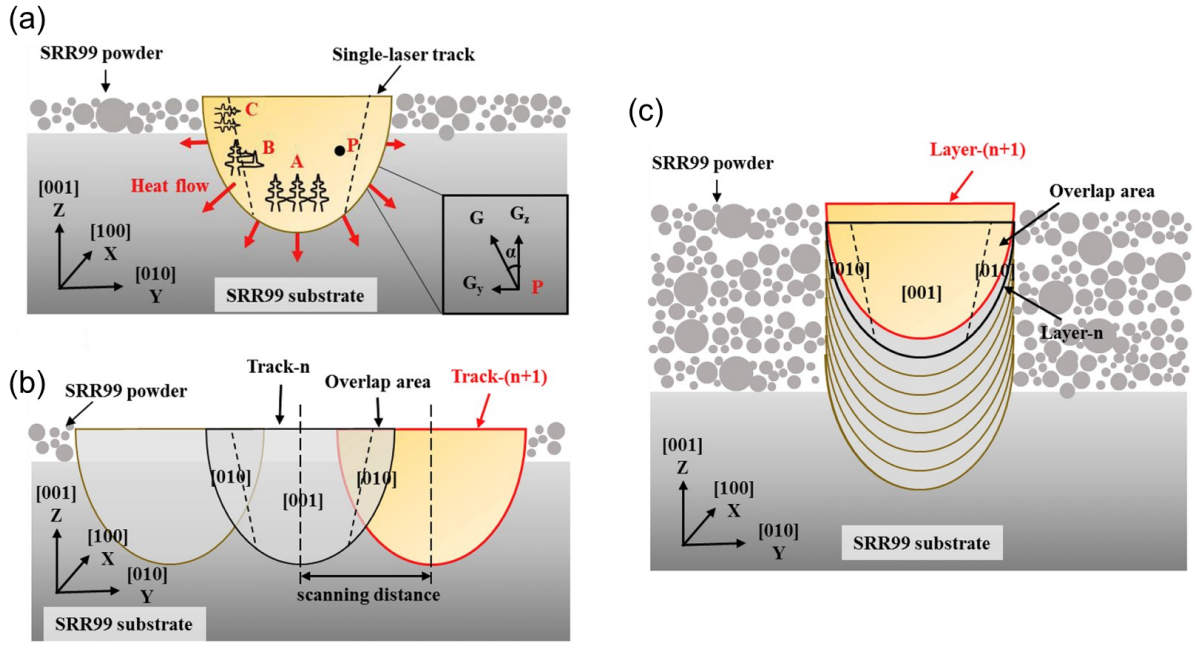

Fig. 9. Schemetic illustration showing the dendritic growth within (a) single-track molten pool, (b) multi-tracks molten pool, and (c) overlap zone between successive layers [160]. (d) Microstructural profile of L-PBF IN718 and different zones within the cross-section of molten pool [162].

The grain structure in AM processed samples is affected not only by a single bead but also due to the successive tracks or layers. Yang et al. [160] reported that the competitive growth in overlapping region away from the middle of melt pool results in cellular structures (see Fig. 9 b) while the grain growth is dominated by [001] direction in the middle of melt pool , which accounts for the growth of elongated grains (see Fig. 9c) due to the successive layers or tracks. This competitive growth followed by thermal gradient also changes the grain orientations along build direction when different scan strategies are utilized. Helmer et al. [165] reported that the columnar grains grow in a zigzag pattern corresponding to the rotation of scan pattern whose borders reveals the existence of a high fraction of equiaxed grains owing to highly competitive growth along different directions. Similarly, the coupling of competitive growth and scan tracks also result in a complex texture with respect to the transverse direction depending on the scan strategy applied. For example, the “chessboard-like” scan pattern is typically present in samples built by zigzag scanning rotation between successive layers. Additionally, the average grain size of built parts was found to increase with increasing heights attributed to the decreasing cooling rate. This microstructure evolution is more pronounced in E-PBF processed samples as compared with L-PBF ones because the cooling rate is lower due to the pre-heated substrate. As displayed in Fig. 10, the columnar grain width increased substantially due to the increased sample height [101]. Likewise, the lower cooling rates during E-PBF and DED process are also favorable for epitaxial growth for Nickel-based superalloys. By comparing the grain structures of L-PBF processed (see Fig. 12a) and E-PBF processed (Fig. 12b) SB-CoNi-10 superalloy, it could be seen that the columnar grains grew continuously in E-PBF processed

specimens, i.e., exhibited more predominant <001> texture than that in L-PBF processed specimens [166].

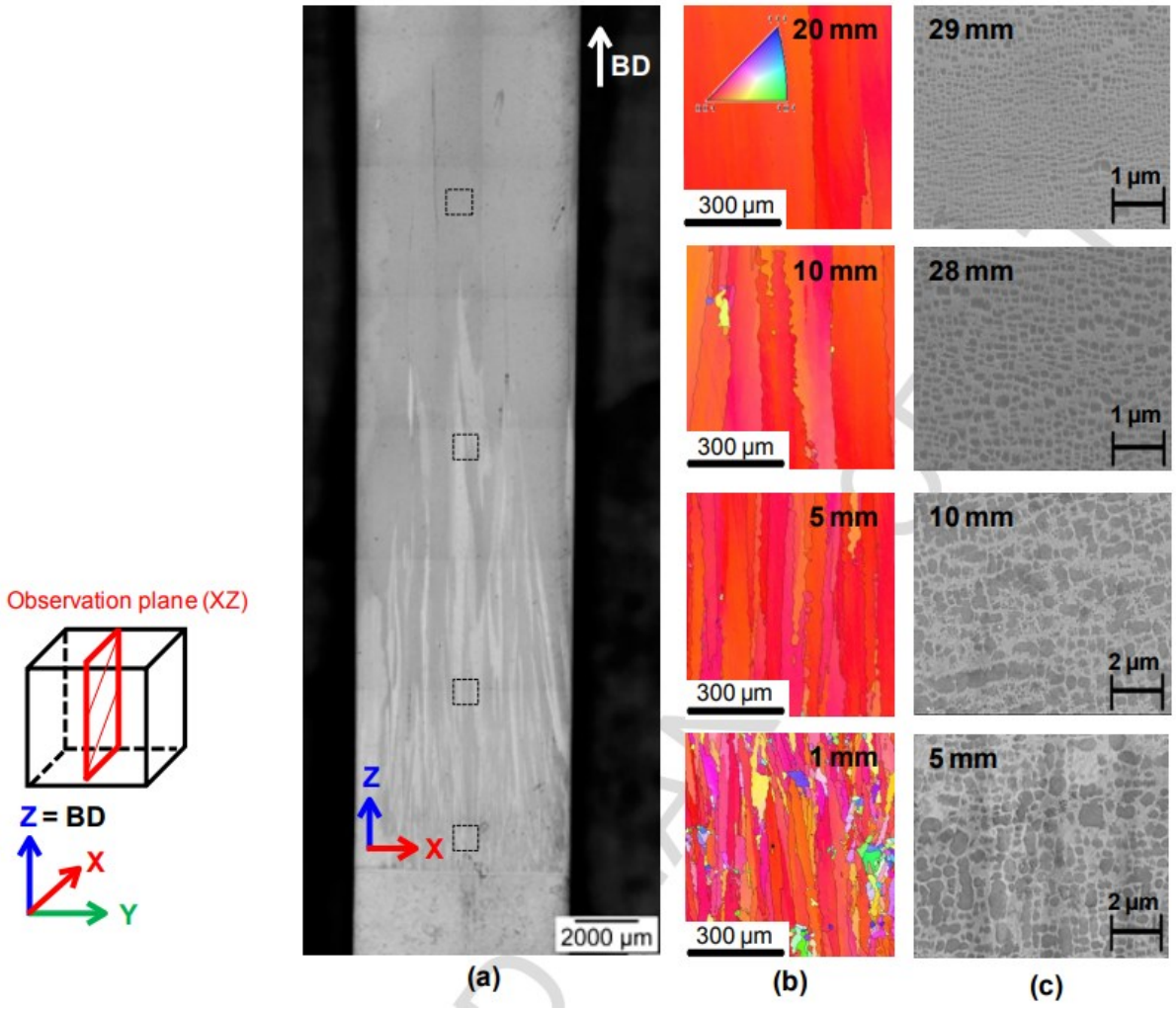

Fig. 10. Microstructure of E-PBF processed non weldable Ni-Co-Cr-Mo-Al-Ti-B Nickel-based superalloy from bottom to top observed by (a) optical microscope, (b) EBSD, and (c) backscattered electron scanning electron microscopy (BSE-SEM) [101].

By adjusting scan parameters and therefore changing the thermal history the columnar-to-equiaxed transition (CET) are facilitated. In addition to reduced degree of anisotropy, it is found that the equiaxed grain structure can effectively inhibit the crack propagation in AM processed Nickel-based superalloys [167]. A more comprehensive discussion on process optimization and controls of microstructures for Nickel-based superalloys will be elaborated in next sections such as 5 and 6. For the non-weldable Nickel-based superalloys with small processing window, the parameter optimization may not be easily achieved without porosities and cracks that are detrimental to the mechanical performance.

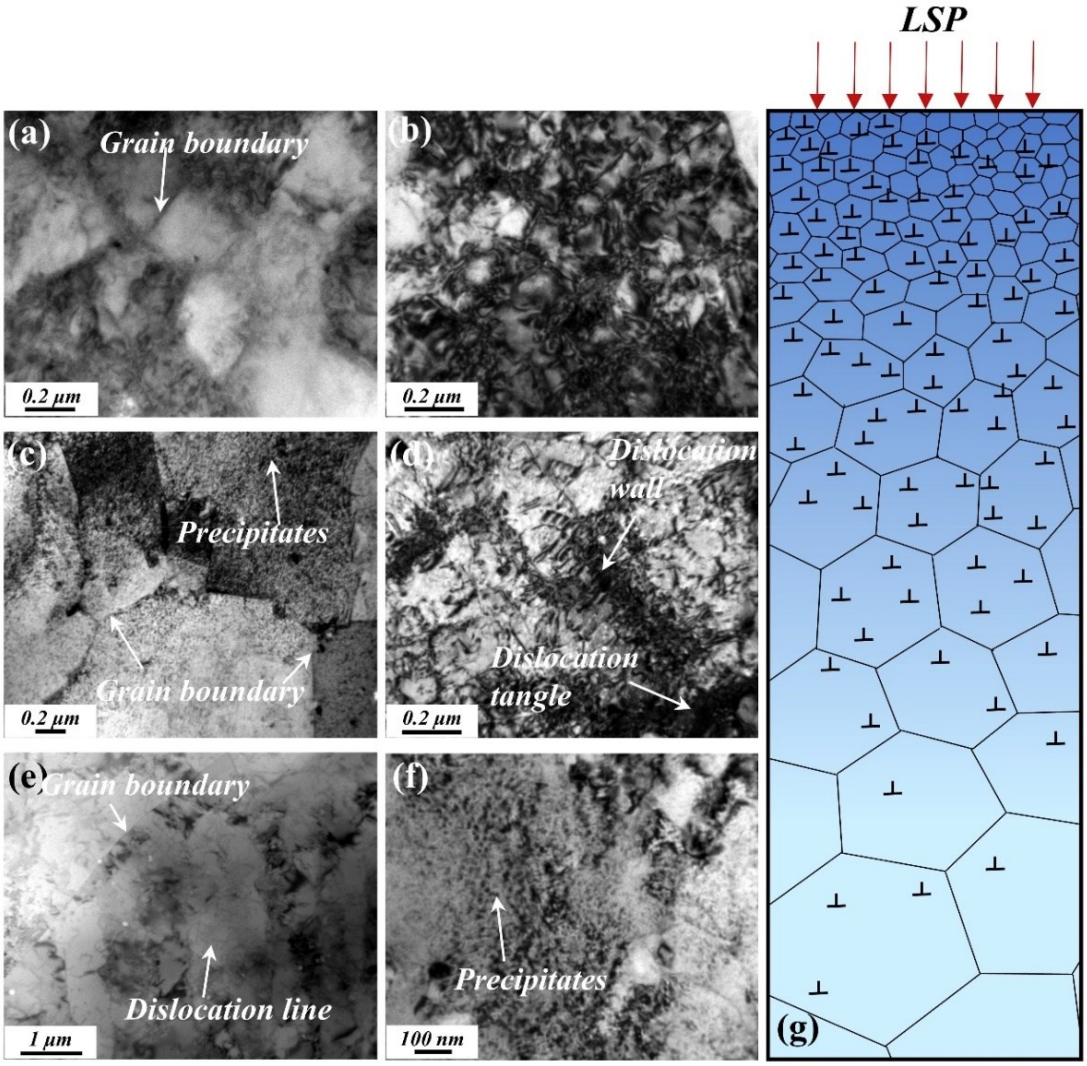

Fig. 11. TEM micrographs of IN625 upon treated by laser shot peening at different areas along the build direction: (a,b) near the top surface, (c,d) at a depth of 100 μm, and (e,f) at a depth of 1000 μm. (g) A schematic showing an overview of the microstructure [168].

After heat treatment, the texture was found to be less pronounced. Previous studies have shown that the formation of isotropic grain structure can be achieved when supersolvus heat treatments are applied [169]. With insufficient temperature applied, however, the pinning effect contributed by precipitates may inhibit the migration of grain boundaries resulting in an unchanged grain structure. This is corresponding to the predominant anisotropy within AM processed Nickel-based superalloys upon heat treatment with their standard conditions based on the conventional process [170]. The grain structures after heat treatment are also affected by the selected processing technique. Attributed to sufficient pre-heating that eliminates the majority of the residual strains while reduces the cooling rate, a comparatively coarser grain structure would be obtained in E-PBF processed parts when compared to L-PBF processed parts. The EBSD IPF Z maps shown in Fig. 12 (a-7) clearly demonstrated the increase in grain size by more than 100 μm within SB-CoNi-10 superalloy [166].

Park et al. [171] reported that the number fraction of low angle grain boundary (LAGB), which is believed to be associated with the crack initiation point, and the average misorientation angle were significantly lowered with 5% energy density of the laser remelting for the first scan. Other studies focused on the use of heat treatments. Studies have demonstrated that the tensile residual stresses responsible for cracking can be relieved by compressive stresses induced by laser shock peening [168] or high-pressure rolling [172]. As confirmed by the transmission electron microscopy (TEM) in Fig. 11, dislocation entangled with fine precipitates and fine recrystallized grains can also be achieved that strengthen the materials with superior resistance with crack propagation [168].

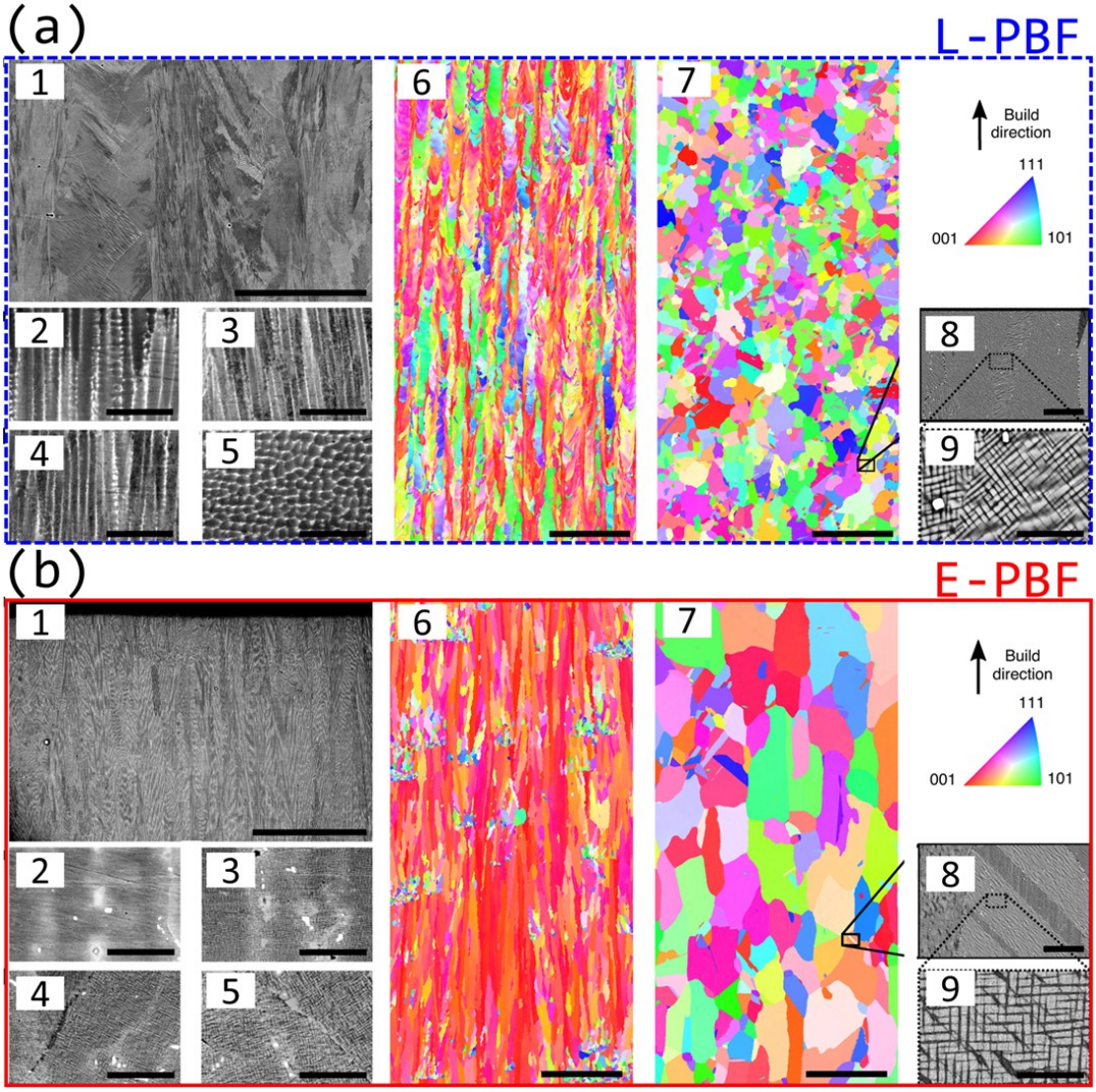

Fig. 12. SB-CoNi-10 superalloy processed by L-PBF in (a) and by E-PBF in (b) [166]: (1) Stitched BSE image showing the as-built microstructure . The particular microstructures near, 1 mm below, 2 mm below, and 4 mm below the final build layer are shown in (2), (3), (4), and (5), respectively. IPF Z maps showing the vertical section of as-built and heat-treated samples are displayed in (6) and (7), respectively. Observations at high magnification showing the γ-γ′ structures of heat-treated samples are further emphasized in (8) and (9). Note that the scale bar for (1) is 50 μm; the scale bars for (2–5) are 5 μm; the scale bars for (6) and (7) are 500 μm; the scale bar for (8) is 25 μm; the scale bar for (9) is 5 μm [166].

4.3.2. Phase formation

The thermal history occurring during the AM processes determines the microstructural evolution of Nickel-based superalloys. In the fusion-based AM techniques, the cooling rate is within 10^3-10^8 K/s, which is significantly larger than that in welds or castings [173]. This high cooling rates result in a fine dendritic grain structures and features surrounded by high density of dislocations. In addition, the solidified region may be influenced by re-melting or heat affected zone (HAZ) occurring during the successive scanning sequences. The cyclic heat input enables faster diffusion of refractory elements for nucleation as well as higher cooling rate and thermal gradient rendering larger undercooling and sufficient nucleation sites. Both factors contribute to fine-dispersed precipitates with limited growth in AM processed Nickel-based superalloys [174]. As shown in Fig. 13, the microstructure of L-PBF processed IN718 [175] consists of more delta phase precipitates along dendritic boundaries and grain boundaries with smaller particle size as compared to those processed by forging or casting [170].

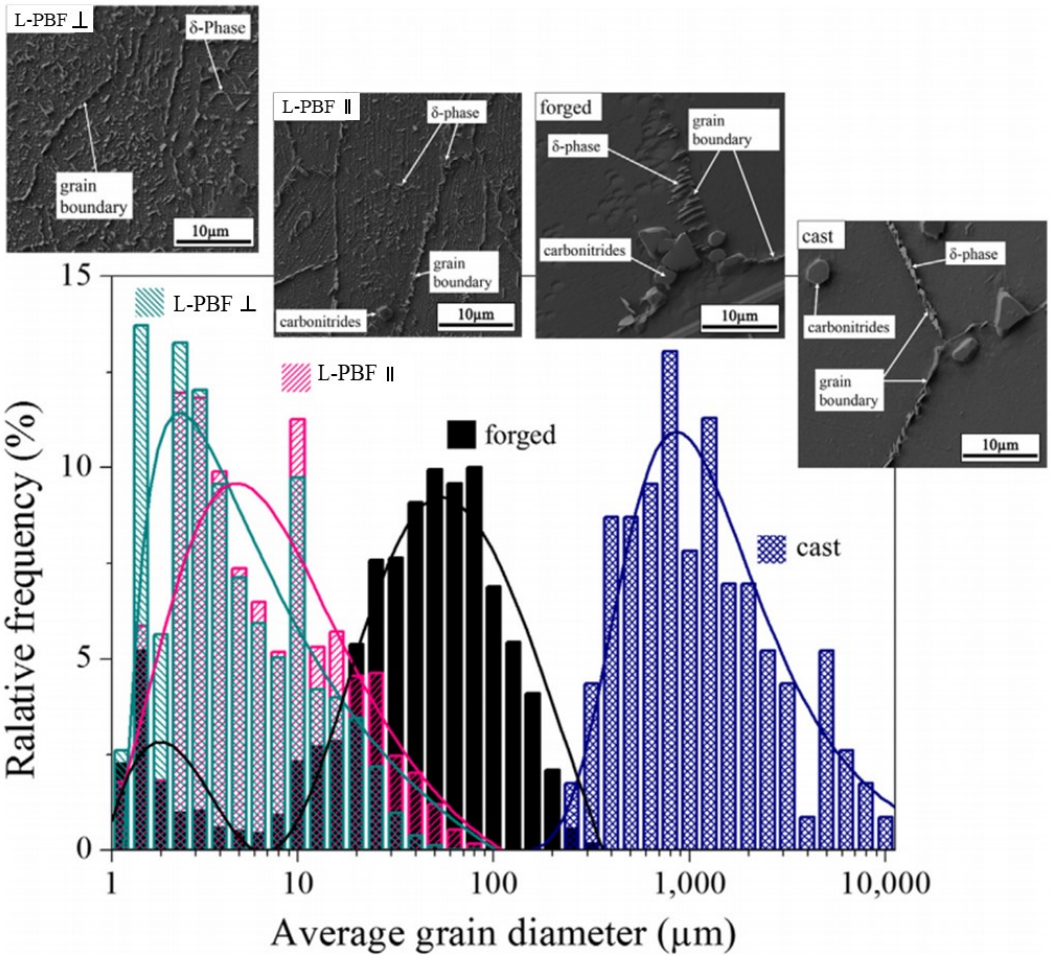

Fig. 13. Microstructure and grain size distribution of L-PBF processed IN718. Forged and cast microstructure with corresponding SEM pictures are also included [170].

Interestingly, depending on the differences in thermal gradient and cooling rate, the dendritic structure and phase transformation may vary, and pre-heating of substrate may further influence the size distribution of precipitates in different AM processes. Based on

experimentally derived cooling rate/dendrite arm spacing (DAS) relationships, DAS was found to vary inversely with the cooling rate [176]. Due to the pre-heating during E-PBF process, the cooling rates in laser-based AM processes including L-PBF and DED have been reported to be 1000 times greater [174]. As a result, it would be expected that E-PBF promotes coarser dendritic structure as compared with the laser-based AM processes, which in turn could further result in a larger degree of segregation in the former. This is evidenced by the works conducted by S. P. Murray et al. [166], as demonstrated in Fig. 14. The largest DAS with severe micro-segregation in alloy processed by Bridgman casting confirmed the cooling rate-controlled solidification process. Similar observations were summarized by Murr et al. [177]. Simultaneously, the pre-heating in E-PBF process allows the growth of precipitates but reduces the residual strains. As a result, although the fraction of precipitates is decreased, the average size of precipitates would be larger in the E-PBF processed Nickel-based superalloys. This is evidenced by the observations reported for IN625 [166] and IN718 [178]. Nandwana et al. [179] reported that the size of needle-shaped δ phase (Ni_3Nb) can approach over 10 μm when a pre-heat temperature of 915 °C was utilized in E-PBF fabricated IN718. Similarly, the comparison between CM247LC fabricated by L-PBF [180] and E-PBF [181] revealed that the pre-heating during the E-PBF process facilitated the γ′ precipitates to grow from a nano-scale size to micro-scale size. The high pre-heat temperature also allows the growth of precipitates as building process proceeds, and thereby, the size of γ′ precipitates presented an inverse proportionality to the sample's height (Fig. 10(c)) [101]. Likewise, the comparatively large melt pool dimensions in parts fabricated by DED allows longer solidification time leading to more pronounced nucleation and growth of precipitates. This was evidenced by the presence of nano-sized γ″ precipitates in the DED processed IN718 [182].

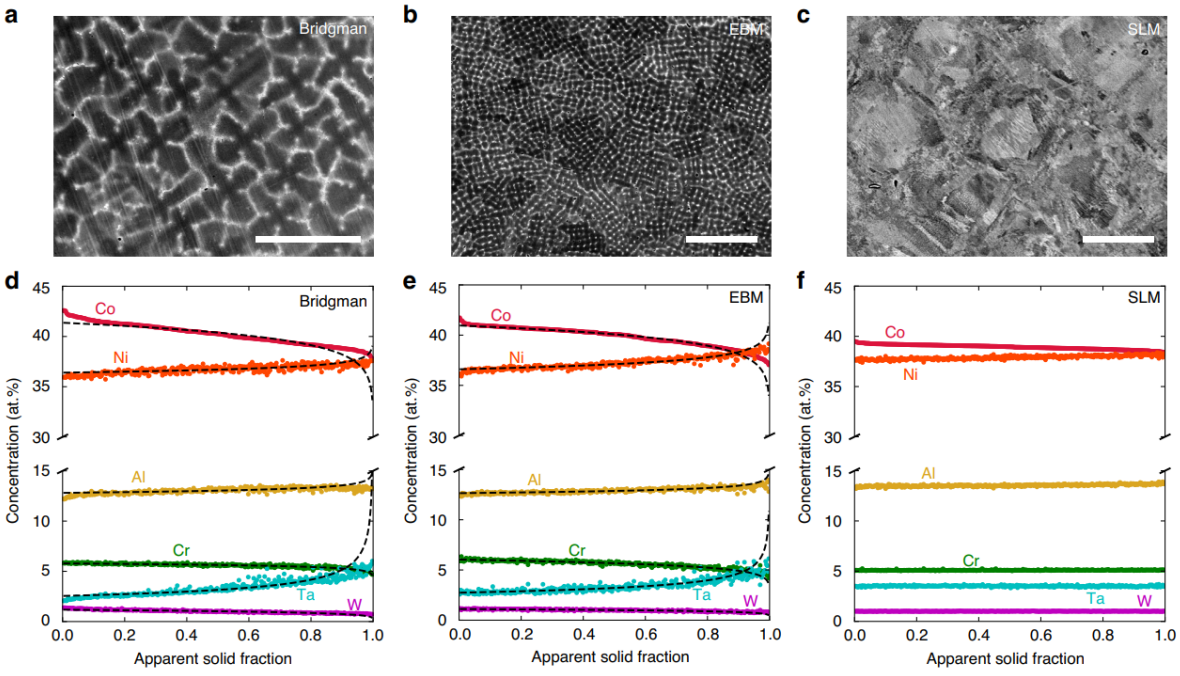

Fig. 14. The BSE micrographs showing as built microstructure of SB-CoNi-10 Nickel-based superalloy after (a)

Bridgman casting, (b) E-PBF, and (c) L-PBF along the transverse direction. The corresponding quantitative compositional data performed by EPMA and Scheil curve showing the chemical segregation are shown in (d), (e), and (f) for Bridgman, E-PBF, and L-PBF samples, respectively. The BSE micrographs and chemical analysis were obtained from [166].

After heat treatment, the high density of dislocations that yields considerable amount of nucleation sites facilitates the phase transformation in laser-based AM processed samples. Similar to the observations in Fig. 12 a-b (i), it was found that both γ′ and γ″ are larger in E-PBF processed superalloys because of reducing the dislocation density would reduce the number density of nuclei [166]. In addition to the primary precipitates, this change can also affect the formation kinetics of the other minor precipitates. Kuo et al. [183] reported that needle-shaped δ precipitates grew continuously along the grain boundaries and sub-grain boundaries in AM processed IN718. Interestingly, upon solution heat treatment and aging, the E-PBF processed IN718 samples appeared to exhibit less amount of δ precipitates when compared to those processed by L-PBF. The higher pre-heating temperature during the E-PBF process reduced the residual strains, thus, retarded the phase transformation during the subsequent heat treatment.

Considering the metallurgy of Nickel-based superalloys, their microstructures induced by AM processes can be roughly categorized using their main strengthening phases. In particular, the microstructural evolutions can be divided into two separated systems, γ″-strengthened and γ′-strengthened superalloys. In γ″-strengthened superalloys, Nb segregates to the inter-dendritic regions leading to precipitation of Nb-rich phases such as Laves, δ and NbC, as shown in Fig. 15. Upon an appropriate solution heat treatment, these phases are dissolved to achieve a homogeneous distribution of Nb. Thus, a microstructure with a uniform distribution of γ′/γ″ precipitates can be achieved upon the aging heat treatment, as shown in Fig. 15(a). If subsolvus heat treatment is applied at temperatures below 1010 ^{o}C, δ phase will survive and distribute along the region where segregation of Nb took place [184], as shown in Fig. 15(c-e). This morphology has been widely reported in AM processed IN718 [185] and IN625 [186]. In γ′-strengthened superalloys such as Haynes 282, on the other hand, segregation of γ′-forming elements including Ta and Ti also accounts for the formation of (Ta, Ti, Hf)C carbides as well as other types of carbides such as Cr-rich $M_{23}C_6$ and Mo-rich M_6C [187], which in turn could limit the dislocation mobility and thus contributes to pile-up of dislocation within inter-dendritic region. The γ’ in cellular inter-dendritic region is significantly larger than that in dendritic regions owing to the eutectic formation and low energy diffusion path provided by the presence of dislocations, as shown in Fig. 15(b). Upon appropriate heat treatment, the bimodal distribution of γ’ precipitates as well as carbides can be identified, as shown in Fig. 15(d) and (f), respectively. The primary γ’ precipitates are present along the grain boundaries when subsolvus heat treatment is applied, as shown in Fig. 15(d-f). Similar morphology was characterized in AM processed CM247LC [64], IN738LC [65], CMSX-4 [66], Mar M-247 [67], Rene 104 [68], Rene 65 [188], Haynes 282 [187], and Rene 142 [69].

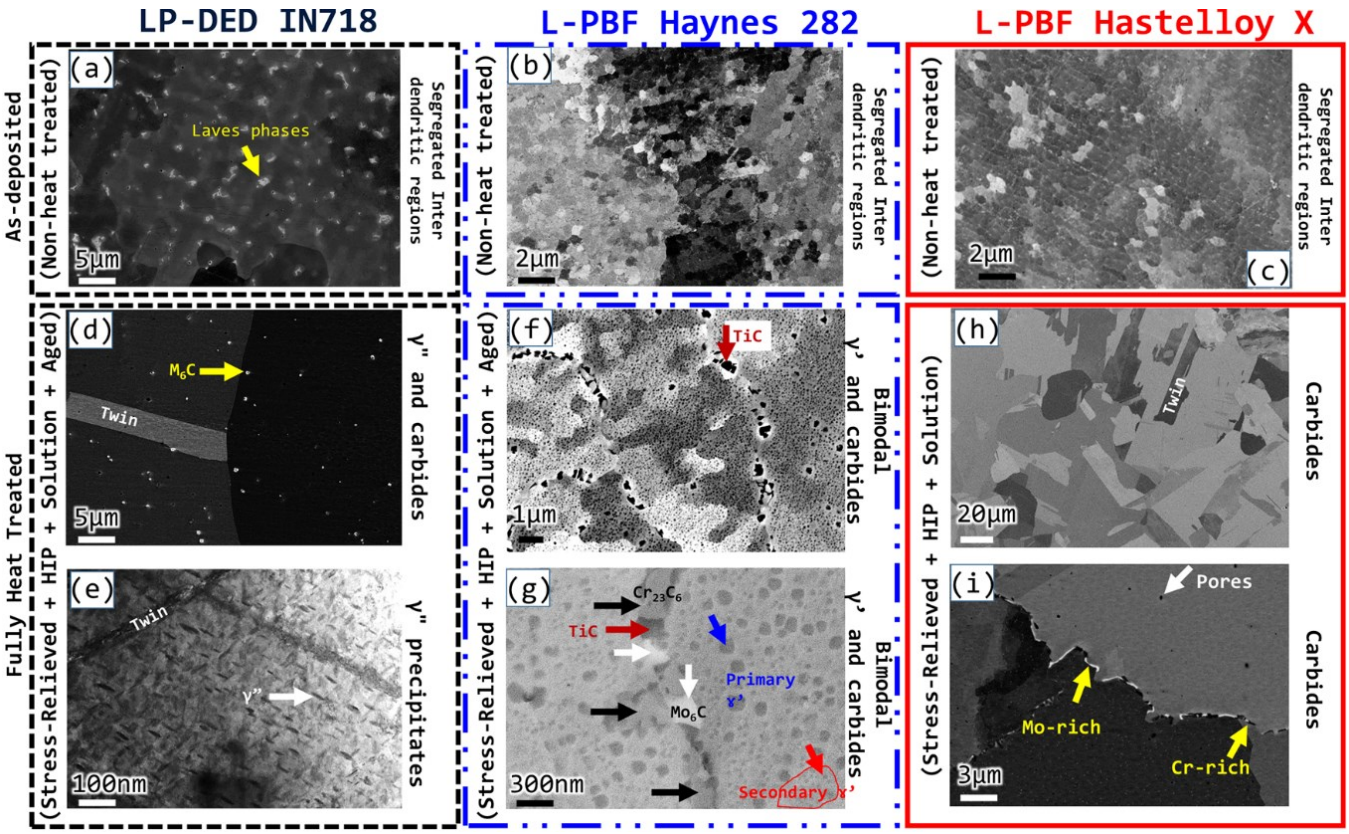

Fig. 15. Typical SEM micrographs of IN 718 LP-DED, Haynes 282 L-PBF, and Hastelloy X L-PBF specimens in various heat treated conditions: (a)-(c) as-deposited (NHT), (d)-(e) fully heat treated IN 718 LP-DED (i.e., stress relived (SR) at 1065 ºC/1.5hr + homogenized at 1162 ºC/3.5hr + solutioned at 1065 ºC/1hr + fully aged at 760 ºC/10h+650 ºC/10h) [189]; (f)-(g) fully heat treated Haynes 282 L-PBF (i.e, stress relived (SR) at 1065 ºC/1.5hr + HIPed at 1165 ºC/3.5hr/100 MPa + solutioned at 1135 ºC/1hr + fully aged at 1010 ºC/2h+788 ºC/8h) [187]; (h)-(i) fully heat treated Hastelloy X L-PBF (i.e, stress relived (SR) at 1065 ºC/1.5hr + HIPed at 1165 ºC/3.5hr/100 MPa + solutioned at solutioned at 1177 ºC/3hr [190].

4.4. Defects and anomalies

The fusion of metallic layers during the AM process can result in formation of defects and anomalies associated with powder chemistry, powder trapped gas, powder spreading dynamics, lack of fusion, keyhole porosity, end of the track, spattering during the scanning process, residual stress and cracking, distortion and delamination, inclusions, elemental evaporation, surface finish and roughness, and porosity induced during post processing. Recently, Mostafaei et al. [18] and Wang et al. [191] have published an in-depth reviews on the AM metals. Defects in fusion-based AM processes can influence the quality of the built and therefore cause degradation in properties, so detection and mitigation are important, especially for Nickel-based superalloys that are mostly used at elevated temperatures under severe and complex loading conditions.

As discussed in previous section, there are factors that could significantly influence the defects formation in the AMed Nickel-based superalloys such as feedstock and processing anomalies. In this section, the formation mechanisms of different types of defects and anomalies found in the AM Nickel-based superalloys forming during the fabrication process

will be briefly summarized and discussed. Also, the state-of-the-art methods currently used for defects detections are discussed with respect to different types of defects. The underlying mechanisms of defect formations as well as practical approaches for elimination will be discussed.

4.4.1. Sub-surface/internal defects

In section 3.2.1, the influence of powder characteristics on the fusion-based AM technologies were introduced and discussed. The key point to make a dense AM component is the feedstock with acceptable powder flow and good packing density. However, powder bed condition might be influenced by powder spreading process and lead to poor powder bed density or rough (uneven) powder bed, which is detrimental to final AM components. Porosity is a common defect observed in AM components and is detrimental to mechanical properties especially fatigue [192]. Generally, porosity of fusion-based AM Nickel-based superalloy primarily results from powder characteristics or improper fusion processing parameters used during the AM fabrication. Complex composition of the Nickel-based superalloys has less influence on porosity formation during AM process. Depending on the porosity morphology and formation mechanism, the process-induced porosities could be generally divided into following categories: lack of fusion, entrapped gas, and keyhole pores.

- ***Lack of fusion (LoF)***

Generally, the classic morphology of LoF is irregular void and is formed as a result of insufficient energy input. High scanning speed or low source energy creates a smaller molten pool during fusion process. If the small molten pool cannot generate sufficient metallurgical bonding between the neighboring molten tracks or subsequent layers, an irregular void will form. Tang et al. [193] developed an analytical index in which molten pool dimension, hatch distance and layer thickness were the main elements to predict the LoF porosity during L-PBF process. However, their model did not consider other pores caused by balling effect and keyhole melting. Ning et al. [194] proposed a new analytical method based on the correlation between thermal behaviors and pore formation, which has an improved predicting accuracy. Examples of LoF porosity are shown in Fig. 16(c,d).

- ***Keyhole pores***

While LoF is formed due to insufficient energy input, keyhole induced pore is formed a result of high energy density of fusion source and usually has near spherical morphology. Keyhole is a term for the opening hole forming inside the molten pool. High energy input of fusion source leads to high temperature inside the molten pool which vaporizes the material. The thermal gradient also creates large surface tension which drags the molten material from the hot center to the cold nearby borders. The combined force of material vapors and surface

tension creates a keyhole inside the molten pool. Once the energy input is cut or removed, the keyhole collapses because the force cannot support the molten material. Then metal vapors or inert gases from the chamber are entrapped inside the molten pool as bubbles [149]. The depth of keyhole increases with energy input. A deeper keyhole increases the tendency of porosity formation since gas is less likely to escape from the keyhole. It is also reported that keyhole induced pore is much severe at the end or at the turn point of molten track where the energy density abruptly changes. This may result in a deeper keyhole or a sudden collapse [195], which is also known as "turnaround" or "end-of-track" porosity. Examples of keyhole porosity are shown in Fig. 16 (i-k). The formation of keyhole porosity relies on the AM processing variables (i.e., laser or electron beam power, spot size, scan velocity, etc.), material-specific properties (i.e., boiling point, powder particle size and distribution, powder bed thickness, etc.), and choice of the atmosphere [196]. Thus, both machine and material-specific analysis are needed to minimize the pore formation, mainly with a focus on the impact of processing variables on the melt pool size and morphologies as well as the vapor cavity characteristics.

- ***Entrapped gas pores***

In Fusion-based AM process, an inert gas is purged into the build chamber to protect liquid metal against oxidation. Due to high tendency of gas absorption in liquid metal, gas pores are frequently formed upon solidification. They are typically round with sphericity of > 0.7 and size of 50 μm. Another source of gas pore in the final build could come from the powder feedstock also known as entrapped gas in powder. The gas in metallic powders is primarily induced during the powder production processes. Typically, gas atomized powders have higher fraction of pores while mechanically milled or plasma rotating electrode powders have minimal pores. Upon laser or electron beam interaction with powder, the gases are introduced to the molten pool and potentially dissolve, then, part of them is entrapped in the solidified metal and form pores. Moisture on powder can be another source of gas porosity during the powder feeding. Melt pool surface fluctuation also results in gas pores during fusion-based AM processes. The surface protrusion on the molten metal pool as well as droplets or spatters induced by melt surface fluctuation may trap the surrounding gas and cause gas pore formation. Hojjatzadeh et al. [197] also demonstrated if solidification cracks upon rapid cooling, the surrounding gas flows into the cracks connecting to the top surface of the deposited layer/substrate, resulting in the formation of gas pores. Finally, if the Nickel-based superalloys are composed of volatile elements, they may evaporate due to high energy and heat input, thus, could bring gas pores in the solidifies metal [198].

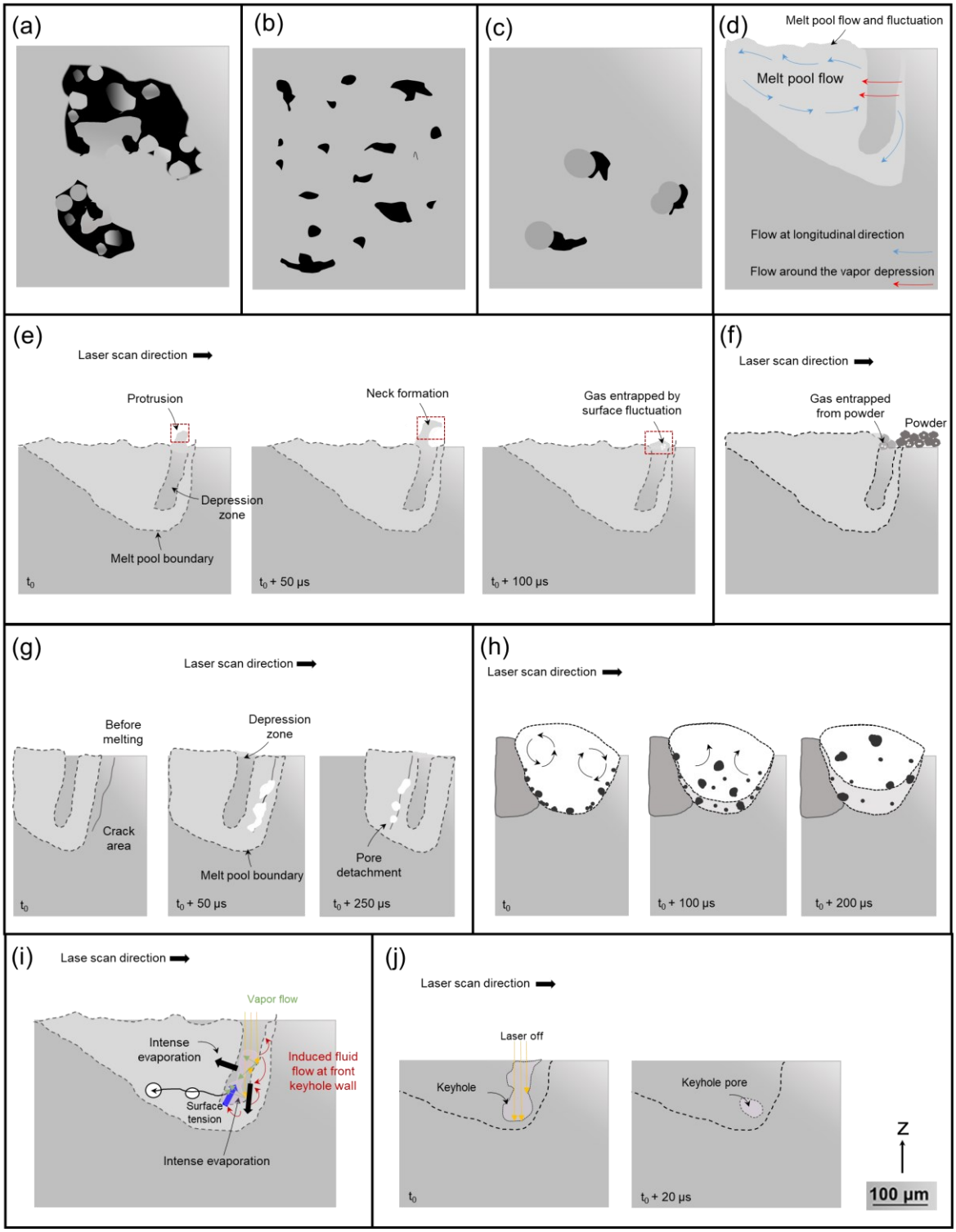

Fig. 16. Schematic of formation mechanisms for different defects. **Lack of Fusion (LoF)** in (a) with unmelted powder particles inside large irregular pores, in (b) with incomplete melting-induced porosity, in (c) with negative effect of metal spattering leading to shadowing effect and LoF formation, and in (d) with unstable fluid flow in molten pool leading to surface roughness. **Gas pore** in (e) gas entrapped by surface fluctuation, in (f) gas entrapped in raw powders entering molten pool, in (g) gas entering a molten pool through a substrate surface crack, in (h) gas pores precipitated during solidification. **Keyholes** in (i) due to rear keyhole wall collapse in the transition area occurring because of temperature reduction which in turn enhances the surface tension, leading to the combined recoil and stagnation pressure, and in (j) due to sudden laser shut off.

The mechanisms of gas trapped pores in atomized powder are illustrated in Fig. 17 [199]. During the atomized process, the high velocity of inert gas could blow the molten droplet into a "bag''. The bag bursts and turns into smaller droplets. This is called "bag break-up" mechanism and could lead to small satellites attached on the atomized powder. However, if the viscosity of the molten droplet is high enough, the "bag" might not collapse into small droplets but close itself into a hollow sphere with inert gas trapped inside, which is observed as powder with spherical pores. Since the powder trapped gas is relative to high velocity of inert gas flow, a review from the work of Anderson et al. [98] suggested the atomized process with a reduced kinetic energy gas could avoid the "bag'', suppressing the formation of satellites and powder trapped gas. It was also reported that small powder has less tendency to have trapped gas [200] since small particle results from the "bag'' collapsing and at the same time, high cooling rate of small droplets leads to higher surface tension and thus inhibits the gas entrapment.

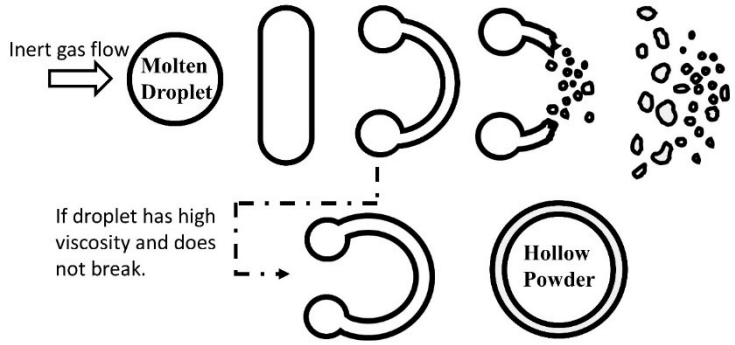

Fig. 17. The illustration of "bag break-up" mechanism. Inert gas flow blows the droplet into a "bag". If the "bag" does not collapse into smaller droplets, gas could trap inside the solidified powder [199].

Qi et al. [201] reported the influence of powder pores on AM components. The authors used direct energy deposition to build IN718 components with different powder feedstocks which were manufactured by gas atomized and plasma rotating electrode processed. The images of different feedstocks and corresponding AM IN718 components with same process parameter were shown in Fig. 18. It is obvious that powders with more trapped pores inside could lead to higher porosity to final AM components. Similar result on the influence of powder pores was reported by Zhong et al. [202]. They also found that gas entrapped pores in gas atomized IN718 powder could transfer into molten trackers during fusion process. Examples of gas pore formation are shown in Fig. 16(e-h).

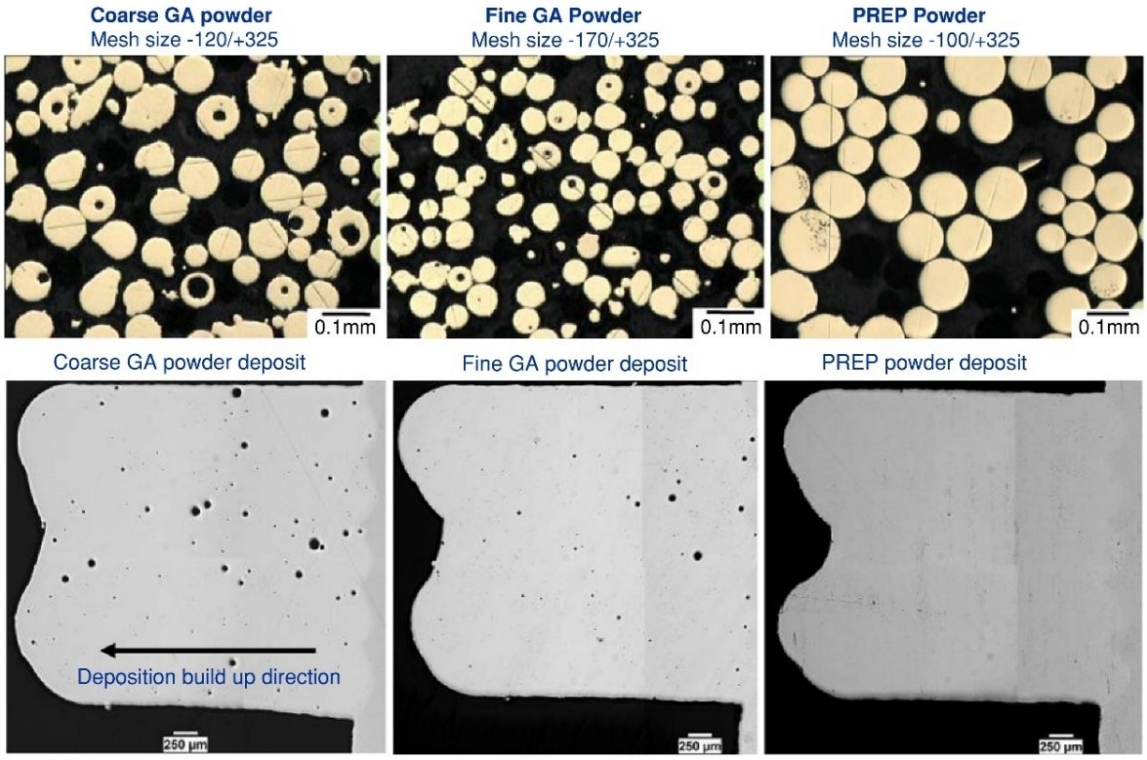

Fig. 18. Powder with different porosity and corresponding AM components with similar deposition parameter. It clearly shows that pores inside powder feedstock could transfer to final components [201].

- ***Inclusions***

In the cast or wrought Nickel-based superalloys, the main source of inclusions is the debris from the melt crucible. The inclusions are usually within a size range of several hundred micrometers which are detrimental to the mechanical property of Nickel-based superalloy especially fatigue performance [203]. In contrast, in the fusion-based AM Nickel-based superalloys, the inclusions are induced by trace elements and contamination in the feedstock or oxidation films on the molten pool and recycled powder. These inclusions including oxide [204], nitride [205], carbide [206], and trace element segregation on the grain boundary [115]. The size of inclusions in fusion-based AM Nickel-based superalloy is ranging from several micrometers to nanoscale, which is much smaller than those observed in the cast or wrought Nickel-based superalloy.

As discussed earlier in previous section 3.2 (Processing effects), apart from the gas entrapped, the gas contamination such as Oxygen is a common processing issue in AMed Nickel-based superalloys which could attach on the surface of powders or form oxide films on the particles, especially recycled powder. It was reported that oxidation of Nickel-based superalloy during fusion-based AM process is unavoidable, based on Ellingham diagram in which the oxygen partial pressure of chamber is always higher than the threshold values for the oxidation of Al, Cr, Fe and Ti [207]. Oxidation happens at the surface of the molten track and oxides attach on the surface of spattered particles [105], which increases the oxygen content of recycled powders.

Typically, excessive oxygen in powder could influence the molten pool kinetics. Studies have shown that oxygen could change the flow of Marangoni convection within the melt pools generated by fusion-based techniques from centrifugal to centripetal [208]. The centripetal flow drives the gas bubble into the bottom of molten pool, which cause higher porosity to the AM components. Oxide film also stabilizes the gas bubble inside the molten pool, inhibiting the pore healing. Also, oxygen could lead to larger spattering effect with irregular structure during the fusion-based AM processes. In addition to oxygen, nitrogen is also another source of inclusion formation during the fusion-based AM processing of the Nickel-based superalloys. It was found that the built materials using nitrogen-atomized powder did not recrystallize because of pinning effect due to the formation of nitrogen-included minor phases forming at the grain boundaries [209].

One of the concerns of inclusions is that they are the cracking initiation sites during fusion-based AM process (see Fig. 19). The trace elements such as Zr [115] and B [101] could also form inclusion particles with low melting point at the grain boundaries, which lead to liquation cracking or solidification cracking. It is also reported that in the L-PBF processed Hastelloy X, carbides at the grain boundary caused liquidation cracking during the AM fabrication [206]. Large oxide is also confirmed as a crack initial site and causes embrittlement to the grain boundaries [204].

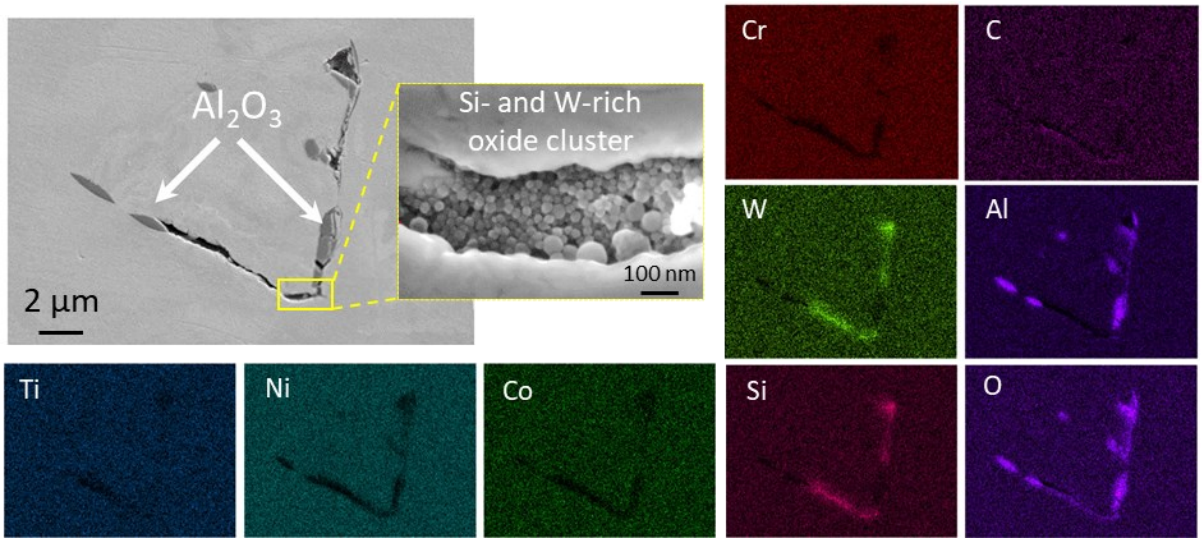

Fig. 19. SEM micrographs and elemental analysis maps showing oxide inclusions and corresponding cracking observed in L-PBF 738 LC [204].

Another concern of inclusion is that they influence the mechanical property of the fusion-based AM Nickel-based superalloy. It was reported that such inclusions, especially oxides, could increase the strength but degrade the ductility of AM Nickel-based superalloy [210]. As mentioned earlier in previous section 3.2 (Processing effects), the oxygen content of fusion-based Nickel-based superalloy is much higher than cast or wrought Nickel-based superalloy. It is reported that gas atomized IN718 powder has ten times higher of oxygen content than in

wrought ingot (~275 ppm vs. ~20 ppm) [93]. The oxygen content is even higher in the recycled feedstock, which is a result of the interaction between the spatter and oxygen inside the chamber [146]. The oxide then forms nano-particles and provides dispersion strengthening to AM Nickel-based superalloy. This would influence the consistency of different batches with recycled feedstock. It is also reported that oxide inclusions can affect the surrounding composition and influence the phase formation in the microstructure of the AM Nickel-based superalloys. Kakehi et al. [211] found that the oxides can react with the Al and Ti elements in exist in the IN718 matrix, which in could destabilize the γ′ formation and promote the transformation of γ″ to δ phases during heat treatment. As a result, the creep resistance are decreased with inter-dendritic δ precipitation.

Sometime the inclusion is beneficial to the AM Nickel-based superalloys and is added purposely for dispersion strengthening [212]. Another target of inclusion addition is grain refinement, in which inclusion plays as inoculant and refines the grain structure of the fusion-based AM Nickel-based superalloy [213]. The refine grains also decrease the susceptibility of AM Nickel-based superalloy to cracking by decreasing the fraction of columnar grains [212] or high angle grain boundary [214], which are sensitive to cracking.

The AM component usually requires heat heat treatment such as homogenization and aging process. It is widely known that high temperature treatment could lead to porosity in the Nickel-based superalloy. Entrapped gas, phase transformation, and Kirkendall effect are the major factors inducing the post processing induded porosity such as those formed upon HIPing [215]. Tammas-Williams et al. [216] reported that additional heat treatment on HIPed AM alloy could lead to coarsening of porosity because of internal pressure resulting from entrapped gas. It is also discussed in the following paragraphs (cracking) that segregation at inter-dendrite causes a lower solidus temperature, which could in turn form incipient melting during heat treatment [217]. Another case is the heat treatment inducing kirkendall porosity forming on the dissimilar material joint boundary such as between Nickel-based superalloy and other materials. An example is thermal barrier coating on Nickel-based superalloy. Kirkendall voids formed at the boundary of MCrAlY coating due to interdiffusion [218]. These voids could be important for the AM metal matrix composites (MMCs) of Nickel-based superalloys reinforced with nanoparticles such as graphene. Thus, post processing induced porosity of AM Nickel-based superalloy is expected to be similar to the traditional Nickel-based superalloy.

- ***Micro-cracking and delamination***

As summarized by Carter et al. [219,220], the mechanism of cracking in fusion-based AM Nickel-based superalloys is similar to the one observed in welded Nickel-based superalloy, and the cracking mechanism of AM parts could be categorized into four types as summarized below.

Solidification cracking forms in the mushy zone of molten pool, where solid dendrite grows into the molten material and inhibits the liquid flow at the inter-dendrite. The remaining

liquid is the cracking initial site when the residual stress or solidification shrinkage tear up the liquid region. Solidification cracking thus creates an opening dendrite structure to the cracking surface. Solidification cracking could be observed in any kind of fusion-based AM superalloy, especially the non-weldable Nickel-based superalloys. The susceptibility of Nickel-based superalloys to solidification crack is closely related to the segregation and formation of dendrites within the material. Fig. 20 presents the typical morphologies of solidification cracking in AM processed CM247LC [221].

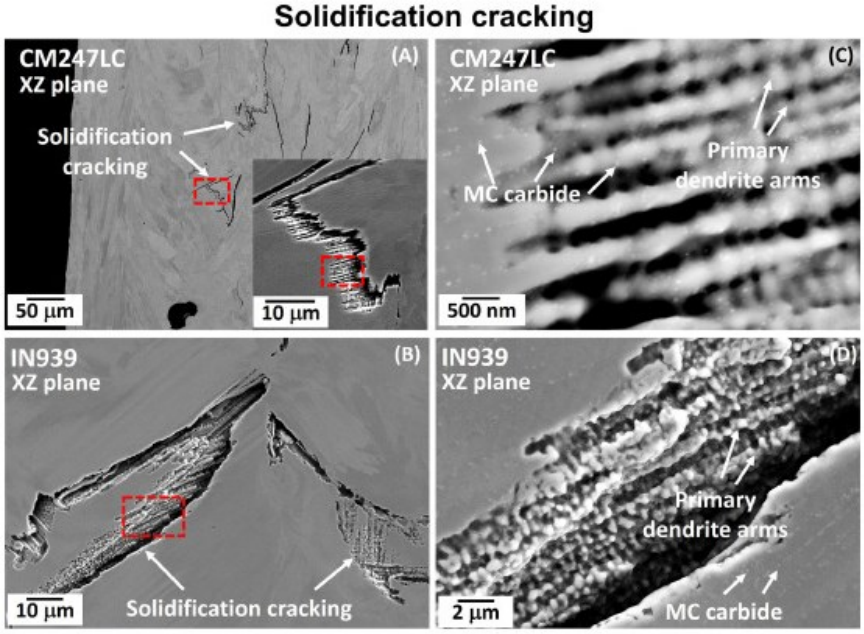

Fig. 20. Solidification cracking observed in both CM247LC and IN939 processed by L-PBF. The jagged cracks were identified as dendrite arms were separated in the final stage of solidification [221].

Hot tearing occurs when fast cooling induces the formation of a large thermal gradient that results in uneven thermal contraction along solid-liquid interface [222]. Although the semi-solid material during solidification can accommodate this thermal strain via plastic deformation, creep, and filling of porosities, the lack of sufficient time due to fast solidification rate during AM fabrication will inhibit this thermal strain accommodation and hence lead to crack propagation along the inter-dendritic structure. Since hot tearing mainly occurs when solid and liquid phases coexist, alloys that present a high tendency for micro-segregation (e.g., Nickel-based Mar-M-247 alloy) are more susceptible to hot tearing. If the materials fail to inhibit the crack propagation through the deposited layers, more severe *delamination* would occur.

Liquation cracking of fusion-based Nickel-based superalloy occurs at the heat affecting zone of fusion. The material is heated to the temperature range between solidus and liquids temperature and causes a partially melted zone. If the liquid in the partially melted zone cannot resist the applied stress induced during AM fabrication process, cracking forms as a result. Similar to solidification cracking, eutectic phases [217], carbide [223], Laves [224] or trace

element segregation [115] decrease the solidus temperature locally, leading to the liquation cracking in the heat affecting zones. An example of liquation cracking in L-PBF processed Hastelloy X is illustrated in Fig. 21 (a-d), where Mo-rich carbide grew and liquified after cyclic heating [206]. Another example is the L-PBF processed IN738LC superalloy, which is showed in Fig. 21 (e), where the liquation cracking occurred at the site of eutectic γ′ [217].

Strain-age cracking (SAC) happens during either the heat heat treatment or the re-heating process when adjacent layers or tracks are subject to the heat source. The quick precipitate of γ′ as the result of stress relief decreases the ductility of Nickel-based superalloy while the residual stress relaxes slowly [225]. Formation of precipitate also induces more stress to γ matrix. The high densities of dislocations at the grain boundary can cause failure once the grain boundary cannot sustain the induced high strains.

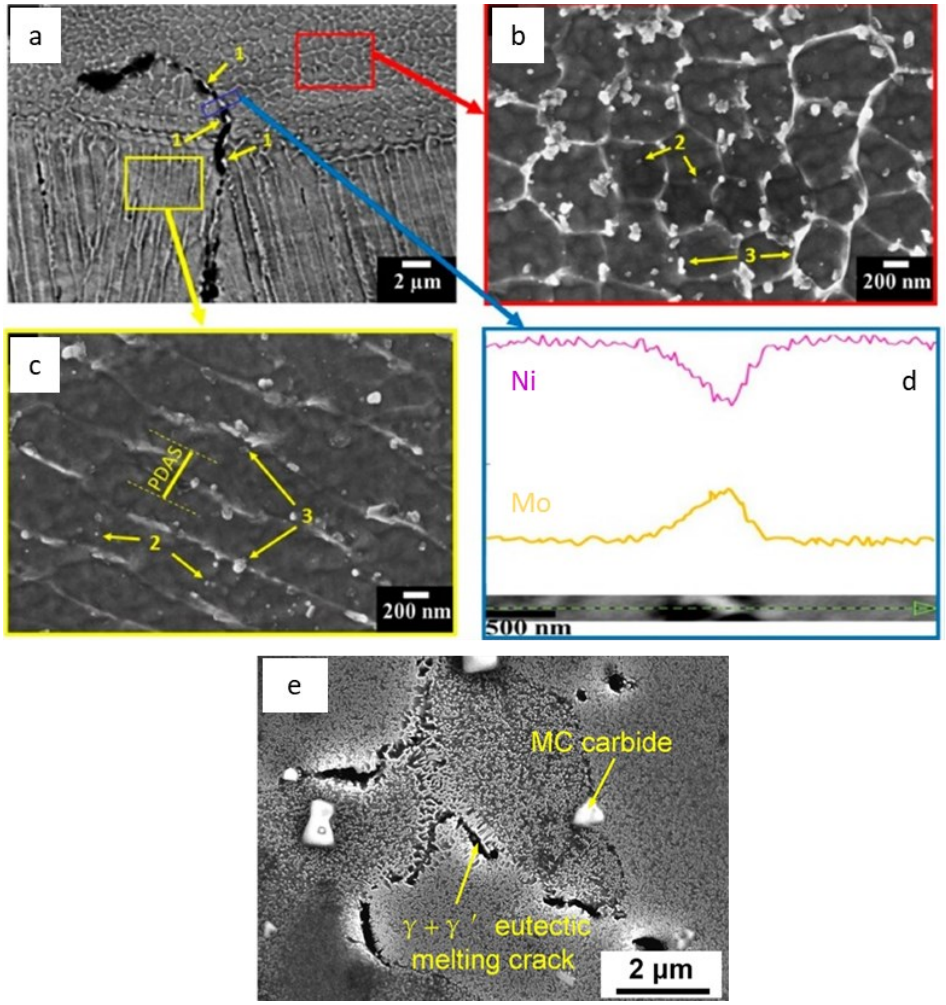

Fig. 21. Liquation cracking of AM Ni-superalloy: (a)~(d) the liquation cracking observed in L-PBF Hastelloy X with Mo-rich carbide liquefying [206] (e) Liquation cracking at eutectic γ' of IN738LC superalloy [217].

Ductility-dip cracking (DDC) is a cracking resulting from ductility drop of grain boundary at the intermediate temperatures (approximately 0.4-0.7 of liquidus temperature of material) in the Nickel-based superalloys with low fraction precipitates. The mechanism is

complicated and sometime is categorized into *strain-age cracking* or *liquation cracking* [220]. *DDC* in fusion-based AM Nickel-based superalloy is referred to the cracking caused by creep like mechanism [226]. They concluded that during the reheating of welded Nickel-base superalloy, grain boundary sliding causes high strain and void coalescence. These voids segregate at the stress concentration sites such as triple point junction of grain boundaries and forms cracking eventually. It was noted that continuous carbide particles are harmful to ductility-dip cracking resistance since the voids near the carbide particles nucleate into the cracking [227]. Since *DDC* and *SAC* are only associated with solid phase, these two types of cracking are also referred as solid-state cracking. Fig. 22 presents the typical morphologies of solid-state cracking in AM processed Ni-superalloys [221].

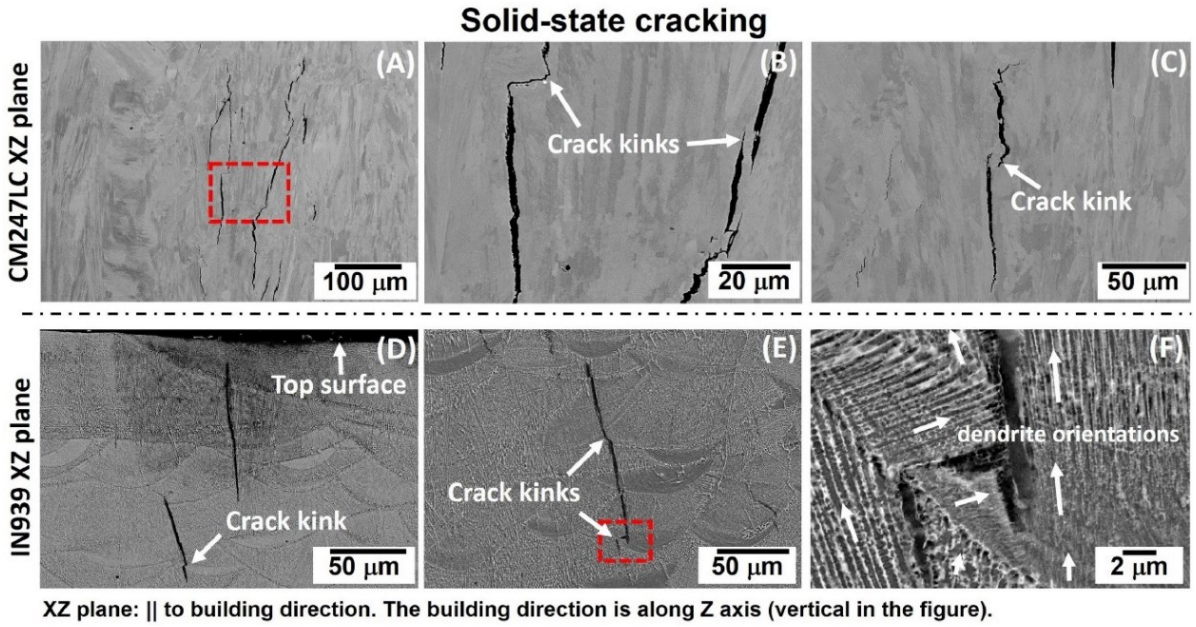

Fig. 22. SEM micrographs showing the solid-state cracking in L-PBF processed (a-c) CM247LC and (d-f) IN939. Cracks normally propagate through several layers of melt pool with straight feature and sharp kink. Area in red boxes are shown in more detail in the subsequent figure [221].

4.4.2. Residual stress

As discussed earlier, although the layer-wise manufacturing manner of the laser-based AM processes allow complex design structures, it may also cause large thermal gradients due to the localized heat input and rapid solidification, which in turn may give rise to large internal stress (IS) induced during the process and consequently the residual stress (RS) at the end of production process generated within the AM components [228]. These internal stress and residual stress causes not only cracking but distortion to fusion-based AM Nickel-based superalloys, which degrades the dimensional precision of AM components. Part distortion is also the major cause for "super-elevation" of powder bed anomalies. Delamination and warping happen at the sides with LoF or the weak points of geometry, which damage the powder spreading rake and cause following failure during fusion-based AM process [137]. Though it

is possible to relieve the problem of residual stress and distortion by heat treatment [229,230], serious distortion and existing failure are hard to be eliminated.

Among the cases of distortion in AM Nickel-based superalloys, serious distortion usually occurs in the support structure [231] and lattice structures [232] as well as at the edge or the overhang structure of AM components [233]. This is because these sides have different thermal conductivity since they are surrounded by powders or inert gas during the AM process. The heat from the energy source concentrates at the regions, which leads to a high thermal gradient and corresponding high residual stress and distortion [139]. Delamination also decreases the thermal conductivity since the heat cannot pass through the macro cracking and thus concentrates at the de-bond material [234]. It is also reported the energy input increased at the corner side due to shorter line scan lengths, which leads to a heat concentration and following warpage at the corner [139]. An example of AM Nickel-based superalloy component with distortion is illustrated in Fig. 23 where the distortions are concentrated at the corner. Similar issue occurs in the components with thin-walled feature, heat accumulates at the thin-wall and causes higher temperature and residual stress. The thin-wall also has a lower geometric stiffness, which increases the susceptibility to distortion [235].

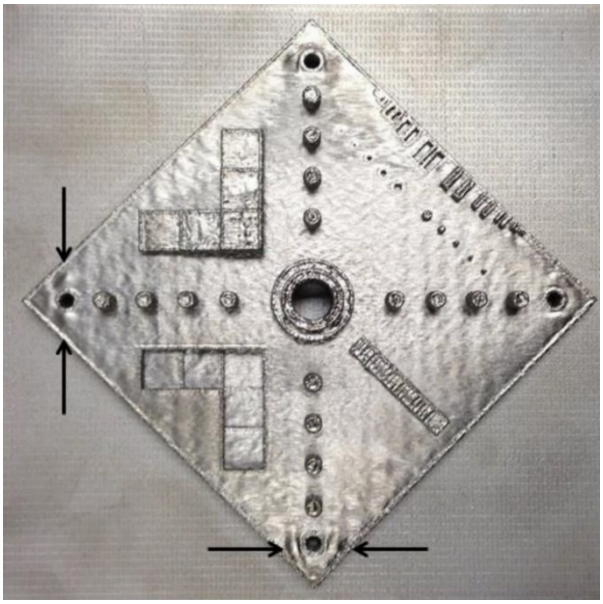

Fig. 23. An example of distortion at the corner of E-PBF Nickel-based superalloy [139].

It is notable that the subsurface residual stress is a critical issue of fusion-based AM technology of Nickel-based superalloys [236]. Due to the inherent AM processing characteristic, it is unavoidable and usually is hard to prevent residual stress developing in the built compartment [237]. The high levels of residual stresses could further deteriorate the mechanical response by inducing cracks, distortion, and unexpected phase transformation. Hence, it is crucial to predict and measure magnitude of residual stress and understanding how residual stress develops during the repeated iteration of scanning so that remedies can be incorporated to minimize its impact on industrial application.

Residual stress occurs in both macroscopic and microscopic scale. The origin of macroscopic residual stress during fusion-based AM technology typically results from the non-uniform thermal deformation induced by local thermal gradient, i.e., thermal gradient mechanism. When the newly added material is heated and fused during the subsequent deposition layer, it will first expand and then shrinkage after solidification while the cold underlayer has smaller thermal deformation and restricts the shrinkage of the newly deposited material, which causes tensile stress to the new layer but compressive stress to the underlying material (Fig. 24a) [238]. The repeated fusion leads to the accumulation of residual stress in AM component. Since the thermal gradient may vary along different directions, the magnitude of residual stress was also found to be different with respect to the sample orientation and dimension. Fig. 24(b) presents an example showing the non-uniform distribution of residual stress along different stress directions in L-PBF processed Nickel-based Waspaloy [239].

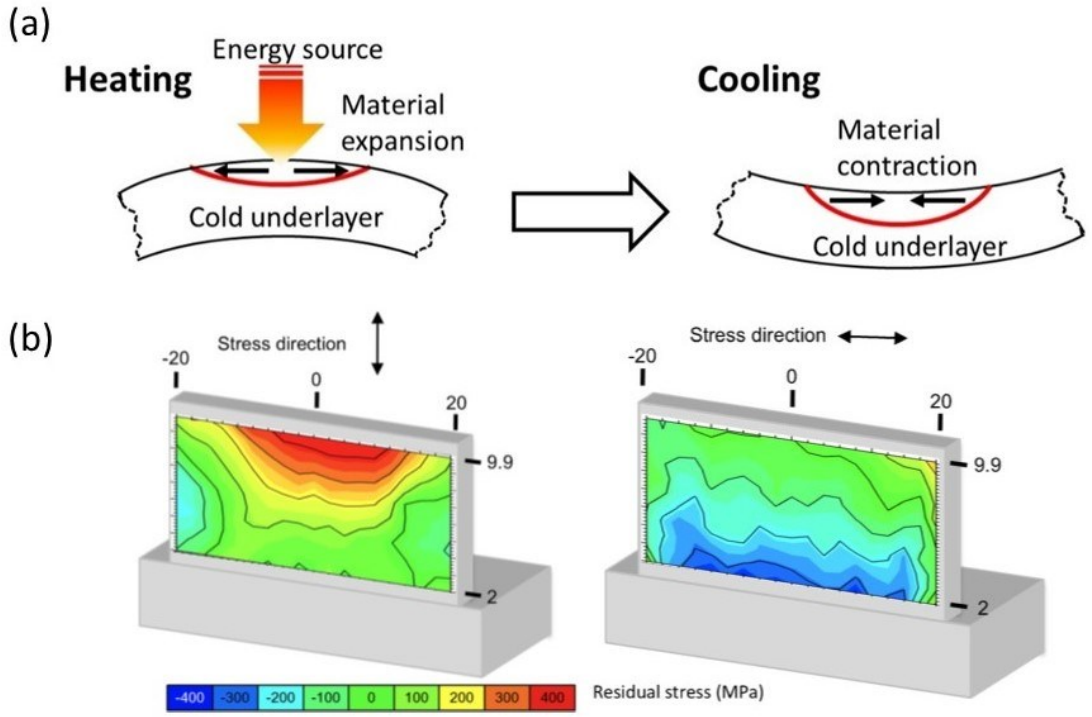

Fig. 24. (a) Schematic illustration showing the mechanism of residual stress happening during fused based AM process. Modified from the diagram of [238], and (b) Residual stress maps measured from neutron diffraction for the vertical direction stresses and horizontal direction stresses, respectively [239].

The microscopic residual stresses are generated as a result of differential thermal contraction between different phases and dendritic structures coexist in the microstructure of the Nickel-based superalloys during the AM fabrication process. The presence of residual strains can be affirmed by the high magnitude of dislocation density attributed to the formation of geometrically necessary dislocations (GNDs) along the inter-dendritic boundaries or phase boundaries [240]. Through the strain monitoring and temperature monitoring performed by in-situ neutron diffraction and thermal camera, respectively, it should be noted that strain

development resulting from thermal contraction of the melt pool is minor when compared to that contributed by phase precipitation and dendrite formation during laser metal deposition [241]. Hence, the formation of cracks in fusion-based AM processes is generally initiated from the grain boundaries or inter-dendritic boundaries. Strategies for reducing the degree of residual stress in fusion-based AM processed Ni-superalloy and minimizing the probability to delamination and cracking could be generally categorized into the AM process optimization and heat treatment.

Studies have shown that adjustment of scan parameters and strategies can significantly reduce the level of residual stress and hence decrease the susceptibility to cracking or delamination in AMed Nickel-based superalloys [242]. Different combinations of laser power, scan speeds [243], hatch distance [244], layer thickness [245], and scan pattern [246] are adopted to reduce the cooling rate of the molten materials. It is found that the cooling conditions are closely related to the melt pool physics. In general, a decrease in laser power and layer thickness can contribute to higher Fourier number while lower Marangoni number, leading to less degree of residual stress. It should be noted that the movements of scan tracks can largely influence the heat transfer and resulting accumulation of residual strains. Increasing the randomness of scan directions has been found to significantly reduce the residual stresses in AM processed Nickel-based superalloys [128]. Similarly, due to the strong dependence on temperature gradients in three dimensions, the level of residual stress also varies with different directions [247]. Therefore, the design of sample geometry should also be considered when analyzing the residual stress.

Another approach for stress removal is the heat treatment. The large thermal energy allows the inter-diffusion and hence annihilates the high densities of dislocations and reduces the tensile residual stresses. Despite the reduction in tensile strength attributed to the characteristic coarser grain structure and less density of dislocations, the ductility was improved in several AM processed Nickel-based superalloys [248]. As the trade off, however, the phase constitution and grain structures may change significantly with different heat treatment temperatures and isothermal incubation time, and therefore unexpected phase transformations may occur such as brittle phases that are detrimental to the mechanical properties.

Lastly, since the majority of the residual strains initiates from the phase boundaries and inter-dendritic boundaries, alloy compositions can profoundly impact the magnitude of the residual stress upon processing. Mukherjee et al. [242] reported that the strain parameter is relatively higher for IN718 deposits in comparison with that for 316 stainless steel, in addition to nominal increase with increasing laser power or decreasing scan speed (see Fig. 25); the underlying mechanism is attributed to the large solidification range while comparatively lower liquidus temperature that accounts for the shrinkage of larger melt pool. To effectively reduce the level of residual stresses without defects formation or expected microstructural evolution, the compositional modification may inhibit the susceptibility to dislocation pileups and

resulting crack formation.

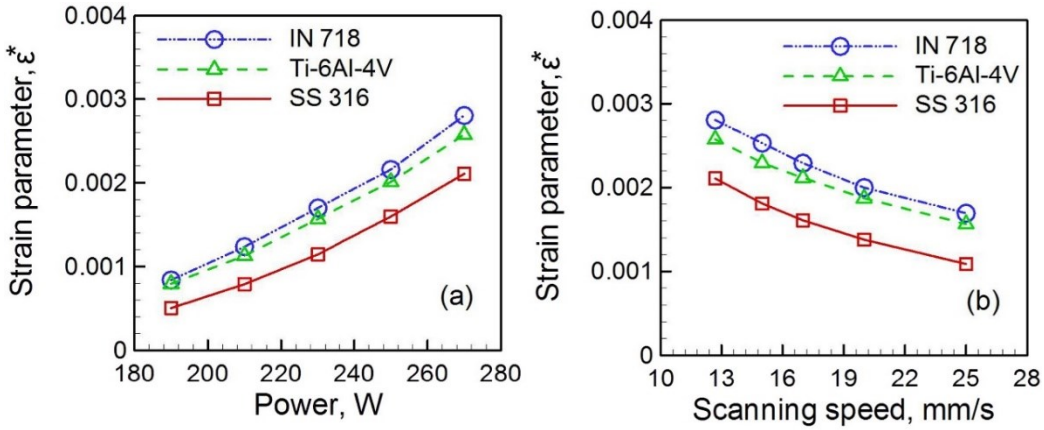

Fig. 25.Variation of strain parameters of IN718, Ti-6Al-4V, and 316 stainless steel as function of (a) laser power for a constant scan speed and (b) scan speed for a constant laser power [242].

4.4.3. Detection methods

Defects detection methods can be classified into destructive and non-destructive techniques. The traditional metallography is a destructive approach, it involves sectioning samples in order to observe region of interest, and different length scales of structure defects from several centimeters to nanometers could be analyzed by microscopes, such as optical microscope, scanning electron microscope, transmission electron microscope. Although defects can be detected and analyzed in detail by microscopes, significant number of samplings and observations would be required to obtain representative information of defects in the bulk structure.

- ***Non-destructive tests***

The non-destructive techniques (NDT) would be more efficient to gain an overview of the distribution and variation of defects within a bulk structure; it could also allow remedy to be performed during the AM process. Examples like penetrant testing [249], magnetic particle testing [250], and eddy current testing [251], which could reveal near-surface defects. For deeper under surface internal defects, mechanical wave testing such as ultrasonic [252] or acoustic testing [253] can be employed, these techniques use the change of mechanical wave data (echo and velocity) to estimate the location and size of internal defects (see Fig. 26a). However, rough surface of AM components could cause background noise during near-surface inspection or mechanical wave testing (see Fig. 26b) [254]. On the other hands, complex geometry of AM components makes the internal structure hard to be inspected. It is also tricky for these NDT methods to locate the accurate sites or reveal the shape of defects inside the AM components.

There are two types of evaluation methods for surface defects and surface roughness (such

as R_a) of AM components: contact and non-contact methodologies [255]. A commonly used contact method is the standard stylus profilometry, which could capture the surface profile of the AM parts provided that the appropriate stylus tip radius and cone angle are selected to ensuring the reliability of the surface data and avoiding any damage to the probe and surface [255]. It should be noted that when using contact methods, the accessibility of the surface for detection should be of great concern. However, when using non-contact methods, there's no risk of surface damaging. Some of the commonly used non-contact surface roughness measurement methodologies are the areal topography measurement methods such as confocal microscopy and atomic force microscopy (AFM), and 2D surface imaging methods such as optical microscopy (OM) and scanning electron microscopy (SEM) [255].

The other example for non-contact detection testing method commonly used for AM parts is eddy current testing (ECT). However, the detection capabilities of ECT techniques are limited to the surface and near-surface features located at shallow depths and they cannot detect the deep volumetric discontinuities. Although, the ECT of AM parts is very similar to that of conventionally processed components, the level of noise is higher in the former due to rough surface condition of AM parts. Moreover, the effect of AM fabrication process on the grain structure may affect the ECT signals [254]. The ECT of AM parts need reference and calibration blocks which is mainly because of their thickness and surface anisotropy due to the directional material deposition process [256]. Besides, further non-destructive evaluation (NDE) might be needed using mechanical testing and metallographic analysis of the same AM blocks used as ECT calibration references. As an electromagnetic technique, the ECT can be influenced by several parameters such as material electric conductivity, magnetic permeability, part thickness, and the lift-off distance (i.e., the distance between the detection probe and the part surface) as well as other microstructural features affecting these parameters such as porosity, voids, cracks, lack of fusion, inclusions and residual stresses. Prior to the actual inspection, the ECT instrument undergo performance verification measurements, according to manufacturer specifications performed on the calibration test blocks, to adjust the instrument operational settings [257].

Typical resolutions of ECT techniques are of an order of 1 mm [256] depending on the test parameters such as sensors size, array spacing, spatial resolution of the scan, acquisition rate, and scanning speed. In case of AM parts, the rough surface condition and possible dimensional distortion may have negative effect on the detection capabilities of the ECT technique for the discontinuity, although the ECT probe does not necessarily need to touch the AM parts' surface. This is because surface ECT often requires covering of the surface of test piece with a thin non-conductive tape, to avoid the possible damage to the probe by the rough surface AM components. Yusa et al. [257] have tried to set a reference value for resolution limit of the ECT technique in AM parts, by creating specific branched defects, such as those observed in the stress-corrosion cracking. They have used the L-PBF process for the 316L SS

to deliberately generate the cracks with 30 μm width which were smaller than the ECT probe detection limit.

Eddy current thermography inspection method, which is also known as induction thermography, is another version of ECT used for the AM metallic parts, especially the ferromagnetic materials [258]. The thermography is temperature gradient mapping, which can reveal the geometrical and microstructural non-uniformities due to their effect on heat transfer, e.g., by conductive, convective, radiative, or inductive [259]. For instance, the infrared (IR) thermography is not only sensitive to the surface properties, but also to the heat transfer inside the examined test piece.

The thermography inspection method is fast, and non-contact and it can be used for large areas. However, in the case of the AM metallic parts, it does not provide the same level of details as ultrasonic or radiography-based techniques. It should also be noted that thermography inspection method is an in-process technique and used extensively for process monitoring during the fabricated process [256]. However, for the most metallic components, the induction thermography inspection method is more applicable to reveal surface and near-surface anomalies [260].

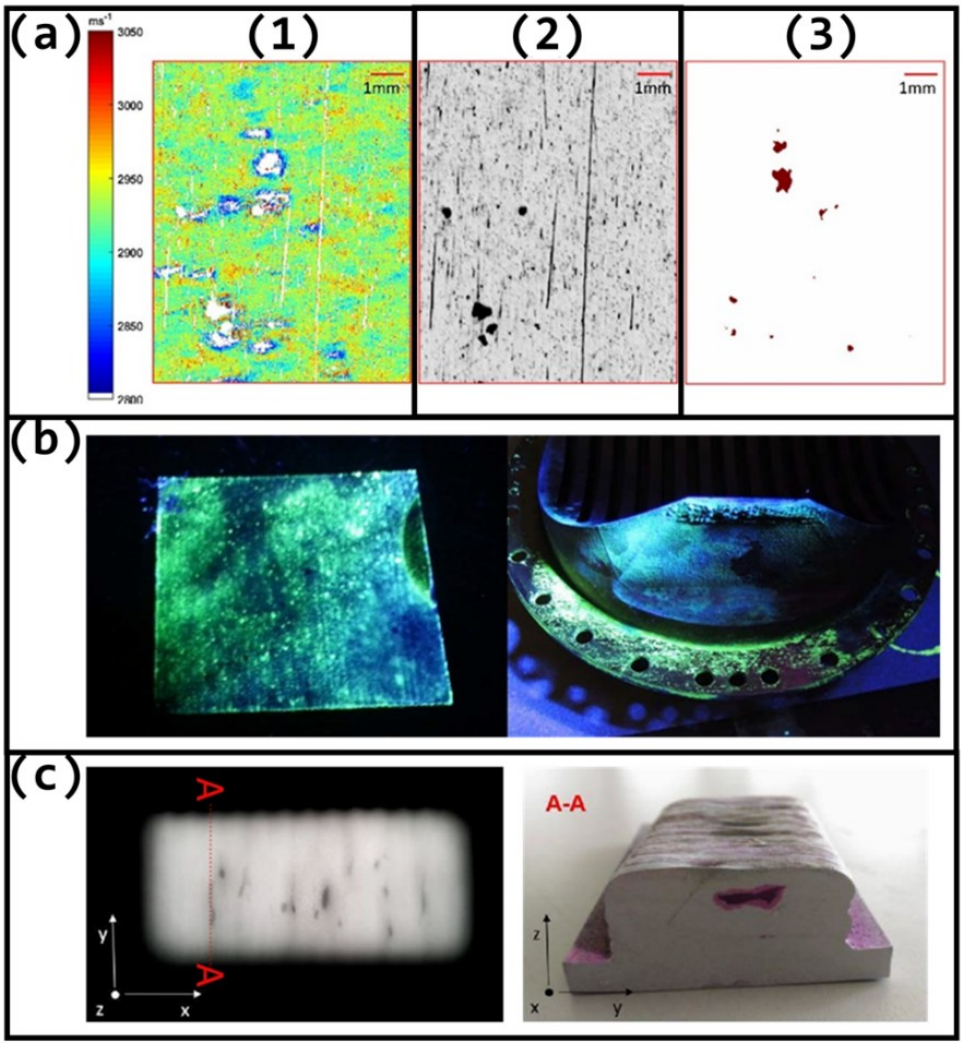

Fig. 26. (a) Defects at surface and sub-surface were detected based on the change of acoustic signal velocity. (1)

Detected velocity of acoustic signal, (2)Surface optical image, and (3) X-ray CT scanning [261]. (b) Penetrant testing of AM components. Rough surface caused noise spots [254]. (c) An example of radiographic testing. The AM component was sectioned along the line A-A. Defect detected by the testing was confirmed [252].

- ***Internal defects***

To inspect the deep internal defects with a clear image, radiographic testing [252] is employed for detection of internal defects. The radiation absorption images of AM components are recorded and demonstrated as 2D pictures (see Fig. 26c). It can provide more details of defects in the AM components compared with other NDT methods. However, the radiation absorption is sensitive to defect orientation and thus can cause misleading when distinguishing the types of defects, therefore, it is still hard for radiographic testing to inspect the AM components with complex geometry.

To overcome the challenge, Digital Image Correlation (DIC) and Digital Volume Correlation (DVC) techniques are introduced to the radiographic testing, which is also known as the "micro (μ) X-ray Computed Tomography (μ-XCT) scanning". The μ-XCT consists of a series of optical imaging and measurements combined into an overall data set. The 2D radiation absorption images of AM components from different angles are recorded and reconstructed as a spatial distribution of radiation absorption [262]. The reported resolution of μ-XCT scan results is several micrometers and it is capable to detect most of defects of metal components. Lack of fusion [263], porosity [264] , cracking [265], and even inclusion [266] could be revealed and mapped by μ-XCT scanning (Fig. 27a-c). Except for bulk defects, μ-XCT scanning could inspect surface roughness [267] and part distortion as well, which make μ-XCT scanning an all-round inspection technique for AM defects analysis. The main restriction of μ-XCT scanning is depending on the penetration of radiation source. Large specimens take much time and decrease the resolution inevitably. Specimens sized from 10 to 100 mm are recommended. Another restriction is that μ-XCT scanning cannot detect the sharp corner morphology defects such as crack tips or sub-micron pores, which is because of resolution limitation. Alternatively, there are destructive methods for defect detection that are more frequently used for examination of the AM parts by cross-sectional characterization using OM and SEM. It should be noted that such inspection methodologies can provide high-resolution and detailed microscopic information of internal cracks and pores, however, their capabilities in overall quantification of internal defects in the AM parts are limited [268]. In addition, Archimedes method and mass/volume method are the other commonly experimental methods used to determine the overall porosity content or bulk density of AM components. Although, these density measurement methods are easy-to-implement and cost-saving, they cannot provide any detailed information about pore size, distribution and morphologies.

Radiography [269] and mechanical wave methods with sensors embedded in the substrate [270] could detect defects formation during AM processing. It is even possible for high-speed radiography to record the melting pool kinetics. Keyhole, element vapor, and spatter could be detected with high-speed image. Except for the bulk defects detection, it is also important to

ensure the building condition during AM process especially for the powder bed techniques [271]. Optical camera is also commonly used to monitor the powder bed condition of AM components, which could reveal anomalies of powder bed or as-build surface [272]. Another monitoring method for AM process is the full-field infrared thermography [273]. It used an infrared camera to collect infrared radiation from the powder bed and as-build components. The intensity of radiation would vary with temperature and surface condition during fusion process, making the thermography a possible way for in-situ defects monitoring [274]. Pore and cracking have different thermal conductivity compared with nearby material and thus could be detected on the temperature profile (Fig. 27d-e). Thermography also reveals the thermal gradient of AM components, which is an important factor on microstructure evolution [273]. However, the resolution of thermography is not significantly lower that other inspection methods [275], which make it inaccurate and ineffective for precise quantification, identification and classification of the defects.

- ***Residual stress***

To precisely estimate the influence of residual stress on cracking and resulting mechanical performance, several techniques are employed to measure the magnitude of residual stress. Table 2 summarizes the examples of common measuring tools for the fusion-based AM Nickel-based superalloys. Recently, Schröder et al. have published a review article on diffraction-based characterization methodologies of residual stress in laser AM of metals [228]. They emphasized the importance of the spatial distribution of residual stress for which the appropriate non-destructive characterization such as diffraction-based methodologies are needed. They have further listed and discussed the common diffraction-based methods used to determine residual stress induced during laser-based additive manufacturing processes. They have the following recommendations to have the best results in residual stress measurements: (1) to use mechanically relaxed specimens in several orientations to find the most strain-free lattice spacing; and (2) to use a grain structure model approach along with their experimental measurements to calculate diffraction-elastic constants which are material-, texture-, and process-dependent factors.

Table 2. Summary of the use techniques for measuring residual stress in fusion-based AM Ni-superalloys.

Alloy	**AM process**	**Measurement**	**Ref.**
IN718	Laser rapid forming	Microhardness	[276]
	L-PBF	EBSD	[277]
	L-PBF	Synchrotron X-ray diffraction, neutron diffraction	[228,237]
	L-PBF	XRD	[171]
	L-PBF	Neutron diffraction	[278]
IN625	DED	Neutron diffraction	[247]

	L-PBF	EBSD	[279]
	L-PBF	Microhardness, XRD	[168]
Waspaloy	DED	Microhardness	[239]
Hastelloy X	L-PBF	Hole drilling, XRD, EBSD	[280]

Microhardness method - Proposed by Carlsson and Larsson [281,282], the Vickers microhardness method can be interpreted as the function of residual stress and residual strain which is defined as $H=C\sigma(\varepsilon_{repr} + \varepsilon_{res})$ and $c^2 = (c_0)^2 - 0.32$ Ln $[1 + (\sigma_{res})/\{\sigma(\varepsilon_{res})\}]$; where c is the ratio between the real and nominal projected contact areas of the indentation which is calculated by the diagonal lines of the indentation (assuming a prefect diamond shape); H is the measured micro-hardness of the tested point; C is a constant, which depends on the geometry of the sharp indenter only; $\sigma(\varepsilon_{repr} + \varepsilon_{res})$ is the flow stress at an effective plastic strain $(\varepsilon_{repr} + \varepsilon_{res})$; ε_{res} is a representative value of the effective plastic strain; and ε_{res} is the von Mises effective residual plastic strain in an equi-biaxial situation. By incorporating the uniaxial tensile test where the stress-strain curve obeys the power-law function, i.e., $\sigma=K(\varepsilon_P)^n$ MPa, the magnitude of residual stress and strain can be finally estimated.

Hole drilling test - Hole drilling is a destructive technique that applies a strain gauge toward the surface of a sample. By drilling blind or through holes to relieve stresses, the initial residual stresses can be estimated based on the elastic deformation that occurs when the hole is drilled and the stresses at the surface are relieved [283]. Considering the contribution of non-uniform strain relaxations within the AM processed materials, the integral method was further developed. The test is divided into several small depth increments, and the produced relaxation will be recorded for every single incremental step. A strain/depth curve can thus be plotted from these experimental measurements and can then be used to determine the residual stress as the function of thickness.

X-ray/neutron radiography - Diffraction radiography is one of the non-destructive strategies to analyze the residual stress based on the Bragg's law of diffraction. The specific lattice strain along with a plane, ε_{hkl}, is calculated from the relative change in the stressed planar spacing, d_{hkl}, with respect to the nominal, or stress-free spacing, d^0_{hkl}. In particular, the lattice strains, ε_{hkl} can be computed as $\varepsilon_{hkl} = \frac{d_{hkl}-d^0_{hkl}}{d^0_{hkl}}$, where $d_{hkl} = \frac{2\sin\theta_{hkl}}{\lambda}$ and θ_{hkl} is the angle between the incident beam and the (*hkl*) lattice plane; λ is the wavelength of the incident beam. If the incident beam is neutron, the λ can be further estimated according to the Broglie relation or $h/\lambda=mL/t$ (h is Planck's constant, m is the neutron mass, L is the length of the neutron flight path, and t is the time of flight). The diffraction can be carried out with laboratory sources (e.g., 30 keV), however, the low energy restricts the penetration depth of X-rays and thereby restricts thickness that can be inspected. In contrast, the diffraction carried out by synchrotron

X-rays and neutron can reach a deeper penetration depth which is on the order of cm [284]. This allows better approach to analyze the distribution of residual stress within the samples.

Electron backscattered diffraction - Although EBSD does not have the ability to compute the exact magnitude of residual stress within the AM parts, it is still a powerful means for visualization of strains that allows the qualitative analysis of the distribution of residual strains under the micro-scale. In particular, residual strains can be described by the formation of dislocations that causes local variations of lattice orientation, and hence the level of misorientation revealed by orientation imaging microscopy (OIM) can well indicate the strain distribution within the materials. The technique is extremely helpful for assessing the strain levels within the AM processed superalloys due to the non-uniform distribution of the strains induced by dendritic structure or different phases.

- ***In-situ monitoring***

In-situ non-destructive Digital Image Correlation (DIC) and laser displacement sensor (LDS) [285] detection testing methods are commonly used for quantifying the part distortion or the residual stress. The DIC technique could be used for AM component inspection with DIC camera [286], which can reconstruct the 3D surface morphology and part geometry of material. Though DIC camera cannot detect deep internal defects (Fig. 27d-e), it could cooperate with computer software to measure the geometrical distortion, which is more efficient than radiography methods [287]. The LDS method is also used to measure the distortion and residual stress at certain positions, while the DIC method can provide full-field distortion measurement and stress estimation. However, the other destructive or *Ex-situ* testing methods for quantifying the residual stress more commonly used for the powder bed AM processes such hole drilling, slitting, X-ray and neutron diffraction methods. This is because the *in-situ* methods are less applicable for the powder bed AM process due to the existence of powder. A list of available non-destructive techniques for defects detection of fusion-based AM components is presented in Table 3, along with their advantages and restrictions.

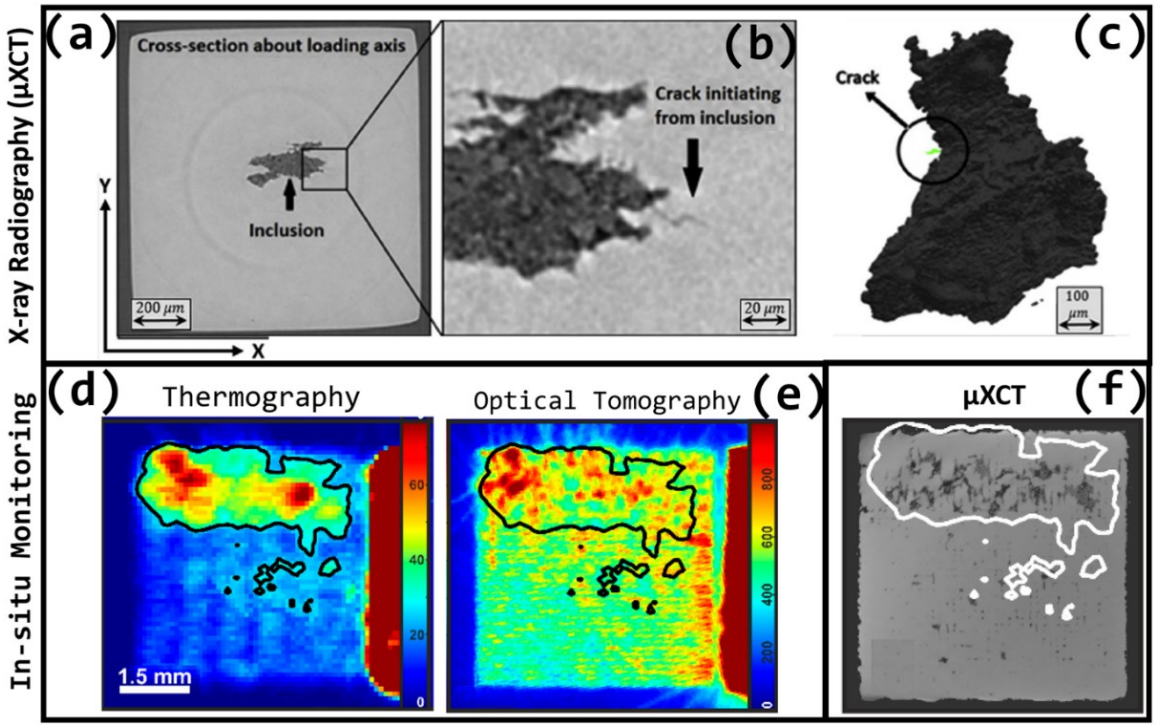

Fig. 27. Defect Detection. (a-c) μ-XCT analysis: inclusion detected in heat treated powder metallurgy (PM) Nickel-based RR1000 superalloy. (a-b) crack initiating at the interface between γ-grain matrix and inclusion, and (c) reconstructed 3D image of crack and inclusion, reproduced from [266]. (d-f) comparison between data obtained by in-situ monitoring (by Thermography in (d) and Optical Tomography in (e) with that of μ-XCT analysis in (f) for L-PBF 316L SS [274].

Table 3. A summary of Non-destructive techniques for defects detection of fusion-based AM components.

	Method	Detected Defect	Pros	Cons	In-situ monitoring
Image analysis	Radiography (X-ray, neutron) [252,269,275,288]	•Crack •Pore •Inclusion (~10μm)	•Large component	•Health concern •Time-consuming with high resolution •Flaw orientation depending. •Extensive training and experience	Yes
	Computer tomography (X-ray, neutron) [262–267,288,289]	•Crack •Pore •Geometry distortion •Surface roughness. (~10μm)	•Spatial distribution of defects	•Time-consuming with high resolution •Size limitation (<20cm, X-ray).	No
	3D scanning [286]	•Geometry distortion •Surface roughness (~10μm)	•Large component	•No internal defects	No
	Penetrant testing [249]	•Crack •Pore	•Low cost	•Surface roughness noise •Shallow defects	No
	Camera-based Monitoring [271,272]	•Crack •Pore •Powder bed anomalies •Spatter (~10μm)	•Powder bed and surface monitoring	• Not suitable for post processing	Yes
Mechanical wave analysis	Ultrasonic testing/ Acoustic testing [252,253,261,270]	•Crack •Pore •Inclusion (~0.1mm)	•Quick Inspection	•Surface roughness noise •Limited geometry •Extensive training and experience	Yes
Electromagnetic analysis	Eddy current testing[251]	•Crack •Pore •Inclusion (~0.1mm)	•Quick Inspection	•Surface roughness noise •Limited to conductive material •Shallow defects	No
	Magnetic particle testing [250]	•Near surface	•Low cost	•Surface roughness noise •Limited to ferromagnetic material •Shallow detects	No
Thermography analysis	Infrared Thermography [273–275]	•Crack •Pore (~0.5mm)	•In-situ Monitoring	•Not suitable for post processing •Limited resolution	Yes
Diffraction stress analysis	Neutron/ X-ray diffraction [278,287,290–292]	•Residual stress.	• High resolution	•Near surface defects •Geometry restricted	No

The qualification of AM parts is not a straightforward task due to the process-induced defects forming during the AM fabrication process. The in-situ process monitoring enables the real-time observation of defects formation during the AM process. Although limited, the in-situ or in-layer process monitoring during the AM fabrication process can provide valuable information for better understanding of formation mechanisms of such defects that could in turn help us finding the mitigation solution for them by further modification of process parameters [293]. Additionally, application of in-situ process monitoring for the powder bed fusion AM processes include powder dispensing, laser-powder interaction, melt pool, scan path, and slice [294]. A suitable in-situ process monitoring technique using high-speed imaging could be employed for each case to detect the possible defect formation during the AM process. The following paragraphs provides a summary review for the available high-speed imaging

techniques in the literature that are commonly utilized for the in-situ (in-layer) monitoring of the AM processes.

High-speed imaging using visible optical light, and infrared radiation (IR) has been commonly used for the real time observation of the fusion-base AM processes. As discussed earlier, the IR and near-IR (e.g., silicon focal plane [295]) high-speed imaging uses two-color pyrometry to measure thermal graphs (thermographs) (Fig. 28b) to identifies materials processing anomalies based on the heat transfer reflection [296]. One of the benefits of the high-speed optical imaging or IR thermography is that they can be coupled with the data driven techniques (e.g., convolutional neural networks, computer vision) to identify and classify defect formation and minimize in-process defects [137]. The high-speed optical and IR imaging data can validated with the ex-situ post processing characterization such as synchrotron laboratory x-ray imaging (Fig. 28c) [297]. Majority of L-PBF studies have used in-layer thermography technique to monitor the temperature profile of melt pool and therefore, to identify the process-induced defects and anomalies [298,299]. Alternatively, the full-field IR thermography (with a lower frame rate and data storage requirement) of entire layers can be employed to identify material defects (e.g., keyhole and lack-of-fusion pores) and subsequently to correlate with the ex-situ observations for further validation [298]. The primary benefits of the pyrometry and high-speed IR imaging (or in-situ thermography) is a non-contact technique to measure the temperature profile during the process. However, the setups and calibration of digital imaging is not a straightforward task.

High-speed synchrotron X-ray imaging was first used as an in-layer real time observation technique during the AM fabrication of metallic alloys in 2017 [300]. Different from the laboratory synchrotron X-ray imaging techniques, in the high-speed versions, the X-rays are not directly used for the imaging where the X-rays are converted to visible light rays to high-speed cameras (

Fig. 29a-c) [301]. Using the in-situ X-ray imaging with micrometer spatial and sub-nanosecond temporal resolutions, the AM processes can be studied even in three dimensions [302] with great details such as melt pool dynamics, powder ejections, rapid solidification, keyhole dynamics, and nonequilibrium phase transformation [303]. Additionally, the high-speed synchrotron x-ray diffraction has been utilized as an in-situ monitoring technique to study the details of solidification mechanism of AM processes (

Fig. 29(d-f) [304].

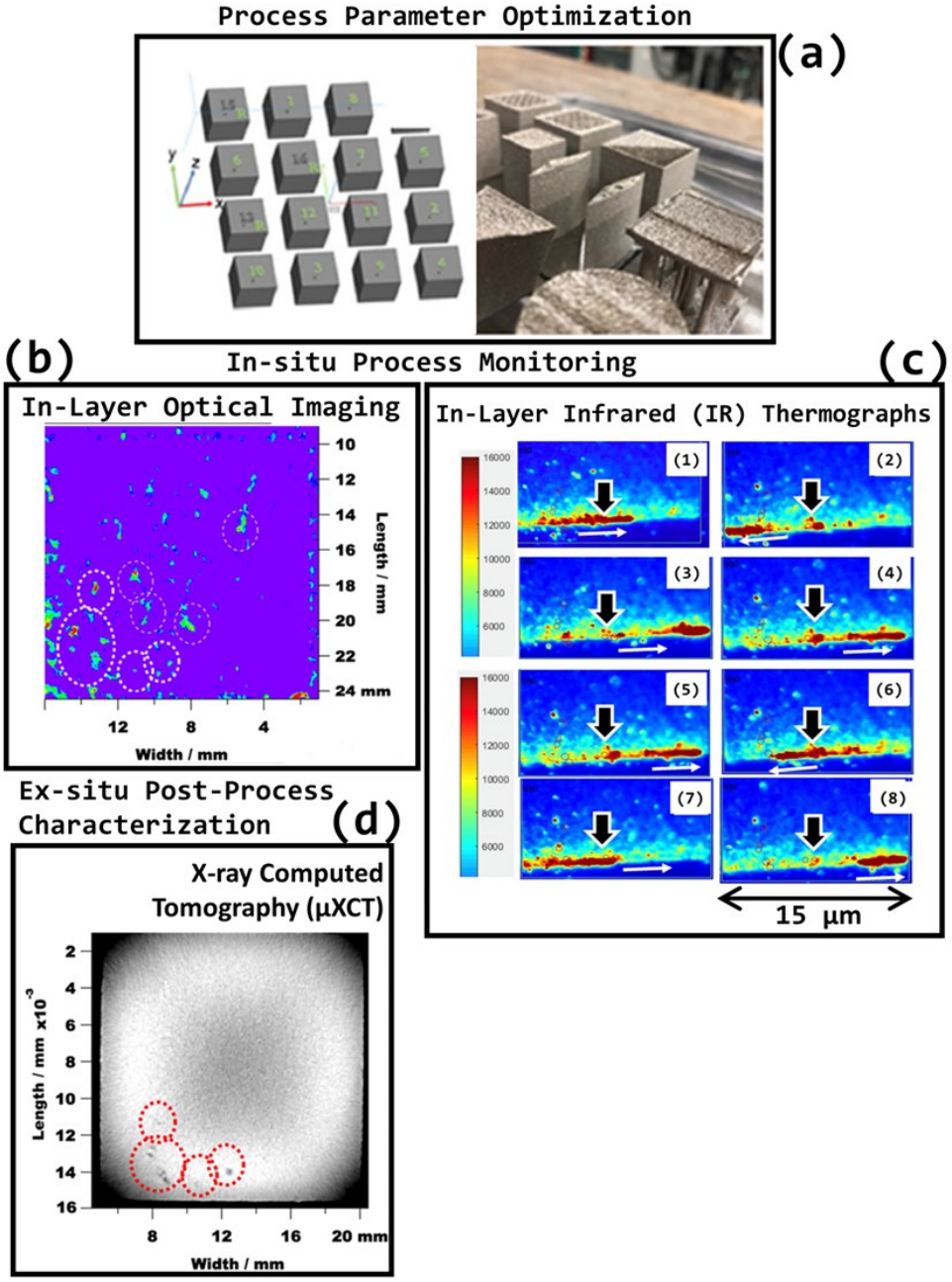

Fig. 28. In-situ monitoring for defect identification in Nickel-based CM247-LC superalloys during L-PBF process. (a) design of geometries and L-PBF process parameter optimization using cubes; (b) In-situ (in-layer) process monitoring using high-speed optical imaging (processed data corresponding to deposited layer #309); (c) In-situ (in-layer) process monitoring using the infrared (IR) thermographs obtained from the same layer within the region obtained over several time frames; (d) Ex-situ post processing characterization using the X-ray computed tomography (µXCT) of the same layer [297].

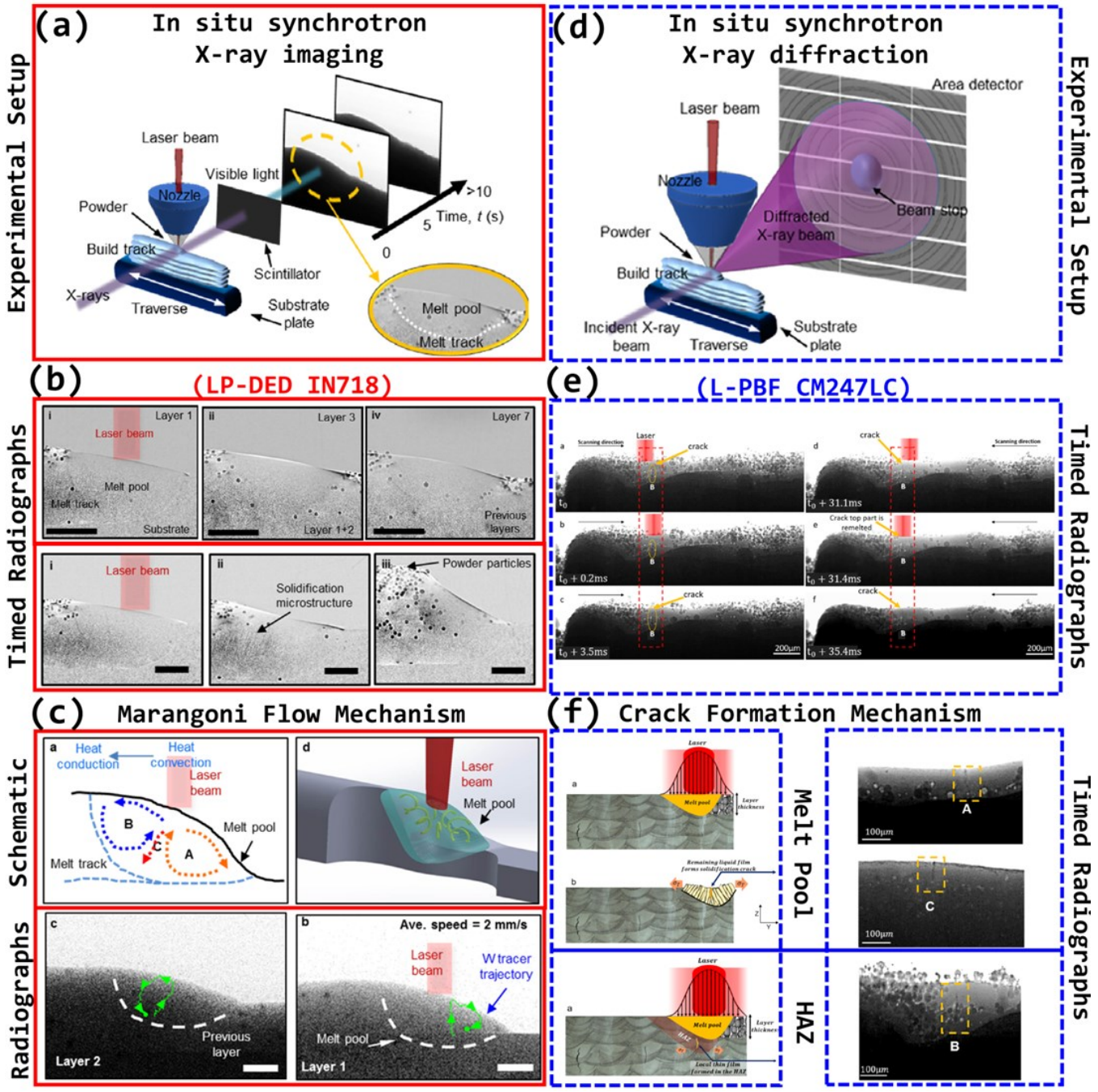

Fig. 29 In-situ and Operando Synchrotron X-ray radiography for AM Nickel-based superalloys in (a)-(c) for LP-DED IN718 [305] and in (d)-(f) for L-PBF CM247LC [306]: Schematic presentations for experimental setups for X-ray imaging and diffraction in (a) and (b), respectively. The timed radiographs in (b) and (e) for X-ray imaging and diffraction, respectively. The melt pool formation mechanism presented using the schematic diagrams as well as the X-ray imaging and diffractions in (c) and (f), respectively. Reproduced from [305] and [306].

5. Mechanical properties

In this section, the mechanical properties of AM Nickel-based superalloys including tensile, fatigue and creep will be reviewed based on existing literature and according to the influential factors.

5.1. Tensile behavior

Tensile properties at room and elevated temperatures are widely used to characterize the mechanical properties of the Nickel-based superalloys [26]. Fig. 30 summaries the room-and-elevated-temperature tensile properties for various AM Nickel-based superalloys such as laser beam powder bed fusion (L-PBF) Haynes 282 [187], L-PBF Hastelloy X [190], electron beam powder bed fusion (E-PBF) IN718 [307,308], L-PBF IN718 [170], laser powder direct energy deposition (LP-DED) IN718 [189], L-PBF IN738LC [309] ,L-PBF IN625 [310], powder bed binder jet (PB-BJ) printed IN625 [311]. Most relevant data reported in Fig. 30 for the room and elevated temperature tensile properties of the AM Nickel-based superalloys are focused on the IN718, IN625, Haynes 282, and Hastelloy X. This could be because of good fabricability and weldability of these alloys [312].

5.1.1. Effect alloy composition

Since the AM processed IN718 alloy shows significantly different tensile properties in as-build or non-heat treated (NHT) condition as compared to heat treated ones which could be attributed to the γ″-precipitates forming upon subsequent aging treatment. The tensile properties of the NHT AM IN718 is roughly similar that of the NHT and heat-treated AM IN625 and Hastelloy X alloys [313], which is reasonably ascribed to the small amount of γ″-precipitates in the NHT condition of AM IN718 alloy. This in turn makes its tensile properties comparable to that of the solid solutioned IN625 and Hastelloy X alloys. Therefore, in Fig. 30, all AM materials are compared in heat-treated conditions.

Furthermore, the tensile properties of heat-treated AM Nickel-based superalloys may vary due to deviation in heat treatment (HT) schedules [187]. Relatively complete precipitation of the strengthening phases such as γ′/γ″ in Haynes 282/IN718 and the grain boundary carbides in IN625/Hastelloy (as partial hardening precipitates) X will occur only after a set of carefully customized aging processes and solution treatments respectively, leading to enhancement in strength of these alloys. Despite many efforts to develop a novel customized heat treatment procedure for the Nickel-based alloys [314], still there is knowledge gap for heat treatment development of such AM alloys based on their unique microstructure characteristics (e.g., columnar grains aligned with build direction and micro-segregation within the inter-dendritic cellular regions), which are significantly different from what observed for the cast or wrought counterparts [33]. Considering the application-driven excellent high-temperature performance of Nickel-based superalloys, the grain boundaries are of crucial importance due to their

strengthening effect on high temperature properties such as creep, leading to a preferred design criteria for the columnar grain structure especially when it's parallel with the applied load. Therefore, in Fig. 30, all data points were considered for the vertically fabricated AM specimens (i.e., direction of applied load parallel to the build direction).

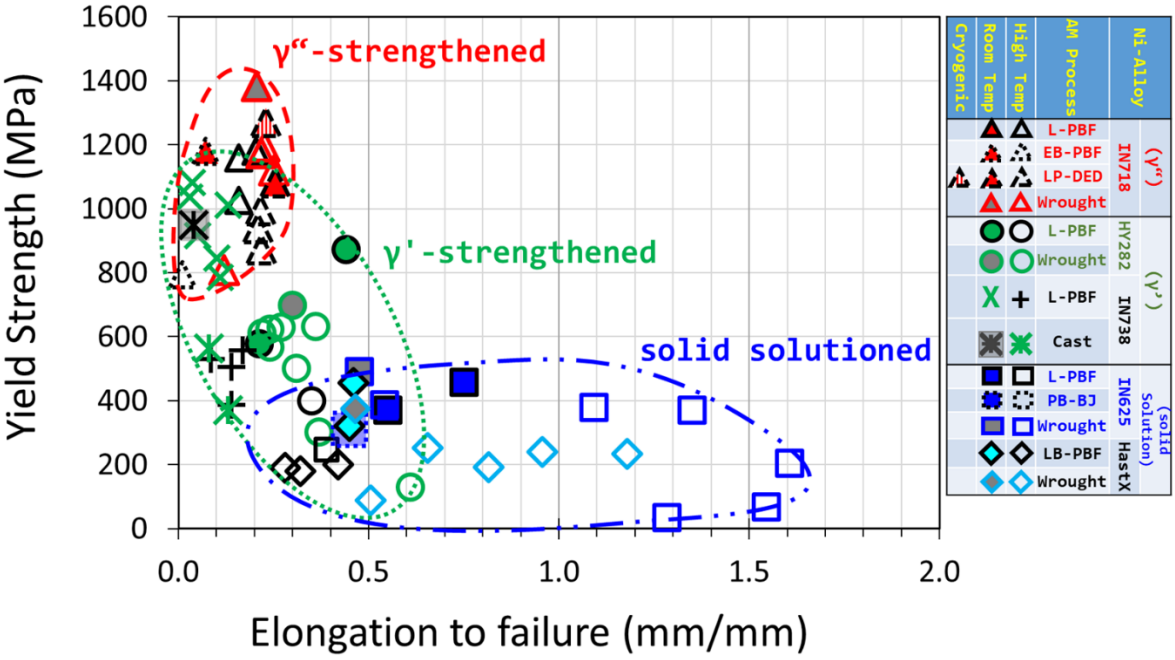

Fig. 30. A property map summarizing the combination of room- and elevated- temperature-yield strength and elongation to failure for various AM Nickel-based superalloys such as L-PBF Haynes 282 [187,315,316], L-PBF Hastelloy X [190,317], E-PBF IN718 [307,308], L-PBF IN718 [170], LP-DED IN718 [189], L-PBF IN738LC [35,309,318–324], L-PBF IN625 [310,325], PB-BJ IN625 [311]. Note all data consisted in this figure were in heat treated (HT) condition and obtained from vertical specimens, i.e., load direction is parallel to build direction. The wrought data were obtained for the sheet metals in fully heat treated conditions from Haynes International website [326].

5.1.2. Effect test temperature

As shown in Fig. 30, distinct types of Nickel-based superalloys show different high-temperature tensile properties. For instance, the solid solutioned Hastelloy X and IN625 alloys have shown the lowest strengths at room as well as elevated temperatures, while γ"-strengthened IN718 superalloy showed the highest strength even better than that of the γ′-strengthened Haynes 282 superalloy. This is further shown in Fig. 31 using separate graphs for the tensile properties (i.e., yield and ultimate strengths, and elongation to failure) of these alloys as a function of test temperature. It is notable that the elevated temperature tensile properties of γ'-strengthened Nickel-based superalloys presented in Fig. 31 are not conclusive due to the limited existing literature for AM materials. However, it is well known that the strengthening effect of γ"-phase is better than that of γ'-precipitates due to the higher lattice misfit generated by the former in the matrix [327].

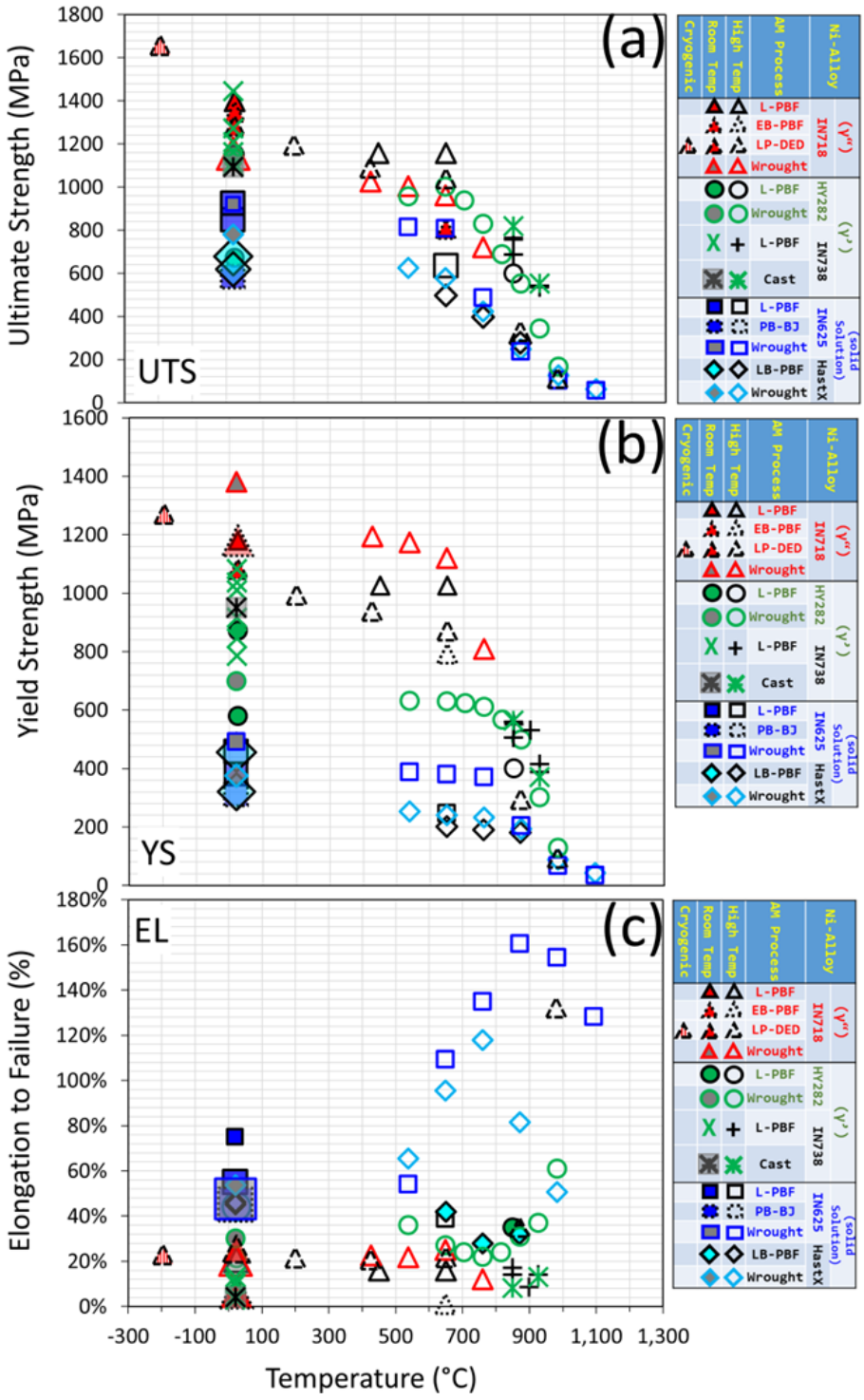

Fig. 31. Tensile properties, i.e., ultimate tensile strength (UTS) in (a), yield strength (YS) in (b), and elongation to failure (EL) in (c) at room and elevated temperatures for various AM Nickel-based superalloys such as L-PBF Haynes 282 [187,315,316], L-PBF Hastelloy X [190,317], E-PBF IN 718 [307,308], L-PBF IN 718 [170], LP-DED IN 718 [189], L-PBF IN738LC [35,309,318–324], L-PBF IN 625 [310,325], PB-BJ) IN 625 [311]. Note all data consisted in this figure were in heat treated (HT) condition and obtained from vertical specimens, i.e., load direction is parallel to build direction. The wrought data were obtained for the sheet metals in fully heat treated conditions from Haynes International website [326].

In general, the grain boundaries (GB), particularly those perpendicular to the applied load direction, are the weakest regions under tension load at elevated temperatures [328–330]. This is partly because, the GB's are the last regions solidified during the solidification where the brittle intermetallic/impurity phases could form and therefore they could play as a major source for the crack initiation points under tensile load [190]. For the NHT γ"-strengthened AM superalloy such as IN718, the intergranular fracture has been reported to be the main failure mechanism [329]. Similar failure mode has been observed on the room- and elevated-temperature tensile fracture surfaces of AM Hastelloy X [328]. Thus, the lower the number of grain boundaries (i.e., the larger grain sizes), the better the high-temperature tensile properties of Nickel-based superalloys due to lower number of microcracks/voids initiation points as well as propagation paths [331]. Due to specific microstructural features such as columnar epitaxial grain growth along the build direction, the laser additive manufacture technologies (LAM) could result in an improved creep performance in vertical direction (i.e., when the load direction is parallel to the build direction).

However, it has been reported that the brittle Laves phases (normally formed within the inter-dendritic regions during the last stage of solidification of the AM processes in the Nickel-based superalloys, such as IN718) can act as the void initiation sites by the "debonding" or "fragmentation" under tensile test at room and elevated temperatures [314] (see Fig. 32), and the creep rupture test [314]. This can explain the inferior tensile elongation to failure of AM IN718 alloys, as shown in Fig. 31 (c), which can be improved by eliminating these detrimental Laves phases either by increasing cooling rate during the AM fabrication processes [332] and/or upon carefully customized heat treatments [333] with special attention to preserving the original and desirable columnar grains.

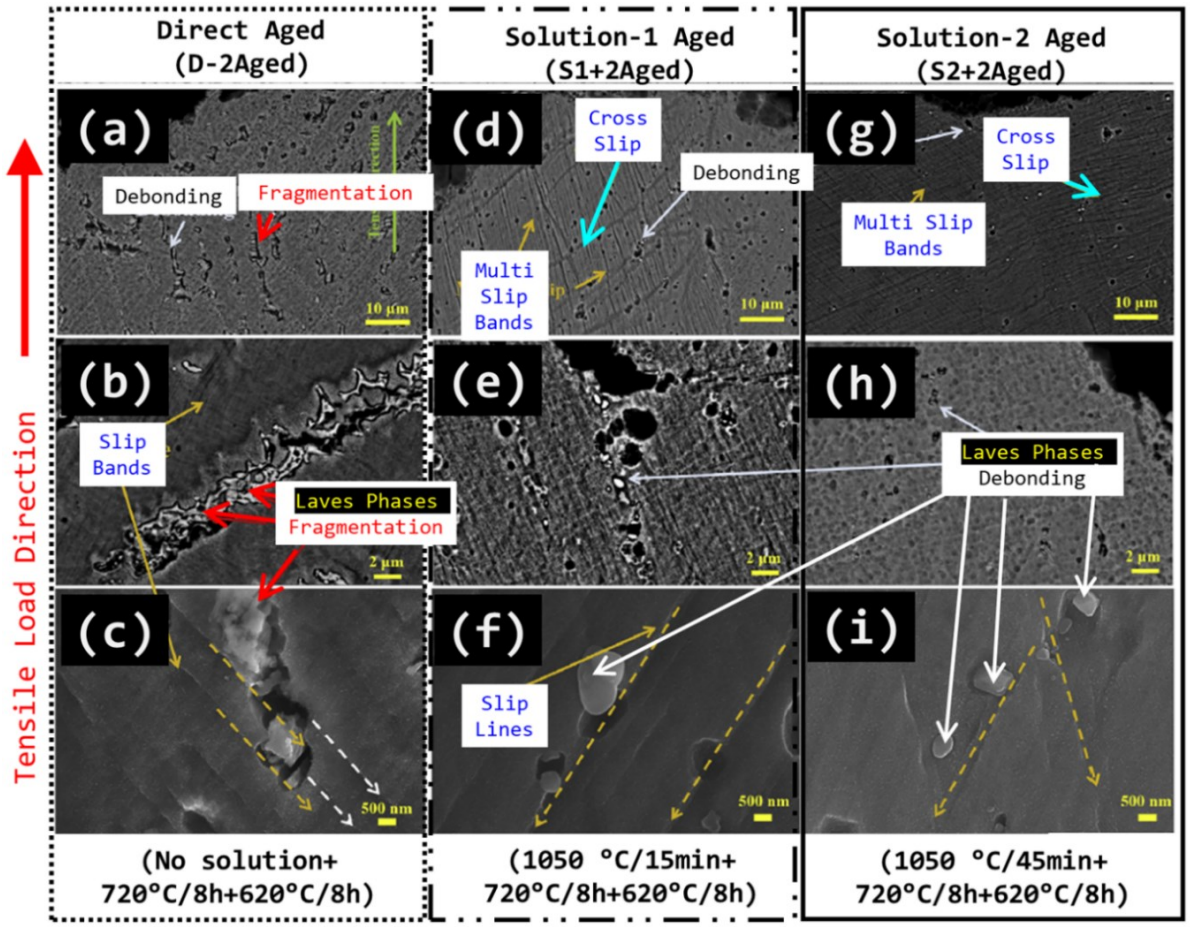

Fig. 32. The SEM micrographs obtained from the room temperature uniaxial tensile fractured surfaces on longitudinal cross-section, i.e., parallel to load direction, of the IN718 specimens fabricated by LAM technology in various hear treatment conditions. (a)-(c): directly fully aged (D-2Aged) condition (i.e., 720 ºC/8h+620 ºC/8h); (d)-(f): the fully aged following a 15-minutes solution treatment at 1050 ºC (S1+2Aged) condition (i.e., 1050 ºC/15min+720 ºC/8h+620 ºC/8h); and (g)-(i): the fully aged following a 45-minutes solution treatment at 1050 ºC (S2+2Aged) conditions (i.e., 1050 ºC/45min+720 ºC/8h+620 ºC/8h). Note the original micrographs used in this figure were adopted with permission from Sui et al. [314].

5.2. Fatigue properties

It is well known that fatigue is the common failure mechanism for the aeroengine components operating below the nominal yield stress [334]. Fatigue failure is a complex phenomenon which occurs as a result of progressively degradative response of material under repetitive or cyclic loading, which in turn leads to the localized microstructural damage due to the formation and propagation of cracks [335].

In general, fatigue failure occurs during three stages: 1) crack initiation, 2) crack propagation and 3) final fracture [336]. In the first stage, the micro-cracks are initiated from the process-induced defects such as gas pores, and inclusions, which could be originated at the grain boundary and the surface morphology. In the second stage, these microcracks propagate either on the maximum shear stress plane and/or along the maximum tensile stress plane [337]. Eventually, in the final stage, when the stress is large enough and the microcracks propagates unsteadily, the final fracture occurs which is characterized by the microstructure features such

as striation on the fracture surfaces. For the low cycle fatigue (LCF) tests, the crack propagation stage controls the total fatigue life, while for the high cycle fatigue (HCF) tests, the crack initiation is the dominant failure mechanism [335].

Complication in understanding and interpretation of materials' fatigue failure are largely because it is indeed an interactive result of several factors such as the size, volume fraction and morphology of process-induced defects as well as microstructural features. Such interpretation of materials' fatigue failure could even be more complicated for the additively manufactured processes due to their specific characteristics such as high cooling rates during layer-by-layer materials deposition, leading to significantly different microstructure and defect features as compared with those of the wrought processes [338].

Recently, fatigue performance of the AM Nickel-based superalloys such as IN718 [339] and IN625 [340] have received a lot of attention, majority of which reported an inferior fatigue performance for the AM components as compared with the wrought processed counterparts [341]. However, there are limited research works reported otherwise. For instance, Gribbin et al. [342] reported a cross-over for the *low* cycle fatigue (LCF) lives of L-PBF IN718 with that of the wrought alloy at 1% strain amplitude. In other words, below 1% strain amplitudes, the AM alloys have outperformed the wrought ones. Similarly, Sui et al. [343] reported a cross-over for the *high* cycle fatigue (HCF) lives of the laser powder direct energy deposited (LP-DED) IN718 at 647 MPa stress amplitude with that of wrought IN718, i.e., above 647 MPa stress amplitude, the AM alloy outlived the wrought one. Additionally, Poulin et al. [344] have found that the L-PBF IN625 alloy showed comparable fatigue crack propagation rates with that of the wrought alloy within the Paris regime. It is notable that in all the above-mentioned studies the microstructure of the AM Nickel-based superalloys was tailor-made using carefully customized heat treatments, which is emphasizing on the complication of fatigue failure mechanism in the AM alloys due to several interactive factors such as microstructural features and various types of process-induced defects. In the following paragraphs, some of these influential factors on fatigue behavior of two well-known Nickel-based superalloys, namely, IN718 and IN625, which have been studied in the AM conditions more than the other Nickel-based superalloys, will be briefly discussed.

5.2.1. Effect surface roughness

Surface roughness is a crucially important factor on the fatigue behavior particularly for the AM alloys due to their characteristic process-induced defects such as surface and subsurface defects, e.g., micro pores, unfused powders, and LoF [345]. Additionally, the post processing surface treatment of AM components such as shot peening, machining and polishing is a challenging task due to their intricate and complex near-net geometries. Moreover, it is a well-accepted fact within the AM community that most fatigue failures are caused by the cracks originated from the process-induced defect located on surface or sub-surface areas [346].

Yamashita et al. [192] has shown by a comprehensive defect analysis that surface defects are more detrimental than internal defects for the fatigue performance of the L-PBF IN718. Moreover, Wan et al. [347] have shown in the L-PBF IN718 by using finite element simulations that the morphology of surface defects has a stronger counter-effect than their depth on the fatigue properties especially if the depth-location of such defect is 200 μm or deeper below the outer surface of the test specimen. Fig. 33 shows the fatigue properties of the IN718 and IN 625 alloys fabricated by various AM processes such as L-PBF IN718 [348], E-PBF IN718 [349], L-PBF IN625 [350,351] and PB-BJ IN625 [352] in two surface conditions, namely, as-build surface and post processing surface treated conditions such as machined or polished.

As shown in Fig. 33, regardless of heat treatment condition, the post processing surface treatments such as machining, mechanical griding, and polishing have been shown to have an improvement effect on the fatigue performance of the tested AM Nickel-based superalloys. In brief, in order to improve the fatigue properties of the AM Nickel-based superalloys, it seems necessary to remove the surface/subsurface defects induced during the AM fabrication processes by means of post processing surface treatment such as machining, polishing and electrochemical processing technologies [353].

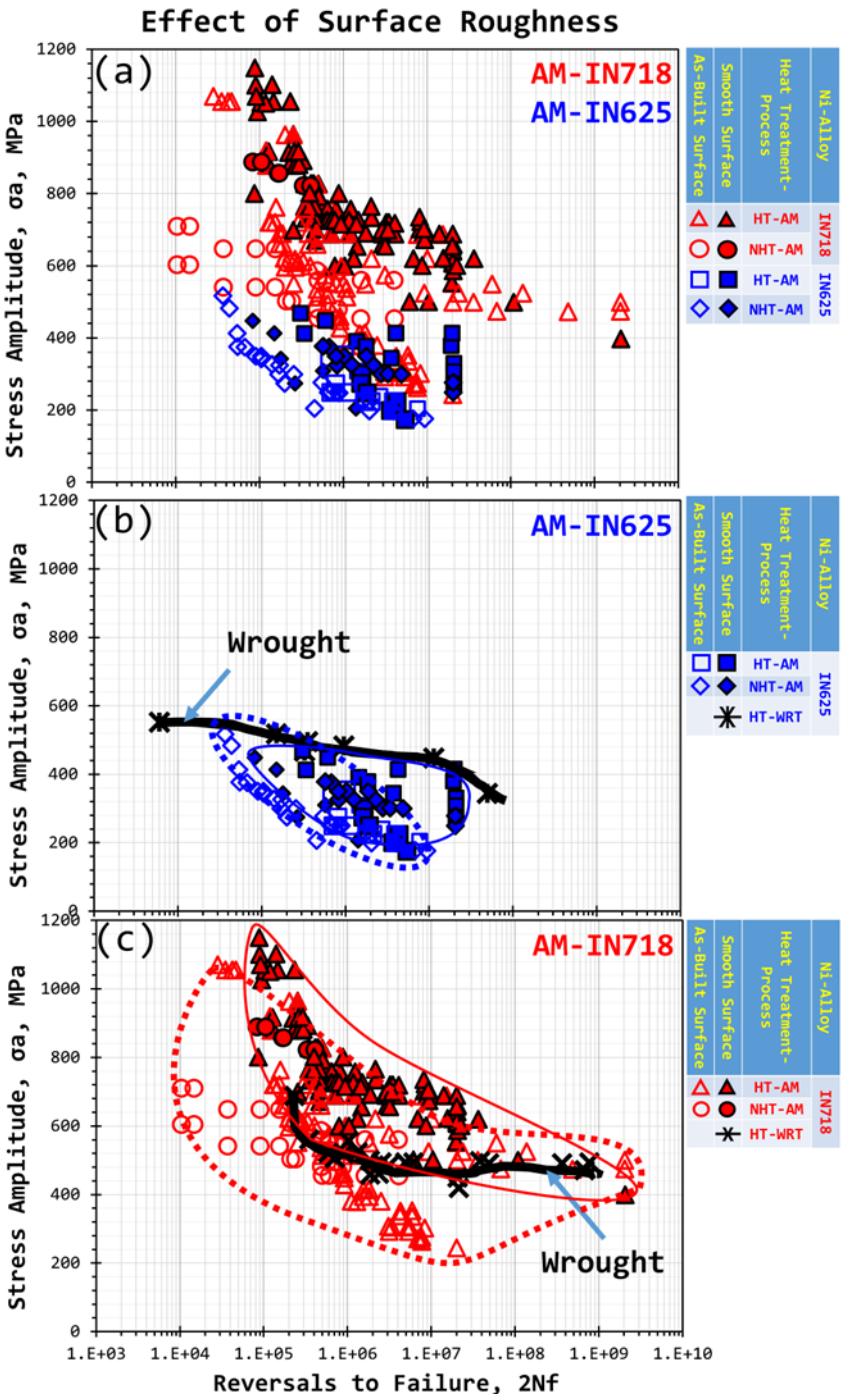

Fig. 33. (a) Effect of surface condition on room temperature fatigue properties obtained in fully reversed test condition (R = -1), i.e., stress amplitude (MPa) versus reversals to failure ($2N_f$), for IN625 (in (b)) and IN718 (in (c)) fabricated using various AM processes as L-PBF IN718 (HT) [348,354–357], E-PBF IN718 (NHT) [349], L-PBF IN625 [350,351] (HT/NHT), and PB-BJ IN625 (NHT) [352]. (Note data presented in figure are both in NHT and HTconditions obtained from the vertical specimens, i.e., load direction is parallel to build direction, in two surface roughness conditions, i.e., as-build surface condition and surface treated condition such as by machined, mechanically ground and polished.) The wrought data were obtained from the references [338,358].

5.2.2. Effect of hot isostatic pressing (HIP)

As discussed earlier, the process-induced defects located on surface/subsurface regions are the most detrimental factors on the fatigue properties of AM metal alloys. The pores/voids are considered as the most common process-induced volumetric defects which are also the

dominant source for the crack initiation points in AM metals under cyclic loads. Additionally, it is generally accepted that the size, shape, and morphology of such voids as well as their location relative to the outer surface of the specimen are the other important factors affecting fatigue properties of AM metal alloys.

Amongst the influential post processing treatments on fatigue behavior of an AM metal alloy such as surface treatments as briefly discussed earlier, hot isostatic pressing (HIP) is also considered as an effective heat treatment on the fatigue behavior of some AM metal alloys such as titanium alloys [359,360]. Several studies have reported that the AM Ti-6Al-4V alloy has shown significantly better fatigue resistance in HIPed condition which is also comparable with that of their wrought counterparts [359,361–366]. This could be attributed to the homogenization effect of HIP on the AM process-induced microstructural anisotropy (i.e., grain structure and crystallographic orientation) and the defect directionality (i.e. voids' shape and morphologies relative to the build orientation) through partial/complete recrystallization of the matrix grain structure, removal of the void directionality in their shapes, smoothening of sharp edges in their morphologies and even by closing some voids [338].

However, the effect of HIP on fatigue behavior of AM metals cannot be generalized. An example is the AM IN718 superalloy. Gribben et al. [342] have observed that the HIPhas insignificant effect on the fatigue properties of L-PBF IN718 at low strain amplitudes; therefore, they concluded that the role of porosity is less significant on the fatigue properties of the L-PBF IN 718 alloy at lower strain amplitudes. Additionally, Yadollohi and Shamsaei [338] have reported that the L-PBF IN718 alloy showed inferior fatigue behavior in HIPed condition as compared with HIPed counterparts. Based on a comprehensive analysis on fatigue fracture surfaces, they have rationalized their observations by the large-sized un-melted regions (>100 um) located near-surface which were connected to the outer surface of the test specimens, acting as crack initiation sites.

Yadollahi and Shamsaei [338] have, based on the X-ray CT scans results obtained from the gage section of an NHT L-PBF IN718 alloy containing large voids along the perimeter of test specimens on the surface, further concluded that the direct contact of the outer surface of the test specimens with the powder bed during AM manufacture process may have caused the *"melt pool thermal/fluidic edge effects (i.e., instabilities)"*, which in turn may result in the large-sized subsurface voids. Fig. 34 summarizes the results of effect of HIP heat treatment on the fatigue performance of the IN718 and IN625 alloys fabricated by various AM processes such as L-PBF IN718 [367]; LP-DED IN718 [368], E-PBF IN718 [369], L-PBF IN625 [358] and laser consolidation (LC) IN625 [340]. As shown, the HIPing has shown an insignificant effect on fatigue performance of AM IN625 while it has shown counter-effect on the fatigue properties of AM IN718.

As shown in Fig. 34(b), the HIP has an insignificant effect on the fatigue behavior of the AM IN625 alloys regardless of the heat treatments. Further, these results show that the fatigue

response of the alloy in HIPed condition is comparable with that of the wrought counterparts. Similarly, in the case of AM IN718 alloys (Fig. 34 (c)), HIP has shown a slight improvement effect on the fatigue response of the alloy regardless of heat treatments which are also comparable with that of the wrought counterparts. These results could be attributed to the negligible effect of porosity on the fatigue properties of the AM IN625 and AM IN718 alloys.

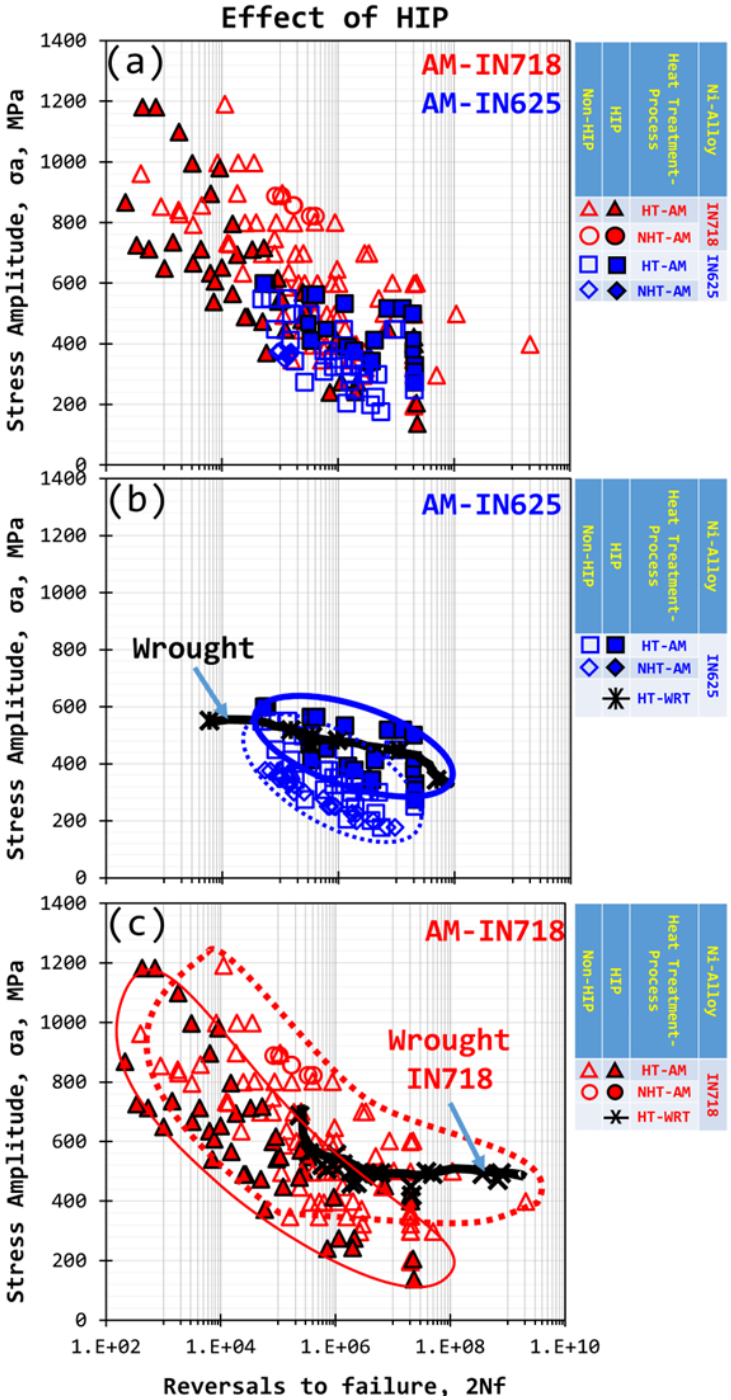

Fig. 34. (a) Effect of HIP on room and elevated temperatures fatigue properties obtained in fully reversed condition, i.e., stress amplitude (MPa) versus reversals to failure (2Nf), for IN625 (in (b)) and IN718 (in (c)) fabricated using various AM processes such as L-PBF IN718 [192,338,349,357,367], LP-DED IN718 [368,370], E-PBF IN718 [349,369], L-PBF IN625 [325,351,358,371], PB-BJ IN625 [352], and laser consolidation (LC) IN625 [340]. (Note data are both in the NHT and HT temper conditions obtained from the vertical specimens, i.e., load direction is parallel to build direction, in smooth surface condition) The wrought data were obtained from the references [338,358].

5.2.3. Effect test temperature

Effect of test temperatures on fatigue properties of IN625 and IN718 fabricated using various AM processes such as L-PBF IN718 [357], LP-DED IN718 [368], E-PBF IN718 [369], L-PBF IN625 [358], and laser consolidation (LC) IN625 [340] are presented and compared in Fig. 35. Note that data points shown in the plots were obtained in similarly fully heat-treated condition with smooth surface condition under the fully reversed (R=-1) fatigue test condition. As shown in Fig. 35 (b), the AM IN625 alloy has shown little effect of test temperature on their fatigue performance. This could be explained by the hardening response of the alloy under cyclic loading. In the solid solution strengthened Nickel-based superalloys such as IN625, the cyclic response of the alloy could essentially be attributed to the "deformation induced microstructural mechanisms" occurring during cyclic deformation such as (i) dynamic strain ageing (DSA) (i.e., solute drag of mobile dislocations) [372], (ii) increase in dislocation density and dislocation–dislocation interactions, and (iii) precipitation of metal carbides ($M_{23}C_6$ and/or M_6C) and their subsequent pinning effect on dislocations mobility [373]. Since all these deformations induced microstructural mechanisms are active simultaneously during cyclic deformation, determination of individual effect of each constituent is not easy and it requires a detailed modeling approach to be explored.

The Cr and/or C elements can produce DSA (solute drag) effects in Ni-austenite (γ-grain) matrix during cyclic deformation. For instance, in IN625, DSA occurs under cyclic loading within temperature range 200-700 °C [372]. Similarly, in Hastelloy X, another solid solution strengthened Nickel-based superalloy, DSA can occur under cyclic loading within the temperature range of 200°C -700°C [373]. Under cyclic deformation and as a result of the interactive reactions between diffusing solutes/solute-clusters and mobile dislocations at local obstacles such as carbide particles in the glide plane, the matrix hardens. This phenomena is also known as "viscous glide type motion" [374], which in turn result in negative strain rate and inverse temperature dependency [375]. Such combined effect of DSA and dislocation–dislocation interactions on cyclic response have reported in literature for other solid solutioned metals such as low carbon steels [376] and austenitic stainless steels (304H, 316H, 316L, 310, 316LN) [375,377].

Furthermore, under cyclic loading, the nucleation and growth of the metal carbides (i.e., Cr-rich ($M_{23}C_6$) and/or Mo-rich (M_6C) [33]) at lower test temperatures and/or lower test durations are promoted by rapid nucleation on heterogeneous sites such as dislocations and stacking faults [378] and non-equilibrium vacancies [379]. Such deformation induced carbide precipitation has also been reported in literature for the other solid solution strengthened Ni-base superalloys such as Haynes 188 [378], Alloy 617 [380] and Alloy 800 [381]. It was reported that in Alloy 800 [381] that the cyclic softening due to (gamma-prime) shearing has been compensated by the intragranular carbide strengthening induced in the matrix under cyclic loading (through dislocation pinning), which in turn resulting in continuously cyclic hardening

till failure.

As further shown in Fig. 35 (c), the AM IN718 alloy have shown slightly better fatigue performance at room temperature, which can be explained by effect of test temperatures on deformation mechanism in such precipitation hardened Nickel-based superalloy, i.e., dislocation interaction with precipitates under cyclic loading. Fournier and Pineau [382] have comprehensively studied the high-temperature low-cycle fatigue and cyclic behavior of IN718 at room and 650 °C. They have reported a substantial decrease in fatigue life occurred as the temperature was increased from room to 650 °C. They have observed initial hardening at room temperature while at 650 °C, they only observed constant softening under cyclic loading. They have further shown using transmission electron micrographs that γ”-precipitates were sheared in the course of cyclic straining and that plastic deformation proceeded by the propagation of planar bands, which were characterized as deformation twins. Similar results have recently been reported for the L-PBF IN718 at high temperature under static loading [189]. Further, Fournier and Pineau [382] have reported that the twinning deformation mechanism to be more abundant at elevated temperatures than at room temperature.

It could also be generally said that, there are some slight cyclic softening discernable in the stress response of the AM IN718 alloy at some high temperatures, which could be attributed to the combined effect of shearing mechanism of precipitates and anti-phase boundaries (APBs) on the glide plane [383] as well as deformation twining mechanism [382]. Similar cyclic stress behavior has been reported in the other Nickel-based superalloys [384] such as Haynes 282 [383] and NIMONIC 80A [385]. Barat et al [383] has comprehensively studied the “high-temperature low-cycle fatigue and cyclic behavior of Haynes 282” (another precipitation hardened Nickel-based superalloy) and revealed that the main deformation mechanism at the higher temperatures was precipitate shearing, which in turn result in pronounced dislocation activities within slip bands [383].

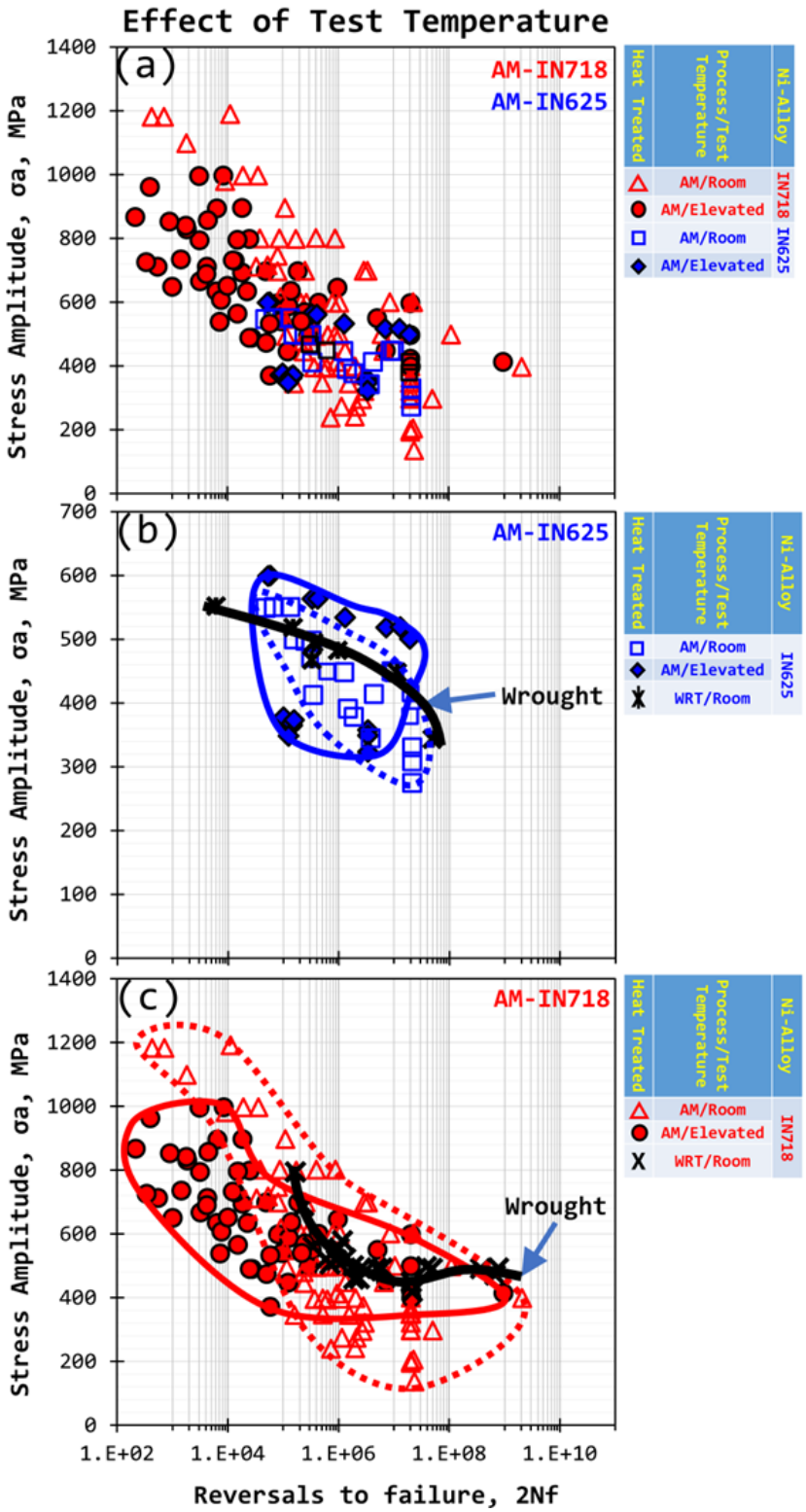

Fig. 35. (a) Effect of test temperatures on fatigue properties obtained in fully reversed condition, i.e., stress amplitude (MPa) versus reversals to failure (2Nf), for IN625 (in (b)) and IN718 (in (c)) fabricated using various AM processes such as L-PBF IN718 [192,338,349,357,367,386], LP-DED IN718 [368,370], E-PBF IN718 [349,369], L-PBF IN625 [325,358], and laser consolidation (LC) IN625 [340]. (Note data are both in the heat treated HT conditions obtained from both vertical and horizontal specimens, i.e., load direction is parallel and perpendicular to build direction respectively, in smooth surface condition) The wrought data were obtained from the references [338,358,386–389].

5.2.4. Effect of secondary phases

As discussed earlier for tensile fractures of AM Nickel-based superalloys, there are some research works, on one hand, that have reported that the brittle secondary phases such as carbides/nitrides (e.g., NbC, TiN), oxidation inclusions [390], delta (δ) [339] and Laves phases [343] can play a role in the fracture phenomena of the AM Nickel-based superalloys under cyclic loads. Fig. 36(a)-(c) present the sequential behavior of the Laves phases during the fatigue fracture mechanism of LP-DED IN718 alloy, in directly aged (D-2Aged) condition (i.e., 720 ºC/8h+620 ºC/8h). At the initial formation and growth stages of fatigue cracks, the Laves phases can hinder the crack growth, while towards the final stage of fatigue rupture these brittle phases start to break down, as shown schematically in Fig. 36 (c) to (f). On the other hand, there are limited research that demonstrated the effect of such brittle secondary phases on the fatigue fracture properties [391].

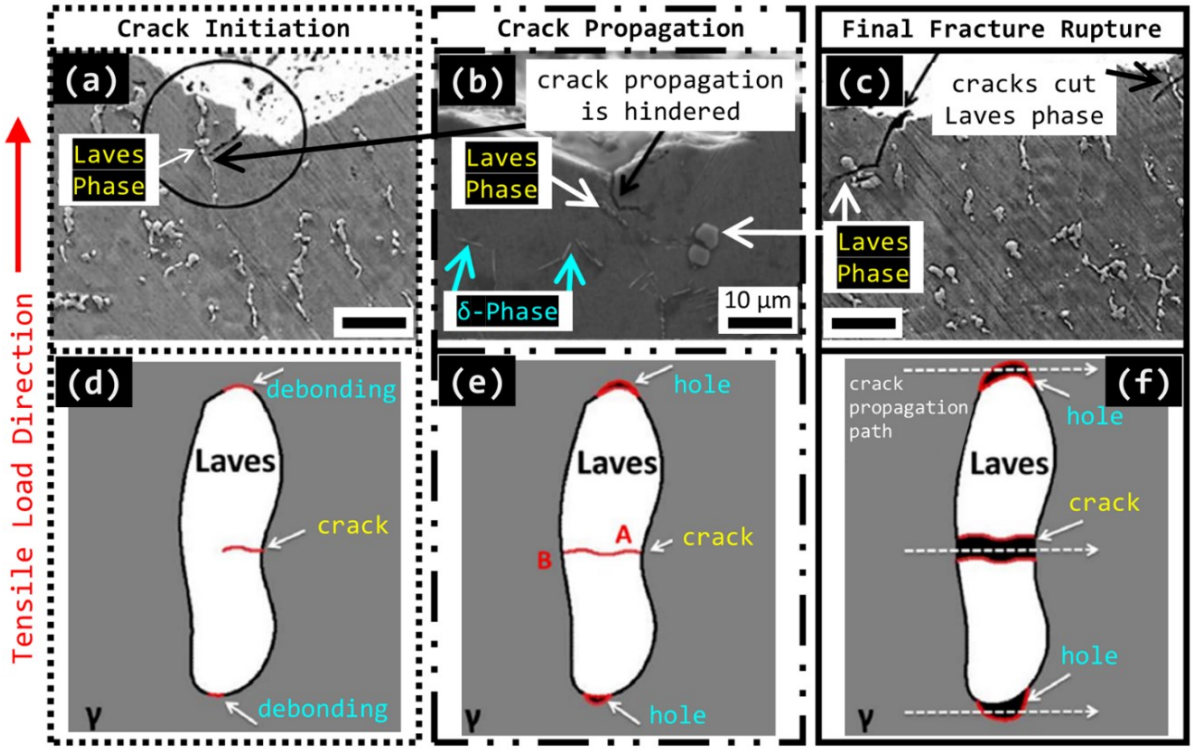

Fig. 36. The SEM micrographs in (a)-(c) obtained on longitudinal/cross-sectional plane, i.e., parallel to load direction, from the room temperature fatigue fractured surfaces of the laser AM IN718 specimens in D-2Aged heat treatment condition, tested at 650 °C/690 MPa; (d)-(f): The schematic presentation of the fragmentation and the debonding of the Laves phases and the surrounding austenitic matrix. Note the original micrographs used in this figure were adopted with permission from Sui et al. [343].

5.2.5. Fatigue crack growth behavior

Fatigue crack growth (FCG) behavior is an important criterion to characterize the damage tolerance and durability of AM metal alloys, according to the USAF Structures Bulletin EZ-SB-19-01 [392]. The following paragraphs endeavors to briefly discuss the FCG behavior of AM IN 625, and AM IN 718.

In addition to the heat treatments, the microstructure texture and directionality could have critical impact on the FCG behavior of AM Nickel-based alloys. It is believed that columnar grain structures with strong <001> texture are the typical microstructure of laser AM Nickel-based superalloys [393]. There is a long overdue debate over the impact of texture (collective orientation of grains) on fatigue properties of AM metals. Some researchers such as Konečná et al. [341] have shown that in the NHT IN718 alloy, the crack growth direction depends on the grain orientation, i.e., cracks propagation lines were mostly aligned trans-granularly along the fine elongated grains (parallel to build direction). Others [394] have further shown that the vertical samples (applied stress direction is parallel to the build direction) had the shortest fatigue lives. It has also been shown that even after heat treatments , the fatigue properties of the horizontal and vertical samples may still vary [395]. However, there are investigations showing no significant differences in the fatigue behavior of the horizontal and vertical nickel based superalloys [396].

Fig. 37 presents the fatigue crack growth rate (FCGR) (da/dN) vs. nominal stress intensity factor (SIF) range (ΔK) obtained for AM IN625 and AM 718 in various heat treatment conditions. Fig. 37(a) presents the results of FCGR investigation by Poulin et al. [392,397] for L-PBF IN 625 in various heat treated (HT) conditions as compared with the wrought counterparts. They have found that the FCG behavior of NHT L-PBF IN625 is comparable with that of the wrought counterparts, within Paris regime; however, upon further HT such as the stress relieving (SR) and HIP, the HT AM IN 625 specimens showed higher crack growth resistance at lower stress ratios (i.e., higher ΔK_{th}) as compared with that of the wrought specimens. They have ascribed this observation to the coarse grain structure on the crack tip shielding by promoting the crack closure mechanisms such as (1) the roughness-induced crack closure mechanism in the fine-grained materials as well as (2) the crack hooks, sliding and deflection mechanism in the coarse-grained materials. Therefore, the threshold intensity stress factor (SIF) range (ΔK_{th}) is larger for the HT AM IN625 (with coarser grain structure) as compared to the NHT IN 625 (with finer grains). This is because in the latter and similarly in the wrought counterparts, no crack closure occurs due to their relatively fine-grain structure.

However, this is not the case for the AM 718 in various heat-treated conditions. Fig. 37(b) presents the results for the FCG investigation by Yu et al. [398] for the L-PBF and LP-DED IN 718 in various HT conditions as compared with the wrought counterparts. As shown, the effect of various HT on the FCG behavior of AM IN 718 is not only more pronounced than the HT AM IN 625 but also most of heat treatment conditions of AM 718 have shown lower FCG resistance, i.e., lower FCGR as well as smaller ΔK_{th} (compared to wrought). They have observed the lowest FCGR and ΔK_{th} in the as-build (NHT) IN 718 specimens which they have ascribed to the supersaturated and unreinforced matrix of as-deposited specimen and therefore better ductility as compared with the HT specimens (see Fig. 38(a)-(b)).

Upon direct aging (D-2Aged) (i.e., 720 ºC/8h+620 ºC/8h),, the AM IN 718 specimens

could retain the columnar grain structure with an uneven distribution of both coarse Laves phases and γ'/γ" precipitates (see Fig. 38(c)-(d)), leading to severe decrease in the FCG resistance, possibly due to subsequent ductility loss. Similarly, after the solution at 950 ºC/1hr + fully aging (S3+2Aged) heat treatment, the formation of soft "precipitate free zones" around the short acicular δ-phases will act as the fast paths for the FCG, resulting in decreasing the FCG resistance of the S3+2Aged specimens (see Fig. 38(e)-(f)). Finally, the homogenized at 1100 ºC/1.5hr and solution plus aged (H+S3+2Aged) specimens shows comparable FCGR and ΔK_{th} with those of the wrought counterparts due to bimodal grain structure with high volume fraction of γ'/γ" precipitates distributions as shown in Fig. 38(g)-(h).

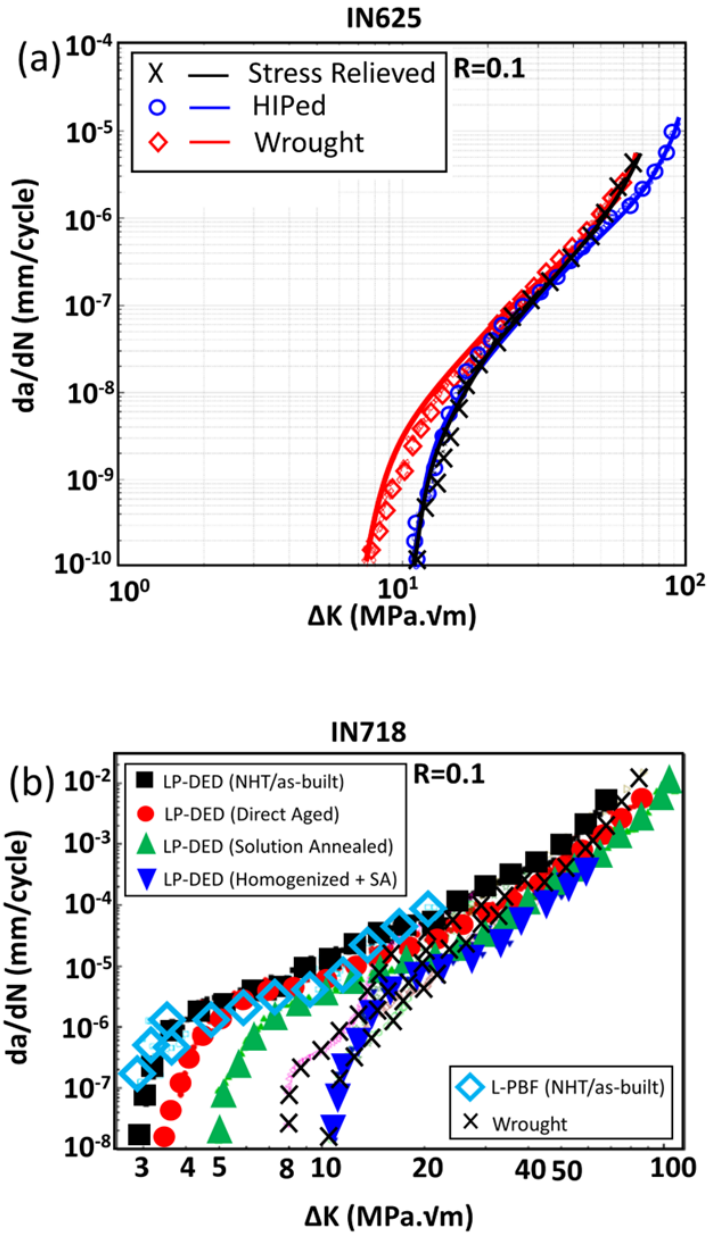

Fig. 37. Fatigue crack propagation diagrams obtained in R=0.1 test conditions: comparison of wrought and AM IN625 [397] in (a) and AM IN718 [392] in (b) in various heat treatment conditions along with the predicted curves using Hartman-Schijve model [399] for the former. The wrought data for IN718 were obtained from [400–403] while the wrought data for IN625 was obtained from NASGRO database [344,392].

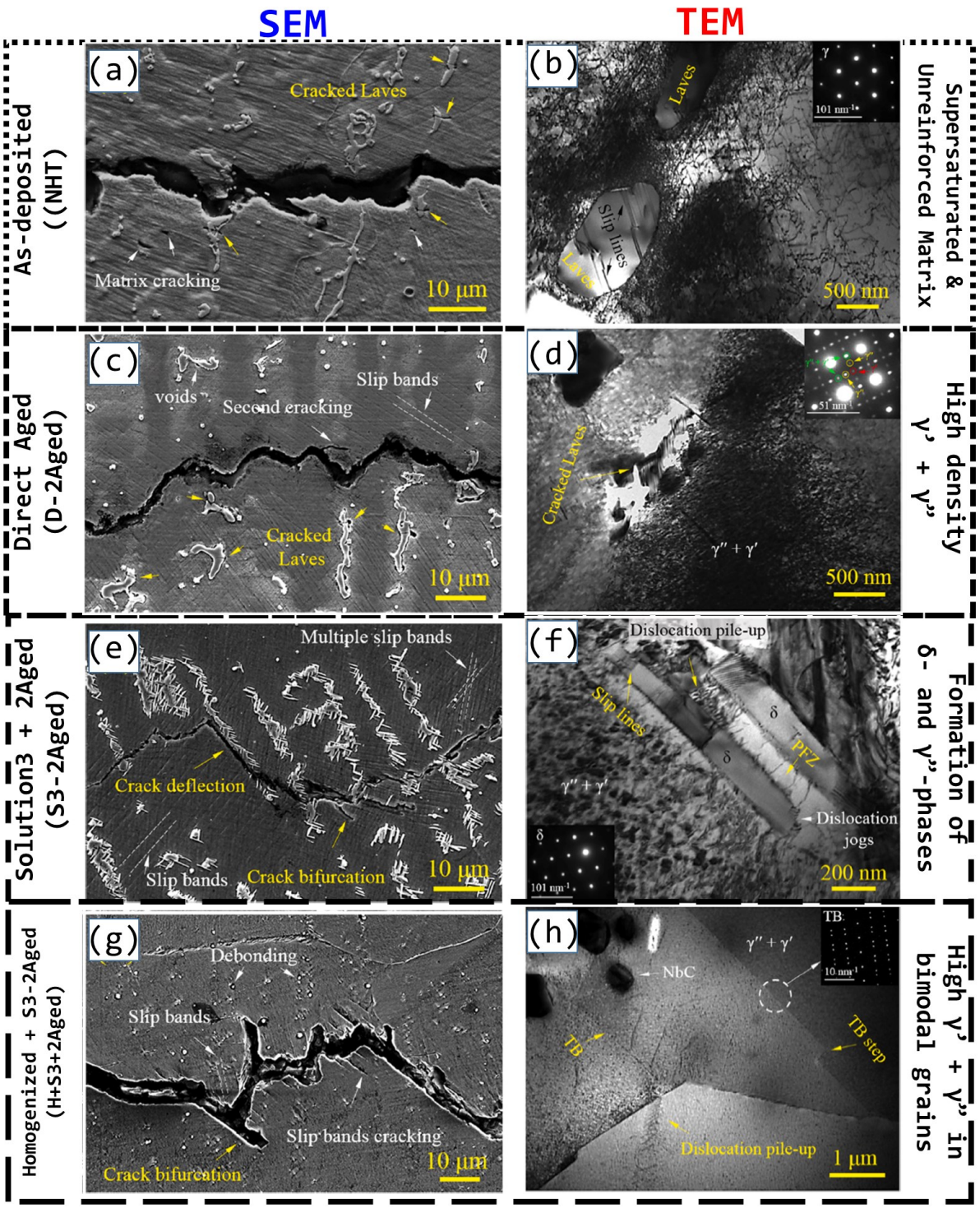

Fig. 38. Typical cross sectional scanning and transmission electron micrographs (SEM and TEM) of fracture surfaces showing the fatigue crack growth (FCG) paths of the near Paris regime in IN 718 LP-DED specimens in various heat treated conditions: (a)-(b) as-deposited (NHT), (c)-(d) direct aged (D-2Aged) (i.e., 720 ºC/8h+620 ºC/8h), (e)-(f) solutioned at 950 ºC/1hr and fully aged (S3+2Aged), and (g)-(h) homogenized at 1100 ºC/1.5hr and solutioned plus fully aged (H+S3+2Aged) [398]. Note the original micrographs used in this figure were adopted with permission from X. Yu et al. [398].

5.2.6. Fracture toughness behavior

Fracture toughness behavior is a key property index for engineering materials and applications, especially from a damage tolerance design viewpoint. This is partly because fracture toughness

can reflects upon the material's capability to resist cracks propagations during the final stages of static and cyclic failure mechanisms [404]. The importance of fracture toughness as a material property indicator is even more critical for the AM metal alloys due to their sensitivity to the process-induced defects which in turn could act as crack initiation sites under cyclic load in their service applications [405]. Puppala et al. [118] has studied the fracture toughness of LP-DED IN625 and reported that crack-tip opening displacement (CTOD) of the alloy is comparable with that of IN625 weldments while being inferior to that of wrought counterparts.

Furthermore, they have revealed that upon the SR at 950 °C for 1 hr, the impact toughness of the alloy (obtained by the instrumented V-notch Charpy test) has marginally improved by about 10% with insignificant change in the CTOD responses of the alloy in SR conditions as compared with NHT one. Additionally, using the fractographic examination of the Charpy test specimens, they have concluded that during the crack growth under dynamic loads the crack propagation controls the failure mechanism.

However, the effect of HT on the fracture toughness of AM IN718 is not the same as AM IN625. Recently, Seifi et al. [406] have studied the fracture toughness in as-deposited (NHT) L-PBF IN718. They have reported that upon the HT including HIP at 1120 ◦C/100 MPa/4 h + solution plus aging (AMS 5662), the fracture toughness of the alloy is much lower as compared with that of the as-deposited (NHT) condition. Additionally, they have revealed that the fracture toughness in NHT condition is strongly location- and orientation-dependent because the porosity content of NHT vertical samples is lower than that of the NHT horizontal ones. They have concluded that both the powder properties and HT have a great influence on the fracture toughness of L-PBF IN718 alloy.

Furthermore, using small scale mechanical testing methodologies, Gotterbarm, et al. [407] have studied the effect of sample orientation on the tensile properties and fracture toughness response of the as-deposited (NHT) E-PBF IN718 alloy in two different grain structures, i.e., single-crystals and columnar multi-grains obtained by optimizing process parameters. They have reported a strong anisotropy of fracture toughness values between the horizontal and vertical orientations, i.e., pre-crack direction is perpendicular and parallel to the build direction, respectively, for both grain structures investigated.

They have revealed that the fracture toughness values of vertical specimens were comparable for both single-crystalline and columnar multi-grains specimens while for the horizontal specimens the single-crystalline sample showed much lower fracture toughness values. They have rationalized this based on the fracture surfaces of single crystalline specimens where the cracks were observed to propagate mostly intra-granularly through the low angle grain boundaries (GB) as they were well aligned along the build direction, i.e., the pre-crack direction or perpendicular to load direction, resulting in "minimal crack bifurcation, blunting and deflection as compared with the more randomly distributed GB's in columnar samples".

Similarly, Yu et al. [408] have investigated the influence of HT on the microstructure and room-temperature fracture toughness of LP-DED IN 718. Fig. 39 presents the room-temperature fracture toughness-yield strength diagram of LP-DED IN 718 alloy. As shown in Fig. 39, they have reported the as-fabricated (NHT) sample possesses the lowest fracture toughness mainly due to its lowest elastic modulus and yield strength [408]. Additionally, they have reported that the fracture toughness of D-2Aged is close to that of as-fabricated (NHT) sample, which they have ascribed mainly to their low ductility and strain-hardening exponent, which in turn could result in lesser capability of strain accommodation of a matrix during the crack propagation stage. However, they have revealed that upon the S+2Aged and H+S+2Aged heat treatments, the fracture toughness of the alloy has increased quite significantly mainly because of the better performance in the "strength–plasticity" (i.e., the strength-ductility, measured from the tensile test curves) of the HT specimens. Particularly, H+S+2Aged sample with bimodal grains showed even higher fracture toughness than the lower limit of wrought IN718 (AMS 5662) counterparts. They have concluded that an appropriate HT possesses obvious toughening effect on the LP-DED IN 718 alloy. Further, Fig. 40 typical SEM micrographs of fracture surfaces for the fracture toughness LP-DED IN718 specimens in various heat-treated conditions.

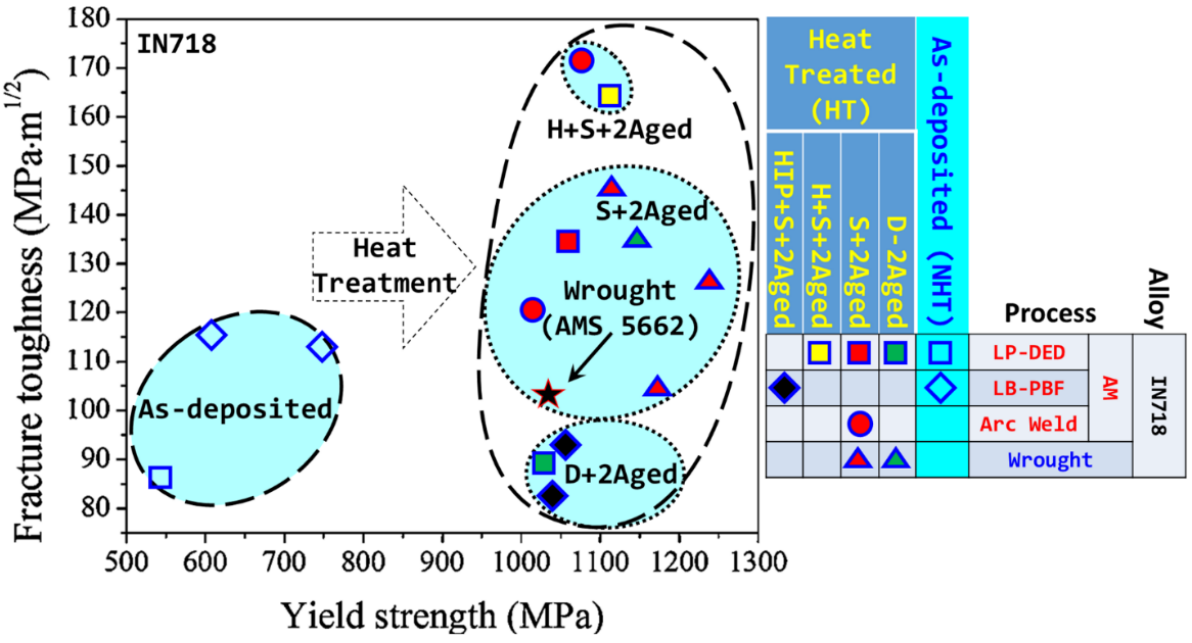

Fig. 39. Relationship between RT fracture toughness and yield strength for IN718 fabricated by various laser AM technologies such as LP-DED [398], LB-PBF [406], gas tungsten arc weldment [409] and wrought [410–413] processes in various heat treated conditions including as-deposited (NHT), direct aged (D-2Aged), solutioned and fully aged (S+2Aged), and (g)-(h) homogenized and solutioned plus fully aged (H+S+2Aged) [398]. Note the solution treatment at different temperatures are grouped and shown using similar symbols for ease of presentation.

As shown in Fig. 40(a)-(d), The degree of micro-segregation is almost similar in as-fabricated (NHT) and D-2Aged samples. Upon the fully aged HT (S+2Aged), the micro-segregation decreases and the γ″/γ′ precipitates almost homogeneously within the inter-

dendritic regions (see Fig. 40(e)-(f)). Furthermore, once the specimens were homogenized prior to the fully aged HT (i.e., H+S+2Aged) where the micro-segregation was completely removed in addition to precipitation of high-volume fractions of the γ′ ′/γ′ phases (~30 nm) within the grain interiors (see Fig. 40(g)-(h)).

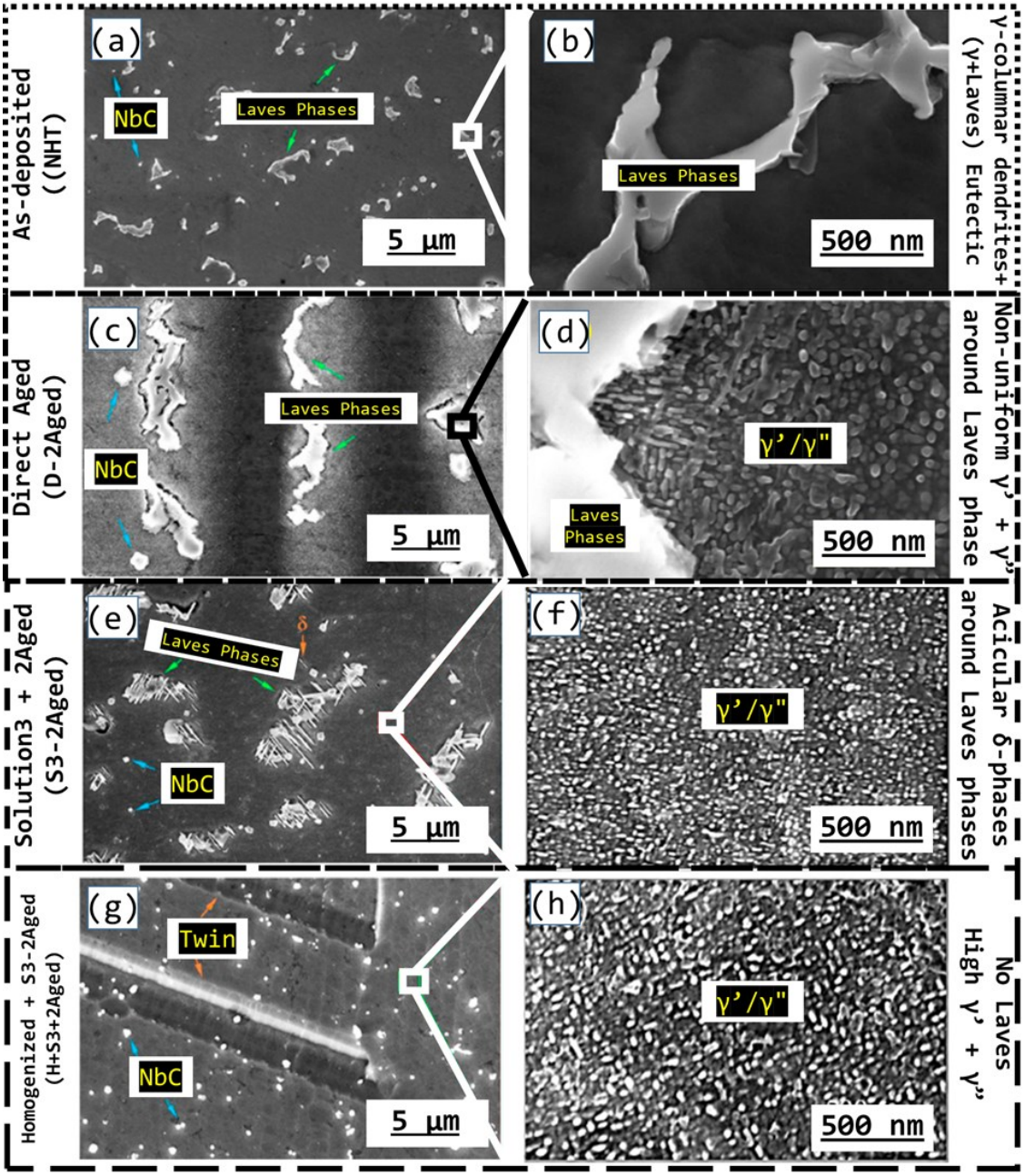

Fig. 40. Typical SEM micrographs of fracture surfaces for IN 718 LP-DED specimens in various heat treated conditions: (a)-(b) as-deposited (NHT), (c)-(d) direct aged (D-2Aged) (i.e., 720 ºC/8h+620 ºC/8h), (e)-(f) solutioned at 950 ºC/1hr and fully aged (S3+2Aged), and (g)-(h) homogenized at 1100 ºC/1.5hr and solutioned plus fully aged (H+S3+2Aged) [398]. Note the original micrographs used in this figure were adopted with permission from Yu et al. [398].

5.3. Creep properties

Creep resistance is an important performance characteristic of high temperature metal

alloys such as Nickel-based superalloys. Interestingly, the creep performance of AMed Nickel-based superalloys has not been fully investigated. Among all the AMed Nickel-based superalloys, the majority of the creep performance studies have been focused on the L-PBF processed IN718 [414] and E-PBF processed IN718 [415,416], while there are some researchers conducted on the L-PBF processed IN738LC [417], L-PBF processed CM247LC [418], L-PBF processed C263 [419], L-PBF processed Hastelloy X [420] were studies as well.

5.3.1. Effect of build orientation

The effect of anisotropy, i.e., the built orientation with respect to the applied tensile loading direction, on the creep performance of AMed Nickel-based superalloys has been widely studied [421]. For instance, Rickenbacher et al. [417] have indicated that the vertically built L-PBF processed IN738LC specimens (i.e., the applied stress is parallel to the build direction or along the elongated columnar grains) had shown better creep resistance, as compared with the horizontally built AM and cast counterparts. Similar results were reported for the L-PBF processed IN738LC [421], L-PBF processed CM247LC [418] and L-PBF processed IN718 [414] alloys showing similarly better creep resistance and strengthening mechanisms in the vertically built test specimens as compared with those of the horizontally built AM and the directionally solidified single crystal Nickel-based superalloys [422].

The effect of anisotropy on the creep resistance of the AMed Nickel-based superalloys seems to be significant even after heat treatments [423] (Fig. 41). It was reported that the creep life and ductility of the vertically built AM Nickel-based superalloys are increased (Fig. 41 (a)) while decreasing strain rates as compared with the horizontally built counterparts (Fig. 41 (b)) [424]. This could be attributed to the "crack growth" mechanism under creep test condition. It was reported that in the vertically and orthogonally built L-PBF processed IN718 creep test specimens [425], the intergranular cracking occurred on the planes of maximum tensile stresses, i.e., between the AM deposited layers, therefore creating some cleavage steps (Fig. 42 (g) and (h), respectively). However, in the horizontally built creep specimens, the intergranular cracking occurred on the plane of maximum shear stress, i.e., between the melt pools, therefore creating quasi-cleavage (Fig. 42(i)). This could be most likely because of their microstructure and the fact that creep damage accumulated on the grain boundaries are aligned with the plane of maximum stress [425]. However, in presence of a surface micro-notches, the influence of the anisotropy doesn't seem to be the prime factor affecting the crack growth mechanism [426].

Shassere et al. [415] have comprehensively studied the effects of different grain morphologies (i.e., equiaxed/columnar grains) and loading directions (i.e., longitudinal/transverse) with respect to the build direction on the creep deformation/failure mechanism of E-PBF processed IN718, i.e., at 923 K (650 °C) under 580 and 600 MPa applied tensile stresses. They have reported similar creep lifetimes obtained for the HIPed E-PBF processed IN718 specimens as compared to the conventionally processed wrought IN718

counterparts. They have further reported the superior creep properties for the vertically built E-PBF processed IN718 specimens tested longitudinally with respect to the loading direction, i.e., the stress axis was parallel to the elongated direction of columnar grain structured E-PBF processed IN718 specimens. They have observed similar creep damage mechanism for both the E-PBF and wrought processed IN718 specimens wherein the micro-voids and cracks were initiated at grain boundaries from areas around the δ-phases (Fig. 43 (d) to (f)). They have further observed the maximum number of the micro-voids and cracking on grain boundaries that were transverse to the tensile load direction (Fig. 42 (d) to (f)). Their fractography analysis revealed that the equiaxed grain structured E-PBF processed IN718 specimens were dominantly consisted of the grain boundary cleavage (Fig. 42 (h) and (l)) while only ductile shear failure (Fig. 42 (j)) was observed in the columnar grain structured specimens which were loaded longitudinally, i.e., parallel to build direction. In brief, they have concluded that the transverse grain boundaries aligned with the loading direction are more detrimental to the overall creep rupture properties of E-PBF processed IN718, such as those found in the equiaxed grain structured or the horizontally built specimens as opposite to those in the vertically built specimens [415].

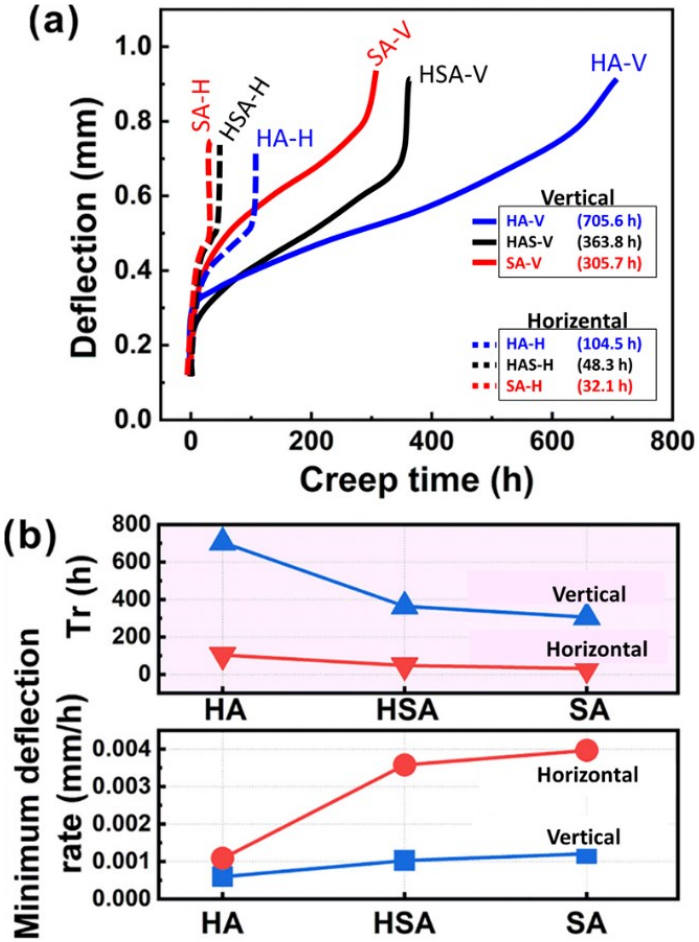

Fig. 41. Creep properties of L-PBF processed IN718 specimens in two different built directions, i.e., vertically built (parallel to load direction) and horizontally built (perpendicular to load direction) specimens [427]: (a) variation of central deflection of the creep tested specimen as a function of creep time and (b) variation of deflection and t_r as a function of various heat treatments such as HA (homogenized at 1065°C/1.5h + aged at

760°C/10h and 650°C/8h), HAS (homogenized at 1065°C/1.5h + solution annealed at 980°C/1h+ aged at 760°C/10h and 650°C/8h), and SA (solution annealed at 980°C/1h+ aged at 760°C/10h and 650°C/8h) [427].

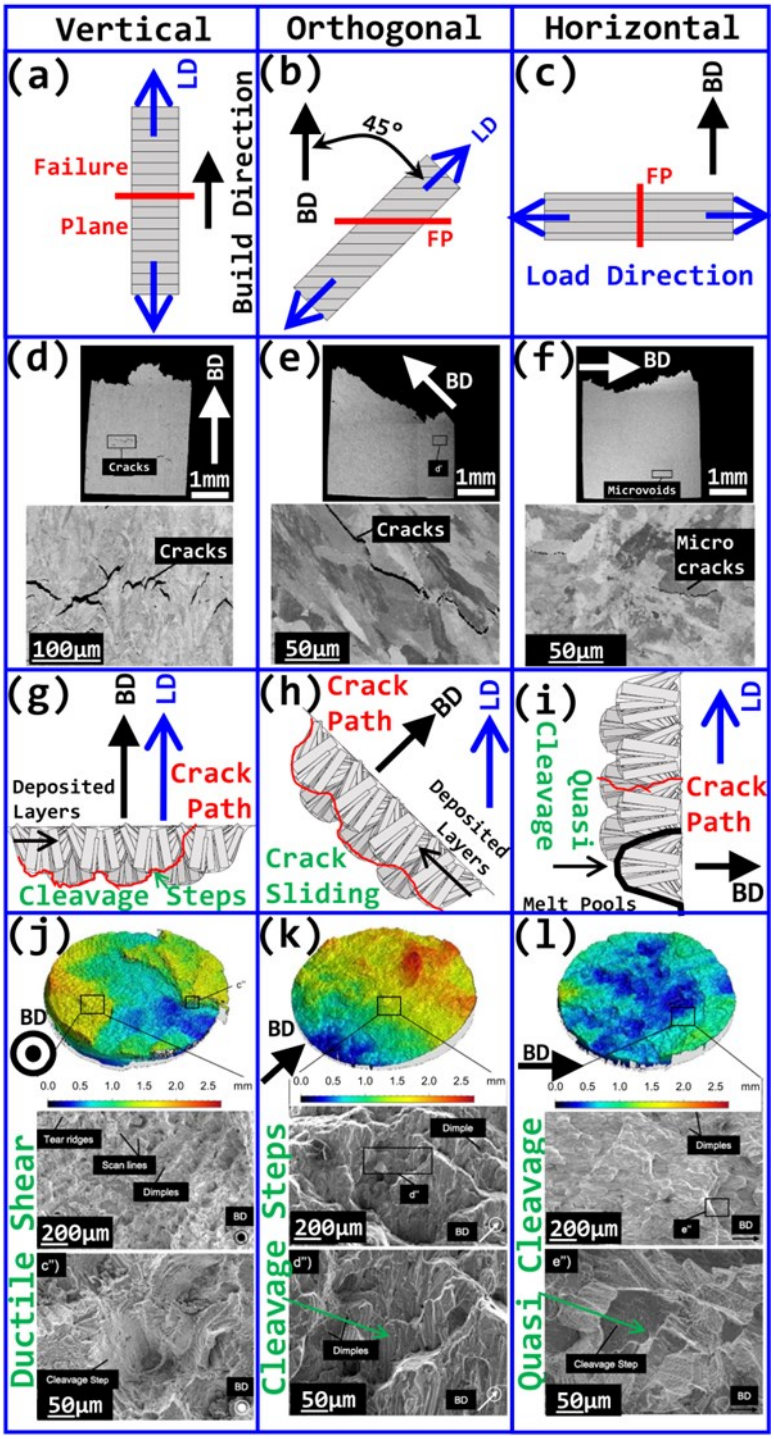

Fig. 42. Creep crack growth mechanism of L-PBF processed IN718 [425]: Schematic representation of the failure planes of the different test cases for the vertically, orthogonally, and horizontally built specimens in (a), (b), and (c) respectively. SEM images obtained from the cross section of actual creep fracture surfaces showing microscopic indicators of the failure mechanisms for the vertically, orthogonally, and horizontally built specimens in (d), (e), and (f) respectively. Schematic representation of creep crack path mechanism in (g) for vertically built specimens, where intergranular cracking occurred with some cleavage steps; in (h) orthogonally built specimens, where the intergranular cracking caused grain boundaries decohesion and sliding; and in (i) for horizontally built specimens, where Quasi-Cleavage occurred. Alicona scans processed by Mountains Maps and SEM images of the fracture surfaces for the vertically, orthogonally, and horizontally built specimens in (j), (k), and (l) respectively. Reproduced from [425].

The other important process parameters affecting the creep performance of the AMed Nickel-based superalloys are the laser power (or energy density) [428], laser focus height [424], oxidation [429], surface integrity [430] and ceramic reinforcements [213]. For instance, Popovich et al. [431] has reported inferior creep resistance in the L-PBF processed IN718 specimens manufactured using higher laser power (950 W) with dominated ductile fracture (as compared with lower laser power of 250 W). They have explained their results to be because of presence of a large number of built-in defects such as LoF that were induced due the excessive laser power during AM deposition process. Changing the scan strategy can further affect the creep behavior [424], but the use of multiple laser beams reportedly does not have detrimental effect on the creep performance of the vertically built L-PBF processed IN718 specimens [424].

5.3.2. Effect of heat treatment

As a result of the rapid solidification during AM processes such as L-PBF, the resultant AM Nickel-based superalloy components consist of significantly refined grain structure in the non-heat treated (NHT) or as-built condition, which as partially discussed above could directly deteriorate their creep resistance [432]. This could be attributed to two main reasons: (1) the grain boundary sliding and (2) intergranular cracking, both of which are identified as the dominant creep failure mechanisms especially under low strain rates in the AM Nickel-based superalloys such as L-PBF processed IN718 [433], L-PBF processed IN625 [434], and L-PBF processed IN738LC [330]. Such degradation of creep resistance could be further aggravated by the severely segregated microstructure induced in the non-heat treated (NHT) AM Nickel-based superalloys [435], resulting in formation of brittle intermetallic phases such as Laves and δ-phases at grain boundaries.

The as-solidified microstructure of the L-PBF processed IN718 alloy is composed of columnar grain microstructure (Ni-austenite γ-matrix) with highly dispersed γ'/γ"-phase precipitates inside the grains [436]. The metastable γ"-phases serve as strengthening phases. Furthermore, the δ-phases precipitate by nucleation at the grain boundaries in presence of γ"-precipitates followed by their growth as thin plates extending into the columnar γ-grains. In thermomechanically processed wrought IN718, the δ-phases exist in globular morphology (i.e., equiaxed or slightly elongated, and relatively coarse particles) originating from the fragmentation of δ-plates. The δ-phase, that developed along the grain boundaries, can significantly reduce the fracture toughness and ductility of the IN718 alloy. Both γ"- and δ-phases are Nb-based, although the δ-phase is thermodynamically more stable than the γ"-phase below 1000 °C [26]. Due the rapid solidification during the AMed IN718, the solid-liquid (SL) melt pool interface moves with severe inter-dendritic micro-segregation of massive elements such as Nb, which in turn leading to the formation of the hexagonal Laves phase, i.e., (Ni, Fe,

$Cr)_2$(Nb, Ti, Mo) [437].

Although, Laves phases are considered as undesirable phases for creep resistance due to their high brittleness, which in turn leading to nucleation of intergranular cracking at grain boundaries [438], effect of δ-phases on creep resistance of AMed Nickel-based superalloys is at controversy. As discussed earlier, while some researchers such as Shassere et al. [415] have shown that the creep damage in the AMed Nickel-based superalloys such as E-PBF processed IN718 alloy were initiated from the precipitation free zones (PFZ) around the δ-phases at grain boundary areas (Fig. 43 (d) to (f)), there are other studies showing the δ-phases acting as a crack barrier [430], preventing the grain boundary sliding by pinning effect, and therefore impeding the micro-void coalescence [425]. Nonetheless, it was also reported that the creep resistance [439] and the grain growth [439] in the AMed Nickel-based superalloys were increased in the absence the δ-phases. Therefore, one of the benefits of heat treatments is to dissolve such intermetallic phases, which instead will increase the size and volume fraction of γ’ and γ’’ strengthening precipitates (Fig. 43) and subsequently improve the creep resistance [440].

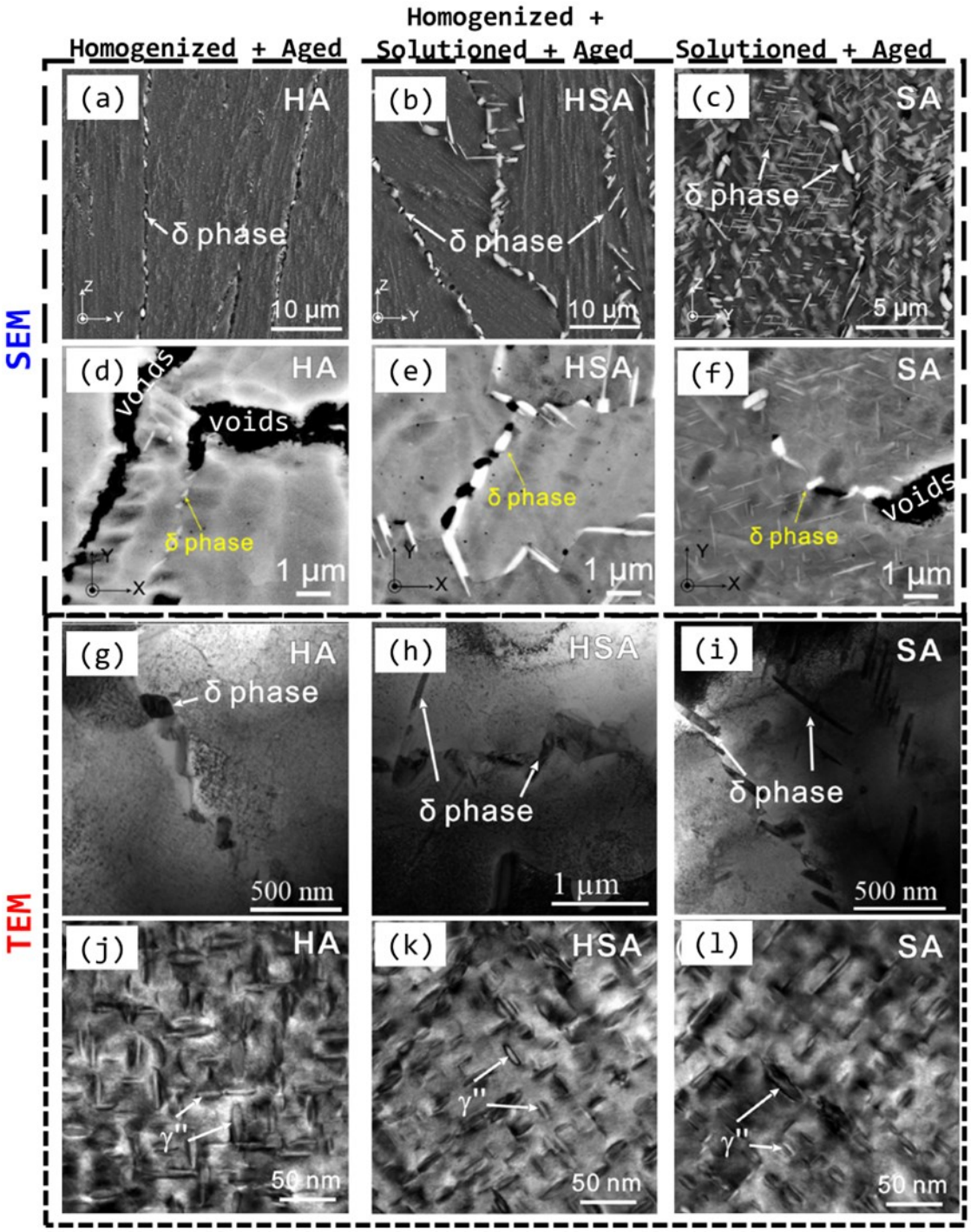

Fig. 43. Effect of various heat treatments on the size and distribution of primarily influential phases on the creep properties of L-PBF processed IN718 superalloy such as δ- and γ′′-phases [427]: SEM micrographs in (a)/(c) for HA-treated, in (b)/(e) for HSA-treated and in (c)/(f) for SA-treated specimens. Note (c), (e), and (f) were obtained from the cross section of failed creep specimens. TEM micrographs in (g)/(j) for HA-treated, in (h)/(k) for HSA-treated and in (i)/(l) for SA-treated specimens. Note that the above-mentioned abbreviated heat treatments are as follows: HA (homogenized at 1065°C/1.5h + aged at 760°C/10h and 650°C/8h), HAS (homogenized at 1065°C/1.5h + solution annealed at 980°C/1h+ aged at 760°C/10h and 650°C/8h), and SA (solution annealed at 980°C/1h+ aged at 760°C/10h and 650°C/8h). Reproduced from [427].

The effect hot isostatic pressing (HIP) heat treatment on the creep behavior of AMed Nickel-based superalloys have been extensively studies in the literature [441]. It was reported that the HIP may increase the creep life when applied before solution annealing and two step aging heat treatments [439]. However, Xu et al. [329] has reported that if an intermediate homogenization step at 1100 °C was applied between HIP and standard heat treatment of solution annealed plus two step aging, the creep life is reduced. They have attributed their results to the excessive dissolution effect of intermediate high-temperature homogenization step on the growth rate of grain boundary intermetallic phases such as metal carbides (MC, M_6C, and $M_{23}C_6$) as well as the γ′-/γ′′- strengthening precipitates, which in turn reduces the hindering effect of such carbide and strengthening phases on the grain boundary sliding and subsequently deteriorates the creep resistance of these alloys [442].

Multiple studies have compared the effect of various heat treatments on the creep performance of AM Nickel-based superalloys such L-PBF processed IN718 specimens [439] and L-PBF processed C263 [419]. Hautfenne et al. [414] have shown that L-PBF processed IN718 specimens exhibited better creep performance once solution annealed at 1065 °C followed by two step aging process (at 720 °C/8 h + 620 °C/8 h) as compared with the lower solution annealing temperature at 980 °C. Similar results have been reported by Probstle et al. [185] and Kuo et al. [443] where they have shown that the fully heat treated L-PBF processed IN718 specimens with solution temperature at higher than 1000 °C have exhibited better creep performance than directly aged counterparts.

The two possible reasons can explain the above results of effect of solution annealing temperature on the creep behavior of L-PBF processed IN718 alloy. First possible explanation is the effect of solution temperature on phase formations, i.e., δ- and γ′′- phases, occurring during heat treatment in the L-PBF processed IN718 alloy. As discussed earlier, the γ′′- phases can have more improving effect on creep performance of L-PBF processed IN718 alloy due to their pinning effect on the grain boundary sliding [442], while the δ particles can act as the micro-voids/cracks initiation sites at grain boundaries (Fig. 43 (d) to (f)) [427]. Therefore, upon solution annealing at temperatures above δ-solvus (~1000 °C) such as 1065 °C, the δ- phases are dissolved, releasing Nb atoms into the surrounding γ- matrix [185], therefore promoting the formation of γ′′- precipitates. This in turn can result in improved creep resistance of the L-PBF processed IN718 alloy. On the contrary, when the alloy is solution annealed at temperatures below δ-solvus such as 930 °C, more δ-phases are formed at the expense of γ”-phase, which in turn have a deteriorating effect on the creep performance. The second possible reason is the effect of higher solution annealing temperature on the size of γ”-phase, with the average size of 13.4 ± 5.8 nm in specimens solution annealed at 1065 °C, as compared with those of solution treated at 930 °C with the average size of 9.1 ± 5.8 nm [185].

Similar results have been reported for L-PBF processed C263 by Davies et al. [419] using two different solution temperatures above δ-solvus temperature, i.e., 1150 ◦C and 1275 ◦C.

They have found that the higher the solution temperature results in the better the creep resistance [419]. They have attributed their results to the effect of higher solution temperature on generation of a more equiaxed microstructure, smaller average local misorientation, shorter random grain boundary network segment length and higher amount of metal carbides (MC, M_6C, and $M_{23}C_6$) precipitation at grain boundaries. They have concluded that that shorter random grain boundary network segment length (i.e., shorter potential intergranular crack paths) and higher amount of metal carbides at grain boundaries could hinder grain boundaries deformation, therefore leading to improved creep resistance.

6. Simulation and modeling

In the fusion-base AM processes, a moving heat source melts feedstock and materials go through repeated heating, melting, cooling and solidification, thus multiple, thermal cycles occur at any location. The formation of a small molt pool, strong recirculating motion of the liquid materials driven primarily by Marangoni convection, the heat source movement, and the significant temperature gradient due to rapid temperature changes make the measurement of transient temperature and other imperative variables challenging. Also, experimental measurements are only practical on accessible surfaces by cameras and not on interior locations. Thus, it is essential to advance models of heat transfer, fluid flow and mass transfer to compute the temperature fields, size and geometry of fusion zone, and other parameters required for the predictions of pore, grain structure and texture, residual stresses, and distortion. Fig. 44 summarizes the critical role of main mechanistic models to calculate heat transfer, fluid flow and mass transfer and to understand the physical processes in fusion-based AM. Wei et al. [444] recently published a state-of the-art review on mechanistic models for additive manufacturing of different metallic components. However, the current review will mainly focus on understanding simulation and prediction of feedstock-process-structure-defect-property relationship in fusion-based AM processed Nickel-based superalloys.

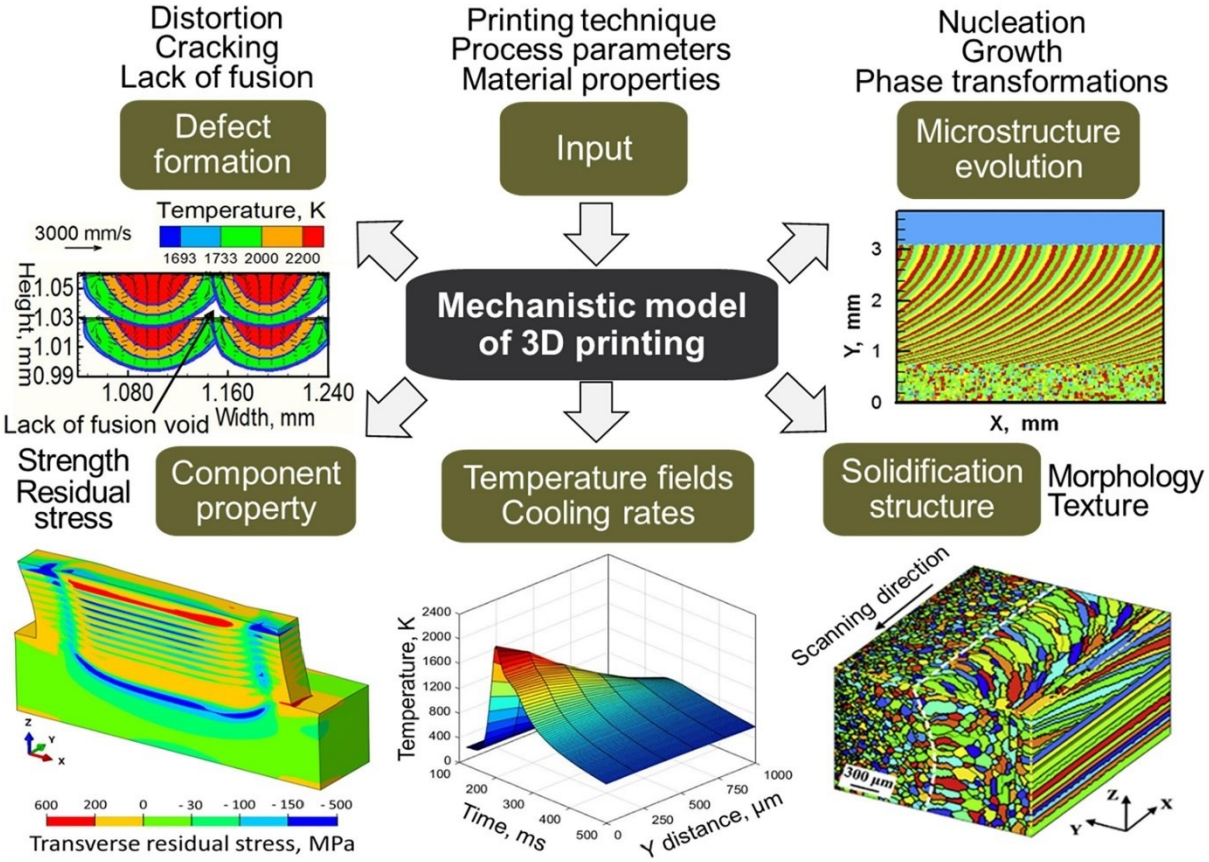

Fig. 44. Schematic representation of mechanistic models for heat transfer, fluid flow, and mass transfer to simulate and predict feedstock-process-structure-defect-property relationship [444].

6.1. Process modeling

6.1.1. Laser-powder interactions

Accurate simulation of AM processes necessitates an understanding of the complex interactions between the laser beam and powder particles, namely, the heat source absorptivity by the feedstock material. In AM, the absorptivity is defined as the ratio of energy absorbed by the solid material (e.g., metal powder or wire) to the total input energy from the heat source (e.g., laser or electron beam) [445]. Different AM processes absorb energy in distinct ways owing to the disparity between various energy sources [446]. The method of energy absorption is critical since it induces distinct modes of melting, and thus, different absorptivity depending on the process. For example, photons are absorbed only some nanometers from the surface of the material, whereas electrons deposit their energy several micrometers beneath [447]. Therefore, laser-assisted processes undergo multiple laser reflections within a relatively small area, which gives rise to substantial material evaporation yet comparatively low absorptivity. For L-PBF processes using a laser wavelength of 1.06 μm, the absorptivity of IN718 was reported to vary from 0.3–0.87 [448]; similar trends have also been observed for other materials [449]. Similarly, for DED processes where powder emerges from multiple nozzles before adjoining and traveling through the laser beam, the absorptivity was reported to range from 0.3 to 0.7 for a 1.06 μm wavelength laser beam, depending on whether the material is in the liquid

or solid-state [450]. Contrarily, in electron beam processes, most of the energy will be initially absorbed by the material while the evaporation is mitigated [44]; the absorptivity for electron beam processes is generally in the range of 90% [451].

Besides its dependence on the process itself, absorptivity also depends on the laser properties (energy density, wavelength, polarization, and angle of incidence), feedstock material characteristics (thermophysical properties, size distribution, preheating temperature, surface roughness, chemistry (oxidation), and contamination), as well as the melt pool morphology and temperature [452]. For DED processes, the absorptivity also depends on the particle flight duration and shield gas velocity [450]. All these factors make the absorptivity challenging to measure experimentally, and thus, it is typically assumed as a constant in the process simulation model that is to be calibrated with experimental data in simulations involving laser-powder interactions [453]. One promising avenue for estimating the absorptivity under different process parameters was provided by Khairallah et al. [449] using their high-fidelity Multiphysics model, which was verified using in-situ x-ray data. The full ray-tracing method was employed to track the multiple laser beam reflections as they interacted with both a bare plate and a 35 μm thick layer of SS316L powder. Using the full ray-tracing method permitted the absorptivity to be a predicted output rather than an input approximated using a constant value; their results demonstrated that, especially at low laser power, absorptivity increases with a layer of powder than without due to the additional reflection events (Fig. 45 (a) and (b)). Also, absorptivity was shown to increase with laser power, owing to a widening depression at higher energy that accommodates more energy absorption events (Fig. 45 (c) and (d)). Similar studies should be performed with Nickel-based superalloys to elucidate these parameters' influence on the material absorptivity.

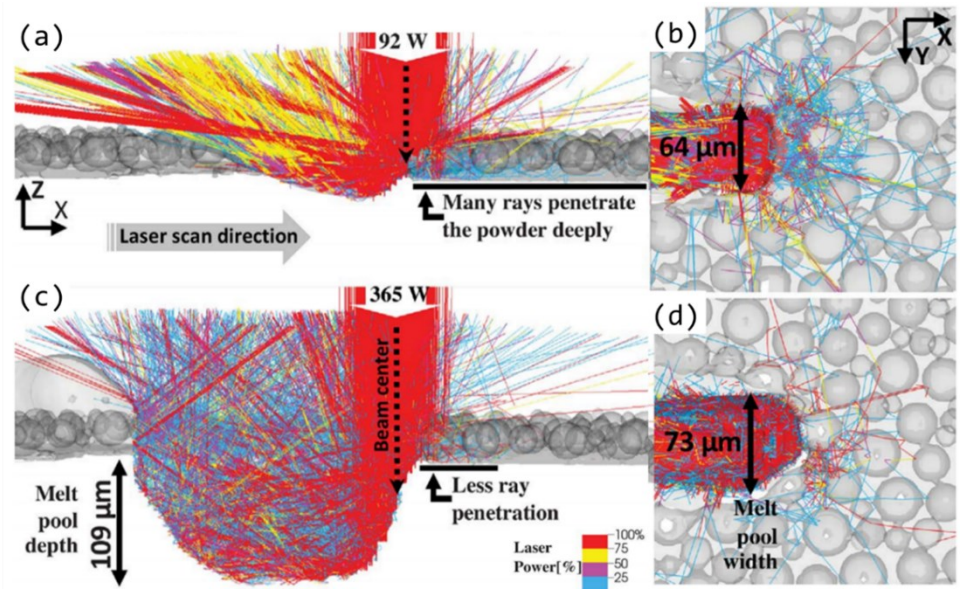

Fig. 45. Laser-powder interactions. The laser rays are grouped into four distinct colors representing four different power bins. The laser rays arrive at 100% power (red) and lose energy as they are reflected. A blue ray is at 25% or less of the initial power. At low power (92 W), the rays penetrate the powder bed through multiple reflections (a), leading to a higher absorptivity than that of a flat plate. At high power (365 W), the rays are concentrated inside the melt pool depression zone (c). The laser-powder interactions become less pronounced at higher laser power, while the overall absorptivity increases as more rays are absorbed within the melt pool. The 3D melt pool is cross-sectioned and made semitransparent for visual clarity. The X, Y, and Z axes act as the frame of reference. (b) and (d) depict a transparent bottom view, showing more laser reflections in the powder for (a). Reproduced from [449].

6.1.2. Melt pool

Different analytical and numerical approaches have been employed to understand the melt pool geometry, heat transfer, and fluid flow for various AM processes. These include analytical approaches [454], heat conduction models [455], heat transfer and fluid flow models [456], level set method [457], the volume of fluid (VOF) method [458], Lattice Boltzmann and Lagrangian-Eulerian methods [459], which are summarized in Table 4.

Table 4. Comparison among the various approaches currently used for simulating the heat transfer and fluid flow within the melt pool in AM.

Approach	Features	Ref.
Analytical	• Analytical solution to heat conduction equation • Outputs are temperature fields and cooling rates • Low computational expense; simple and easy to use • Ignores dominant mechanism of heat transfer (convection); large computational error and limited fidelity	[454]
Heat conduction models using the finite element (FE) method	• Solves steady-state/transient energy conservation equation with convective, radiative, or prescribed temperature boundary conditions • Outputs are 3D steady-state/transient temperature distribution • Existing software packages allow for easy implementation and complex geometries	[455]

	• Does not consider effects of convective (fluid) flow within the molten pool; typically overestimates the peak temperatures and cooling rates	
Heat transfer and fluid flow models using finite difference method (FDM)	• Solves 3D transient conservation equations of mass, momentum, and energy • Outputs are 3D transient temperature and velocity fields, solidification parameters • Considers effects of convective flow within the molten pool and therefore provides more accurate temperature distributions • Assumes flat-top geometry to make the calculations tractable	[456]
Level set method (LSM)	• Tracks the free surface of the molten pool • Outputs are 3D transient temperature and velocity fields with free curved surface • Melt pool morphology in good agreement with experiments • Computationally expensive and tends to suffer from non-conservation of mass	[457]
Volume of fluid (VOF) using finite difference method (FDM)	• Tracks the free surface of the molten pool • Outputs are 3D transient temperature and velocity fields with free curved surface • Melt pool morphology in good agreement with experiments, conservation equations satisfied • Computationally expensive	[460]
Lattice Boltzmann method (LBM) and Lagrangian-Eulerian (LE) method	• 2D and 3D numerical methods involving cellular automation modeling of particle kinetics discretized in time, space, and particle velocities • Involves free surface boundary conditions regarding thermodynamics, surface tensions, phase transitions, and wetting • Outputs are molten pool geometry • Can accurately predict melt pool morphology and phenomena such as balling and surface roughness • Computationally expensive, well-parallelized	[47]

As previously mentioned, experimental temperature measurements in AM are challenging since the process is highly transient and very high temperatures are typically reached, e.g., peak temperatures within the melt pool can be several hundred degrees above an alloy's liquidus temperature, and sometimes surpass the boiling point of the alloy upon sufficiently high heat input. The most common way to obtain temperature measurements is to place thermocouples on various monitoring locations on a dense substrate sufficiently far away from the laser scanning path. However, while thermocouples provide the temperature measurements at the local monitoring locations, it is impossible to obtain a comprehensive view of the 3D temperature field. Infrared thermography can be used to measure the surface temperature of an entire layer; yet, this method also lacks the ability to provide the entire transient temperature field. Thus, a more suitable manner of obtaining the 3D temperature profile is via computational models that are validated with either (a), the far-field temperature-time history obtained experimental thermocouple measurements, or (b), the melt pool dimensions (width and depth) obtained through optical microscopy measurements.

Fig. 46 (a) and (b) demonstrate such a prediction, showing the computed temperature distribution for the 1st and 10th layers, respectively, during a 10-layer LP-DED of IN718 powder [235]. The various colors in these figures represent the different temperatures which the material is subject to. As shown, the substrate in AM acts as a heat sink through which heat can conduct away from the molten pool. Heat accumulates as more layers are added due to the additional heat input from the laser beam. As a result, heat conduction through the substrate also diminishes, which traps the heat in the upper layers. The temperature contours are significantly elongated behind the heat source and depressed near the heat source due to the rapid scanning of the laser beam and Marangoni flow. The thermal cycles are in excellent agreement, which assures the validity of the computational model. Although the material is different, similar trends should be observed for Ni-based superalloys. Fig. 46 (d) demonstrates the molten pool morphology at the mid-length of the scan during the deposition of the 10th layer. The melt pool is at its highest temperature directly near the heat source and at its lowest near its peripheral boundary. The temperature gradient induces spatially variant surface tension (Marangoni stress), which drives the fluid flow from areas of high to low temperature.

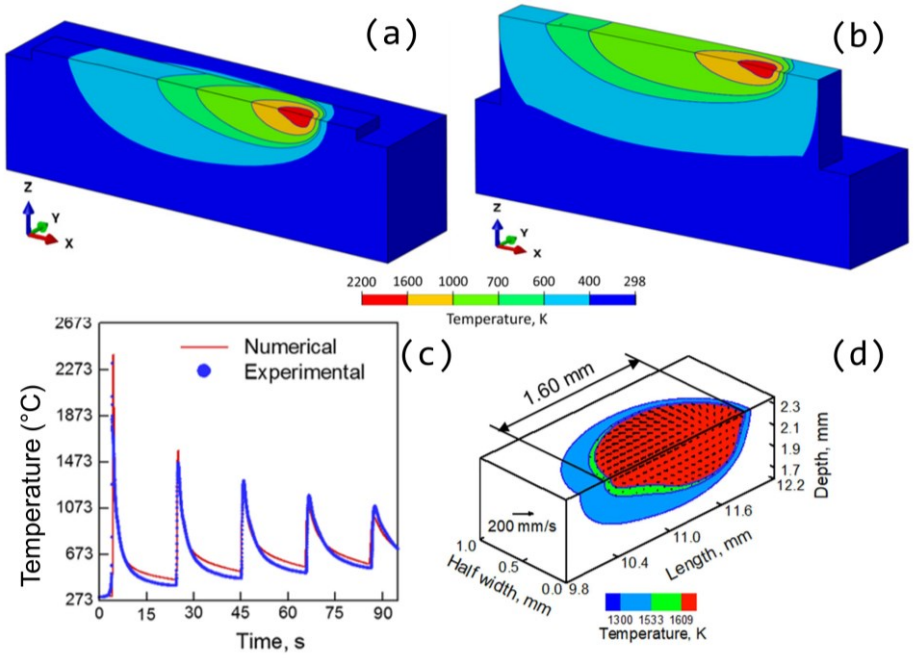

Fig. 46. Temperature distribution of (a) 1st and (b) 10th layer deposition during LP-DED processing of IN718 powder on IN718 substrate with 300 W laser power and 15 mm/s scanning speed; (c) comparison of experimentally measured [461] and numerically computed thermal cycle for 5-layer deposition using 2000 W laser power and 10.5 mm/s scanning speed; (d) temperature and velocity distributions during the 2nd layer deposition for IN718 using 250 W laser power and 15 mm/s scanning speed. Reproduced from [235].

Owing to the difference in operating scales, melt pools attained through L-PBF are much smaller than those obtained via traditional welding processes. The combination of repeated rapid heating and cooling cycles and mesoscale molten pools invokes high heating and cooling rates, especially for L-PBF, where the scan speed is relatively fast. Heat accumulation throughout the build (Fig. 46 (a) and (b)) provokes an effective preheating temperature for

subsequent layers, which also affects the cooling rate. Namely, in upper layers, heat accumulation reduces conduction heat transfer effects through the substrate (heat sink), resulting in lower cooling rates and G/R ratios. These variations contribute to the formation of spatially variant melt pools, microstructures, and mechanical properties. Fig. 47(a) and (b) show the 2D computed and experimentally measured melt pool geometries using 285 W laser power and 1000 mm/s scan speed during a multi-track L-PBF processing of IN718 powder on an IN718 substrate [448]. The melt pool geometry changes significantly from the 1st to 2nd track due to the preheating effect and local powder particle arrangement, increasing conductivity and thus causing the 2nd track to become skewed towards the 1st. Additionally, due to the preheating temperature effect, the G/R ratio significantly decreases from the 1st to the 2nd track. Such reductions may prove desirable to achieve homogenous microstructures with equiaxed grains rather than inhomogeneous structures with columnar grains.

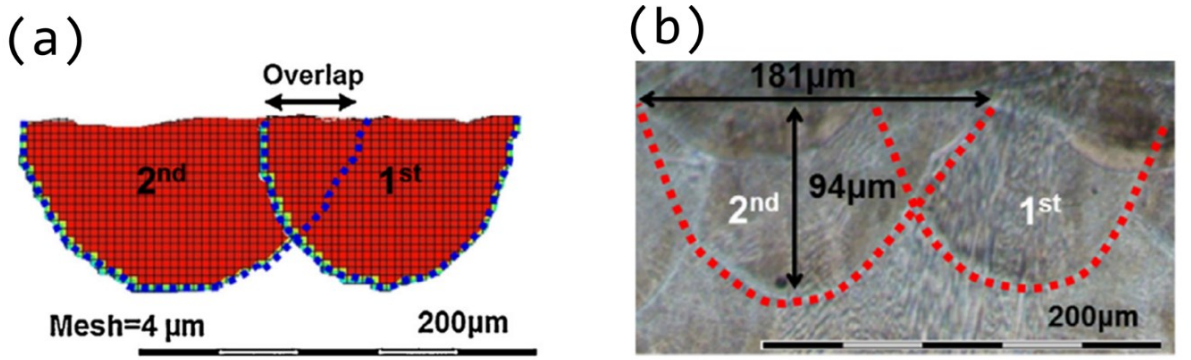

Comparison of calculated and measured molten pool dimensions.

Track no.	Dimension	Experiment	Modeling	Error
1	Width	144 μm	132 μm	9.1%
	Depth	90 μm	84 μm	7.1%
2	Width	181 μm	176 μm	2.8%
	Depth	94 μm	86 μm	9.3%
1–2	Overlap	63 μm	56 μm	12.5%

Caclulated $\bar{G}_n$ and $\bar{R}_s$ at the side and trailing edges of the molten pool for the 1st and 2nd tracks.

Location		Temperature Gradient ($\bar{G}_n$)	Solidification Rate ($\bar{R}_s$)
1st track	Edge	1.84×10^7 (K/m)	0.05 (m/s)
	Tail	2.93×10^6 (K/m)	0.70 (m/s)
2nd track	Edge	7.88×10^6 (K/m)	0.09 (m/s)
	Tail	3.42×10^6 (K/m)	0.71 (m/s)

Fig. 47. 2D (a) numerically computed and (b) experimentally measured melt pool geometries using 285 W laser power and 1000 mm/s scan speed during a multi-track L-PBF processing of IN718 powder on an IN718 substrate. The quantitative comparison of melt pool dimensions and G, R values are provided in the tables. Reproduced from [448].

Under certain processing conditions, peak temperatures within the melt pool can surpass the boiling temperature of an alloy. The subsequent material evaporation exerts a recoil pressure on the free surface of the melt pool that invokes a significant vapor cavity and promotes enhanced laser absorption. This phenomenon changes the mode of laser melting from conduction to the so-called "keyhole mode". In the conduction mode, the depth of the melt pool is dictated by conduction heat transfer through the solid material. Melt pools in this regime are semicircular in shape, in accordance with the solutions of Eagar-Tsai [454] and Rosenthal [462]. Whereas, in the keyhole mode, the laser beam is able to "drill" much deeper into the solid material and form a very large and unstable melt pool. As with keyhole welding, the incomplete collapse of the vapor cavity leaves voids in the wake of the laser beam [463]. A void resulting from keyhole mode melting will remain in the final part if it becomes trapped in

the solidification front and not expelled by the melting of subsequent tracks in current and subsequent layers. The regime laying in-between the conduction and keyhole modes is called the transition mode [464]. Regarding melt pool morphology, the transition mode displays elements of both conduction and keyhole melting. The temperature field (extent of vaporization) is the primary factor determining the threshold between the three different modes. Powder-scale models including all the relevant physics can be used to simulate these various melting regimes and help understand their formation and characteristics. For example, Fig. 48 (a), (b), and (c) show a comparison between the experimental and simulated melt pool morphology in the conduction, transition, and keyhole mode, respectively, on a flat Inconel 718 substrate [465].

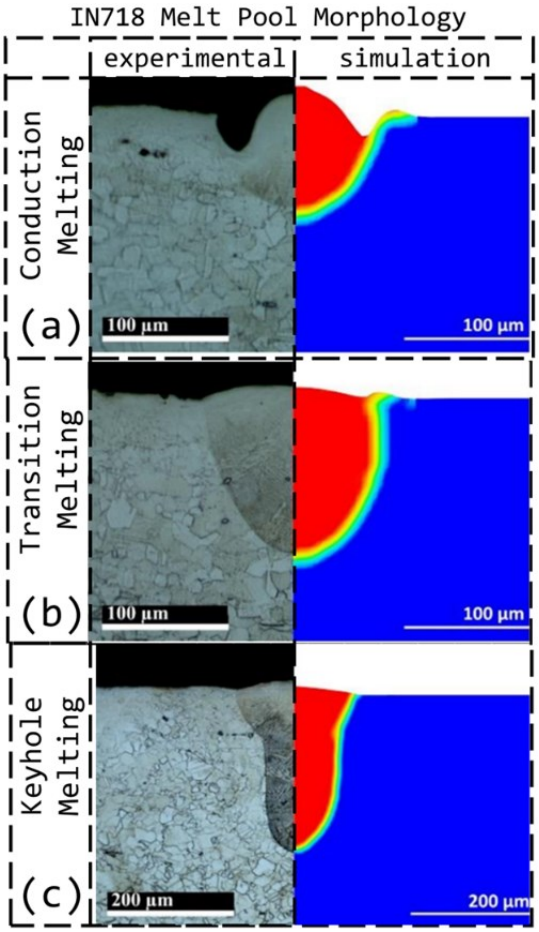

Fig. 48**.** Comparison between experimental (left) and simulated (right) melt pool morphology in the (a) conduction, (b) transition, and (c), keyhole mode of melting on a flat Inconel 718 substrate [465].

6.1.3. Spattering

An extensive investigation on the role of preheating temperature on melt pool morphology reveals the favorable effect of higher preheating temperature on the formation of larger melt pools for Nickel-based superalloys [465]. Specifically, at higher preheating temperatures, the melt pool dimensions across conduction, transition, and keyhole regimes of melting experience an increasing trend (Fig. 49(a)-(b), (e)-(f)). This observation is attributed to (1) enhanced heat

conduction via temperature-dependent thermal properties; (2) increased evaporation mass invoking stronger vapor depression and recoil pressure (Fig. 49(c), (d)); (3) increased keyhole front wall angle indicating a stronger laser drilling rate; and (4) stronger backward flow originating from the laser hot spot driven by larger flow velocities inducing stronger Marangoni forces (Fig. 49(f)).

Hence, while increased preheating temperature proves favorable for achieving homogeneous microstructures and melting between subsequent tracks and layers, it also increases the likelihood of porosities caused by keyhole collapse and laser spattering invoked by increased flow rates. Preheating has also been found to lead to larger residual stresses in the part [466]. Thus, a suitable medium for preheating temperature is desirable to optimize the solidification parameters while preventing high residual stresses and defects such as keyhole porosity and laser spattering. Furthermore, powder particle spattering induced by the metal vapor jetting and vortex flow near the melt pool could significantly influence the porosity of final product. Chen et al. [467] have developed a high-fidelity Multiphysics model to study the spattering and porosity formation mechanism in laser powder bed fusion process. They have reported two porosity formation mechanisms due powder particle spattering in experiments and simulation: (1) direct particle spattering into melt pool, resulting in un-melted or partially melted pores; and (2) the near-melt-track particles dragging to the melt pool bead, resulting in partially melted particles due to heat conduction.

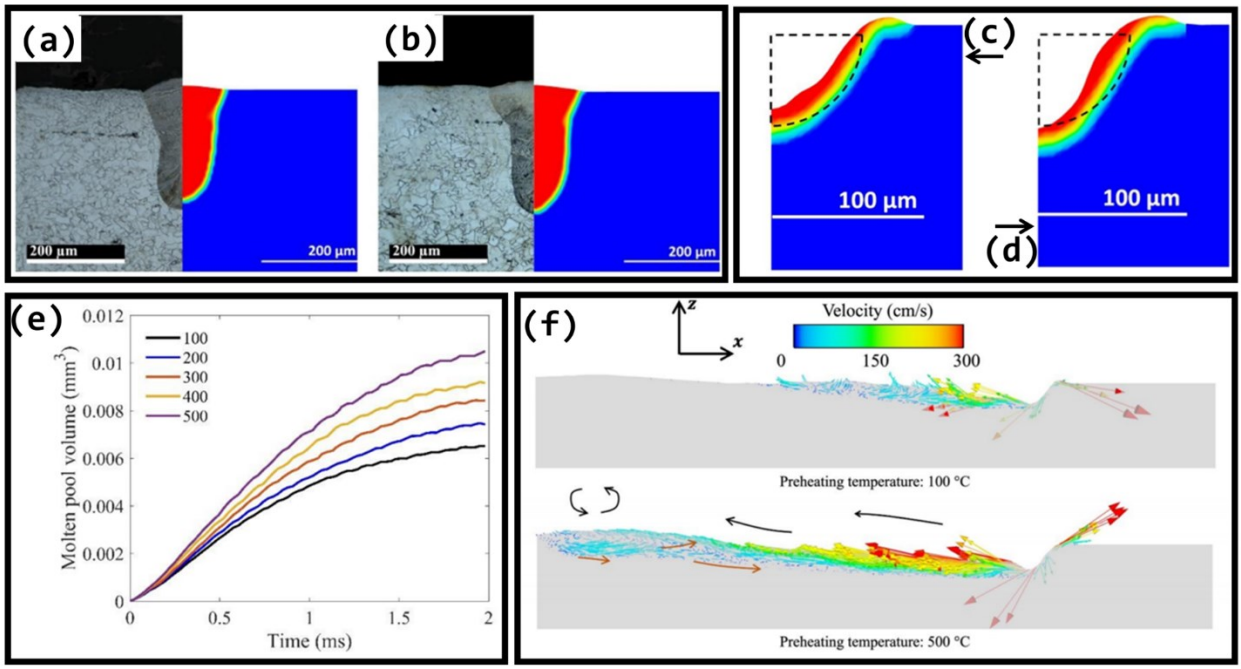

Fig. 49**.** Comparison of experimental and simulated melt pool morphology in keyhole regime (P = 250 W, v = 500 mm/s) at the preheating temperature of (a) 100 °C and (b) 300 °C; vapor depression during the formation of the melt pool in conduction regime (P = 250 W, v = 1500 mm/s) at (c) 200 °C and (d) 300 °C preheating temperature; molten pool volume in keyhole regime (P = 250 W, v = 500 mm/s) at various preheating temperatures; (e) Molten pool volume for different preheat temperatures; (f) global melt pool velocity profile in conduction regime (P = 250 W, v = 1500 mm/s) at 100 °C and 500 °C preheating temperature. All results are for L-PBF processing on an IN718 substrate (no powder). Reproduced from [465].

6.1.1. Balling effect

During AM processing, a faster scanning speed is desirable to increase productivity. However, too fast of speeds can cause the melt pool to become elongated such that it breaks into separated islands, otherwise known as the "balling defect". The cause and formation of such a defect are illustrated in Fig. 50 [468]. Fig. 50(a) demonstrates the computed 3D temperature distribution using 200 W laser power and 1100 mm/s scan speed during a single-layer L-PBF processing of IN718 powder. In this case, the melt pool is continuous, and the *balling defect* is not observed. In contrast, in Fig. 50(b), by increasing the scan speed to 2,300 mm/s, there is a very shallow melting of the substrate due to the rapid scanning speed and the resultant decrease in linear energy density. Small disconnected islands, also known as "*balls"*, from throughout the trailing end of the melt pool, which is attributed to Rayleigh instability [469]. Such instability is initiated when the length to width ratio of the melt pool is greater than π. By increasing the scan speed, the molten pool length increases while the width decreases slightly, thus leading to larger instabilities. Other factors influencing the formation of Rayleigh instability include the local powder particle distribution, wetting effect, Marangoni flow, and gravity [470]. The *balling defect* can lead to porosity in the final part and negatively impacting mechanical performance.

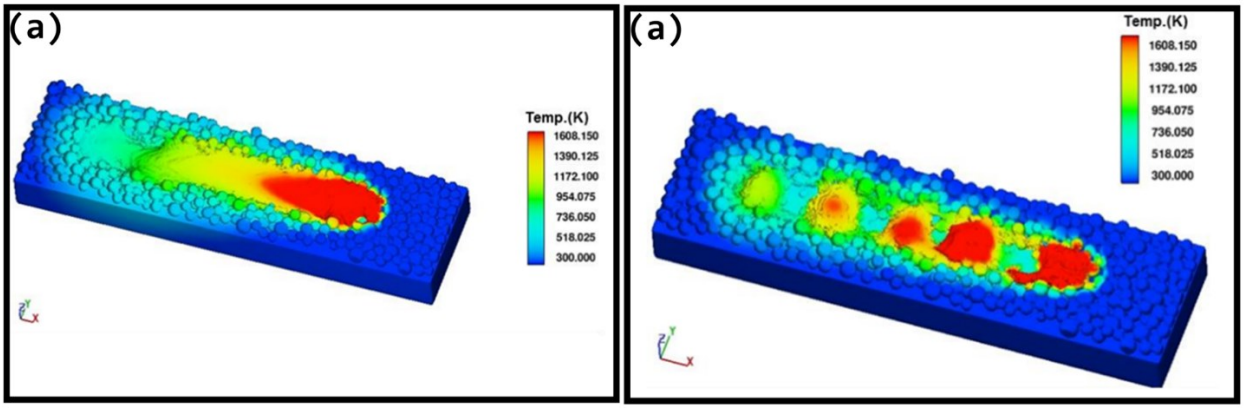

Fig. 50**.** Evolution of melt pool profile illustrating the formation of balling defect during L-PBF processing of IN718 powder on IN718 substrate using 200 W laser power and (a) 1100 mm/s scan speed, (b) 2300 mm/s scanning speed [468].

6.2. Microstructure modeling

The various numerical approaches to model the solidification and grain microstructure growth during the directional solidification processes have been used for AM. Cellular Automaton (CA), Monte Carlo (MC), Dendritic Needle Network (DNN), and Phase Field (PF) methods are among these numerical approaches. Note that, columnar grains resulting from dendrite mode solidification has predominantly been reported for the AM of Nickle alloys in literature. The nucleation of dendrites and their subsequent growth during solidification is called dendrite mode solidification. These methods are briefly discussed.

The prediction of grain microstructure and texture in AM processes has been modelled

mostly using MC and CA methods. The MC Potts model is based on the reduction of total energy at the grain boundary rather than kinetics of dendrite growth, which raises questions about its suitability for simulating the dendrite mode solidification phase in AM processes [471]. The PF approach is a tool for simulating mesoscale microstructure evolution that can predict intricate details during dendritic growth and estimate the anatomy of evolving dendrites [472]. To model the kinetics in alloys with several components, the PF approach uses thermodynamically based partial differential equations [473]. But, the material properties and various physical variables required in PF models to understand the dynamic development of the microstructure are seldom available through AM experiments [474]. Alternatively, the CA model which is based on multiphase solidification, can simulate the process of dendrite nucleation and formation [475]. The output values of a cell (crystallographic alignments) on the fixed grid are simultaneously modified based on dendrite growth laws. Tourret et al.'s Dendritic Needle Network (DNN) approach [476–478] assumes the dendrites as needles and as function of the solute flux power to calculate the velocity and radius of the dendrites. The PF [474], CA [479] and DNN [476–478] techniques, however, are computationally intensive, limiting their implementation to comparatively small spatial and time scales. To simulate the evolution of the microstructure in the as-built AM IN718 [474], IN625 [480], PF modeling is used. Secondary element classification, and dendrite quantities, orientation, and morphologies are all modeled in these simulations. Lattice Boltzmann method paired CA model [471] has been used to estimate the grain microstructure of E-PBF IN718 [481] for lengths up to a few millimeters. Literature [482] reports that the integrated CA-PF method to predict the growth of multi-phase and multi- component alloy dendrites. The dendrite growth kinetics is calculated by the 1D PF model. This is used as input at the CA interface cells in the micro-scale CA model, to calculate the mass redistribution and the dendrite growth. This model, however, can estimate a few tens of micron length scale for the microstructure. For grain microstructure prediction, MC simulation of LP-DED IN718 is recorded in a single-track deposition [483] with a cross-section of a few hundred microns. The model DNN [475] bridges the difference between CA simulations of dendritic grain sizes and PF calculations of dendrite tip radius (a few nanometers), which is many orders of magnitude smaller. About Al-7 wt., the DNN model is reported by percent Si and can predict dendrite growth for length scales of up to a few millimeters [476]. The full-length range of the simulation methods for the grain microstructure mentioned above is limited to a few millimeters. The recently reported Discrete Dendrite Dynamics (DDD) model has shown promise in simulating grain-microstructure and texture for the entire length scale of an AM fabricated component. The popular CA and newly developed DDD methods are briefly discussed below.

6.2.1. Grain structure

Cellular Automaton (CA) method - A prominent work for predicting grain structure of AM fabricated IN718 is reported by Lian et al. [484], which couples a finite volume (FV) method with a 3D Cellular Automaton (CA) method. The FV model accounts for the heat convection due to thermocapillary flow inside the melt pool to calculate the temperature field. The CA model implements an enriched grain nucleation scheme to capture the epitaxial grain growth in AM of IN718. With a face-centered cubic (fcc) or body centered cubic (bcc) lattice structure, several alloys solidify. A collection of cubic cells is used in the CA model to discretize a region of material, as shown in Fig. 51. There may be variables associated with each cell, such as temperature and a state index that correlates the cell with a specific grain. Two sub-models, for nucleation and grain growth kinetics, control the evolution of the grain structure. The location of nucleation sites, activation requirements and the crystal orientation of nucleated grains are determined by the nucleation model used in CA. Contrary to casting simulations by the CA method, where nucleation can occur both at the surface of the mold and in the bulk of the liquid volume, epitaxial grain growth is often reported in experiments in AM. Lian et al., [484] considers bulk nucleation and activation of existing grains along the molten pool boundary. In the CA model, a combination of envelopes models the details of the dendritic structure; an envelope is described as a "smooth surface" surrounding all the dendrite tips of a grain. For cubic crystals, the coupled FV-CA model identifies the preferred half-diagonals of the octahedral envelope with the preferred dendritic growth direction along <100>, representing the <100> crystallographic directions identified by the angles of Euler, along which the grain grows most rapidly.

Monte Carlo method - To simulate microstructural evolution on a discrete lattice, the Monte Carlo (MC) Potts model evolves spins (or grain identifiers). By assigning spins to each lattice site, the starting microstructure is digitized on a 3D lattice to initialize the simulation [485]. Since the reduction in grain boundary energy is the driving force for curvature-driven grain growth, wherein the sum of bond energies between neighboring lattice sites is used to calculate grain boundary energy with different spins. By choosing a lattice site and trying to shift its spin to that of a randomly chosen neighbor with a different spin, grain growth is simulated. The system's total energy is then recalculated by the Metropolis function [486], the probability of accepting the shift is determined. The formulation permits all configurational modifications that decrease the energy of the global system. The configurational modifications which increase the energy of the global system are based on the Boltzmann distribution. In a single Monte Carlo step (MCS), all lattice sites attempt one spin shift. With correct kinetics and topology, this formulation has been shown to simulate curvature-driven grain growth.

Wei et al., [483] studied the heterogeneous grain structure in multi-layer laser deposition of IN718 using the MC Potts method. The MC model considers repeated heating and cooling during multi-layer deposition, local temperature gradient and solidification growth rate, deposit

geometry, and molten pool shape and size govern the evolution of the grain structure in multi-layer LP-DED process. Note that, the heterogeneous grain structure is a source of the inhomogeneity in structure and properties of the metallic components. Wei et al., [483] found that epitaxial columnar grain growth from the substrate or previously deposited layer to the curved top surface of the deposit is controlled by the molten pool shape and size as illustrated in Fig. 51(a). Their predictions for the grain structure of LP-DED IN718 in both built directions have shown good consistency with experimental results as shown in Fig. 51(b,c), respectively.

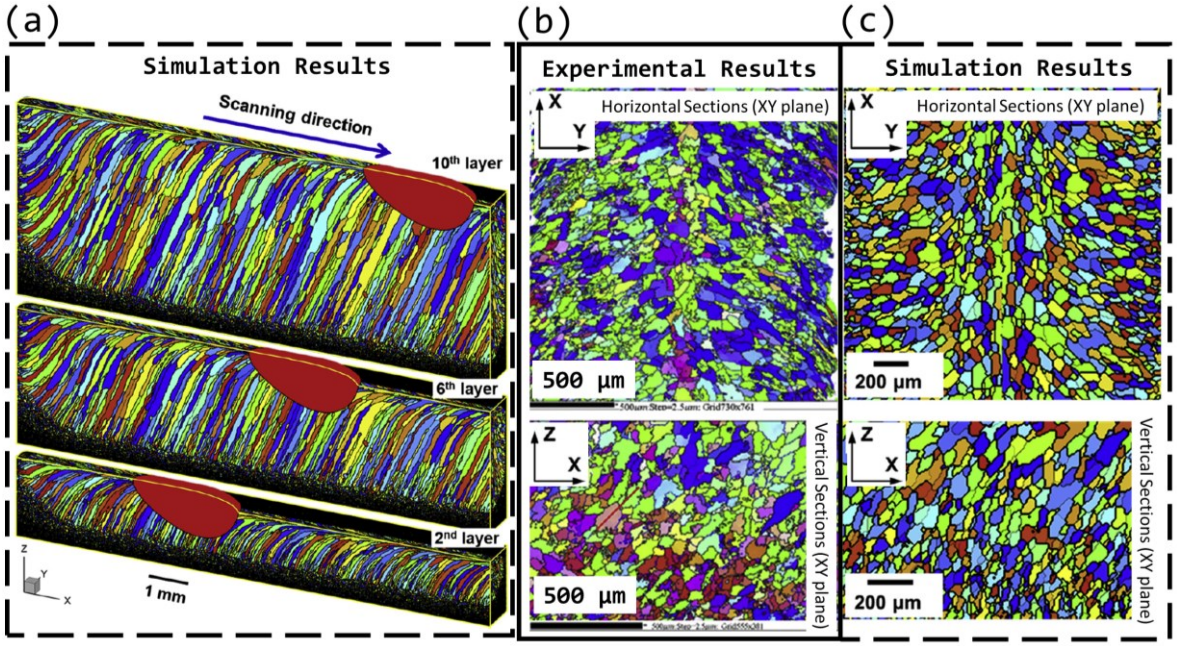

Fig. 51. Evolution of grain structure in LP-DED IN718: (a) simulation results visualized in the longitudinal central plane and the top surface of the deposit [483]; (b) experimental results obtained from EBSD analysis of horizontal and vertical planes [487]; (c) simulation results obtained for horizontal and vertical planes [483]. (Laser power 840 W, scanning speed: 10 mm/sec). Reproduced from [483].

Discrete Dendrite Dynamics (DDD) method - The DDD model is based on the classical competitive grain growth model for columnar dendritic grains by Walton and Chalmers [488]. According to the competitive grain growth theory the preferable orientation of the dendrite's growth depends on the undercooling difference. From experimental studies and computational simulations of the directional solidification process [472], welding [489], and AM [474], it is understood that stable primary columnar dendrites expand in the preferred direction, which for cubic crystals (fcc and bcc) is along one of its <001> crystallographic orientations that intersect the local temperature gradient at the smallest angle [475]. In addition, prior research [490] has shown that the nucleation of new grains in AM metals with cubic unit cell lattice structures is dominated by the epitaxial growth along one of the <001> directions to escape the high free energy requirement for nucleation.

The DDD model traces the instantaneous dendrite tip location growing from the evolving the contact surface and is based on geometrical shape based epitaxial growth by Lian *et al.* [484]. The seed crystals in the un-melted zone near the surface are activated during

solidification. The crystallographic orientations of the selected seed crystals are used as input to determine the growth direction for the epitaxial growth of columnar dendrites. In the DDD model, each dendrite arm is idealized as a line segment, with one endpoint representing as the start and the other endpoint as the dendrite arm tip at the present time instant. The state variables associated with each tip point are: (1) the spatial position of the tip point, (2) the local temperature gradient (G), (3) the three Euler angle crystallographic orientations, and (4) the dendrite arm's growth direction. The model accounts for the different situations arising due to interaction of a primary dendrite (PD) with its neighboring dendrites, namely, (1) change of growth direction of a PD with change in the local G, (2) convergence of two dendrites, and (3) divergence of dendrites. The DDD model is comparable to the coarse-resolution mesoscale CA model with only undercooling-dependent tip kinetics (cell size such as primary dendrite arm spacing (PDAS)). While the mesoscale CA model follows a Eulerian approach during solidification, the DDD model employs a more computationally efficient Lagrangian approach that tracks the tip locations of the dendrite arms at each time step as the solidification front progresses. Unlike the CA model, the DDD model does not require a change in the frame of reference to account for the cells undergoing liquid-solid transformation. In contrast to CA, this leads to greater computational efficiency for the DDD model. Note that the sub-grain level microstructure specifics such as dendrite arms spacings and composition segregations, are not modelled by both the DDD model and the mesoscale CA process, which would require higher resolution models such as the PF models or CA microscale models. The microstructure predicted by the DDD grain growth model for L-PBF IN740H [491] is compared with the results reported in Ni et al. [492] and shown in Fig. 52. Paul et al. [491] have studied the versatility of the DDD model by the accurate prediction of grain texture using scan vector rotation of 67° per layer of the EOS M290 DMLS machine for the L-PBF IN718 alloy. They [491] have also compared the grain texture analyzed with mtex-5.1.1 extension used with the MATLAB code. The model compares the Aspect ratio (ASR) of the grains in the x − z plane. The ASR predicted by the DDD model is 2.74 ± 1.37 compared to 2.92 ± 1.59 reported by Ni et al. [492].

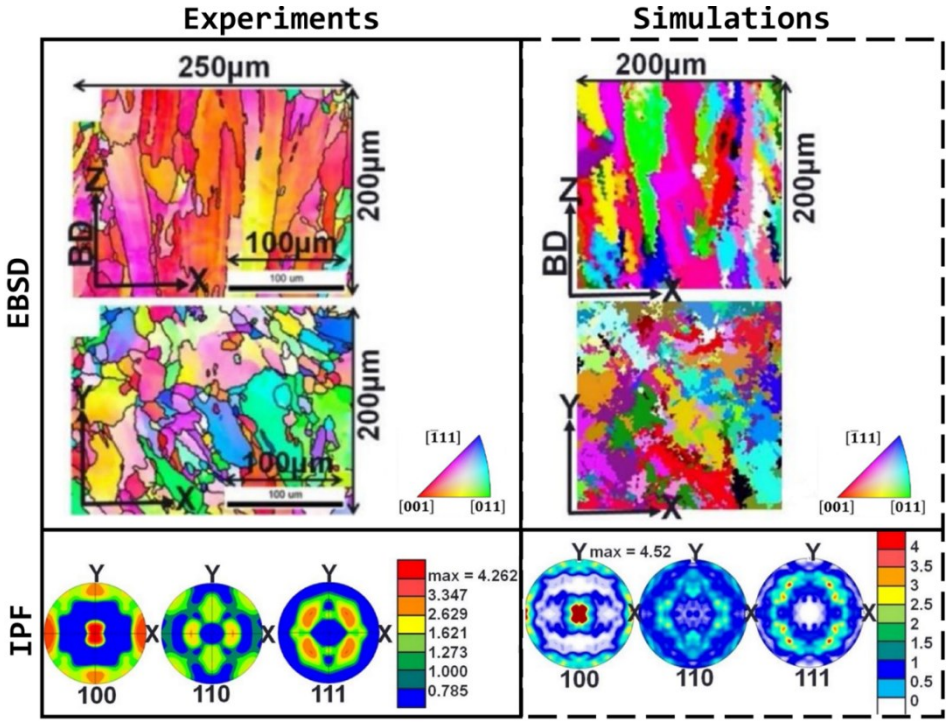

Fig. 52**.** Comparison of grain structure for L-PBF IN740H obtained by experiments versus the simulation results obtained by DDD modeling approach: (a) EBSD IPF, after [492], (b) DDD predictions [491], (c) inverse pole figures (IPF) obtained using EBSD analysis, after [492] and (d) IPF predicted by the DDD model [491].

6.2.2. Solidification

- ***Phase Field (PF) methods***

PF along with MC models are two widely used techniques to model solidification of metals deposited by AM processes. PF techniques rely on thermodynamically dependent partial differential equations and can be used to deal with the growth kinetics of multi-component alloys. However, in terms of computation, PF calculations are costly and are therefore limited to small domains and fine time scales. The region of the phase diagram where the liquid and solid phase of the system are in equilibrium is considered for the investigation of solidification [493]. Wang and Chou [494,495] investigated the microstructure evolution during L-PBF of IN718 by a PF model. Their FP simulation results are shown in Fig. 53 (a) to (c) along with the experimentally measured microstructural features from SEM micrograph in (d). The temperature gradient and the solidification velocity are first determined from an L-PBF FEM and are used to simulate the growth of the microstructure with time as the input of the PF model. The effects of the build height and scan speed of the laser beam on the evolution of the microstructure are calculated. The results show that the PF simulated primary dendritic arm spacings (PDAS) are comparable to the results of experiments and analytics, as shown in Fig. 53. The cooling rate and the thermal gradient first decreased with the rise in build height, and then slightly increased at the very top of the AM built layers. Furthermore, the temperature gradient increased to a certain value and then decreased with the increase in the scanning speed of the laser beam, and the direction of the maximum temperature gradient appeared to be parallel to the direction of the component construction. In addition, the temperature gradient

greatly influences the growth of the dendrite due to a higher temperature gradient that results in a higher growth speed.

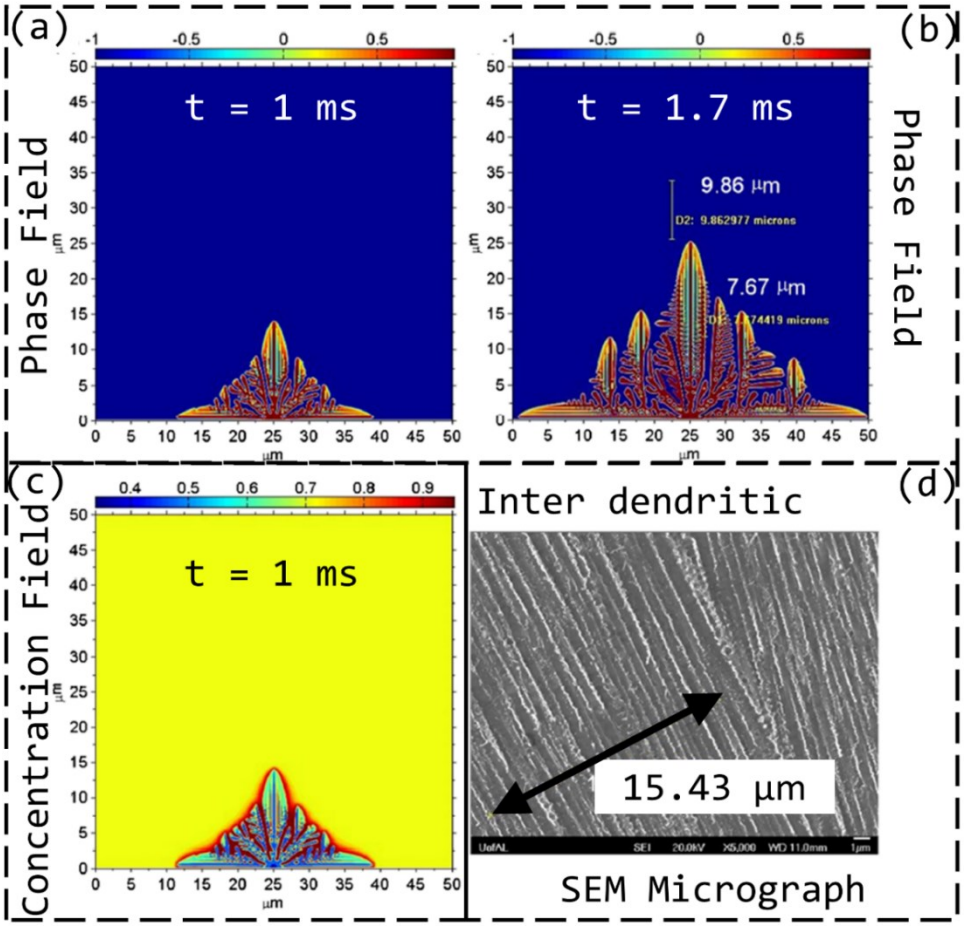

Fig. 53 Solidification simulation of L-PBF IN718 using phase field modeling: at the average dimensionless thermal gradient of 0.498 (temperature gradient ~1.04 × 10^6 °C/mm). Phase field simulations at time step of t = 1 ms in (a), and t = 1.7 ms in (b). Concentration profile at time step of t = 1 ms in (c). In (f), an example of SEM micrograph for measuring the Secondary Dendritic Arm Spacing (SDAS) in the as-build L-PBF IN718 sample [495].

The PF model has been widely used for the simulation of microstructure evolution and severe elemental micro-segregation occurring during the AM of Nickel-based superalloys due to rapid solidification [496]. The attractiveness of the PF method is that there is no need to track the moving solid-liquid (SL) interface as the sharp interface. This is because the SL interface is part of the mathematical model used by PF to solve the heat and diffusion equations at SL interface. The need to track the SL interface is eliminated using an order parameter that varies smoothly in a sine wave curve form between the two solid and liquid phases [493]. Additionally, computational thermodynamics and CALPHAD (CALculation of PHAse Diagrams) modelling are also used for the fast and accurate prediction of the compositional variations due to multiple cyclic heating and cooling with different heating/cooling rates and high magnitude of solidification rate at 10^6 K/s during the AM processes [497]. The following paragraphs discuss the work on simulating the severe elemental micro-segregation of these phases in the AM of Nickel-based superalloys.

Ghosh et al. [498] used PF simulations to predict the size and micro-segregation of the cellular microstructure formed along the melt pool boundaries for the solidification conditions of L-PBF of IN625 as a function of melt pool dimensions. Keller et al., [480] investigated microstructure and micro-segregation during rapid solidification of L-PBF of IN625. Geometric and thermal features of the melt pools were simulated using a thermal FE model and used in the subsequent mesoscale simulations. The solidification in the melt pool was simulated on two length scales. For the PF simulations, Ni-Nb was used as binary analogue to IN625. The simulated primary cellular/dendritic arm spacings (PDAS) agree well with experimental measurements [480].

PF models can investigate the influences of the build height and laser beam scanning speed on the microstructure evolution [495]. PF model is also coupled with DICTRA software, to study micro-segregation during solidification of AM processed IN625 [480]. In this 1D for diffusion-controlled phase transformation model micro-segregation and back-diffusion in multicomponent materials (such as Nickel-based superalloys) is simulated by combining CALPHAD thermodynamic and kinetic materials descriptions [480,493]. There are also confounding factors that affect the exact compositions predicted by our phase-field and DICTRA models. The accuracy of these predictions is linked to the correctness of the FE models in capturing the complex temperature-time cycles during AM processes, including the effects of depositing additional layers. A detailed thermal history of the AM process can account for the influence of solid-state diffusion, avoiding the artificially high compositions in the enriched regions of the microstructure, as predicted by the PF models [480].

In IN718 alloy, the formation and growth of γ′- and γ″-phases precipitating from the supersaturated solid solution (SSSS) γ-grain matrix during the subsequent thermomechanical processes can also be simulated using a PF modeling approach, wherein the evolving molar fraction of γ′- and γ″-precipitates can be traced. A pseudo-ternary (Ni-Al-Nb) thermodynamic database can be developed from the AM specific continuous cooling transformation (CCT) and time-temperature-transformation (TTT) diagrams of IN718 [480,499]. The pseudo-ternary database can determine the apparent composition of Alx (xAl) as the weighted summation of γ′-forming elements (Al, Ti, Fe). Similarly, the apparent composition of Nbx (xNb) can represent the weighted summation of γ”-and δ-forming elements. Note that, the composition of both γ″ and δ-phase could be treated as Ni_3Nb with γ″-being a metastable phase and δ-being the stable phase. During precipitation, the time evolution of the concentration fields is governed by the generalized diffusion equation, i.e., the Cahn–Hilliard and Ginzburg–Landau equations [500].

Usually a multi-scale model is combined with finite-element method (FEM) and PF modeling approach to simulate the evolution of solidification microstructures at different locations within a molten pool of an additively manufactured IN718 alloy [494]. FE model is used to calculate the shape of molten pool and the relative thermal gradient G at the macroscale.

Then, the results are employed as inputs to PF model. In the PF model, a scalar variable Ø introduced to distinguish the type of phases at a fixed point and time. The field / takes on the value Ø= -1 in the liquid phase and Ø= +1 in the solid phase and varies smoothly across the diffuse interface. Wang et al. [494] compared the predicted morphology of as-solidified microstructures and formation of Laves phase at different sites for the AM IN718 (see Fig. 54). They estimated that the solidification site with a large angle between the temperature gradient and the preferred crystalline orientation could build up a high niobium (Nb) concentration in the liquid during solidification but has less possibility of forming continuous long chain morphology of Laves phase particles. These findings provide an understanding of the microstructure evolution inside the molten pool of IN718 alloy during rapid solidification of AM processes. Further, the findings indicate that the site with a large misorientation angle will have a good hot cracking resistance after solidification.

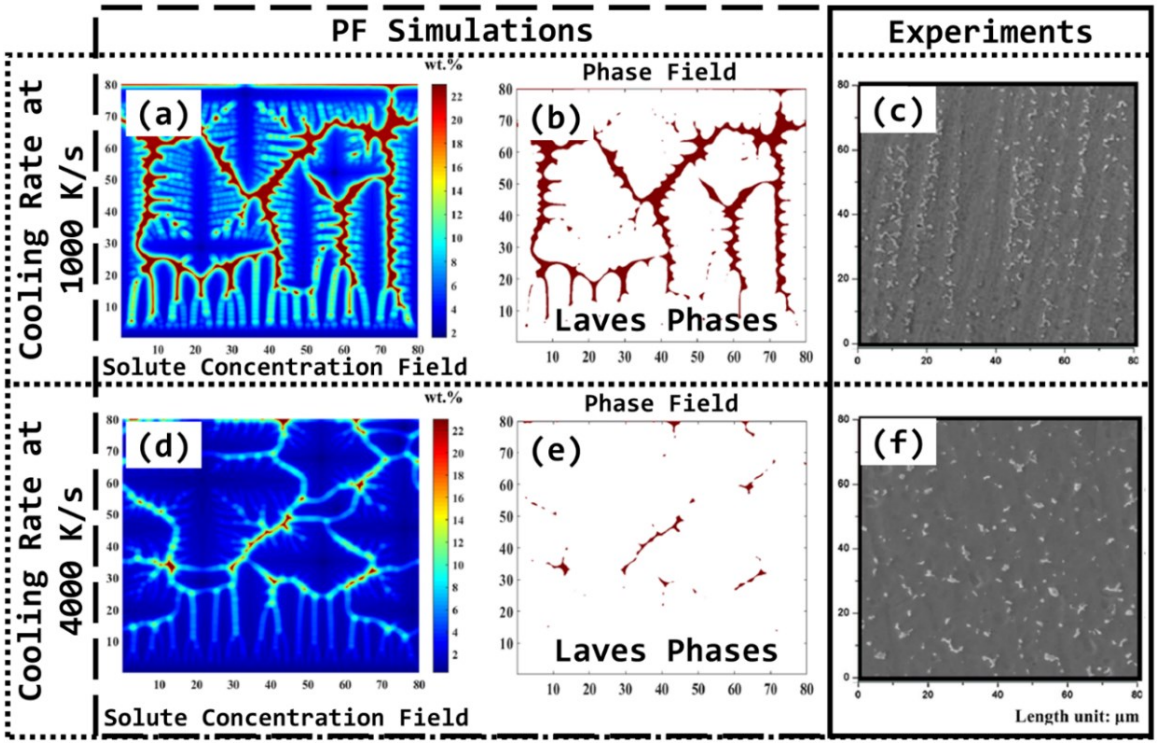

Fig. 54 Comparison of Phase Field modeling simulations with experimental results in AM IN718 alloy for the morphology of Laves phase forming during solidification at two cooling rates of 1000 K/s in (a)-(c) and 4000 K/s in (d)-(e). The solute concentration profile of Nb in (a) and (b). The phase distribution of Laves phase particles in (b) and (f). Experimental observation by SEM of Laves phase particles from [501] in (c) and (e). Reproduced from [494].

- ***Thermodynamic databases***

During the AM processes, and after solidification, due to their characteristic thermal history, i.e., subsequent reheating during continuous cooling, various solid-state transformation takes place, which can in turn result in different as-fabricated microstructures for different AM processes. For instance, the microstructure of L-PBF IN718 consists of fine γ" strengthening precipitates while that of E-PBF IN718 and DED IN718 consist of substantial amount of aging

or grain growth [502]. This is because the entire build experiences a higher overall cooling rate during L-PBF process while during DED process due to significant heat build-up and during E-PBF process due to the high pre-heating, a large portion of the entire build can experience higher temperatures up to above 900 ˚C over an extended period of time, resulting in coarse γ" precipitates and larger grain structures [502]. The subsequent effect of such complex thermal characteristics on microstructure may increase the anisotropy in mechanical properties of the AM components. For instance, a non-uniform hardness profile was reported for LP-DED IN718 over the build height, i.e., higher hardness in the lower part due to excessive aging effect on formation of fine γ" precipitates [174]. The other effect of unique AM thermal characteristics is the severe micro-segregation of alloying elements observed in the AM Nickel-based superalloys such L-PBF IN625 [503], E-DED IN718 [504], and E-PBF CMSX-4 [505], which can not only can affect the local compositions of the microstructure deviating from the nominal composition but also can alter the precipitation kinetics of various phases in the alloy. For the modeling purpose of the effect of unique thermal characteristics of AM processes on the microstructure experienced during the fabrication process, there are some thermodynamic databases available for the Nickel-based superalloys such as JMatPro database and TC-PRISMA database.

Kumara et al. [504] used the JMatPro thermodynamic database to generate the continuous cooling transformation (CCT) diagrams of IN718 with nominal composition during E-PBF process (Fig. 55(a)). Using the precipitation kinetics, they have revealed the mechanisms for the formation of the diverse precipitates in E-PBF IN718 based on severe micro segregation formed during AM fabrication. They showed that local compositions of the solidifying structure are significantly location dependent, e.g., severely micro-segregation of alloying elements form the core of inter-dendritic regions towards the area near the Laves phase [4]. Subsequently, the γ', γ", and δ phases precipitated faster in the regions near the Laves phases (dotted lines) compared with that at the dendrite core (solid lines) [504] (Fig. 55(a)). Zhang et al. [503] used the TC-PRISMA thermodynamic database to simulate the solid-state phase transformation during isothermal heat treatment at 870 °C in the L-PBF IN625 with nominal composition (Fig. 55(b)). As shown in Fig. 55(b), the δ phase started to form at the peak volume fraction of γ″ after over 100 h. The big challenge in the solid-state phase transformation modeling of AM process is the inclusion of repeated phase formations or dissolution during multiple thermal cycles serving as in situ heat treatments. As discussed earlier, the precipitation rates of the phases depend on prior micro-segregation in the as-fabricated microstructure and the strength of the thermal cycles, i.e., isothermal holding time at local temperature. For instance, In E-PBF CMSX-4, a significant size gradient for the γ' precipitates was reported along the build height [505].

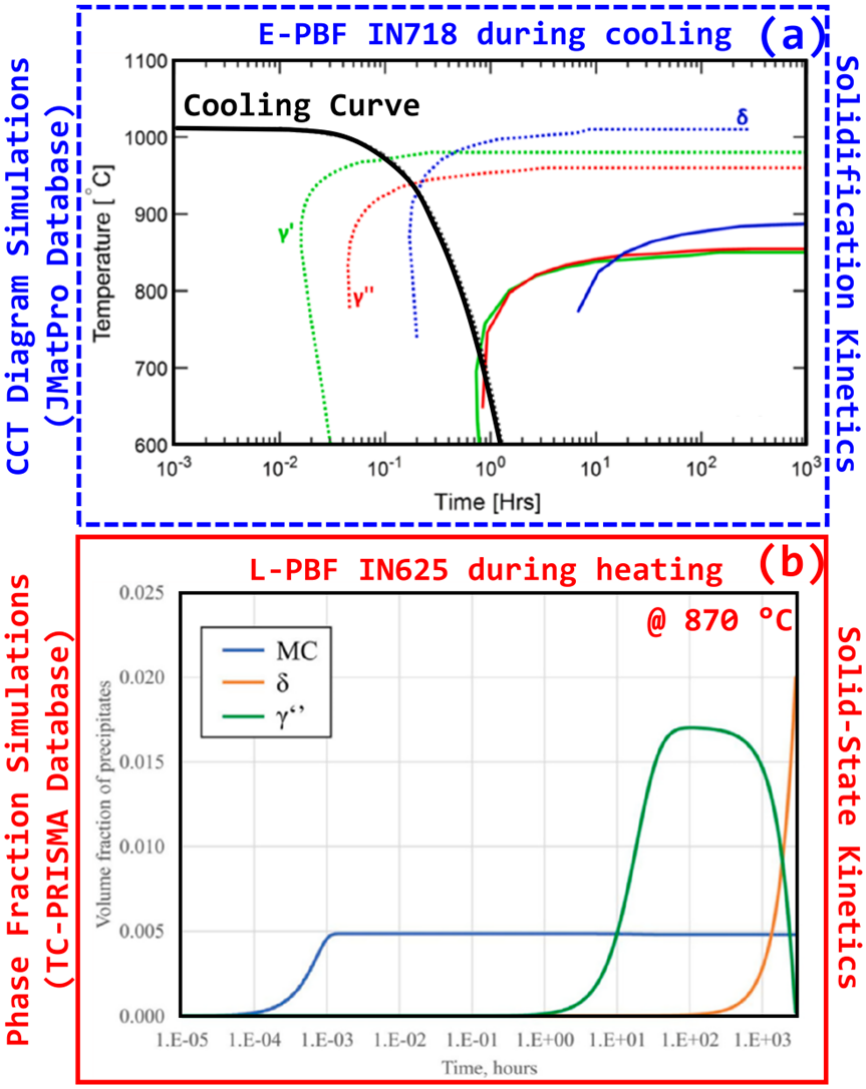

Fig. 55 Simulation results for Nickel-based superalloys during AM processing using commercial thermodynamic databases: (a) Continuous Cooling Transformation (CCT) diagram created using JMatPro database simulated for nominal composition of IN718 alloy along with the experimentally measured cooling curve by thermocouples during E-PBF process. Notably, the dotted lines represent the region close to Laves phase and solid lines represent the dendrite core for 0.5 wt.% transformation [504]. (b) Simulated precipitation kinetics of IN625 (Ni-20.70Cr-9.00Mo-4.00Nb-0.72Fe-0.05C) at 870 °C using TC-PRISMA database during L-PBF process [503].

6.3. Defects modeling

Some of the most common defects in AM are LoF and keyhole porosity, whose formation stems from the temperature distributions and melt pool geometries throughout the build [153]. These defects have an adverse influence on the part's density and can be detrimental to its mechanical properties, such as fatigue behavior [366]. Thus, it is critical to understand the physical mechanisms causing the development of such defects and discover ways to prevent their formation. Since experiments cannot provide such a detailed understanding, well-tested 3D transient heat transfer and fluid flow models are typically employed.

There are three primary mechanisms through which porosity forms during AM processing. The first is the formation of LoF pores caused by inadequate melting of upper layers into

previously deposited layers [506]. The second is keyhole pores caused by the collapse of the vapor cavity in keyhole mode melting [463]. Recall that for processes operating under high energy densities, preheating temperatures, or a combination of both, peak temperatures within the melt pool can surpass the boiling temperature of some of alloying elements in the alloy composition. Therefore, the subsequent evaporation of such elements exerts a recoil pressure on the melt pool free surface that invokes a significant vapor cavity and promotes laser absorptivity, which is also known as the keyhole mode. The incomplete collapse of the vapor cavity leaves voids in the wake in the laser beam, which will remain as a keyhole pore in the final part if trapped in the solidification front and not expelled by the melting of next tracks or layers [463]. The size of such pores depends on the melt pool dynamics, while the shape will be mostly spherical due to the hydrostatic pressure of the liquid metal acting on the pore and therefore the liquid surface tension acts inwardly toward inside the pore, leading to minimize the pore's surface area, i.e., shrinking the pore's overall size [507]. Finally, during the powder atomization process, entrapped gas might form inside the powder particles, leading to mesoscopic spherical gas pores in the AM parts [508]. Gas pores may also form due to the entrapment of shielding gas used in the AM fabrication as well as the alloying elements evaporation within the melt pool during AM fabrication [16].

While many researchers have employed numerical simulations to study the development of LoF and keyhole porosity for various other materials, there has been relatively little work performed for Ni-based superalloys [506]. Bayat et al. [509] studied the evolution of LoF pores in the multi-track/multi-layer processing of IN718 by L-PBF, as shown in Fig. 56, where the thermal field during scanning of the second layer at different times is shown on a cross-section parallel to the laser scanning direction. Note that, in this figure, there are some existing pores formed from the first layer deposition. At t = 320 μs (Fig. 56(a)), the laser just reaches the location of the cross-section, where significant vapor depression is observed owing to the recoil pressure caused by the alloying elements evaporation. As time progresses, the laser eventually reaches the plane again while scanning the second track (t = 890 μs, Fig. 56(c)). At this point, the recoil pressure creates a significantly deep melt pool, resulting in eradication of some of the pores developed during previous layer. At t = 1160 μs (Fig. 56(d)), as this molten pool continues to solidify, a new pore is formed near the top right side of the track, while a previously formed pore begins to shrink. During the scanning of the 3rd and 4th tracks, a series of pores are also formed due to the inert gas being trapped below the melt pool. That is because the depression zones formed during the 2nd layer are not sufficiently wide/deep to eradicate pores formed during the previous layers. These pores, also known as interlayer pores, are likely to form when the melt width is partially smaller than the hatch spacing, causing them to align vertically, as shown in Fig. 56(g-i). The lack of sufficient overlap between the adjacent tracks and layers, is one of the primary mechanisms by which the LoF pores are formed in both the L-PBF and E-PBF processes. Thus, the results from this model suggest that modification of the

process parameters such as laser power, scan speed, or hatch spacing would help mitigate the formation of LoF pores.

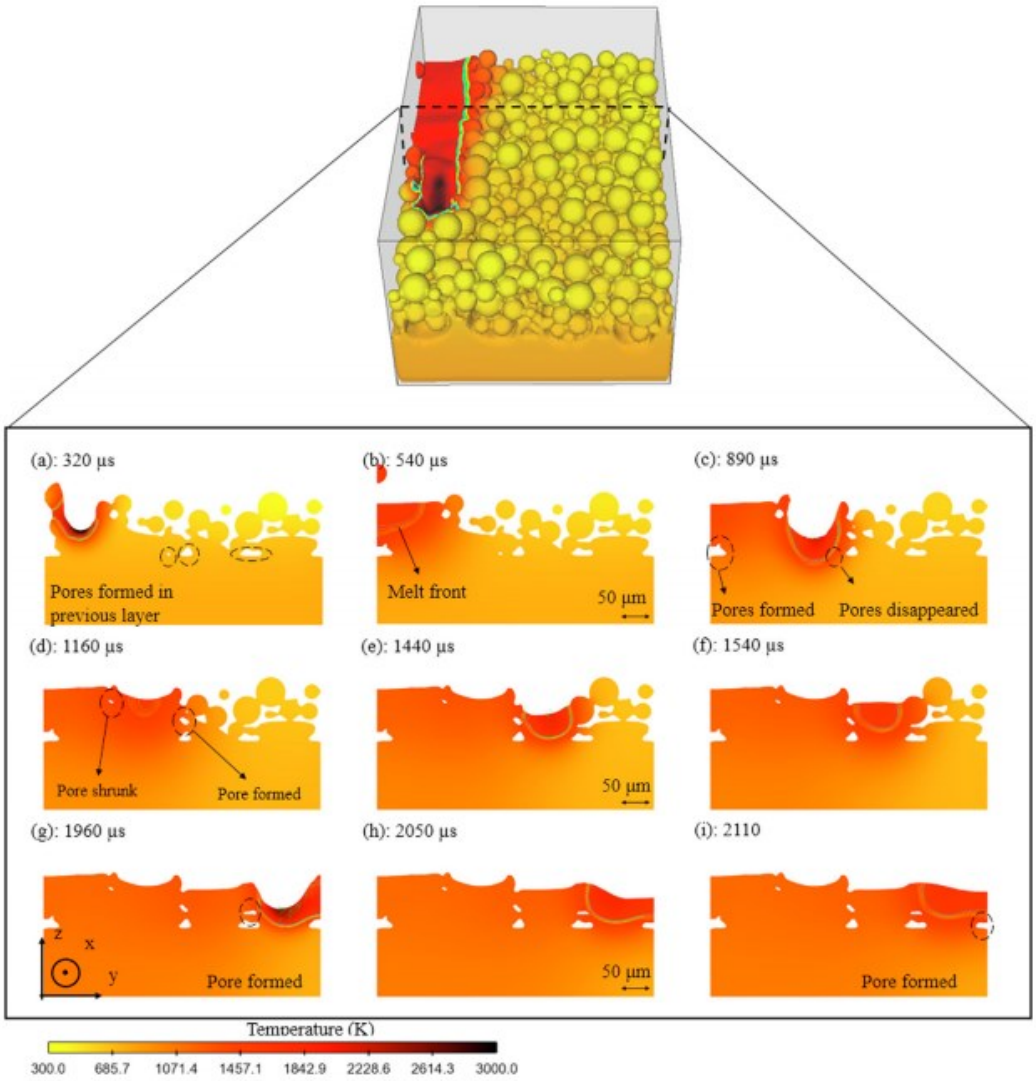

Fig. 56. Evolution of lack-of-fusion pores during scanning of the second layer of IN718 by L-PBF [509]. The thermal field and melt pool dynamics are depicted at different times on a cross-section parallel to the laser scanning direction. (a) 320 µs, (b) 540 µs, (c) 890 µs, (d) 1160 µs, (e) 1440 µs, (f) 1540 µs, (g) 1960 µs, (h) 2050 µs, (i) 2110 µs.

6.4. Residual stress modeling

During the AM fabrication process, the residual stress is induced due to either (1) differential heating of large thermal gradients forming solids or (2) differential cooling. Previous work [510] using an unheated construction chamber to experimentally quantify residual stress in the L-PBF process has shown that residual stress is compressive near the center of parts and tensile at the edges. In addition, measurements of parts attached to the building plate showed concentration of residual stress near the interface of the substrate [511]. Residual stress of 50-80% of the yield stress was shown by laser free-formed material [512], whereas E-PBF material shows only 5-10% of UTS [513]. Laser melting has noted substrate warping, or deformation during the AM process, and its physical relationship to residual stress [514].

Prabhakar et al. [515] developed a thermo-mechanical model for predicting the substrate deformation during E-PBF of IN718.

Cheng et al. [516] studied the effect of scanning strategy in the L-PBF of IN718 on the stress and deformation distribution using a sequentially coupled thermomechanical FE model. Some limitations and assumptions in these thermomechanical models include: (1) Assuming increase in the melt pool conductivity [517] to account for the convection of liquid in the melt pool and (2) Neglecting powder layer volume shrinkage due to solidification.

Pant, et al. [518] developed a thermomechanical FE model to predict the 2D residual stress distributions (see Fig. 57) and compared the predicted residual stress with Neutron Diffraction measurements for the L-PBF IN718. Slightly lower than the experimentally determined values are the expected stresses near the surfaces attached to the base plate is attributed to the assumptions for the material behavior and uncertainty in material properties used for the simulations. The lack of material properties of the as-build alloy means that the material properties for aged wrought IN718 are used in the simulations [515]. Additionally, anisotropy in material behavior has been reported in experimental study [519], but in the FE simulations usually isotropic material behavior is assumed.

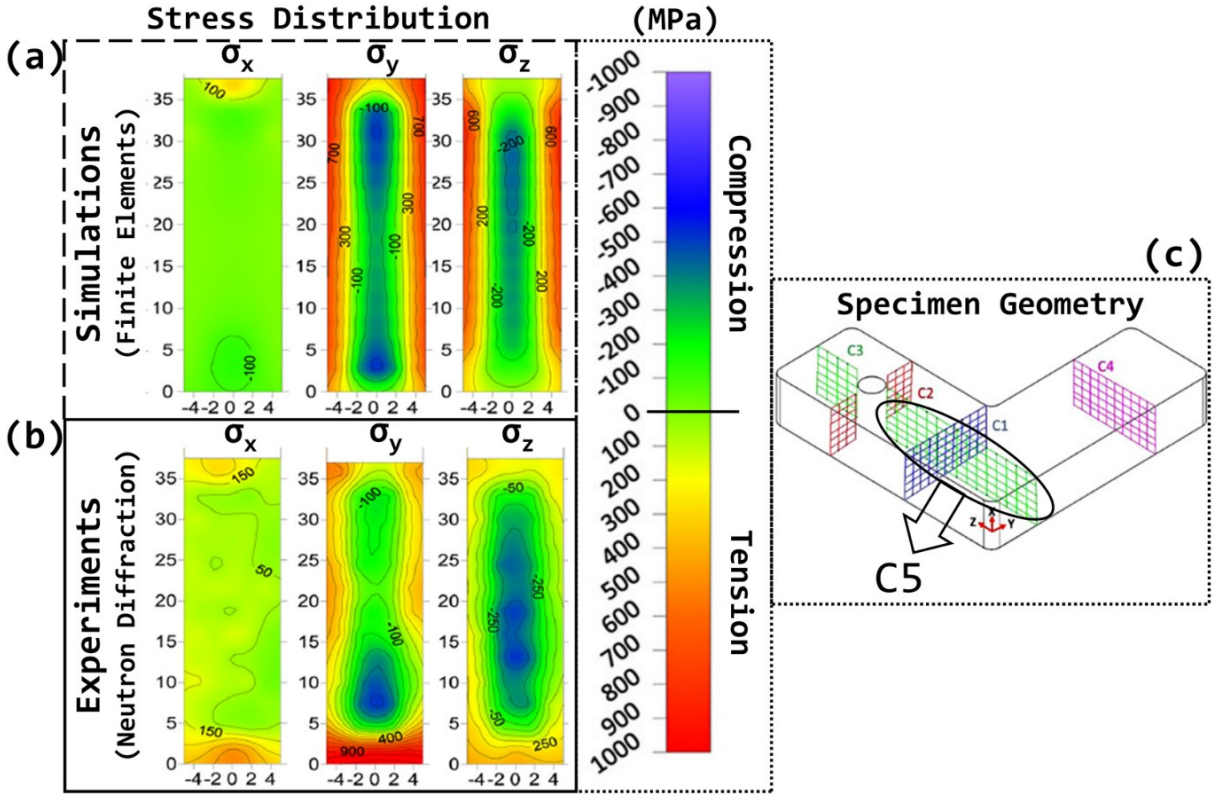

Fig. 57. Comparison of stress distribution measured by Neutron Diffraction experiments with FE simulations for L-PBF IN718. Reproduced from [518].

A promising method for ensuring manufacturability and improving component quality [520] is the quick and accurate simulation of residual stress/distortion in AM processed parts. Given the limited computational speed, the primary focus of early simulation efforts for L-PBF was on millimeter-order or even smaller-scale models such as single track [521]. In terms of time

steps, thermomechanical analysis for prediction of part-scale distortion and residual stress requires time steps in orders of millions. Simulation of the L-PBF method involves prohibitively large numbers of elements and high computing costs to account for the ridiculously small laser spot size and thin layer thickness. Numerous techniques have been proposed to increase the computational efficiency of the AM process simulation. These include layer scaling (simultaneously modeling several layers grouped together) to reduce element number and computation cost [522], applying uniform thermal load [523], stress [524], or temperature field [525] from detailed micro-scale analysis and pass the results to macroscale analysis with scaled up layers for distortion and stress prediction. A highly efficient technique to simulate residual stress/distortion at part-scale is the inherent strain method. The inherent strain method was first proposed by Ueda [526] and has been widely used to calculate distortions and residual stress during welding [43].

A detailed thermomechanical simulation for AM processes is computationally expensive. So, a detailed micro-scale thermomechanical model is integrated with multiscale process modeling approach to predict part-scale distortion. A micro-scale detailed process model is employed to extract inherent strains based on the modified inherent strain model. Residual distortion and stress prediction at the part scale is performed using the inherent strains extracted in the layer wise inherent strain method.

A quasi-static mechanical analysis is conducted in sequential thermal load steps using the temperature history obtained to solve the mechanical response. Chen et al. [527] postulates that when the laser passes the point of interest in the bottom layer, the compressive plastic and elastic strain become tensile due to the rapid heating. The remelting on a previously deposited layer due to deposition of a new layer partially relieves the accumulated residual stress and strains. The highly localized heat input in the immediate vicinity of the melt pool results in a steep temperature gradient, which in turn causes non-uniform thermal expansion. The underlying solidified metal constrains thermal expansion and thus induces compressive strain and stress. Since both the yield strength and elastic modulus decrease drastically at high temperatures, compressive plastic strains are readily accumulated by this heating process. As the deposition cools down further, the underlying solidified metal prevents thermal contraction, and the material can develop tensile strain and stress. Due to the subsequent layer depositions, the thermal expansion and contraction cycle repeats and relieves the accumulated plastic and elastic strains.

The original theory of inherent strain implies that elastic strain is relaxed because when cooling to the ambient temperature, the welded parts are not fixed, and therefore the plastic strain produced in the welding process is directly applied as the initial strain in the system. The physical process of L-PBF, however, is very distinct from the problem of welding. With melting and solidification, mechanical limitations begin to arise, and when the component cools to ambient temperature, elastic strain cannot be completely released. The modified inherent strain

model [528] is therefore formulated to extract the inherent strain anisotropic values for AM part distortion and stress prediction. The modified inherent strain is defined as the difference between the intermediate-state total mechanical strain and the steady-state elastic strain Chen et al., [527] performed part-scale distortion and residual stress simulation based on the inherent strain method on a double cantilever beam manufactured by the L-PBF of IN718. The inherent strains derived from the micro-scale model are added in three natural directions to the model as constant coefficients of thermal expansion (CTEs). To form one numerical layer, ten actual physical layers are grouped together and enabled along the build direction in layer-by-layer fashion. A uniform unit temperature increase is added to the newly active components when the grouped layer is activated to add the underlying strains and a quasi-static analysis of equilibrium at room temperature is performed. For deposition of each layer, this simulation process repeats itself. The distortion profiles after cutting of the supports obtained from simulation and experiment are compared in Fig. 58. The simulation result and experimental measurement have highly similar distortion profile and magnitude.

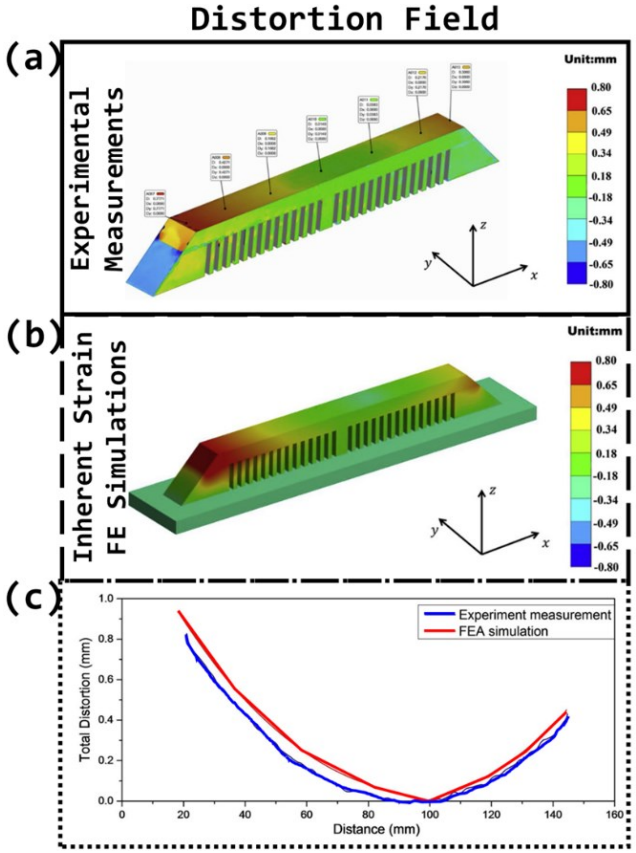

Fig. 58. Comparison of distortion field for the double cantilever beam after cutting off the supports: (A) experimental measurement, (B) inherent strain simulation, and (C) distortion profile along center line of the top surface [527].

To further clarify the development of residual stress in fusion-based AM components, some researchers use finite element method (FEM) to help predicting the residual stress and the distortion [235]. In the FEM, the complex component is discretized into finite number of

elements. Transient thermal analysis and elasto-plastic mechanical analysis are performed in each element, then the individual results are assembled into an overall analysis [529]. FEM could give the relationship of temperature and residual stress distribution in AM components. FEM also gives a quick view to predict the influence of different parameter. Such example of FEM analysis is the work of Mukherjee et al. [242], they used the computer simulation and found that high energy density (high energy source or low scanning speed) could increase the distortion inside the AM components. At the same time, the work of Wen et al. [530] with FEM also pointed out that high energy input causes a higher peak temperature and larger residual stress to Nickel-based superalloy, their simulation demonstrated that the variation of residual stress is 50 MPa or more by changing the scanning speed (900 mm/s to 1300 mm/s) and laser power (250 W to 150 W). Though FEM is a powerful tool for residual stress predication, it is important to do the practical experiment and use the result to improve the FEM model [531]. An example of FEM analysis couples with experiment result about Inconel 718 alloy is illustrated in Fig. 59.

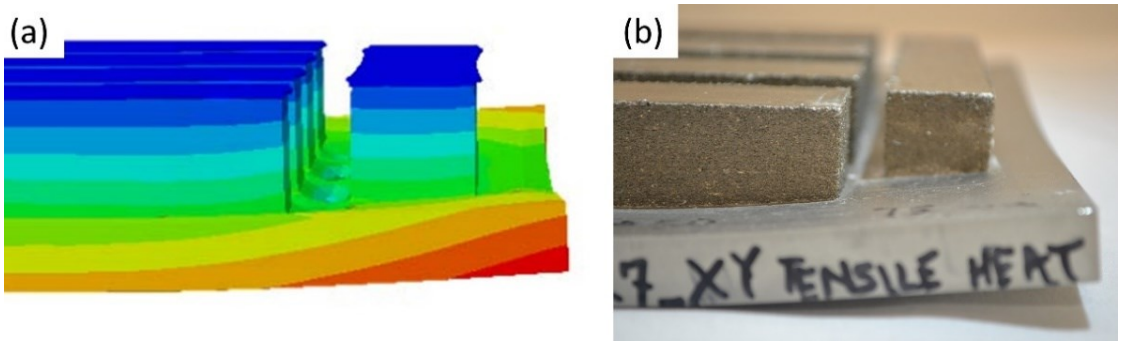

Fig. 59. An example of FEM prediction and practical experiment with E-PBF Inconel 718 alloy [532].

6.5. Mechanical properties modeling

The mechanical behavior of Nickel-based superalloys is governed by the several precipitates and carbides within the γ-grain matrix. The relation between the meso-, microstructures and mechanical behavior of Nickel-based superalloys has been studied using microstructure-based constitutive models. Many of these models have used polycrystalline plasticity schemes or crystal plasticity modeling for the AM Nickel-based superalloys, such as finite elements and self-consistent elements [533]. Common practice is to use the elasto-plastic self-consistent (EPSC) mean-field homogenization formulation. A polycrystal is assumed as a collection of single crystals, with each crystal having a specific orientation, a volume fraction, and an ellipsoidal shape. Each ellipsoidal representative grain orientation is treated in the homogeneous equivalent medium (HEM) as an elastoplastic inclusion which would have the polycrystal's average properties. The deformation of the polycrystal is related to the deformation of the grain using a self-consistent scheme. Ghorbanpour et al. [533] recently developed a temperature dependent mean-field EPSC model for L-PBF IN718, to account for

the effects of precipitates. The model predicts the mechanical behavior such as tensile, compression and cyclic deformation of L-PBF IN718 from room temperature to 550°C by integrating dislocation density-based hardening to the crystal plasticity model. The size of the precipitates is modeled implicitly by including anti-phase boundary (APB) formation for the precipitates and the slip resistance, along with Non-Schmid activation stresses and latent hardening. The EPSC model describes a polycrystal as a set of grains with a distinct volume fraction and crystallographic orientation. Each grain in a homogeneous medium is modelled as an elasto-plastic ellipsoid inclusion. The polycrystalline aggregate's constitutive response is assumed to follow a linear relation.

The importance of implementation of Non-Schmid effect in the mechanical performance modeling of AM Nickel-based superalloys, i.e., mean-field EPSC model, is because of two main reasons: (1) γ'/γ"-precipitation hardened Nickel-based superalloys such as IN718 exhibit pronounced tension-compression asymmetry, i.e., they show higher tension yield stress in [001] crystallographic direction (i.e., {111} <001> glide systems) while higher compression yield stress in [011] crystallographic direction ({111} <011> glide systems) [534]; and (2) the AM processing affects the grain structure orientation, i.e., anisotropy, of the Nickel-based superalloys, which has been discussed earlier, with predominant [001] or [110] texture with respect to the build direction. This is because according to the Non-Schmid law, dislocation glide results not only from the resolved shear stress along the direction of slip (Schmid law) but also from shear stresses resolved along directions orthogonal to the slip direction as well as the three normal stress components [535].

The IN718 alloy has a relatively complex microstructure, with many precipitates and carbides within Ni-austenite γ-grain matrix. These precipitates regulate the alloy's mechanical behavior, and the AM processing can influence their volumetric fraction and distribution. In the γ-grain matrix, the plastic deformation occurs in the octahedral {111} <1-10> slip systems. Additionally, at high temperatures, plastic deformation also occurs in the six cubic {111} <110> glide systems [533]. The strengthening γ'-/γ"-precipitates are shearable by dislocations at the anti-phase boundary (APB). An understanding of the APB energy values is important to understand the contribution of precipitate strengthening.

Ghorbanpour et al., [533] calculated the APB energy values for γ′-/γ′′-precipitates and used in the EPSC constitutive relations. Temperature affects the initial slip resistance, and this dependence is established by measuring the material behavior at elevated temperatures. In summary, the model establishes the temperature-dependent initial slip resistance by fitting the mechanical data and not calculating the temperature-dependent APB energy and the shear modulus. As a result, slip resistance varies with temperature, strain and strain rate on individual slip systems [536]. The comparison between simulated and measured mechanical properties of L-PBF IN718 at different temperatures are provided in Fig. 60. The yield stress, flow stress,

and hardening rate are well agreed upon by the model at various temperatures, with the experimental measurements.

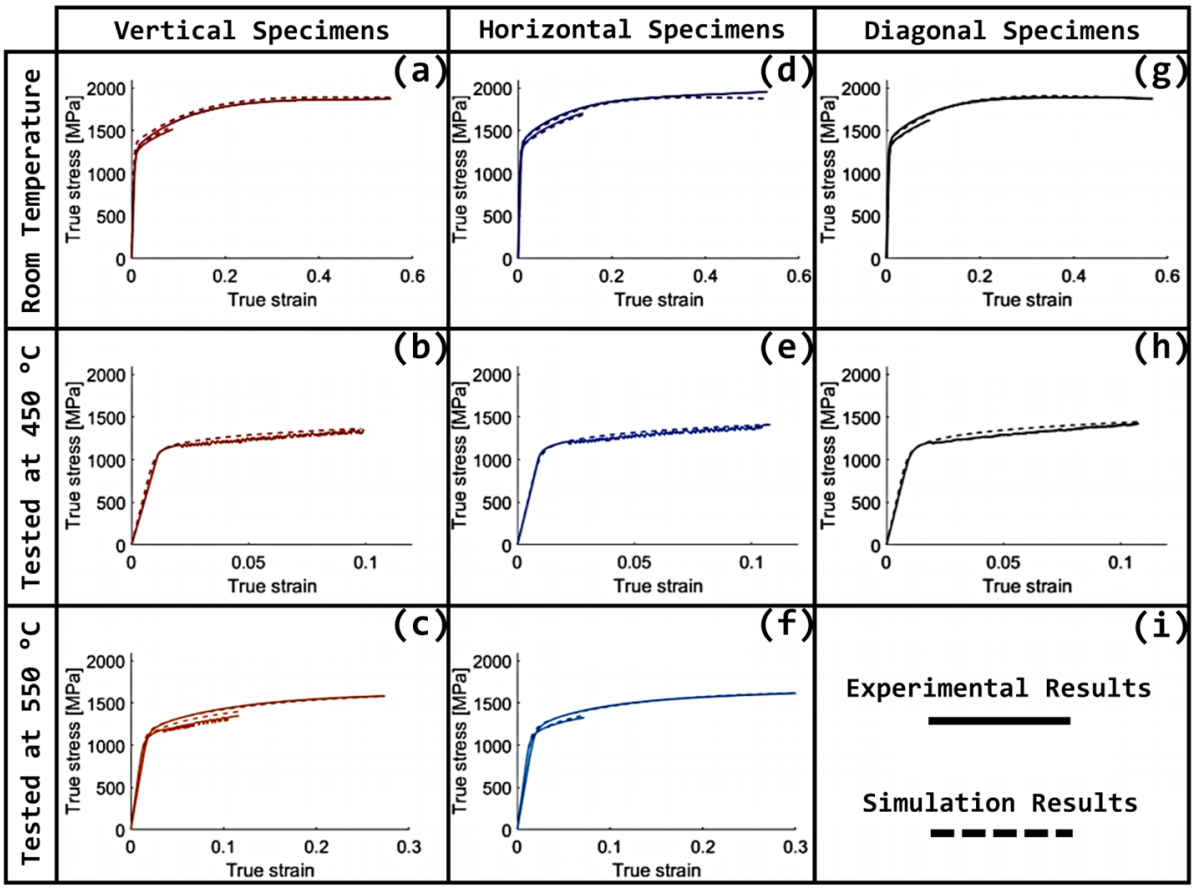

Fig. 60. Comparison of the true stress–true strain responses obtained by experiments and simulation for L-PBF IN718 at different build directions and temperatures [537].

7. Challenges and approaches

7.1. Alloy design

Although limited research has been focused on alloy design specific for AM processed Nickel-based superalloys due to the large time and cost investment associated with the traditional design procedure, several approaches have been conducted that highlight the compositional effects on microstructure and processability. With the combination of several modern research tools, including first principles calculations, CALPHAD based simulations, combinatorial alloy synthesis, and non-destructive characterization techniques, complex alloy compositions that are favorable for AM and also possess favorable mechanical and environmental properties can be developed.

7.1.1. Alloy compatibility

As aforementioned, development of residual strains and cracking during the AM fabrication process is closely associated with the growth of dendrites and secondary phases, so

the material chemistry influenced by the alloy composition would dominate the processability of Nickel-based superalloys by fusion-based AM. The processability of Nickel-based superalloys can be classified based on their characteristic response to high energy density welding. In general, alloys that possess an increased fraction of precipitate-forming elements, such as Al or Ti, generally exhibit poor weldability due to their high susceptibility for hot tearing and cracking during solidification [33]. Since the underlying mechanisms occurring during fusion-based additive manufacturing techniques are similar to those of casting and welding processes, the processability of the AM processed parts can also strongly be correlated to the weldability of superalloys. In recent years, numerous studies suggested that defect formation is unavoidable when processing various commercial, non-weldable superalloys by fusion-based techniques including CM247LC [64], IN939 [221], IN738LC [65], CMSX-4 [66], Mar M-247 [67], Rene 104 [68], and Rene 142 [69], and cracking induced by different mechanisms can be observed simultaneously during the fusion-based AM process [538]. Nickel-based superalloys containing high concentrations of precipitate forming solutes such as Nb, Mo, and Hf and grain boundary elements such as C, B, and Zr tend to be non-weldable as the extreme temperature gradients encountered in all high energy density processes can induce solidification cracking, hot tearing, liquation cracking, ductility-dip cracking (DDC), and strain aging cracking (SAC) as the weld solidifies. As reported by Dye et al. [539], solidification cracking occurs when the volume fraction of solid is in the range of 0.7-0.9. Within this range, the movement of remaining liquid in the weld is hindered by growing dendrites. The insufficient filling of liquid results in void formation that yields additional opportunity for crack initiation as dendrite shrinkages with decreasing temperature. Hence, this phenomenon is more pronounced in non-weldable superalloys as severe segregation between dendritic and inter-dendritic regions could broaden the solidification range and aggravate the susceptibility to crack formation.

Solidification cracking is the main cracking type for solution strengthening Nickel-based superalloys such as Hastelloy X [214,540] and IN625 [541,542] during fusion-based AM process. The solid solution strengthened alloys have Hf, Nb, Mo, and C alloying elements, which form carbide or Laves phase with low eutectic point and increase the solidification temperature range [543]. On the other hand, for the γ′ strengthened superalloys, the solidification cracking is associated with impurity or trace elements such as B [101] and Zr [115]. Although the addition of B and Zr elements improves the creep and stress-rupture resistance by stabilizing the grain boundaries, it was reported that these elements segregated to the inter-dendrite region or grain boundary and decreased the solidus temperature, which lead to the solidification cracking during AM process.

Like the solidification cracking, liquation cracking occurs when high solute content superalloys are heated rapidly to high temperature. According to Henderson et al. [225] and Attallah et al. [544], some secondary phases with low melting point on grain boundaries cannot

dissolve instantly into solid solution due to the rapidly heating rate; instead, they melt directly and form a liquid film along the grain boundaries that act as crack initiation sites as it cannot accommodate the stresses induced by thermal contraction. Moreover, for non-weldable Nickel-based superalloys, the increased driving force to form γ' precipitates leads to the formation of eutectic γ-γ′ pools along the grain boundaries during solidification [545]. This eutectic structure may liquefy if present within the heat affected zone (HAZ) when subjected the heat source, and thereby result in crack propagation along the grain boundaries.

In fusion-based techniques, the rapid cooling rate may potentially inhibit the formation of γ-γ′ eutectic, but the minor elements such as B, Zr, and Si still possess a high tendency to segregate to grain boundaries. The high concentration of these low-melting temperature solutes dramatically lowers the solidus temperature along the grain boundary regime. Consequently, liquation cracking occurs when successive layers solidify. Engeli et al. [65] suggested that the feedstock with high Si content possessed a higher tendency to form cracks. Cloots et al. [115] used atom probe tomography (APT) to conclusively identify that segregation of Zr occurs along grain boundaries in as-built IN738LC processed by L-PBF (see Fig. 61). Similar observations were demonstrated by Chauvet et al. [101] where MB and M_2B type borides were found in the periphery of cracked grain boundary. This finding is also responsible for crack formation reported by Cloots et al. [115], Ruttert et al. [546], and Peng et al. [547]. Due to the characteristic columnar grain structure induced by extremely high cooling condition, residual strains are found to accumulate along these continuous grain boundaries leading to rapid crack propagation. In most of the cases, the cracking of fusion-based AM Ni-superalloy can clearly be observed along the grain boundaries [548].

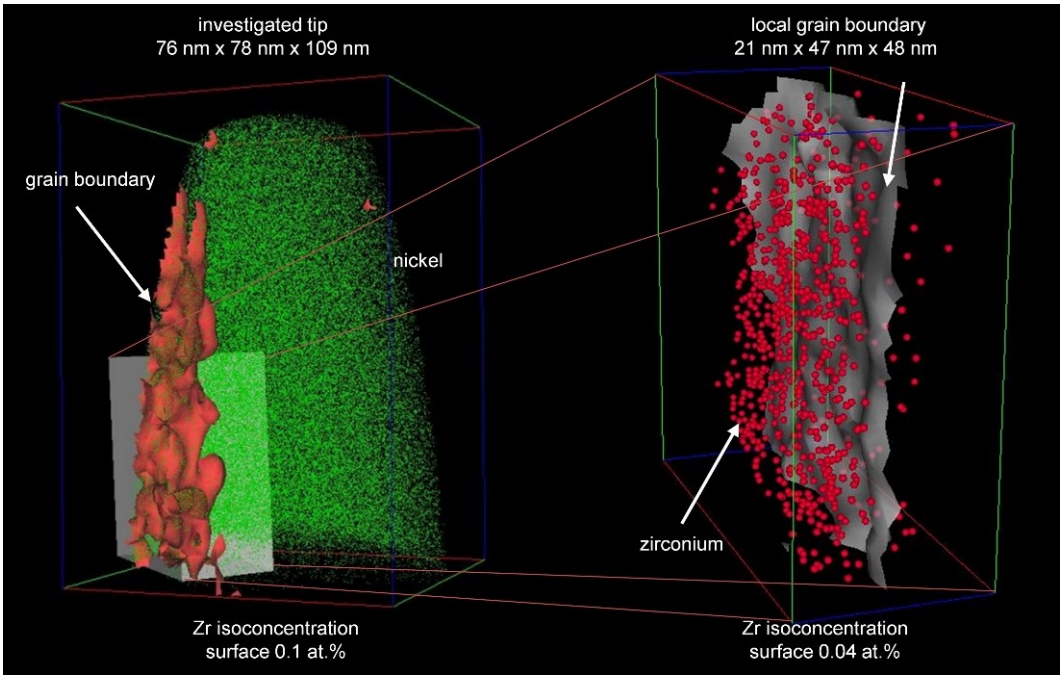

Fig. 61. Isoconcentration surfaces detected and reconstructed by APT and IVAS software. Green dots indicate the Ni atoms while Zr atoms are shown in red color [115].

In addition to the solidification crack and liquation crack, solid-state cracks including DDC and SAC can commonly be found in γ′ strengthening Nickel-based superalloy with high Al and Ti content [548]. Since the borides and carbides were generally found to precipitate along either grain boundaries or cellular boundaries in HAZ during the AM processing, the carbide and boride interfaces are not with the surrounding matrix. Consequently, the residual stresses will lead to the void coalescence along the periphery of these precipitates. Simultaneously, the formation of Hf/W/Ti/Ta-rich precipitates and γ-γ′ eutectic in HAZ will further facilitate SAC and DDC during the processing. The inability of dislocations to glide or climb increases the susceptibility of the alloy for cracking during additive manufacturing [68].

7.1.2. Processability

Sreeramagiri et al. [549] designed a new Nickel-based superalloys "WSU 150" that is capable of being processed by laser metal deposition. In this study, an in-situ technique was utilized by applying powders with high and low content of γ'-forming elements in two powder hoppers so that alloys with different compositions can be built up. The fabricated samples possessed superior tensile properties when compared to Rene 88DT and Haynes 282. A similar method was utilized by Zhou et al. [550]. Since the hot tearing susceptibility is generally proportional to the difference between the liquidus temperature and the eutectic composition melting temperature, and strain-age cracking (SAC) is controlled by the misfit between γ matrix and γ' precipitates, the alloy composition could be selected that is compatible with the AM process. Tang et al. [221] proposed several criteria considering weldability, γ' volume fraction, Scheil freezing range, strain-age cracking merit index, and creep resistance, as shown in Fig. 62.

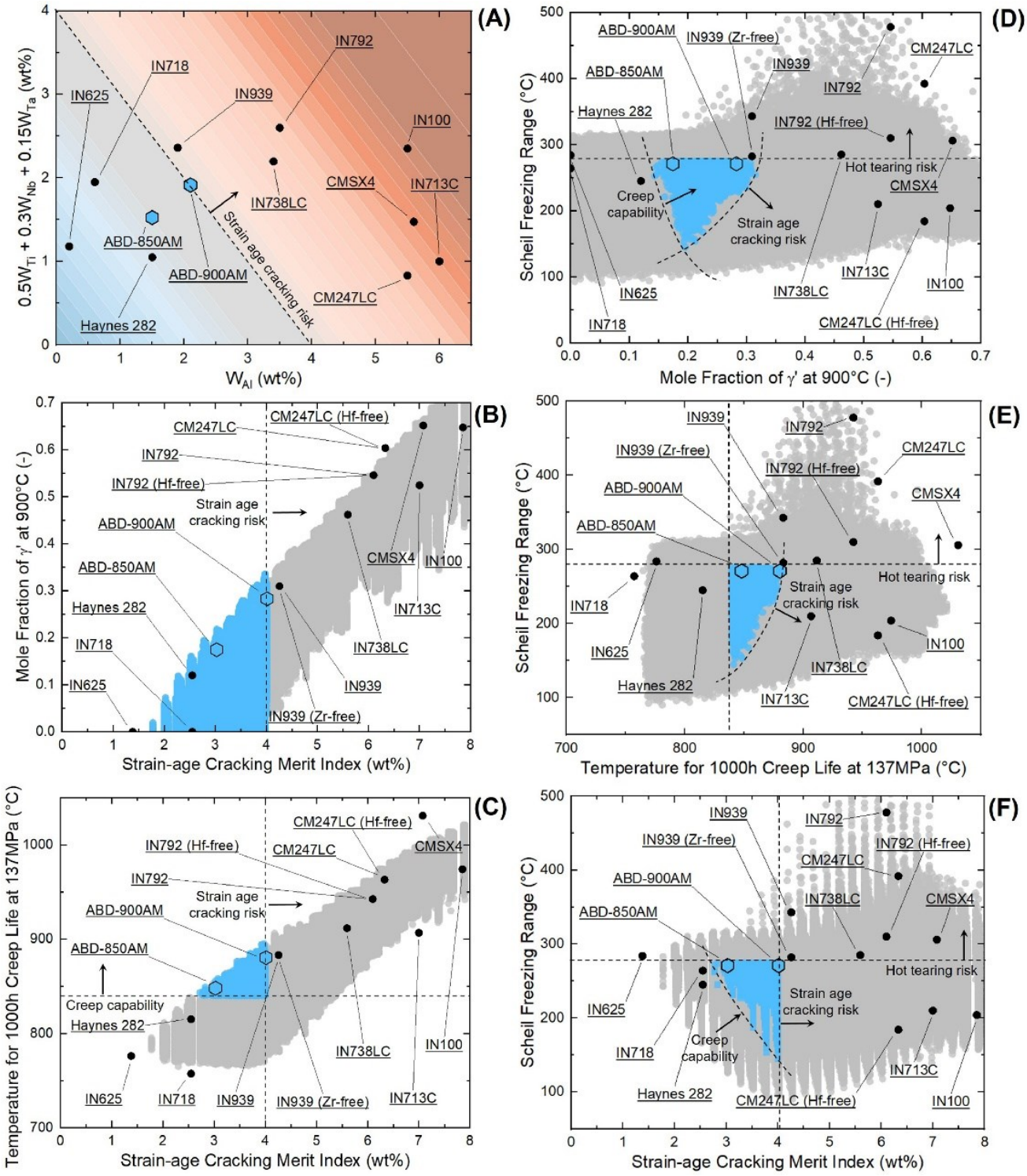

Fig. 62. Computational alloy design spaces used for AM processed Nickel-based superalloy; the corresponding properties of commercial superalloys are also plotted for comparison. In particular, (a) depicts the modified weldability diagram for commercial superalloys; (b) and (c) show the correlation between strain-age cracking merit index and γ' fraction and temperature for creep life of 1000 h with applied stress of 137 MPa, respectively; (d) and (e) presents the magnitude of freezing range in relation to γ' fraction and temperature for creep life of 1000 h with applied stress of 137 MPa, respectively; (f) shows the correlation between strain-age cracking merit index and freezing range. Note that the strain-age cracking and creep merit contours are indicated in each plot. The design spaces where crack-free superalloys with desirable creep capability are achieved are emphasized by blue color [221].

Generally speaking, the need to restrict the solidification range and γ'/γ'' volume fraction that impact the susceptibility to cracking by limiting the elements which promote precipitation hardening should be compromised with mechanical properties. A similar criterion was reported by Shukla et al. [551]. Both physics and experimental data were used to develop the property models that revealed the impact of volumetric change and total strain during solidification on microcrack formation. Other attempts in alloy design for the AM processed Nickel-based superalloys were through the minor adjustment of solute concentration [552]. According to Harrison et al. [14], the crack density of L-PBF Hastelloy X decreased by approximately 65 % with a slight increase of Mo and W. It was demonstrated that this slight modification of Hastelloy X enhanced the solid solution hardening to the flow stress. The strengthened matrix had more capability to impede the crack propagation and dislocation movement, and hence contributed to less susceptibility to stress-induced crack formation and higher tensile strength.

These changes in alloy composition were found to affect the grain structure and phase constitution as well. Cloots et al. [553] demonstrated the effect of compositional change on the grain structure of two distinct Nickel-based superalloys, L-PBF IN738LC and Mar-M509, respectively, as shown in Fig. 63. It could be seen that L-PBF Mar-M509, which contains higher content of Co (~54.7 wt.%,), possessed finer and more isotropic grain structure when compared to that of L-PBF IN738LC with less Co content (~8.3 wt.%) in its composition. The underlying mechanism was ascribed to the reduction of total stacking fault energy (SFE) of the alloy resulting from the excessive Co additions in the L-PBF Mar-M509 alloy composition. Theoretically, materials with low SFE tend to recrystallize while materials with high SFE tend to recover quickly during plastic deformation at elevated temperatures. This is due to the impact of SFE on cross slip mechanisms. As a result, the re-heating process in HAZ only contributes to grain refinement in the L-PBF Mar-M509 whose SFE is lower [553]. Another study carried out by Tang et al. [554] showed that the low SFE associated with the high concentration of Co may inhibit the formation of η precipitates in AM processed Ni-Co base superalloy. With the merits from Co addition, a crack-resistant Co-Ni superalloy was successfully developed by Murray et al. [166] owing to its superior ductility and favorable solute partitioning combined with favorable γ' solvus temperature.

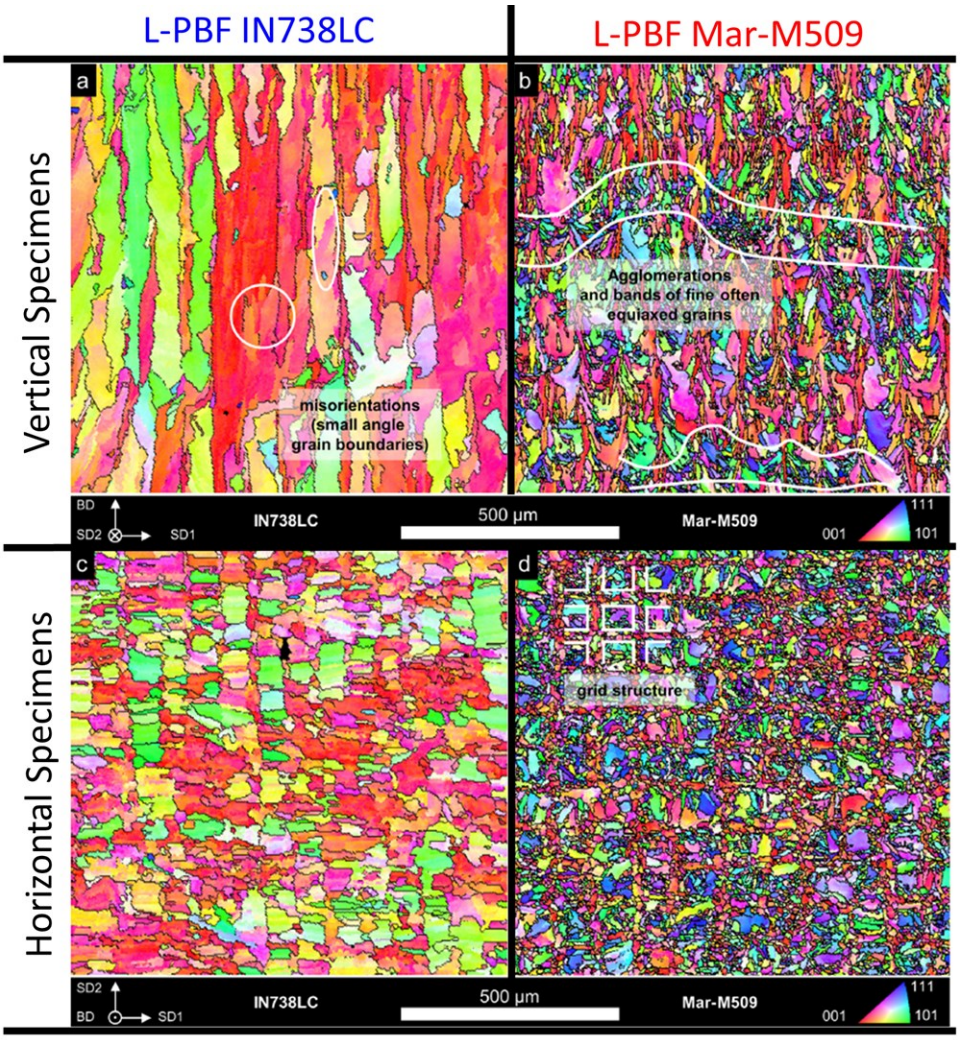

Fig. 63. EBSD IPF Z maps showing the grain structures of L-PBF processed samples fabricated vertically, i.e., parallel with respect to the build direction in (a); and (b) and in transverse direction, i.e., perpendicular to build direction in (c); and (d). Note that (a) and (c) correspond to the microstructure of L-PBF IN738LC while (b) and (d) correspond to that of L-PBF Mar-M509. [553].

Insufficient filling of liquid in dendritic region will lead to solidification cracking. Coniglio et al. [555] summarized the concept of rate of shrinkage (ROS) and the rate of feeding (ROF). Solidification cracking is likely to occur when the ROS value exceeds the ROF value. The ROF value increases with elevated effective feeding pressure while decreases with falling of melt pool temperature. The ROS value, on the other hand, is proportional to the cooling rate and amount of solidification shrinkage. In fusion-based techniques, the comparatively higher cooling rate ranged between 10^3-10^8 K/s imparts a higher ROS value and exacerbates the susceptibility to solidification cracking in non-weldable Nickel-based superalloys. Furthermore, cracks could easily propagate along the continuous grain boundaries as higher magnitudes of strain partition to each individual grain boundary which cannot be accommodated by the liquid film along the solidifying interface [555]. Chauvet et al. [101] further reported that minor precipitates like carbides and borides were more likely to grow along the high angle grain boundaries (HAGB) during processing. This finding was in

agreement with the higher cracking density in grain boundaries with misorientations larger than 15^{o} for non-weldable Nickel-based superalloy processed by E-PBF. The cumulative effects further confine the processing window of Nickel-based superalloys for fabricating the parts without bonding defects or cracks.

Another feature in alloys processed by fusion-based AM process is high magnitude of residual strain. As aforementioned, the residual stains are generated as a result of differential thermal contraction between successive deposited layers, and the formation of the dendritic structure further magnifies the dislocation density due to the formation of geometrically necessary dislocations (GNDs) [240]. Namely, the material systems with high potency to segregate or precipitate such as superalloys possess a higher susceptibility for inducing significant dislocation densities and magnitudes of residual strains. Wang et al. [556] reported that high density of dislocations accumulated around the cellular structure in L-PBF processed CM247LC. Similar microstructures were reported for both non-weldable superalloys [180] and weldable superalloys [183] processed by L-PBF. It could be seen that the complex composition of Nickel-based superalloy increases the susceptibility of AM components to the cracking, which refer to their weldability, and the characteristics of fusion-based AM process further enhances the susceptibility to cracking by high level of thermal contraction and directional heat transfer those accounts for the elongated grain structure and texture.

Inoculants - Another approach to increase the processability of the AM processed Nickel-based superalloys is to add minor amounts of particles as inoculants into the AM alloy powders mixture before fusion. As demonstrated by Hunt et al. [163] and Gaumman et al. [164], the thermal gradient correlates strongly with nuclei density and solid-liquid interface velocity. This correlation was further evidenced by Bermingham et al. [557] and Polonsky et al. [558] as the solute concentration largely enhanced the nucleation density, albeit also increasing the likelihood of solute trapping, leading to restricting the growth of columnar dendritic structure and hence result in more equiaxed structure.

Inoculant particles have recently been reported to facilitate the formation of equiaxed grains and augment the tensile properties of AM processed aluminum alloys [56,559], stainless steels [560], and titanium alloys [557]. The inoculant particles could be any precipitates including oxides, borides, and carbides with high melting point and good coherency to the matrix. The potency of inoculants, i.e., the lower undercooling ($\Delta T_N=4\gamma/(\Delta S_v d)$) {$\Delta S_v$= entropy of fusion; d=inoculant diameter} required for nucleation on inoculants, could be estimated by the lower interfacial energy (γ). In other words, the lattice misfit of the interface directly determines the difficulty to trigger heterogeneous nucleation along a specific orientation on the inoculant particle. To predict this property, Bramfitt [561] defined the planar lattice misfit, which make low index surface of crystal nucleus coincide with low index surface of substrate. For the interface with lattice misfit within 12 %, the nucleating agent would be potent. One

example carried out by Xia et al. [562] has pointed out that TiB_2 and CeO_2 can successfully decrease the grain size of pure nickel whose lattice misfit was estimated to be 6.7 % and 8.4 %, respectively, based on the matching of low index planar interfaces.

Other lattice matching methods with better accuracy such as edge-to-edge matching (E2EM) are usually employed as well. The E2EM model is based on the inverse proportionality between the atomic matching present at a two-phase interface, and the interfacial energy (γ) [563]. The mechanism that maximizes atomic matching between two phases can be extended to heterogeneous nucleation given the solid-solid interface of the nucleus and matrix. For example, Yang et al. [564] predicted the interfacial property between CrFeNb particles and IN718 using E2EM method. It was found that the CrFeNb particles were coherent to the interface of IN718 with a small mismatch when their close-packed planes and directions were aligned under certain correlations, showing that CrFeNb particles are highly potential to act as nucleation sites due to their high coherency to Nickel-based superalloys.

Another factor that determines whether heterogeneous nucleation in solid-state would take place is the size of inoculant particles [565]. Recently, a comprehensive approach to predict the nucleation events on inoculants was conducted by Prasad et Al [566]. Simulations obtained using numerical solidification modeling program (μMatIC) clearly demonstrated that the activation of inoculants is correlated to both the required undercooling (ΔT_N) as well as the processing conditions such as thermal gradient (G) and solidification rate (or solid-liquid interface velocity, V). In summary, at large cooling rate, i.e., higher solidification rate (V), the columnar growth was successfully suppressed with more nucleation events on inoculants with larger ΔT_N, albeit the negative effect from large thermal gradient (G). The underlying mechanism is attributed to a reduced degree of solute trapping combined with solute diffusion and thermal undercooling generated by the "lag" in growth rate (V) of dendrite tips and theoretical diffusion rate of solute elements at the growing solid-liquid interface. Thus, instead of constitutional/compositional undercooling driven by solute diffusion, thermal undercooling becomes dominant and facilitates heterogeneous nucleation on inoculants with higher potency when high cooling rates are present. Prasad et al. [566].have further shown that their results are also consistent with the results of "Interdependence Model" that present a decreased size of nucleation free zone (NFZ) with increasing cooling rate. Thus, the selection of inoculants and the processing conditions is crucial to improve the inhomogeneous grain structure and anisotropy within AM processed Nickel-based superalloys.

Another example of grain refiner inoculants is the $CoAl_2O_4$ particles that were commonly used to promote equiaxed-grained structure in the investment cast Nickel-based superalloys such as the MAR-247 [567], IN100 [567], and IN713C [568]. Interestingly, these particles did not directly act as the heterogenous nucleation sites for the melt during solidification; instead, a chemical reaction between the $CoAl_2O_4$ particles and elemental Cr, Ti, and Al in the liquid alloy leads to the formation of elemental Co or CoAl intermetallic phases that possess a high

coherency to the Ni-austenite γ-grain matrix [568]. Furthermore, as reported by Ho et al. [569], the Co and CoAl particles both possess higher melting temperatures than IN718; leading to the possibility that solid Co or CoAl particles are capable of surviving in the melt and aiding in the nucleation of equiaxed grains. They have reported [569] that the $CoAl_2O_4$ inoculants can facilitate formation of equiaxed grains in L-PBF IN718, leading to a more homogeneous grain structure that was evidenced by the elimination of elastic anisotropy. Moreover, these particles were also found to impede the movement of grain boundaries and dislocations. The comparatively finer grain structure strengthened by dispersed oxide particles yielded superior tensile strength and creep resistance in IN718 with addition of $CoAl_2O_4$.

Composites - In addition, studies have shown the superior compressive strength and wear resistance in Nickel-based superalloys metal matrix composites (MMCs) fabricated by L-PBF process, such as graphene/IN718 [570], TiC/IN718 [571], TiC/Hastelloy X [572], WC/IN718 [573], Y_2O_3/Ni-8Cr-5.5Al-1Ti [574], etc. Ho et al. [575] and Rong et al. [576] identified the nucleation and growth of new grains around the micron-sized WC/W_2C eutectic particles within L-PBF IN718 attributed to the inter-diffusion layer that improved the wetting behavior of WC/W_2C particles and therefore enhanced the coherency between these inoculants and the IN718 alloy melt, as illustrated in Fig. 64(a)-(b). Similar studies were conducted for IN718 MMCs reinforced with NbC/TiC "flakes" [577]. It was found that finer grain structure and dendritic cells were obtained with 0.5 wt. % to 5 wt. % of TiC or NbC reinforcements that accounted for superior yield strength at room temperature and lower steady creep strain rate. Furthermore, Hong et al. [578] observed a coherent interfacial layer with the thickness of 0.8–1.4 μm formed between TiC particles and the matrix in the IN718 MMCs fabricated by L-PBF process, which was identified as (Ti,Nb,Mo)C (see Fig. 64(b)-(c)).

Another significant advancement on the columnar-to-equiaxed transition (CET) was achieved in the LP-DED IN625 [579] and Hastelloy X [580] using the micron-sized or submicron-sized TiB_2 particles. Owing to their lattice misfit of 6.7 % and high melting temperature above 3000 °C, the TiB_2 particles can survive the Nickel-based superalloys melt and facilitate the grain refinement leading to reduced grain aspect ratio and fine grain structure, ultimately. Furthermore, the improved texture and subsequent elimination of micro-cracks were also found to greatly improved the mechanical properties. According to Zhang et al. [167], the L-PBF Hastelloy X/TiB_2 MMCs exhibited an increase in both tensile elongation and ultimate strength (UTS) by 1.16 % and 200 MPa, respectively. Similar results were observed in L-PBF Hastelloy X/TiC addition [572]. It is believed that the increase in the number density of grain boundaries and TiB_2 help inhibit the crack propagation and hence reduce the cracking density.

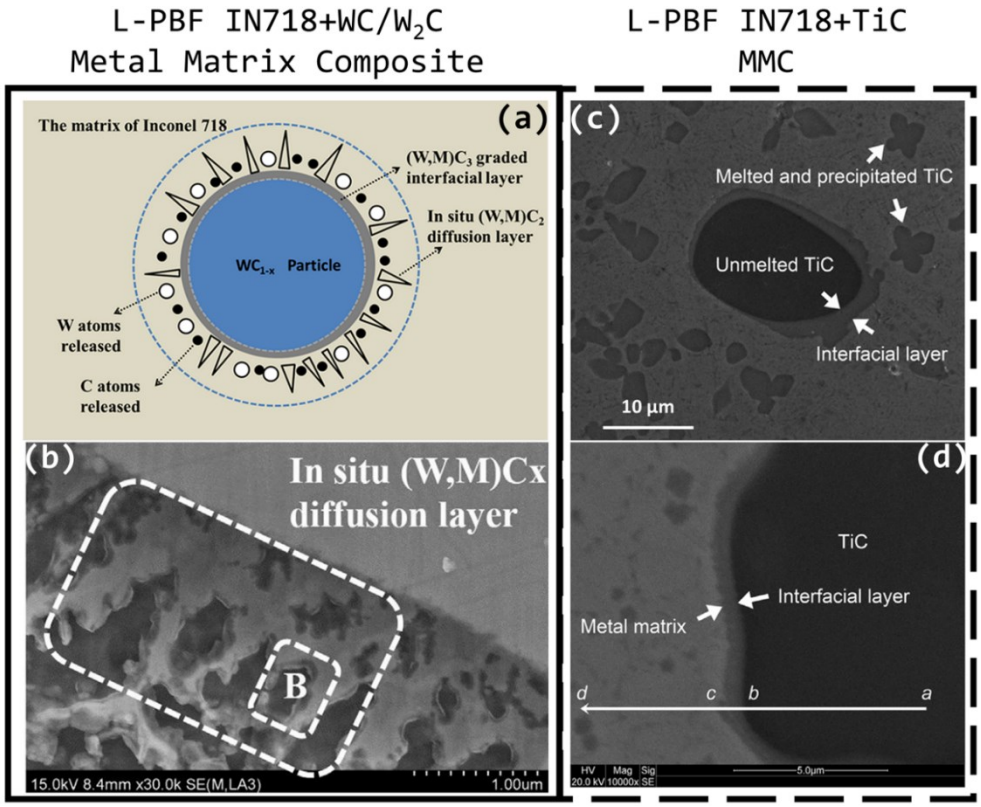

Fig. 64. IN718-based metal matrix composite (MMC) fabricated by L-PBF process (a) schematic illustration of inter-diffusion between WC/W_2C particles and IN718 matrix [576]; (b) corresponding SEM image for (a) obtained experimentally; (c) and (d) SEM micrographs showing the interfacial layer between TiC particle and IN718 matrix [578].

In summary, the use of inoculants could potentially influence microstructure evolution and hence improve the inhomogeneous grain structure as well as mechanical performance. However, the large addition such as 5 vol. % may still cause the ductility drop [581], and the interactions between inoculant particles and the melt pool can result in significant changes in melt pool physics. In the system of pure Ni/Al_2O_3 nanocomposites prepared by Ma et al. using laser manufacturing [582], the nano-oxides were found to reduce the thermal conductivity while increase the viscosity of the system, thus reducing the Marangoni convection and leading to deeper penetration of melt pool while inhibited heat-affected zone (see Fig. 65). Chang et al. [581], on the other hand, presented an opposite result showing that the depth of melt pool during L-PBF processing was decreased from 223.4 µm to 139.4 µm with 5 wt. % addition of micron-sized NbC particles in IN718 metal matrix composite. Although not explicitly reported, it is believed that the un-melted particles might have rebounded to the surface leading to instability of the melt pool that is revealed by the formation of balling morphology with shallow penetration [583].

In addition, agglomeration may occur during the laser additive manufacturing due to the particle migration triggered by intense Marangoni convection and the difference in density between inoculant particles and matrix powders. This has been already confirmed by TiC reinforced Al matrix nanocomposites fabricated using L-PBF process [584]. Similar

observation was reported in IN718/$CoAl_2O_4$ processed by L-PBF [104]. The agglomerated particles larger than 100 μm were characterized even though the initial particle size of $CoAl_2O_4$ was less than 10 μm; larger number of agglomerated particles were found when the applied energy densities increased from 31 J/mm^3 to 55 J/mm^3. The correspondence of agglomeration to energy densities was also reported in Ni-Cr-Al-Ti alloy with 0.5 wt. % of Y_2O_3 addition [574]. The strong affinity between Y_2O_3 and Al led to the formation of $Y_4Al_2O_9$ slag that agglomerated afterwards attributed to the Marangoni convection, thus leading to a reduced density at similar processing conditions. Therefore, the selection of inoculant particles and the fraction of added inoculants still need proper investigation in order to optimize the final properties.

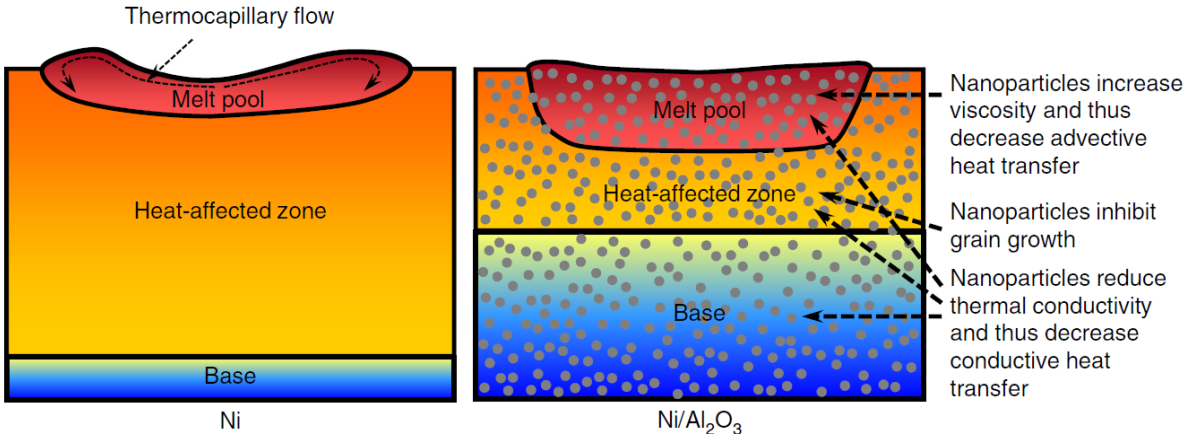

Fig. 65. Schematic illustration showing the mechanisms for melt pool modification by nanoparticles during laser melting of Ni/Al_2O_3 nanocomposites based on the research conducted by Ma et al. [582].

7.2. Microstructure

7.2.1. As-fabricated

Inhomogeneous grain structure - The nature of fusion-based AM processes accounts for the inhomogeneous grain structure and predominant [001] or [110] texture with respect to the build direction. This anisotropic property directly induces negative effects on the mechanical behavior in many respects. Carter et al. [265] reported that L-PBF processed CM247LC revealed an extremely high density of cracks in fine-grained regimes attributed to high fraction of high angle grain boundaries (HAGB). Tucho et al. [585] found that L-PBF processed IN718 exhibits approximately 13% difference in hardness along the build direction attributed to non-uniform distribution of precipitates and inhomogeneous grain structure. This finding was in agreement with previous reports carried out by Tian et al. [174] in DED processed IN718 and Kirka et al. [586] in IN718 fabricated by E-PBF. Furthermore, the inhomogeneous microstructure also impacts the anisotropy of mechanical performance. Numerous studies have demonstrated that the horizontal samples (i.e., load direction is perpendicular to build direction) possessed a superior tensile strength and elastic modulus along the transverse direction (i.e., perpendicular to build direction) as compared with those of vertical specimens (i.e., load direction is parallel to the build direction) for AM Ni-base superalloys including IN718 [587],

CM247LC [588], and IN738LC [553] at room temperature. Cloots et al. [553] suggested that the tensile load direction corresponding to the building direction contributes to the least elastic modulus due to preferred [001] orientation; the higher fraction of grain boundary area in the transverse section yields superior tensile strength owing to the Hall-Petch effect. Similar findings were proposed by Trosch et al. [170] where the coupling of columnar grain growth and layered structure contributed to the variation of tensile strength and ductility. In addition to grain structure, the crystallographic texture plays an important role on tensile properties. As demonstrated by Ni et al. [492], samples that possess predominant [001] texture in the vertical section will lead to a higher value of Schmid factor when an axial load along the building direction is applied. Similar results were reported by Yu et al. [589] that Hastelloy X processed by L-PBF presented a lower yield strength at both room and elevated temperatures attributed to predominant [110] texture that is can be activated easily in fcc crystal structure. Sun et al. [308] further elucidated the influence of crystallographic texture through the tensile testing for E-PBF processed IN718. It was found that the yield strength of as-built IN718 was observed to possess the maximum value as the deviation between the loading axis and build direction approached 55° that exhibited the smallest Schmid factor. Similar correlation was reported by Chlebus et al. [590] in L-PBF processed IN718. The anisotropic tensile properties still persist, albeit slightly reduced upon heat treatment. This is because the subsequent heat treatment does not eliminate the existing crystallographic orientation of the grains nor the distribution of carbide phases [587]. Furthermore, the anisotropic behaviors are not limited to the tensile properties. Seifi et al. [406] proposed that the L-PBF processed IN718 revealed the superior fatigue threshold along the transverse direction attributed to the more equiaxed-grained structure. Kuo et al. [443] reported that IN718 fabricated by L-PBF exhibited anisotropy creep rupture life as δ precipitates closely aligned with grain boundaries would provide the initiation sites of crack during the creep test. Simultaneously, it was found that the columnar-grained structure reduced the creep strain rate along the transverse direction as diffusion is more pronounced along the grain boundaries. The creep tests performed by S. Sanchez et al. [425] have shown that the vertical specimens of L-PBF IN718 had a 144% and 70% longer creep life than the horizontal specimens and 45°specimens after the AMS 5662 standard heat treatment. Similar results were proposed by Kirka et al. [591] showing superior creep rupture life along the build direction. A larger fraction of grain boundary area along the transverse direction promoted intergranular fracture resulting in decreased creep rupture life.

Stress-induced phase transformation - The characteristically high residual stress induced by AM process not only facilitate crack propagation but also can induce microstructural changes in the built parts. It has been found that the coupling of residual stress and micro-segregation may lead to unexpected phase transformations upon heat treatment. This phenomenon was commonly reported in Nickel-based superalloys strengthened by γ”

precipitates such as IN718, IN625, and IN718 Plus. Zhang et al. [503] estimated the incubation time for δ formation in L-PBF processed IN625 is less than 5 min, which is two orders of magnitude lower when compared to wrought IN625, through the in-situ XRD measurements. Another finding demonstrated by Li et al. [592] revealed that more pronounced phase transformation of γ/γ'' → δ in IN718 took place in inter-dendritic region where higher concentration of Nb was identified (see Fig. 66a-b). Idell et al. [593] used Thermo-Calc simulations to estimate the niobium isopleth for IN718 Plus and found that the δ formation only occurred when Nb concentration was greater than a certain value at designated temperature. The underlying mechanism by which δ phase formed earlier in these studies can be ascribed to the same mechanisms of δ phase formation in conventional wrought IN718. Generally speaking, the growth of γ'' precipitates would occur prior to that of δ phase during heat treatment as the growth of δ phase increases the overall interfacial energy due to the incoherent interface between δ phase and γ matrix [594]. Nonetheless, the micro-segregation of Nb to the inter-dendritic regions induce the growth of δ phase, and the residual strains contribute to triggering the nucleation of δ phase. As a result, the metastable γ'' phase does not form as the δ phase forms directly with its long axes aligned with $\{111\}_\gamma[1\bar{1}0]_\gamma$ [595]. This conversion reaction was also confirmed by Probstle et al. [185], Strobner et al. [596], Trosch et al. [170], and Mostafa et al. [157] in AM processed IN718, as well as Dinda et al. [125] and Lass et al. [597] in AM processed IN625.

The unexpected phase changes significantly undermine some mechanical properties of AM processed parts, even though no crack is found in microstructure. Trosch et al. [170] reported that the L-PBF processed IN718 underwent a ductility drop at temperature above 450 °C, and this is partly due to the higher fraction of δ-phase distribution within the inter-dendritic region. Kuo et al. [183] further reported that the needle shape δ phase with incoherent interfaces with the IN718 matrix contributed to inferior creep rupture life in both L-PBF and E-PBF processed specimens when compared to those fabricated by conventional cast and wrought processed following the final-heat treatment. This behavior was in a good agreement with microstructure of ruptured samples that revealed a continuous δ phase inducing coalesce of voids in order to release excess strain energy (see Fig. 66c) [443]. Therefore, managing the sequence of phase transformations becomes another limitation when fabricating Nickel-based superalloys.

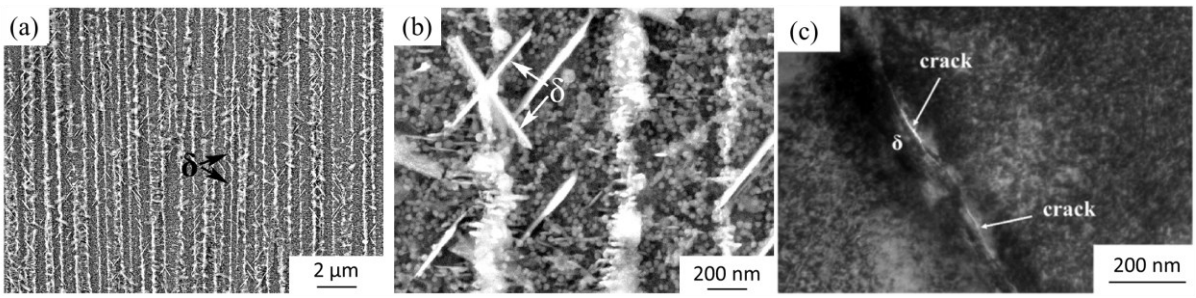

Fig. 66. SEM images showing the needle-like δ precipitates distributed in inter-dendritic region upon heat

treatment under (a) lower and (b) higher magnifications [592]. (c) TEM microstructure of an STA specimen after creep test showing crack and needle-like δ precipitate [443]. Samples were manufactured by L-PBF IN718 alloy.

7.2.2. Heat treatments

In addition to optimization of processing parameters, the optimization for heat treatments could also partially improve the performance of AM processed Nickel-based superalloys. A more homogeneous microstructure can be achieved when proper heat treatments are applied, which in turn can improve the anisotropic properties including tensile strengths and elastic modulus [587]. An appropriate heat treatment could also inhibit the unexpected phase transformation induced by micro-segregation and residual strains. Probstle et al. [185] and Li et al. [592] demonstrated how various heat treatments influence the phase constitution in the L-PBF IN718, as shown in Fig. 67 [592]. Since the solvus temperature of δ phase is approximately 1010 °C [598] in IN718, the heat treatment above 1010 °C dissolved the δ phase and homogenized the micro-segregation. As a result, Nb atoms were released as solid solution atoms into Ni-austenite γ-grain matrix, which in turn provided a higher driving force for γ'' precipitation. When the heat treatment is performed at temperatures below 1010 °C, on the other hand, this promotes the direct formation of δ phase in the Nb-rich regions of the microstructure at the expense of γ'' precipitates. The control of δ phase significantly impacts the creep properties of γ''-strengthening Nickel-based superalloys. Probstle et al. [185] suggested that the minimum creep strain rate decreased with decreasing fraction of δ phase in L-PBF IN718 upon solution-heat treatment and aging as the growth of δ phase occurs at the expense of the γ'' phase. Brenne et al. [331] adopted a similar heat treatment condition that led to a consistent conclusion. In addition to the creep strain rate, the creep rupture life could be also influenced by δ phase that induces stress concentration. Kuo et al. [443] reported that the creep rupture life of L-PBF IN718 can be improved by eliminating the heat treatment at 980 °C where the highest precipitation rate of the δ phase occurs. Nonetheless, the mechanical properties of AM Nickel-based superalloys may still differ when compared with those of wrought alloys as the distribution of δ phase or carbides within these two materials will vary. The distribution of these phases within the respective microstructures cannot be altered significantly during the heat treatment and these phases can impede the movement of grain boundaries, leading to retained texture and inhomogeneous grain structure. Even though supersolvus heat treatments are applied, the lack of the precipitates that stabilize the grain boundary may undermine the creep resistance at elevated temperatures [599]. Therefore, the optimization of processing parameters and modification of alloys are still required for better performance.

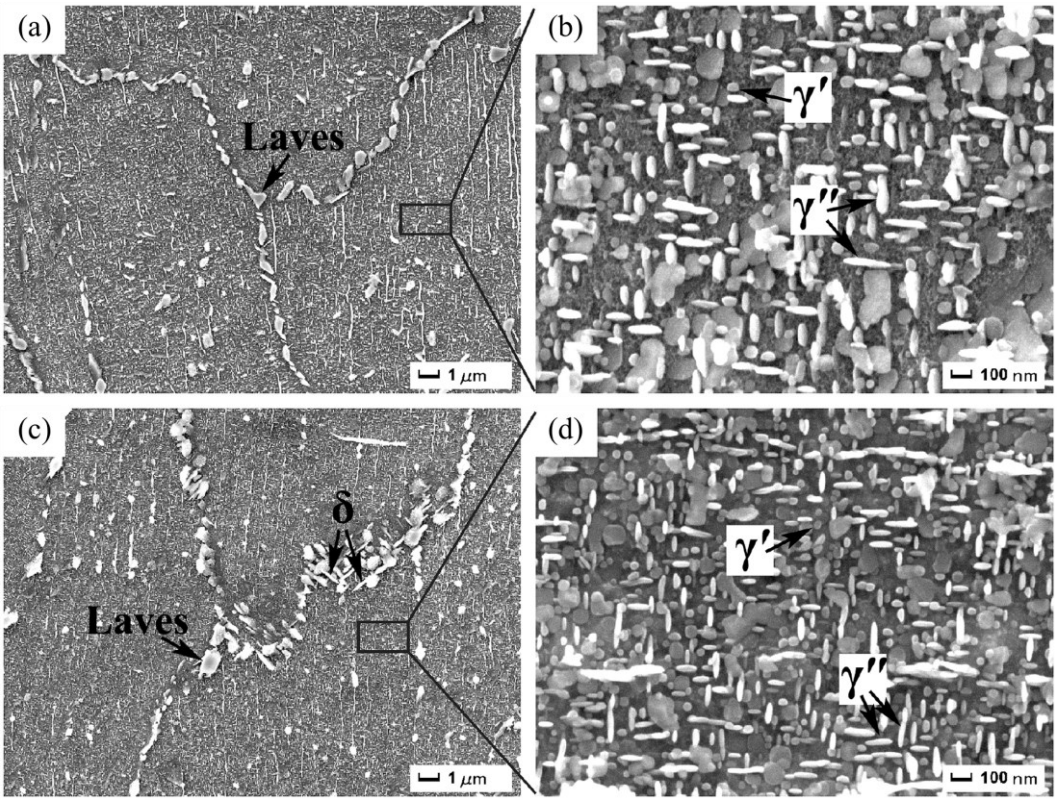

Fig. 67. SEM micrographs showing the microstructures of L-PBF IN718 subjected to solution heat annealed at 1065 °C in (a)-(b) and 980 °C in (c)-(d), respectively, followed by aging [592].

Although one of the primary purposes of heat treatments, including hot isostatic pressing (HIP) and other heat-treatments, is to consolidate the part and eliminate undesirable microstructures that are present through the building process. It should be noted that, however, other defects may appear that undermine the performance of the parts. Zhao et al. [600] explained the presence of long grain boundary cracks surrounded by carbide precipitates cannot be eliminated due to the severe segregation of carbon to grain boundaries. Peng et al. [547] also identified the reappearance of cracks in HIPed DZ125 Nickel-based superalloy during the heat treatment as revealed by the increasing crack ratio shown in Table 5. The cracked region exhibiting features of a residual liquid film, implies that heat treatments cannot eliminate all of the cracks induced by E-PBF [547]. Under the considerations of grain morphology, on the other hand, the supersolvus heat-treatment can promote the formation of homogeneous grain structure and remove the texture. As a trade-off, however, the excess grain growth may lead to reduced ductility and yield strength simultaneously [601].

Table 5. Summary of the spacing, average size, and volume fraction of γ' precipitates as well as the crack ratio for E-PBF processed DZ125 upon fabrication, HIP, and solution and aging heat-treatment (STA). Note that CCG and FCG stand for the comparatively coarser and finer grain size in as-built samples [547].

Sample ID	Condition	γ channel width (μm)	Average γ' size (μm)	γ' (vol %)	Crack ratio (%)
CCG	E-PBF	0.06±0.02	0.31±0.04 (core)	64	2.6

			0.06±0.02 (boundary)		
	E-PBF +HIP	0.19±0.06	1.31±0.08	67	1.29
	E-PBF +HIP+STA	0.06±0.01	0.64±0.05	76	5.69
FCG	E-PBF	0.05±0.02	0.33±0.06 (core) 0.47±0.09 (boundary)	70	2.72
	E-PBF +HIP	0.20±0.08	1.26±0.09	64	1.03
	E-PBF +HIP+STA	0.07±0.02	0.69±0.07	75	4.93
Cast DZ125	As-cast	0.09±0.04	0.61±0.07	66	N/A
	Cast+STA	0.05±0.01	0.54±0.03	77	N/A

7.3. Approaches

As discussed earlier, the grain structure of AM processed Nickel-based superalloys is largely dependent on the thermal history experienced during the AM fabrication processes such as thermal gradient [602], cooling rate [603], and melt pool morphology [604], all of which subsequently control the direction of epitaxial grain growth. It has been a well-established fact that the thermal history experienced during the AM fabrication is a complex function of interactive variables including all processing parameters.

7.3.1. Anisotropy

In addition, the melt pool morphology that may change with different applied scan parameters could influence the grain structure. According to the welding theories [605], the solidification rate (V) with respect to the melt pool boundary can be approximated by the curvature of the melt pool. In particular, the deeper melt pool penetration enables the solidification along with the scan direction and therefore maximizes the solidification rate. This correlation was also observed in other studies on scan parameter optimization for AM processed Nickel-based superalloys [165,278,547].

It should be noted that, however, the above discussion was generally based on the steady-state columnar-to-equiaxed transition (CET) model that assumes a constant solidification direction ahead of the solidification front. Thereby, the actual solidification occurring during the E-PBF process that can be affected by overlapping of subsequent layers or tracks, may not be considered in the model. This argument can be validated by the solidification map simulated by analytical transient modeling (ATM) and corresponding EBSD observations for three distinct scanning conditions used in E-PBF processed Alloy 713ELC, a non-weldable Nickel-based superalloy, which is shown in Fig. 68 [606]. Although the majority of solidification profile for E0 fabrication conditions was located in the columnar regime due to the moderately increased thermal gradient (G) caused by reduced energy density (see Fig. 68(a)), each melt layer was found to be highly overlapped by 2∼3 adjacent tracks along an opposite direction leading to less pronounced directionality of G that impeded the epitaxial growth owing to non-steady state CET (see Fig. 68(b)). The spacious variations in G incorporated with moderately

high solidification rate (V) thereby accounted for the equiaxed grain structure with more dispersed texture in samples processed by E0 (see Fig. 68(c)). The study affirmed the importance of modification of melt pool geometries via not only the process parameters but also the hatching geometries.

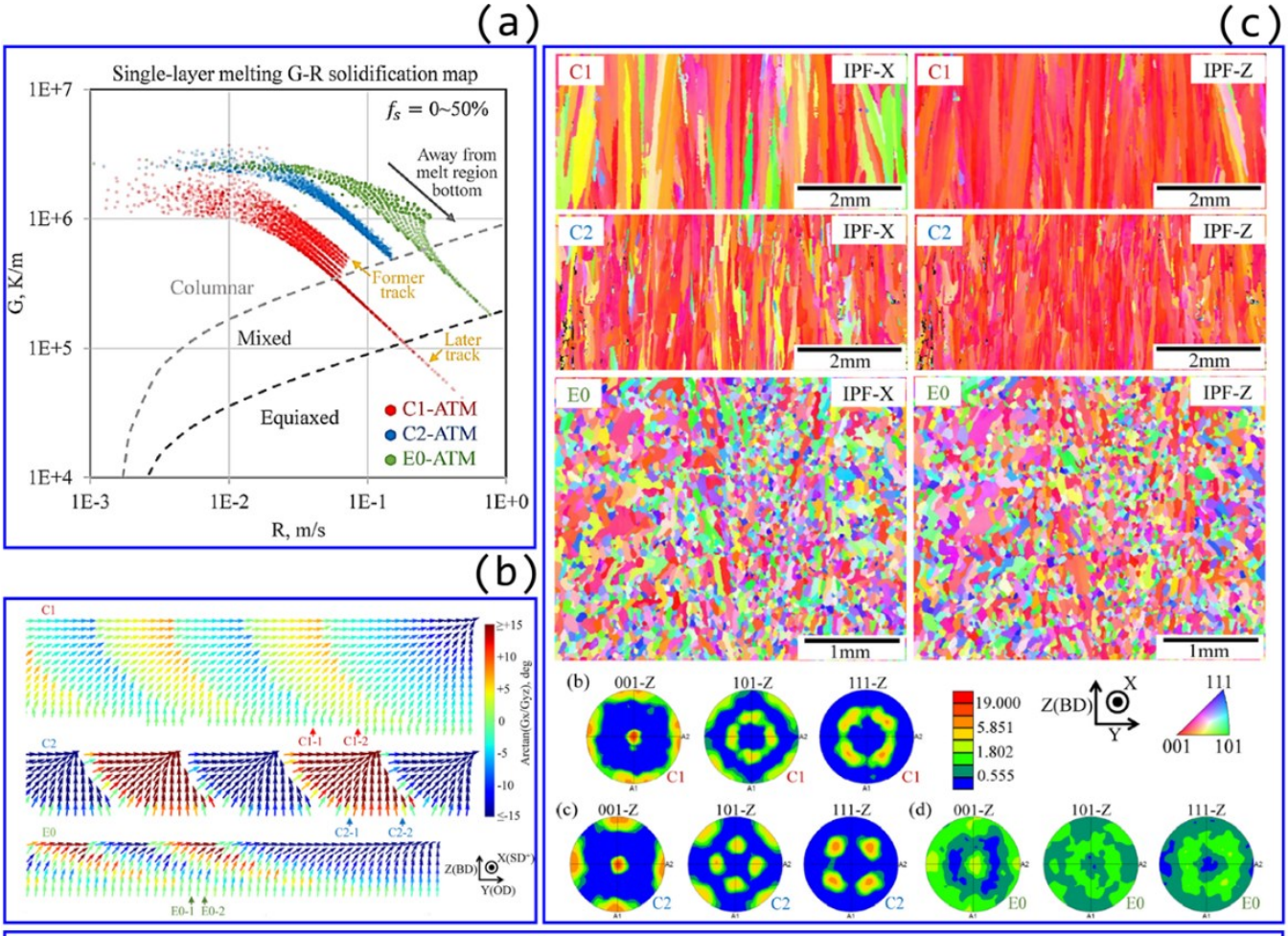

	I, mA	V, mm/s	FO, mA	LO, mm	Line order	γ_b, µm
C1	9.4	500	18	0.18	11	400
C2	2	150	3	0.23	7	260
E0	4	800	30	0.08	50	540

Fig. 68. (a) Solidification map simulated by application of analytical transient mode (ATM) for three distinct scanning conditions used in EBM processed non-weldable superalloy Alloy 713ELC. The arrow plot showing the spatial variations of thermal gradient (G) vectors for each scan condition are shown in (b). The scan parameters C1, C2, and E0 are provided in the table below where I, V, FO, LO, and γ_b denote current, scan speed, focus offset, line offset, and nominal beam radius, respectively. The layer thickness and preheating temperature were controlled under 100 µm and 1000 °C, respectively. The EBSD maps and corresponding pole figures for samples processed by C1, C2, and E0 are provided in (b) [606].

Since the higher energy density normally produces melt pools with a higher depth/width ratio, this would further facilitate the equiaxed grain structure[165]. As shown in Fig. 69, the grain structure in the E-PBF DZ125 alloy [547] has changed gradually from columnar to equiaxed with increasing energy density [547]. Furthermore, it has been found that the scan strategy may affect the crystallographic texture in Nickel-based superalloys. Geiger et al. [607]

have showed that the rotation of the scan pattern reduced the crystallographic texture within L-PBF IN738LC because it enhanced the randomness of melt pool morphologies . Liu et al. [608] also reported that the change of scan direction interrupted the growth of columnar grains along the build direction between successive layers and hence led to a more equiaxed grain structure. Plotkowski et al. [609] have reported that the scan strategy with a short dwell time favored columnar grain growth while that with a longer dwell time favored equiaxed growth due to the significant variation on thermal gradient. The subsequent change in crystallographic texture due to different scan strategy was found to impact the mechanical performance after the heat treatment. Sanchez et al. [425] have reported different the creep rupture life from 320 h to 507 h for the L-PBF IN718, when processed using stripe scan strategy and meander scan strategy, respectively, because the larger laser overlapping zones in the former contributed to an increase in area fraction of δ precipitates by 0.19 % where equiaxed grains were observed.

The control of the columnar-to-equiaxed-transition (CET) through processing parameters was also applied to fabricate directionally solidified (DS) Nickel-based superalloys or single crystal (SX) Nickel-based superalloys. Yang et al. [160] have reported a fully columnar grain structure with minimal levels of misorientation obtained in L-PBF SRR99 by increasing the ratio of G and V with appropriate scan parameters. Chauvet et al. [610] also demonstrated that a single crystal (SX) CMSX-4 could be achieved without the use of seeds and only by tuning the energy density to a desirable value at which the grain growth aligned with [001] direction is dominant.

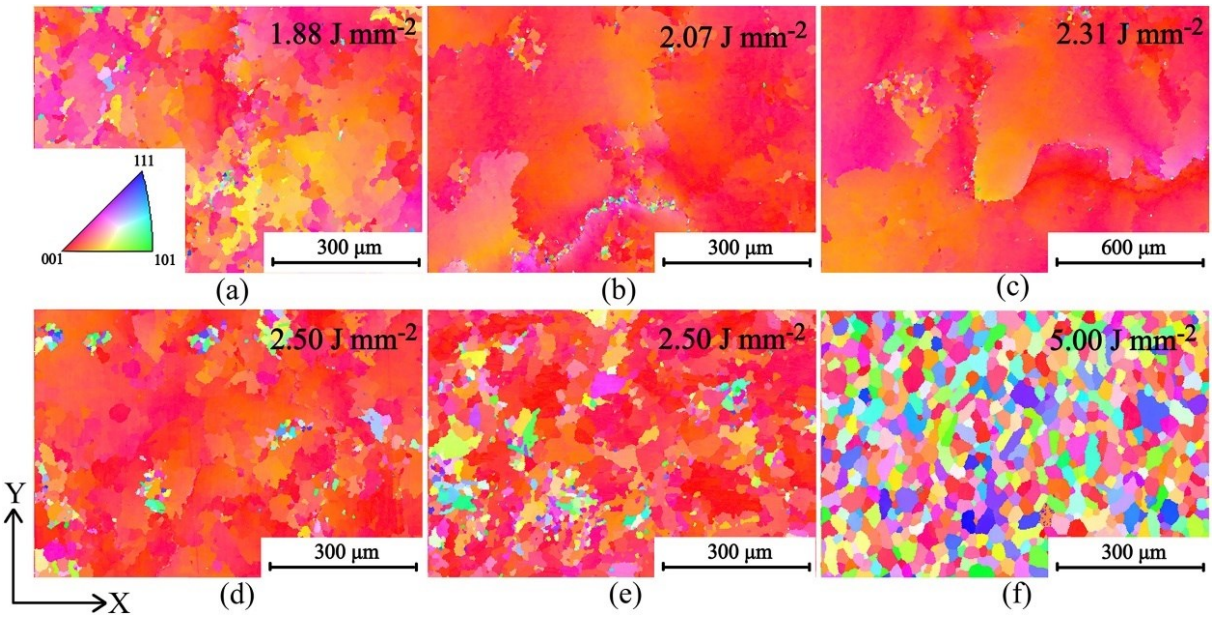

Fig. 69. EBSD IPF Z maps showing the microstructures of E-PBF processed DZ125 Nickel-based superalloy with energy densities of (a) 1.88 J/mm^2; (b) 2.07 J/mm^2; (c) 2.31 J/mm^2; (d) 2.50 J/mm^2; (e) 2.50 J/mm^2; (f) 5.00 J/mm^2 [547].

Potential advantages of heterogeneity in microstructure. Compared to dissimilar welded structures with a sharp interface, as-fabricated AMed Nickel-based superalloy with a gradient

microstructure can be a better choice to permit a smooth transition of properties. Combination of a high surface hardness with adequate wear resistance and a soft core to absorb stresses without cracking can result in a high fracture resistance in functionally graded materials (FGMs) processed by the fusion-based AM. For instance, a turbine blade manufactured by AM process to achieve a FGM with heterogenous microstructure can results in high surface hardness which impedes fatigue growth of surface cracks.

7.3.2. Defects

The process induced features that will lead to crack propagation and inferior mechanical properties can be also mitigated through the process optimization including scanning parameters, scanning strategy, and in-situ process control. Carter et al. [114] attempted to find the correlation between energy density and defect formation by applying a range of scan speeds, laser powers, and hatch distances for L-PBF IN718, IN625, CM247LC, and CMSX486, respectively. It was observed that a clear threshold of high energy density could be found where LoF defects and porosities were inhibited. This energy density threshold seemed to be independent of the alloy composition. Similar findings were reported by Collins et al. [611]. As for the crack density, no clear relationship with energy density was found, indicating that cracking behavior has larger dependence on the individual scan parameters. Generally, high laser powers and low scan spacings result in a high crack density while high scan speeds and scan spacings result in low crack density based on present studies [114]. Interestingly, these parameters seemed to have some coupling effects on cracking density and void fraction. Carter et al. [219] found in another study that the dependence of crack density and porosity in L-PBF CM247LC became more pronounced when greater scan speed and hatch distance (scan spacing) were used. Moreover, it has been observed that the scan strategy and intensity distribution of laser beam could influence the properties of built parts. Carter et al. [265] had further reported in another study that L-PBF CM247LC presented less cracking density when simple “back-and-forth” strategy was used due to less misorientation between grain boundaries, albeit more severe crystallographic texture. Another study carried out by Cloots et al. [115] revealed that using a doughnut profile as the intensity distribution of laser beam could reduce the cracking density of L-PBF IN738LC as the volume of liquid film at grain boundaries was significantly reduced. In addition to scan strategy, Seidel et al. [612] proposed a new approach to suppress hot tearing through the modification of the laser-induced melt pool convection (Marangoni convection) using customized magnetic fields. The underlying mechanism was ascribed to the increase in flow velocity that elevates the interface temperature, leading to less severe thermal contraction. Unfortunately, it is still challenging to fabricate a fully dense non-weldable Nickel-based superalloys without any cracks using the fusion-based AM processes, based on present studies.

7.3.3. Surface roughness

There are different sources cause surface roughness in the final AM part such as unstable fluid flow in the molten pool, gas flow stress, spatters, denudation, balling, and unsuitable hatch spacing. One source is the "balling effect" which typically occurs at high scan speed and laser/electron beam power. Once the energy input is less and the molten material does not *wet* (i.e., generate properly metallurgical bonding with) the underlying layer, surface tension will make the molten material turn into spherical droplet [613]. Unstable molten track resulting from high scanning speed also leads to disconnected droplets [80]. These droplets solidify as "balling" structure later. Rough surface of AM Nickel-based superalloy could also be induced by unfavorable molten pool dynamics. Xia et al. [614] changed the hatch distance of L-PBF processed IN718 and found that a small hatch distance causes higher thermal gradient and larger surface tension. The surface tension drags the molten material to the as-fabricated tracks and leads to the stacking of material, which creates humps and shrinkages on the surface of AM component. Rough surface also causes LoF during fusion-based AM process if the next layer scanning does not heal the valleys of rough surface.

Besides, the surface roughness of powder particles related with the particles' morphology and contamination, and the satellited particles can affect the final surface roughness of the AM part. Although the morphological irregularities of the powder particles can cause the insufficient packing density, they can improve the building efficiency by increasing the rate of heat absorption [615]. The underlying mechanism through which heat absorbing rate increases with surface asperities is believed to be the decreasing laser reflectivity of the powders due to their complex geometry.

Surface finish is a critical limit factor for the fusion-based AM processes to reach the requirement of finial application. Poor surface finish decreases the geometry precision. The irregularities on the surface also provide stress concentration and serve as cracking initial sites especially for fatigue damage [349]. It is also mentioned in section 3.4 (defects and anomalies) that rough surface of AM components could damage powder spreading rake and impact the following process [137].

For the top surface of as-built AM components, the surface finish is depended on the fusion parameters and the spattering. Insufficient energy input leads to balling-effect, in which the molten material cannot *wet* the underlying layer and forms bead-up structure [613]. On the other hand, excess energy input could cause the stacking of material because of Marangoni flow, which creates humps and shrinkages on the surface of AM component [614]. It is also mentioned in section 3.2.2 (about the spattering) that excess energy input could cause an instable molten pool, in which metal vapor expands and ejects molten material to the surrounding [149]. The spatters then stick on the as-build component and degrade the surface finish [616]. Another mechanism for rough surface is the edge-effect. As the discussion earlier in residual stress (3.4.2), it is reported that heat will accumulate at the edge of AM components

[139]. Heat accumulation not only leads to more severe thermal distortion but causes a larger molten pool which grabs material from the nearby. This causes an elevated edge to AM components [617].

For the side and down surface of AM components, the surface finish is depended on the stair stepping effect and partially molten particles attaching to the surface. Decreasing the inclination angle or increasing the layer thickness of AM component could increase the stair stepping effect during AM process [618]. It is also reported that stacking irregularities could happen between each layer, which forms notch like defect (known as "plate-pill") on the surface [349]. Moreover, the fusion at the edge grabs the particles from the powder bed but cannot fuse the particles completely. These partially molten particles stick on the surface and degrade the surface finish [619]. The issue of partially molten particle is much more severe at the down surface of powder bed AM technology, where the molten material wets the powder bed, which leads to balling structure and entangles the particles from the underlying powder bed [620]. Different mechanisms causing rough surface of AM components are illustrated in Fig. 70.

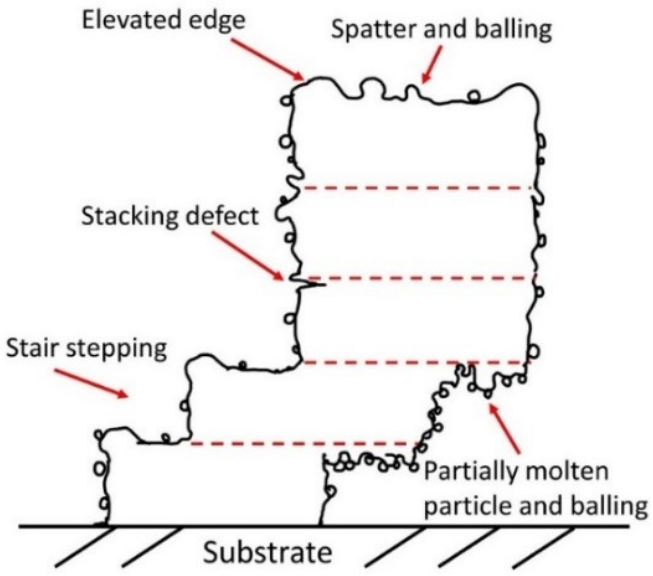

Fig. 70. The irregularities on the surface of fusion-based AM component. The red dotted lines are the boundaries of each layer.

Apart from a proper set of fusion parameters, post processing surface treatments are usually required to remove surface irregularities after fusion-based AM process. These processes including mechanical treatment, remelting, chemical polish or even coating technique [621]. Different post processing surface treatments to improve the surface finish of the fusion-based AM component are listed in Table 6.

Table 6. Post processing heat treatment to improve surface finish of AM component.

Type	Surface treatment	Description
Mechanical based	Finish Machining	Surface materials removing by machining, grinding, and polishing. [621]
	Tumble finishing	The part places inside a barrel with abrasive media. The part tumbles against abrasive media and removes the surface material. [621,622]
	Blasting	The abrasive media is propelled against the part under high pressure and removes the surface material. [621]
	Peening	The surface of the part is bombed by a stream of small shots such as steel balls or laser pulse, which creates cold working effect on the surface. [621,623]
Fusion-based	Remelting	Addition scanning is performed without material applied on the surface during AM process. [621]
	Laser polish	Similar with the concept of remelting, a laser is applied on the surface of parts and remelts the irregularities on the surface. [621,624]
Chemical based	Chemical polish/etching	Material is removed by chemical solution. The process might be enhanced with electrolysis or abrasive media.[621,625]
	Material Coating	The part is covered with other material to improve surface finish [621] (by spark deposition [626] or solution-based coating [627])

7.3.4. Residual stress

Another purpose of process optimization is to mitigate accumulation of residual strains during AM fabrication that may trigger the delamination and microcrack formation/propagation during AM processing, heat treatments, and service performance. To minimize the influence of distortion to AM Nickel-based superalloy components, many researchers built the AM Nickel-based superalloy components with different process parameters and then measured the residual stress or the distortion [628].

Gao et al. [629] measured the dimensional deflection of the substrate plate during the L-DED process of IN718 cylinders using several different deposition patterns to quantify the amount of residual stress. It was found that the raster scanning patterns have a more significant effect on build plate deflection as compared to the contour paths; the back-and-forth scanning patterns generated the least amount of residual stress owing to a minimization of the unnecessary movements of the scan track. Similar studies were conducted for L-PBF processed CM247LC [128] and L-PBF processed IN718 [630]. The use of island and fractal scanning strategies was observed to significantly reduce the extent of residual stress. A simulation obtained from finite element modeling based on L-PBF processed IN718 further suggested that the rotation of scan pattern between successive layers reduces the anisotropic distribution of residual stress [631]. However, it should be noted that the use of island and fractal scanning strategies may result in localized microcracking due to the clusters of high angle grain boundaries (HAGBs) within the fine grain region. Therefore, several in-situ process controls were implemented to reduce the residual stress. For example, pre-heating of the substrate or powder bed allows reduction of thermal gradient between subsequent layers, and thus reduces the thermal strains during solidification. Although not explicitly reported for Nickel-based

superalloys, studies focusing on AM steels and Ti-alloys have demonstrated that the tensile residual stress responsible for cracking can be relieved by compressive stresses induced by laser shock peening [632]. Similar approaches were carried out using a high-pressure roller to reduce thermal distortion [633].

Nadammal et al. [278] have changed the length of the scanning patterns and measured the residual stress of L-PBF IN718. They found a short distance of scanning lead to higher heat concentration and a maximum residual stress 400 MPa while the specimen with longer scanning has a maximum residual stress range from 200 to 300 MPa. The similar result was reported by Lu et al. [630], where the authors changed the size of island scanning and found a small island cause more cracking inside the component. Cheng et al. [634] analyzed the influence of substrate and found that residual stress in L-PBF IN718 was reduced from 350 MPa to 200 MPa by substrate preheating.

8. Summary

8.1. Feedstock

It is clear throughout the review presented here that the characteristic of the powder feedstock used for the AM processes plays a crucial role on the processability of Nickel-based superalloys. In summary, the particle morphology, and size distribution determine the flowability and packing density of the powders. Powders with good flowability and packing density enable efficient flow of the melt into the pores, leading to higher bulk density in both DED and PBF processed Nickel-based supealloy parts. Although increasing surface roughness can enhance the absorptivity of heat, it is suggested that the use of spherical powder without ultra-fine particles may achieve better flowability and resulting bulk density.

The trapped gases (particularly oxygen) and contaminations may also deteriorate the bulk density by forming unfavorable phases that facilitate crack propagation and leaving gas pores within the solidified parts. The findings are also analogous to degrading performance of built parts as recycled powders are used. The heat-affected powders distributing in the periphery of the melted powders may contribute negative effects such as oxidation, loss of elements, reshaping of morphology, and changes in size distribution leading to degrading of flowability. The selection of techniques to fabricate and sieve the powders is highly relevant to the material properties in Nickel-based superalloys.

8.2. AM processing

Although the AM process facilitates part integration through its ability to fabricate many parts required in an assembly into a single component, process optimization is still complex regarding defect formation and microstructures. Since the formation of defects are closely related to the laser-powder interaction and laser-melt interaction that influence the resulting melt pool stability and thermal history, the optimization process can be approached using a

processing window with either independent scan parameters/scan strategies or incorporated factors such as energy density as the variables. Furthermore, the use of shielding gas and its corresponding flow rates used in AM process can also profoundly impact the properties of built parts in terms of oxidation, melt pool geometry, and trapped gas or spatter. Aided by the understanding of underlying mechanisms through which each type of porosity or crack forms, computer-aided processing optimization including machine learning, finite element modeling, and processing monitoring via optical/infrared camera was also conducted for both weldable and non-weldable Nickel-based superalloys.

8.3. Microstructure

Given the combination of high thermal gradient and cooling rate with respect to the melt pool boundary, grains would grow epitaxially with preferred orientation along the [001] direction as Nickel-based superalloys solidify. As approaching the center of the melt pool, the thermal gradient and solidification rate vary leading to transition from cellular dendrite to columnar dendrite. The combination of different scan conditions, strategies, pre-heating, and size and energy the laser/electron beam further contributes to distinct thermal history and fraction of overlapping area that re-configures the grain structure and allows competitive grain growth leading to different degree of columnar-to-equiaxed transition.

The fast-cooling rate in fusion-based AM process also reduces the dendrite arm spacing and resulting micro-segregation as well as restricts the precipitation. Despite the high tendency to forming precipitates for Nickel-based superalloys, only nano-sized γ'/γ'' as well as secondary phases such as Laves, δ and carbides induced by micro-segregation can be found in L-PBF processed Nickel-based superalloys. With decreasing cooling rates in DED and E-PBF process, growth of γ'/γ'' and other secondary phases is allowed resulting in transition from nano-sized particles to micro-sized particles.

The microstructure evolution within AM processed superalloys also depends on the as-built grain morphologies. Due to the presence of precipitates, these particles may pin the grain boundaries leading to remaining texture and columnar feature as sub-solvus heat treatments are applied. The residual strains induced by fast cooling of the fusion-based AM process also facilitate the recrystallization and account for more pronounced grain structural evolution in L-PBF process when compared to that in DED and E-PBF processes. As the trade-off, the large strain energy also allows rapid coarsening of precipitates and formation of undesired phases that undermine the mechanical performance.

Given the anisotropic properties and distinct microstructural evolution in fusion-based AM processed Nickel-based superalloys, attempts were carried out by optimization of processing conditions and chemistry of alloys by the combination of several research tools including computational modeling and destructive/non-destructive characterization techniques. These approaches successfully achieve certain degree of columnar-to-equiaxed transition and

optimize the processibility of Nickel-based superalloys that satisfy the needs for designers to make better and wider use of AM processed Nickel-based superalloys.

8.4. Defects

Fusion-based AM process can fabricate parts with complex geometry and has attracted a large interest in the Nickel-based superalloy community, and defects formation associated with the AM process remain a subject of importance. Most of defects are detrimental to the mechanical properties and can affect the yield of the production, such defects include porosity, crack, and distortion; these defects are induced generally by improper fusion energy or existing defect of the feedstock. On the other hand, high contents of γ' forming elements and trace elements addition can also impact the susceptibility to crack formation during the fusion-based process. Some minor defects have less impact on the mechanical properties but could influence the dimensional consistency of the built; these issues include the elemental evaporation, spattering, inclusion, and rough surface. Some defects, such as oxide or carbide inclusions that can provide dispersion-strengthening and improve mechanical properties of the built.

8.5. Mechanical behavior

This review has highlighted and compared the mechanical properties of the several AM Nickel-based superalloys with the baseline data available in the literature for traditionally manufactured counterparts. First, the *tensile* properties at room and elevated temperatures for various AM Nickel-based superalloys such as L-PBF processed Haynes 282, L-PBF processed Hastelloy X, E-PBF processed IN718, L-PBF processed IN718, L-PBF processed IN625, powder bed binder jet (PB-BJ) printed IN625 were compared and discussed accordingly. It was shown that the solid solution strengthened Hastelloy X and IN625 alloys possess the lowest strengths at room as well as elevated temperatures, while γ"-strengthened IN718 superalloy typically show the highest strength even better than that of the γ'-strengthened Haynes 282 superalloy. Furthermore, it was found that the grain boundaries (i.e., GBs, particularly those perpendicular to the applied load direction) are the weakest regions under tension load at elevated temperatures due to the brittle intermetallic/impurity phases forming at GBs during the last stage of solidification acting as the major source for the crack initiation.

Next, the *fatigue* properties of the AMed Nickel-based superalloys were discussed to specifically provide an overall understanding and interpretation for the complicated failure mechanism due to its several interactive factors such as the size, volume fraction and morphology of process-induced defects as well as microstructural features. These were discussed using some of influential factors on the fatigue failure of two well-known alloys, namely, IN718 and IN625, due to more availability of data in the literature.

The effect of *surface roughness on the fatigue* behavior was reviewed. This is crucially important for the AMed Nickel-based superalloys due to their characteristic process-induced

defects, initiating the fatigue failures. It was shown that regardless of heat treatment (HT) condition, the post processing surface treatments can improve the fatigue performance of the AMed Nickel-based superalloys due to the removal of the surface/subsurface defects induced during the AM fabrication processes.

The effect of *HIP on the fatigue* behavior of some AM Nickel-based superalloys was highlighted. It was shown that the HIP has an insignificant effect on the fatigue behavior of the AM IN625 and AM IN718 alloys regardless of the HT conditions. Further, it was revealed that the fatigue responses of both alloys in HIPed condition are comparable with those of their wrought counterparts. These results could be attributed to the negligible effect of internal porosity content on the fatigue properties of the AM IN625 and IN718 alloys.

The effects of brittle *secondary phases on the fatigue fracture* phenomena of the AM Nickel-based superalloys were discussed. More particularly, the sequential behavior of the Laves phases during the fatigue fracture of HT LP-DED IN718 alloy was highlighted. It was shown that during the initiation and growth stages of fatigue cracks the Laves phases are strong enough to hinder the crack growth, while during the final stage of fatigue rupture the Laves phases start to break down due to their brittleness as compared with the surrounding matrix.

The effect of various *HT conditions on fatigue crack growth rate or FCGR (da/dN)* as an important measure of damage tolerance and durability of AMed Nickel-based superalloys was further discussed. It was shown that within Paris regime the FCGR of non-heat treated (NHT) L-PBF processed IN625 is comparable with that of its wrought counterpart. However, in heat treated condition (HT) conditions such as the stress relieving (SR) and HIP, the FCG resistance is higher (i.e., higher ΔK_{th}) at lower stress ratios as compared with wrought specimens, which could be ascribed to the shielding effect of coarse grain structure on the crack tip opening, which is promoted by the crack closure mechanisms. However, in the case of the AMed IN718, the effect of various HT conditions on the FCG behavior of the alloy is more pronounced than the HT AM IN625, which could be ascribed to the strengthening effect of γ”-precipitates on fatigue crack growth in the former. Furthermore, most of HT conditions of AM IN718 have shown lower FCGR as well as lower FCG resistance, i.e., smaller ΔK_{th} (compared to wrought). Additionally, the minimum ΔK_{th} value is reported for the NHT condition, which could be attributed to the supersaturated and unreinforced matrix in NHT condition and therefore better ductility as compared with the HT specimens.

The effect of various *HT conditions on fracture toughness* of the AM IN625 and IN718 alloys was also discussed. It was shown that the stress relieving (SR) could marginally improve the fracture toughness of the AMed IN625. However, in the case of AMed IN718, various HT conditions such as direct two-step aged (D-2Aged), solution + fully aged (S+2Aged), and homogenized + solution + fully aged (H+S+2Aged) could improve the fracture toughness of the alloy. Interestingly, the lowest fracture toughness values were observed for the NHT and D-2Aged conditions, which could be attributed to their lower ductility and strain-hardening

exponent, resulting in lesser capability of strain accommodation of a matrix during the rapid crack propagation stage.

Finally, the *creep behavior* of the AMed Nickel-based superalloys based on available data in the literature such as for IN718 and IN738LC, CM247LC, L-PBF C263, L-PBF Hastelloy X alloys was briefly reviewed. Similar to tensile properties, it was shown the AMed Nickel-based superalloys has shown anisotropic creep behavior in non-heat treated (NHT) conditions which was removed upon heat treatments. In other words, in NHT condition, the AMed Nickel-based superalloys have shown better creep resistance in vertical direction, i.e., when the stress is applied parallelly with respect to the build direction or elongated grain structure), as compared with the horizontally built AMed and cast counterparts. This could be most likely attributed to the fact that creep damage was accumulated on the grain boundaries that were aligned with the plane of maximum applied stress. Furthermore, the creep failure mechanism in the AMed Nickel-based superalloys were discussed and attributed to the intermetallic phases forming at grain boundary areas such as metal carbides and δ-phases, which could significantly affect the creep response of these alloys

8.6. Computational modeling

A critical review of the computational modeling of Nickel-based superalloys establishes their role in understanding the relevant physical parameters that affect final part quality, including temperature and velocity fields, cooling rates, and solidification morphology. Such parameters are difficult, if not impossible, to obtain via experimental measures, and thus, these simulations provide means of understanding their impact on the formation of the final part's structure and properties. The laser-powder interactions vary with AM processes and play a critical role in determining such parameters. Various methods, including full or partial ray-tracing, have been proposed to simulate these mechanisms and further our understanding of their implications. These results can be provided as input to higher-fidelity thermal models (including heat transfer, fluid flow, and added physics) or approximated in the case of lower-fidelity (conduction-based) simulations. The choice between higher- and lower-fidelity simulations depends on the desired results and application: the former provides better accuracy at exuberant computational cost, whereas the latter degrades the solution accuracy at a significantly decreased expense. Besides, the results obtained from either set of simulations can help elucidate our understanding of and optimize the process, reduce defects, and bridge the gap between product design and certification. Additionally, the results from such simulations can be provided as input to models for microstructure and residual stress prediction.

Techniques including the Monte Carlo (MC) and Phase Field (PF) methods for predicting solidification microstructure were discussed. Regarding prediction of grain microstructure, computationally efficient methods based on dendrite growth kinetics such as the Cellular

Automaton (CA) and Discrete Dendrite Dynamics (DDD) methods were introduced. These methods have been employed to simulate the columnar grain microstructure oriented along the build direction and crystallographic texture with high accuracy. This is evident from the part scale grain microstructure and texture prediction by the DDD model. Regarding prediction of γ' and γ" phase precipitates along with δ-forming elements in the parent γ-matrix during in Nickel-based superalloys, works related to the numerical techniques such as PF were discussed. As prediction of residual distortion and stresses play significant role with regards to the successful AM build, sequentially coupled thermomechanical finite element (FE) models along with the inherent strain method were also discussed in detail. Finally, elastoplastic self-consistent (EPSC) mean-field homogenization formulation based polycrystal plasticity method was identified as a prominent method for predicting the effect of precipitate phases in the parent γ-matrix and processing temperatures on the mechanical behavior of AM processed Nickel-based superalloys.

9. Research outlook

Considering the recent cutting-edge advancements in the field, the following key areas appear to be of primary interest to AM community to enhance the fabrication and mechanical properties of the Nickel-based superalloy materials and parts.

Synergistic effect of defects and microstructure. Recent advanced process control during AM fabrication such as innovative "scan strategies", "beam profiles" and "online process monitoring" have been partially able to mitigate some of process-induced defects for certain difficult-to-print Nickel-based superalloys, which in turn could result in improved mechanical properties such as fatigue. Additionally, advances in thermal management by process controls may even enable the users to point design the AM components by microstructure, leading to enhancement of the mechanical properties of the alloy. However, such innovative approaches may introduce new challenges such as large volume of data generation for which the role of computer scientists and data analysists become crucial in such huge data collection and analyses.

Alloy design. The current review has endeavored to highlight much of existing work for the mechanical properties of popular AM Nickel-based superalloys, namely, IN625 and IN718. However, there are abundant opportunities within the Nickel-based alloy metallurgical framework by compositional modification to specifically design the alloy for AM processing with enhanced AM compatibility and mechanical properties. One example in this regard is to formulate new AM processing methods, and therefore, to develop new Nickel-based alloys with enhanced thermal stability. The other example is to devise new AM processing strategies such as powder reusage for new alloy development in which the alloy performance can be assured.

Design of heat treatments. Designing appropriate HT for the AM Nickel-based superalloy has always been important because of their inherent differences such as the as-solidified microstructural features and process-induced defects which strongly influence the mechanical properties. Although HT

schedules proposed for the wrought alloys are expected to result in similar microstructures and structural integrity for AM ones, this is not always the case. This necessitates a carefully customized HT schedule for the AM Nickel-based superalloy to obtain the desirable microstructure and mechanical properties of the alloy.

Simulation and modeling. Given the high computational expense associated with the methods discussed above, future work in this field will rely on the transfusion of physics-based numerical simulation with modern advancements in GPU computing and machine learning. Process and microstructure simulations that have long relied on CPU cores to obtain solutions will benefit from being placed on GPU clusters in the future. Dimensionality reduction techniques that correlate process parameters (or other physical signatures) to corresponding quantities of interest could play a vital role in fast process optimization. Similarly, machine learning techniques that fully or partially abstract the physics but maintain high accuracy concerning temperature, defect, or microstructure prediction will be pivotal to further elucidate our understanding of the process and help accelerate the widespread adoption of AM for next-generation manufacturing applications.

Acknowledgement

AM acknowledges startup funding from Mechanical, Materials and Aerospace Engineering Department at Illinois Institute of Technology at Chicago, Illinois. ITH and ST acknowledge the support from the National Science Foundation (NSF) under Grant Number CMMI # 1663068. ACY and KCC would like to acknowledge funding support from Ministry of Science and Technology (MOST) in Taiwan under Grant 110-2221-E-007-020-MY3 and 110-2224-E-007-001. Financial support from NASA NSTGRO fellowship (S.T.), Department of Energy Project S001341 (S. P.), and NASA Project 80NSSCM0105 (A.C.T.) are gratefully acknowledged. NS and SS acknowledge the partial support from the National Institute of Standards and Technology (NIST) under Grant Number 70NANB19H170 and National Aeronautics and Space Administration under Grant Number 80MSFC18M0052. This material is partially based upon work supported by the U.S. Department of Energy, Office of Science, Office of Basic Energy Sciences, under Award Number DE-SC0019378.

Reference

[1] Additive manufacturing market analysis by material type 2020:230.

[2] Liu J, Gaynor AT, Chen S, Kang Z, Suresh K, Takezawa A, et al. Current and future trends in topology optimization for additive manufacturing. Struct Multidiscip Optim 2018;57:2457–83.

[3] Zhang LC, Liu Y, Li S, Hao Y. Additive Manufacturing of Titanium Alloys by Electron Beam Melting: A Review. Adv Eng Mater 2018;20. https://doi.org/10.1002/adem.201700842.

[4] Attaran M. The rise of 3-D printing: The advantages of additive manufacturing over traditional manufacturing. Bus Horiz 2017;60:677–88.

[5] Bhavar V, Kattire P, Patil V, Khot S, Gujar K, Singh R. A review on powder bed fusion technology of metal additive manufacturing. Addit Manuf Handb Prod Dev Def Ind 2017:251–61. https://doi.org/10.1201/9781315119106.

[6] English CL, Tewari SK, Abbott DH. An overview of Ni base additive fabrication technologies for aerospace applications. Proc. 7th Int. Symp. Superalloy, Pittsburgh, PA, USA, 2010, p. 10–3.

[7] Brice CA, Needler SD, Rosenberger BT. Direct Manufacturing at Lockheed Martin Aeronautics Co. AeroMat Conf., 2010.

[8] Panwisawas C, Tang YT, Reed RC. Metal 3D printing as a disruptive technology for superalloys. Nat Commun 2020;11:1–4.

[9] Ghoussoub JN, Tang YT, Panwisawas C, Németh A, Reed RC. On the influence of alloy chemistry and processing conditions on additive manufacturability of Ni-based superalloys. Superalloys 2020, Springer; 2020, p. 153–62.

[10] Rahman M, Seah WKH, Teo TT. The machinability of Inconel 718. J Mater Process Technol 1997;63:199–204.

[11] Srivastava RR, Kim M, Lee J, Jha MK, Kim B-S. Resource recycling of superalloys and hydrometallurgical challenges. J Mater Sci 2014;49:4671–86.

[12] Schafrik RE, Ward DD, Groh JR. Application of alloy 718 in GE aircraft engines: past, present and next five years. Superalloys 2001;718:1–11.

[13] Li Y, Chen K, Narayan RL, Ramamurty U, Wang Y, Long J, et al. Multi-scale microstructural investigation of a laser 3D printed Ni-based superalloy. Addit Manuf 2020;34:101220.

[14] Harrison NJ, Todd I, Mumtaz K. Reduction of micro-cracking in nickel superalloys processed by Selective Laser Melting: A fundamental alloy design approach. Acta Mater 2015;94:59–68. https://doi.org/10.1016/j.actamat.2015.04.035.

[15] Vrancken B, Thijs L, Kruth JP, Van Humbeeck J. Microstructure and mechanical properties of a novel β titanium metallic composite by selective laser melting. Acta Mater 2014;68:150–8. https://doi.org/10.1016/j.actamat.2014.01.018.

[16] DebRoy T, Wei HL, Zuback JS, Mukherjee T, Elmer JW, Milewski JO, et al. Additive manufacturing of metallic components – Process, structure and properties. Prog Mater Sci 2018;92:112–224. https://doi.org/10.1016/j.pmatsci.2017.10.001.

[17] Sanaei N, Fatemi A. Defects in Additive Manufactured Metals and Their Effect on Fatigue Performance: A State-of-the-Art Review. Prog Mater Sci 2020:100724. https://doi.org/10.1016/j.pmatsci.2020.100724.

[18] Mostafaei A, Zhao C, He Y, Reza Ghiaasiaan S, Shi B, Shao S, et al. Defects and anomalies in powder bed fusion metal additive manufacturing. Curr Opin Solid State Mater Sci 2022;26:100974. https://doi.org/10.1016/j.cossms.2021.100974.

[19] Li Y, Liang X, Yu Y, Wang D, Lin F. Chinese Journal of Mechanical Engineering : Additive Manufacturing Frontiers Review on Additive Manufacturing of Single-Crystal Nickel-based Superalloys. Chinese J Mech Eng Addit Manuf Front 2022;1:100019. https://doi.org/10.1016/j.cjmeam.2022.100019.

[20] Adegoke O, Andersson J, Brodin H, Pederson R. Review of laser powder bed fusion of gamma-prime-strengthened nickel-based superalloys. Metals (Basel) 2020;10:1–26. https://doi.org/10.3390/met10080996.

[21] Attallah MM, Jennings R, Wang X, Carter LN. Additive manufacturing of Ni-based superalloys: The outstanding issues. MRS Bull 2016;41:758–64. https://doi.org/10.1557/mrs.2016.211.

[22] Haines MP, Rielli V V., Primig S, Haghdadi N. Powder bed fusion additive manufacturing of Ni-based superalloys: a review of the main microstructural constituents and characterization techniques. J Mater Sci 2022;57:14135–87. https://doi.org/10.1007/s10853-022-07501-4.

[23] Kwabena Adomako N, Haghdadi N, Primig S. Electron and laser-based additive manufacturing of Ni-based superalloys: A review of heterogeneities in microstructure and mechanical properties. Mater Des 2022;223:111245. https://doi.org/10.1016/j.matdes.2022.111245.

[24] Hosseini E, Popovich VA. A review of mechanical properties of additively manufactured Inconel 718. Addit Manuf 2019;30. https://doi.org/10.1016/j.addma.2019.100877.

[25] Martin E, Natarajan A, Kottilingam S, Batmaz R. Binder jetting of “Hard-to-Weld” high gamma prime nickel-based superalloy RENÉ 108. Addit Manuf 2021;39:101894.

https://doi.org/10.1016/j.addma.2021.101894.
[26] Donachie MJ, Donachie SJ. Superalloys: A Technical Guide. 2nd ed. Materials Park, OH: ASM International; 2002. https://doi.org/10.1361.
[27] Eurich NC, Bristowe PD. Thermodynamic stability and electronic structure of η-Ni6Nb(Al,Ti) from first principles. Scr Mater 2014;77:37–40. https://doi.org/10.1016/j.scriptamat.2014.01.012.
[28] Sugimura H, Kaneno Y, Takasugi T. Alloying Behavior of Ni3M-Type Compounds with D0a Structure. Mater Trans 2011;52:663–71. https://doi.org/10.2320/matertrans.M2010386.
[29] Krakow R, Johnstone DN, Eggeman AS, Hünert D, Hardy MC, Rae CMF, et al. On the crystallography and composition of topologically close-packed phases in ATI 718Plus®. Acta Mater 2017;130:271–80. https://doi.org/10.1016/j.actamat.2017.03.038.
[30] Brož P, Buršík J, Svoboda M, Kroupa A. Theoretical and experimental study of the γ and γ′ equilibrium in Ni-based superalloys. Mater Sci Eng A 2002;324. https://doi.org/10.1016/s0921-5093(01)01278-3.
[31] Brooks JW, Bridges PJ. Metallurgical Stability of Inconel Alloy 718, 2012. https://doi.org/10.7449/1988/superalloys_1988_33_42.
[32] Flinn PA. Theory of Deformation in Superlattices. Trans Metall Soc AlME 1960;218.
[33] Donachie MJ. Superalloys: A Technical Guide, 2nd Edition. America (NY) 2002:1–409.
[34] Reed RC. The Superalloys fundamentals and applications. vol. 9780521859. 2006. https://doi.org/10.1017/CBO9780511541285.
[35] Ojo OA, Chaturvedi MC. On the role of liquated γ′ precipitates in weld heat affected zone microfissuring of a nickel-based superalloy. Mater Sci Eng A 2005;403. https://doi.org/10.1016/j.msea.2005.04.034.
[36] Milewski JO. Lasers, Electron Beams, Plasma Arcs. Addit. Manuf. Met., Springer; 2017, p. 85–97.
[37] Tepylo N, Huang X, Patnaik PC. Laser-Based Additive Manufacturing Technologies for Aerospace Applications. Adv Eng Mater 2019;21:1–35. https://doi.org/10.1002/adem.201900617.
[38] ASTM International. ISO/ASTM52900-15 Standard Terminology for Additive Manufacturing - General Principles - Terminology 2015.
[39] King WE, Anderson AT, Ferencz RM, Hodge NE, Kamath C, Khairallah SA, et al. Laser powder bed fusion additive manufacturing of metals; physics, computational, and materials challenges. Appl Phys Rev 2015;2:41304.
[40] Zhai Y, Lados D a., LaGoy JL. Additive Manufacturing: Making Imagination the Major Limitation. Jom 2014;66:1–9.
[41] Biamino S, Penna A, Ackelid U, Sabbadini S, Tassa O, Fino P, et al. Electron beam melting of Ti–48Al–2Cr–2Nb alloy: Microstructure and mechanical properties investigation. Intermetallics 2011;19:776–81.
[42] Wooten J, Dennies DP. Electron Beam Melting Manufacturing for Production Hardware. SAE Int 2008.
[43] Cheng L, Liang X, Bai J, Chen Q, Lemon J, To A. On utilizing topology optimization to design support structure to prevent residual stress induced build failure in laser powder bed metal additive manufacturing. Addit Manuf 2019;27:290–304. https://doi.org/10.1016/j.addma.2019.03.001.
[44] Körner C. Additive manufacturing of metallic components by selective electron beam melting - A review. Int Mater Rev 2016;61:361–77. https://doi.org/10.1080/09506608.2016.1176289.
[45] Gong X, Anderson T, Chou K. Review on powder-based electron beam additive manufacturing Technology. Manuf Rev 2014;1. https://doi.org/10.1051/mfreview/2014001.
[46] Gu DD, Meiners W, Wissenbach K, Poprawe R. Laser additive manufacturing of metallic components: Materials, processes and mechanisms. Int Mater Rev 2012;57:133–64. https://doi.org/10.1179/1743280411Y.0000000014.
[47] Helmer HE, Körner C, Singer RF. Additive manufacturing of nickel-based superalloy Inconel 718 by selective electron beam melting: Processing window and microstructure. J Mater Res 2014;29:1987–96. https://doi.org/10.1557/jmr.2014.192.
[48] Saboori A, Gallo D, Biamino S, Fino P, Lombardi M. An Overview of Additive Manufacturing of Titanium Components by Directed Energy Deposition: Microstructure and Mechanical Properties. Appl Sci 2017;7:883.
[49] Selcuk C. Laser metal deposition for powder metallurgy parts. Powder Metall 2011;54:94–9.
[50] Cunningham CR, Flynn JM, Shokrani A, Dhokia V, Newman ST. Invited review article: Strategies and processes for high quality wire arc additive manufacturing. Addit Manuf 2018;22:672–86.
[51] ASTM F3187-16 Standard Guide for Directed Energy Deposition of Metals ASTM International. West Conshohocken, PA: 2016.
[52] Dutta B, Froes FHS. The additive manufacturing (AM) of titanium alloys. Titan. powder Metall., Elsevier; 2015, p. 447–68.
[53] Tang HP, Qian M, Liu N, Zhang XZ, Yang GY, Wang J. Effect of Powder Reuse Times on Additive Manufacturing of Ti-6Al-4V by Selective Electron Beam Melting. Jom 2015;67:555–63. https://doi.org/10.1007/s11837-015-1300-4.
[54] Williams S. Wire+ arc additive manufacturing vs. traditional machining from solid: a cost comparison

2015.
[55] Anzalone GC, Zhang C, Wijnen B, Sanders PG, Pearce JM. A low-cost open-source metal 3-D printer. IEEE Access 2013;1:803–10.
[56] Martin JH, Yahata BD, Hundley JM, Mayer JA, Schaedler TA, Pollock TM. 3D printing of high-strength aluminium alloys. Nature 2017;549:365–9. https://doi.org/10.1038/nature23894.
[57] Metals Handbook Desk Edition. 1998. https://doi.org/10.31399/asm.hb.mhde2.9781627081993.
[58] Basak A. Additive manufacturing of high-gamma prime nickel-based superalloys through selective laser melting (SLM). Solid Free Fabr 2019 Proc 30th Annu Int Solid Free Fabr Symp - An Addit Manuf Conf SFF 2019 2019:554–75.
[59] Dawes J, Bowerman R, Trepleton R. Introduction to the additive manufacturing powder metallurgy supply chain. Johnson Matthey Technol Rev 2015;59:243–56. https://doi.org/10.1595/205651315X688686.
[60] Cordova L, Campos M, Tinga T. Revealing the Effects of Powder Reuse for Selective Laser Melting by Powder Characterization. Jom 2019;71:1062–72. https://doi.org/10.1007/s11837-018-3305-2.
[61] Mancisidor AM, Garciandia F, García-Riesco PM, San Sebastian M. Influence of Hastelloy X composition on cracking susceptibility during SLM. Euro PM 2018 Congr. Exhib., 2020.
[62] Zadi-Maad A, Basuki A. The development of additive manufacturing technique for nickel-base alloys: A review. AIP Conf. Proc., vol. 1945, 2018. https://doi.org/10.1063/1.5030286.
[63] Tian Z, Zhang C, Wang D, Liu W, Fang X, Wellmann D, et al. A review on laser powder bed fusion of inconel 625 nickel-based alloy. Appl Sci 2020;10. https://doi.org/10.3390/app10010081.
[64] Wang X, Read N, Carter LN, Ward RM, Attallah MM. Defect formation and its mitigation in selective laser melting of high γ′ Ni-base superalloys. Proc Int Symp Superalloys 2016;2016-Janua:351–8. https://doi.org/10.1002/9781119075646.ch38.
[65] Engeli R, Etter T, Hövel S, Wegener K. Processability of different IN738LC powder batches by selective laser melting. J Mater Process Technol 2016;229:484–91. https://doi.org/10.1016/j.jmatprotec.2015.09.046.
[66] Lopez-Galilea I, Ruttert B, Theisen W. Integrated HIP-heat treatment of Ni-base superalloys fabricated by SLM. Euro PM 2018 Congr. Exhib., European Powder Metallurgy Association (EPMA); 2020.
[67] Hagedorn YC, Risse J, Meiners W, Pirch N, Wissenbach K, Poprawe R. Processing of nickel based superalloy MAR M-247 by means of High Temperature - Selective Laser Melting (HT - SLM). High Value Manuf. Adv. Res. Virtual Rapid Prototyp. - Proc. 6th Int. Conf. Adv. Res. Rapid Prototyping, VR@P 2013, 2014. https://doi.org/10.1201/b15961-54.
[68] Yang J, Li F, Wang Z, Zeng X. Cracking behavior and control of Rene 104 superalloy produced by direct laser fabrication. J Mater Process Technol 2015;225. https://doi.org/10.1016/j.jmatprotec.2015.06.002.
[69] Murr LE, Martinez E, Pan XM, Gaytan SM, Castro JA, Terrazas CA, et al. Microstructures of Rene 142 nickel-based superalloy fabricated by electron beam melting. Acta Mater 2013;61:4289–96. https://doi.org/10.1016/j.actamat.2013.04.002.
[70] Sato Y, Sugisawa K, Aoki D, Yamamura T. Viscosities of Fe-Ni, Fe-Co and Ni-Co binary melts. Meas Sci Technol 2005;16. https://doi.org/10.1088/0957-0233/16/2/006.
[71] Brooks RF, Day AP, Andon RJL, Chapman LA, Mills KC, Quested PN. Measurement of viscosities of metals and alloys with an oscillating viscometer. High Temp - High Press 2001;33. https://doi.org/10.1068/htwu139.
[72] Franz H, Plöchl L, Schimansky F-P. Recent Advances of Titanium Alloy Powder Production by Ceramic-free Inert Gas Atomization. Titan 2008, Int Titan Assoc 2008.
[73] Dzogbewu TC, Yadroitsev I, Krakhmalev P, Yadroitsava I, du Plessis A. Optimal process parameters for in situ alloyed Ti15Mo structures by laser powder bed fusion. Solid Free. Fabr. 2017 Proc. 28th Annu. Int. Solid Free. Fabr. Symp. - An Addit. Manuf. Conf. SFF 2017, 2020.
[74] Mosallanejad MH, Niroumand B, Aversa A, Saboori A. In-situ alloying in laser-based additive manufacturing processes: A critical review. J Alloys Compd 2021;872. https://doi.org/10.1016/j.jallcom.2021.159567.
[75] Simonelli M, Aboulkhair NT, Cohen P, Murray JW, Clare AT, Tuck C, et al. A comparison of Ti-6Al-4V in-situ alloying in Selective Laser Melting using simply-mixed and satellited powder blend feedstocks. Mater Charact 2018;143. https://doi.org/10.1016/j.matchar.2018.05.039.
[76] Krantz M, Zhang H, Zhu J. Characterization of powder flow: Static and dynamic testing. Powder Technol 2009;194. https://doi.org/10.1016/j.powtec.2009.05.001.
[77] Pleass C, Jothi S. Influence of powder characteristics and additive manufacturing process parameters on the microstructure and mechanical behaviour of Inconel 625 fabricated by Selective Laser Melting. Addit Manuf 2018;24:419–31. https://doi.org/10.1016/j.addma.2018.09.023.
[78] Liu B, Wildman R, Tuck C, Ashcroft I, Hague R. Investigaztion the effect of particle size distribution on processing parameters optimisation in selective laser melting process. 22nd Annu Int Solid Free Fabr Symp - An Addit Manuf Conf SFF 2011 2011:227–38.

[79] Rombouts M, Froyen L, Gusarov A V., Bentefour EH, Glorieux C. Photopyroelectric measurement of thermal conductivity of metallic powders. J Appl Phys 2005;97. https://doi.org/10.1063/1.1832740.
[80] Lee Y, Zhang W. Mesoscopic simulation of heat transfer and fluid flow in laser Powder bed additive manufacturing. Int. Solid Free Form Fabr. Symp., Austin, U.S.A: 2015, p. 1154–65.
[81] Du Y, Mukherjee T, DebRoy T. Physics-informed machine learning and mechanistic modeling of additive manufacturing to reduce defects. Appl Mater Today 2021;24. https://doi.org/10.1016/j.apmt.2021.101123.
[82] ASTM F3049-14: Standard Guide for Characterizing Properties of Metal Powders Used for Additive Manufacturing Processes. 2014.
[83] Hausner HH. Powder characteristics and their effect on powder processing. Powder Technol 1981;30. https://doi.org/10.1016/0032-5910(81)85021-8.
[84] Spierings AB, Voegtlin M, Bauer T, Wegener K. Powder flowability characterisation methodology for powder-bed-based metal additive manufacturing. Prog Addit Manuf 2016;1:9–20. https://doi.org/10.1007/s40964-015-0001-4.
[85] Amado A, Schmid M, Levy G, Wegener K. ADVANCES IN SLS POWDER CHARACTERIZATION. SFF Symp. Int. Solid Free. Fabr. Symp., vol. 22, 2011, p. 438–52.
[86] Sutton AT, Kriewall CS, Leu MC, Newkirk JW. Powders for Additive Manufacturing Processes: Characterization Techniques and Effects on Part Properties. Solid Free Fabr Proc 2016:1004–30.
[87] Thiede T, Mishurova T, Evsevleev S, Serrano-Munoz I, Gollwitzer C, Bruno G. 3D Shape Analysis of Powder for Laser Beam Melting by Synchrotron X-ray CT. Quantum Beam Sci 2019;3:3. https://doi.org/10.3390/qubs3010003.
[88] ASTM International. ASTM B213: Standard Test Methods for Flow Rate of Metal Powders Using the Hall Flowmeter Funnel. Annu. B. ASTM Stand., 2014.
[89] Boley CD, Khairallah SA, Rubenchik AM. Calculation of laser absorption by metal powders in additive manufacturing. Appl Opt 2015;54:2477–82. https://doi.org/10.1201/9781315119106.
[90] Zhao Y, Aoyagi K, Daino Y, Yamanaka K, Chiba A. Significance of powder feedstock characteristics in defect suppression of additively manufactured Inconel 718. Addit Manuf 2020;34:101277. https://doi.org/10.1016/j.addma.2020.101277.
[91] Wang Z, Wang J, Xu S, Liu B, Sui Q, Zhao F, et al. Influence of powder characteristics on microstructure and mechanical properties of Inconel 718 superalloy manufactured by direct energy deposition. Appl Surf Sci 2022;583. https://doi.org/10.1016/j.apsusc.2022.152545.
[92] Holt RT, Wallace W. Impurities and trace elements in nickel-base superalloys. Int Met Rev 1976;21:1–24. https://doi.org/10.1179/imtr.1976.21.1.1.
[93] Rao GA, Srinivas M, Sarma DS. Effect of oxygen content of powder on microstructure and mechanical properties of hot isostatically pressed superalloy Inconel 718. Mater Sci Eng A 2006;435–436:84–99. https://doi.org/10.1016/j.msea.2006.07.053.
[94] Kuo YL, Kakehi K. Influence of powder surface contamination in the Ni-based superalloy alloy718 fabricated by selective laser melting and hot isostatic pressing. Metals (Basel) 2017;7:367. https://doi.org/10.3390/met7090367.
[95] Leung CLA, Marussi S, Towrie M, Atwood RC, Withers PJ, Lee PD. The effect of powder oxidation on defect formation in laser additive manufacturing. Acta Mater 2019;166:294–305. https://doi.org/10.1016/j.actamat.2018.12.027.
[96] Li R, Liu J, Shi Y, Wang L, Jiang W. Balling behavior of stainless steel and nickel powder during selective laser melting process. Int J Adv Manuf Technol 2012;59:1025–35. https://doi.org/10.1007/s00170-011-3566-1.
[97] Renderos M, Torregaray A, Gutierrez-Orrantia ME, Lamikiz A, Saintier N, Girot F. Microstructure characterization of recycled IN718 powder and resulting laser clad material. Mater Charact 2017;134:103–13. https://doi.org/10.1016/j.matchar.2017.09.029.
[98] Anderson IE, White EMH, Dehoff R. Feedstock powder processing research needs for additive manufacturing development. Curr Opin Solid State Mater Sci 2018;22:8–15. https://doi.org/10.1016/j.cossms.2018.01.002.
[99] Cunningham R, Narra SP, Montgomery C, Beuth J, Rollett AD. Synchrotron-Based X-ray Microtomography Characterization of the Effect of Processing Variables on Porosity Formation in Laser Power-Bed Additive Manufacturing of Ti-6Al-4V. Jom 2017;69:479–84. https://doi.org/10.1007/s11837-016-2234-1.
[100] Tomus D, Jarvis T, Wu X, Mei J, Rometsch P, Herny E, et al. Controlling the microstructure of Hastelloy-X components manufactured by Selective Laser Melting. Phys Procedia 2013;41:823–7. https://doi.org/10.1016/j.phpro.2013.03.154.
[101] Chauvet E, Kontis P, Jägle EA, Gault B, Raabe D, Tassin C, et al. Hot cracking mechanism affecting a non-weldable Ni-based superalloy produced by selective electron Beam Melting. Acta Mater 2018;142:82–94. https://doi.org/10.1016/j.actamat.2017.09.047.

[102] Ma C, Zhao J, Cao C, Lin TC, Li X. Fundamental study on laser interactions with nanoparticles-reinforced metals-part II: Effect of nanoparticles on surface tension, viscosity, and laser melting. J Manuf Sci Eng Trans ASME 2016;138. https://doi.org/10.1115/1.4033446.
[103] Han Q, Gu Y, Wang L, Feng Q, Gu H, Johnston R, et al. Effects of TiC content on microstructure and mechanical properties of nickel-based hastelloy X nanocomposites manufactured by selective laser melting. Mater Sci Eng A 2020;796. https://doi.org/10.1016/j.msea.2020.140008.
[104] Ho IT, Chang KC, Tiparti D, Yeh AC, Tin S. Insight to agglomeration and chemical reactions of CoAl2O4 inoculants in IN718 processed by selective laser melting. J Alloys Compd 2021;883. https://doi.org/10.1016/j.jallcom.2021.160753.
[105] Gasper AND, Szost B, Wang X, Johns D, Sharma S, Clare AT, et al. Spatter and oxide formation in laser powder bed fusion of Inconel 718. Addit Manuf 2018;24:446–56. https://doi.org/10.1016/j.addma.2018.09.032.
[106] Basha AKM, Srinivasan S, Srinivasan N. Studies on thermally grown oxide as an interface between plasma-sprayed coatings and a nickel-based superalloy substrate. Int J Miner Metall Mater 2017;24. https://doi.org/10.1007/s12613-017-1451-0.
[107] Nandwana P, Peter WH, Dehoff RR, Lowe LE, Kirka MM, Medina F, et al. Recyclability Study on Inconel 718 and Ti-6Al-4V Powders for Use in Electron Beam Melting. Metall Mater Trans B 2016;47:754–62. https://doi.org/10.1007/s11663-015-0477-9.
[108] Ardila LC, Garciandia F, González-Díaz JB, Álvarez P, Echeverria A, Petite MM, et al. Effect of IN718 recycled powder reuse on properties of parts manufactured by means of Selective Laser Melting. Phys Procedia 2014;56:99–107. https://doi.org/10.1016/j.phpro.2014.08.152.
[109] Kong D cheng, Dong C fang, Ni X qing, Zhang L, Li R xue, He X, et al. Microstructure and mechanical properties of nickel-based superalloy fabricated by laser powder-bed fusion using recycled powders. Int J Miner Metall Mater 2021;28. https://doi.org/10.1007/s12613-020-2147-4.
[110] Nguyen QB, Nai MLS, Zhu Z, Sun CN, Wei J, Zhou W. Characteristics of Inconel Powders for Powder-Bed Additive Manufacturing. Engineering 2017;3:695–700. https://doi.org/10.1016/J.ENG.2017.05.012.
[111] Rock C, Ledford C, Garcia-Avila M, West H, Miller VM, Pankow M, et al. The Influence of Powder Reuse on the Properties of Nickel Super Alloy ATI 718™ in Laser Powder Bed Fusion Additive Manufacturing. Metall Mater Trans B Process Metall Mater Process Sci 2021;52. https://doi.org/10.1007/s11663-020-02040-2.
[112] Sanchez S, Smith P, Xu Z, Gaspard G, Hyde CJ, Wits WW, et al. Powder Bed Fusion of nickel-based superalloys: A review. Int J Mach Tools Manuf 2021;165. https://doi.org/10.1016/j.ijmachtools.2021.103729.
[113] Cobbinah PV, Nzeukou RA, Onawale OT, Matizamhuka WR. Laser powder bed fusion of potential superalloys: A review. Metals (Basel) 2021;11. https://doi.org/10.3390/met11010058.
[114] Carter LN, Wang X, Read N, Khan R, Aristizabal M, Essa K, et al. Process optimisation of selective laser melting using energy density model for nickel based superalloys. Mater Sci Technol (United Kingdom) 2016;32:657–61. https://doi.org/10.1179/1743284715Y.0000000108.
[115] Cloots M, Uggowitzer PJ, Wegener K. Investigations on the microstructure and crack formation of IN738LC samples processed by selective laser melting using Gaussian and doughnut profiles. Mater Des 2016;89:770–84. https://doi.org/10.1016/j.matdes.2015.10.027.
[116] Zhang S, Lei Y, Chen Z, Wei P, Liu W, Yao S, et al. Effect of laser energy density on the microstructure and texture evolution of hastelloy-x alloy fabricated by laser powder bed fusion. Materials (Basel) 2021;14. https://doi.org/10.3390/ma14154305.
[117] Wang W, Wang S, Zhang X, Chen F, Xu Y, Tian Y. Process parameter optimization for selective laser melting of Inconel 718 superalloy and the effects of subsequent heat treatment on the microstructural evolution and mechanical properties. J Manuf Process 2021;64. https://doi.org/10.1016/j.jmapro.2021.02.004.
[118] Puppala G, Moitra A, Sathyanarayanan S, Kaul R, Sasikala G, Prasad RC, et al. Evaluation of fracture toughness and impact toughness of laser rapid manufactured Inconel-625 structures and their co-relation. Mater Des 2014;59:509–15. https://doi.org/10.1016/j.matdes.2014.03.013.
[119] Bi G, Sun CN, Chen H chi, Ng FL, Ma CCK. Microstructure and tensile properties of superalloy IN100 fabricated by micro-laser aided additive manufacturing. Mater Des 2014;60. https://doi.org/10.1016/j.matdes.2014.04.020.
[120] Li J, Wang HM. Microstructure and mechanical properties of rapid directionally solidified Ni-base superalloy Rene'41 by laser melting deposition manufacturing. Mater Sci Eng A 2010;527. https://doi.org/10.1016/j.msea.2010.04.062.
[121] Pinkerton AJ, Karadge M, Ul Haq Syed W, Li L. Thermal and microstructural aspects of the laser direct metal deposition of waspaloy. J Laser Appl 2006;18. https://doi.org/10.2351/1.2227018.
[122] Jinoop AN, Paul CP, Bindra KS. Laser assisted direct energy deposition of Hastelloy-X. Opt Laser Technol

2019;109:14–9. https://doi.org/10.1016/j.optlastec.2018.07.037.
[123] de Leon Nope G V., Perez-Andrade LI, Corona-Castuera J, Espinosa-Arbelaez DG, Muñoz-Saldaña J, Alvarado-Orozco JM. Study of volumetric energy density limitations on the IN718 mesostructure and microstructure in laser powder bed fusion process. J Manuf Process 2021;64. https://doi.org/10.1016/j.jmapro.2021.02.043.
[124] Zhang X, Xu H, Li Z, Dong A, Du D, Lei L, et al. Effect of the scanning strategy on microstructure and mechanical anisotropy of Hastelloy X superalloy produced by Laser Powder Bed Fusion. Mater Charact 2021;173:110951. https://doi.org/10.1016/j.matchar.2021.110951.
[125] Dinda GP, Dasgupta AK, Mazumder J. Laser aided direct metal deposition of Inconel 625 superalloy: Microstructural evolution and thermal stability. Mater Sci Eng A 2009;509. https://doi.org/10.1016/j.msea.2009.01.009.
[126] Serrano-Munoz I, Mishurova T, Thiede T, Sprengel M, Kromm A, Nadammal N, et al. The residual stress in as-built Laser Powder Bed Fusion IN718 alloy as a consequence of the scanning strategy induced microstructure. Sci Rep 2020;10. https://doi.org/10.1038/s41598-020-71112-9.
[127] Peng K, Duan R, Liu Z, Lv X, Li Q, Zhao F, et al. Cracking behavior of rené 104 nickel-based superalloy prepared by selective laser melting using different scanning strategies. Materials (Basel) 2020;13. https://doi.org/10.3390/ma13092149.
[128] Catchpole-Smith S, Aboulkhair N, Parry L, Tuck C, Ashcroft IA, Clare A. Fractal scan strategies for selective laser melting of 'unweldable' nickel superalloys. Addit Manuf 2017;15:113–22. https://doi.org/10.1016/j.addma.2017.02.002.
[129] Gibson I, Rosen D, Stucker B. Additive Manufacturing Technologies: 3D Printing, Rapid Prototyping, and Direct Digital Manufacturing. 2nd ed. New York: Springer; 2015.
[130] Matthews MJ, Guss G, Khairallah SA, Rubenchik AM, Depond PJ, King WE. Denudation of metal powder layers in laser powder bed fusion processes. Acta Mater 2016;114:33–42.
[131] Traore S, Schneider M, Koutiri I, Coste F, Fabbro R, Charpentier C, et al. Influence of gas atmosphere (Ar or He) on the laser powder bed fusion of a Ni-based alloy. J Mater Process Technol 2021;288. https://doi.org/10.1016/j.jmatprotec.2020.116851.
[132] Zhao Y, Aoyagi K, Yamanaka K, Chiba A. Role of operating and environmental conditions in determining molten pool dynamics during electron beam melting and selective laser melting. Addit Manuf 2020;36:101559. https://doi.org/10.1016/j.addma.2020.101559.
[133] Calta NP, Martin AA, Hammons JA, Nielsen MH, Roehling TT, Fezzaa K, et al. Pressure dependence of the laser-metal interaction under laser powder bed fusion conditions probed by in situ X-ray imaging. Addit Manuf 2020;32. https://doi.org/10.1016/j.addma.2020.101084.
[134] Chen H, Wei Q, Zhang Y, Chen F, Shi Y, Yan W. Powder-spreading mechanisms in powder-bed-based additive manufacturing: Experiments and computational modeling. Acta Mater 2019;179:158–71. https://doi.org/10.1016/j.actamat.2019.08.030.
[135] Nan W, Pasha M, Bonakdar T, Lopez A, Zafar U, Nadimi S, et al. Jamming during particle spreading in additive manufacturing. Powder Technol 2018;338:253–62. https://doi.org/10.1016/J.POWTEC.2018.07.030.
[136] F.-J. Gürtler, Karg M, Dobler M, Kohl S, Tzivilsky I, Schmidt M. Influence of powder distribution on process stability in laser beam melting: Analysis of melt pool dynamics by numerical simulations. 25th Annu. Int. Solid Free. Fabr. Symp. - An Addit. Manuf. Conf. SFF 2014, 2014, p. 1099–117.
[137] Scime L, Beuth J. Anomaly detection and classification in a laser powder bed additive manufacturing process using a trained computer vision algorithm. Addit Manuf 2018;19:114–26. https://doi.org/10.1016/J.ADDMA.2017.11.009.
[138] Foster BK, Reutzel EW, Nassar AR, Hall BT, Brown SW, Dickman CJ. Optical, layerwise monitoring of powder bed fusion. Solid Free. Fabr. Symp. Proc., 2015, p. 295–307.
[139] Sames W. Additive manufacturing of Inconel 718 using electron beam melting: processing, post-processing, & mechanical properties. Texas A&M university, 2015.
[140] Wang D, Wu S, Fu F, Mai S, Yang Y, Liu Y, et al. Mechanisms and characteristics of spatter generation in SLM processing and its effect on the properties. Mater Des 2017;117:121–30. https://doi.org/10.1016/j.matdes.2016.12.060.
[141] Kahnert M, Lutzmann S, Zaeh MF. Layer formations in electron beam sintering. 18th Solid Free Fabr Symp SFF 2007 2007:88–99.
[142] Lun C, Leung A, Marussi S, Atwood RC, Lee PD, Towrie M, et al. In situ X-ray imaging of defect and molten pool dynamics in laser additive manufacturing. Nat Commun 2018;9:1–9. https://doi.org/10.1038/s41467-018-03734-7.
[143] Ly S, Rubenchik AM, Khairallah SA, Guss G, Matthews MJ. Metal vapor micro-jet controls material redistribution in laser powder bed fusion additive manufacturing. Sci Rep 2017;7:1–12. https://doi.org/10.1038/s41598-017-04237-z.

[144] Strondl A, Lyckfeldt O, Brodin H, Ackelid U. Characterization and Control of Powder Properties for Additive Manufacturing. JOM 2015;67:549–54. https://doi.org/10.1007/s11837-015-1304-0.
[145] Hryha E, Dudrova E, Nyborg L. On-line control of processing atmospheres for proper sintering of oxidation-sensitive PM steels. J Mater Process Technol 2012;212:977–87. https://doi.org/10.1016/j.jmatprotec.2011.12.008.
[146] Gasper AND, Hickman D, Ashcroft I, Sharma S, Wang X, Szost B, et al. Oxide and spatter powder formation during laser powder bed fusion of Hastelloy X. Powder Technol 2019;354:333–7. https://doi.org/10.1016/j.powtec.2019.06.004.
[147] Yu H, Hayashi S, Kakehi K, Kuo YL. Study of formed oxides in IN718 alloy during the fabrication by selective laser melting and electron beam melting. Metals (Basel) 2019;9. https://doi.org/10.3390/met9010019.
[148] Yan F, Xiong W, Faierson E, Olson GB. Characterization of nano-scale oxides in austenitic stainless steel processed by powder bed fusion. Scr Mater 2018;155. https://doi.org/10.1016/j.scriptamat.2018.06.011.
[149] Khairallah SA, Anderson AT, Rubenchik A, King WE. Laser powder-bed fusion additive manufacturing: Physics of complex melt flow and formation mechanisms of pores, spatter, and denudation zones. Acta Mater 2016;108:36–45. https://doi.org/10.1016/j.actamat.2016.02.014.
[150] Esmaeilizadeh R, Ali U, Keshavarzkermani A, Mahmoodkhani Y, Marzbanrad E, Toyserkani E. On the effect of spatter particles distribution on the quality of Hastelloy X parts made by laser powder-bed fusion additive manufacturing. J Manuf Process 2019;37:11–20. https://doi.org/10.1016/j.jmapro.2018.11.012.
[151] Eschey C, Lutzmann S, Zaeh MF. Examination of the powder spreading effect in electron beam melting (EBM). Solid Free Fabr 2009.
[152] Debroy T, David SA. Physical processes in fusion welding. Rev Mod Phys 1995;67:85–112. https://doi.org/10.1103/RevModPhys.67.85.
[153] Mukherjee T, Zuback JS, De A, DebRoy T. Printability of alloys for additive manufacturing. Sci Rep 2016;6:1–8. https://doi.org/10.1038/srep19717.
[154] Ahsan F, Ladani L. Temperature Profile, Bead Geometry, and Elemental Evaporation in Laser Powder Bed Fusion Additive Manufacturing Process. JOM 2020;72:429–39. https://doi.org/10.1007/s11837-019-03872-3.
[155] Panwisawas C, Tang YT, Ghoussoub J, Reed RC. Additive Manufacturability of Nickel-Based Superalloys: Composition-Process Induced Vapourization. In: Tin S, Hardy M, Clews J, Cormier J, Feng Q, Marcin J, et al., editors. Superalloys 2020, Springer, Cham; 2020, p. 1024–32. https://doi.org/10.1007/978-3-030-51834-9_100.
[156] Shuai L, Wei Q, Shi Y, Zhang J, Wei L. Micro-Crack Formation and Controlling of Inconel625 Parts Fabricated by Selective Laser Melting. Solid Free Fabr Symp – An Addit Manuf Conf 2016:520–9.
[157] Mostafa A, Picazo Rubio I, Brailovski V, Jahazi M, Medraj M. Structure, Texture and Phases in 3D Printed IN718 Alloy Subjected to Homogenization and HIP Treatments. Metals (Basel) 2017;7:196. https://doi.org/10.3390/met7060196.
[158] Parimi LL, Ravi G, Clark D, Attallah MM. Microstructural and texture development in direct laser fabricated IN718. Mater Charact 2014. https://doi.org/10.1016/j.matchar.2013.12.012.
[159] Deng D, Moverare J, Peng RL, Söderberg H. Microstructure and anisotropic mechanical properties of EBM manufactured Inconel 718 and effects of post heat treatments. Mater Sci Eng A 2017;693:151–63. https://doi.org/10.1016/j.msea.2017.03.085.
[160] Yang J, Li F, Pan A, Yang H, Zhao C, Huang W, et al. Microstructure and grain growth direction of SRR99 single-crystal superalloy by selective laser melting. J Alloys Compd 2019;808. https://doi.org/10.1016/j.jallcom.2019.151740.
[161] Siebörger D, Knake H, Glatzel U. Temperature dependence of the elastic moduli of the nickel-base superalloy CMSX-4 and its isolated phases. Mater Sci Eng A 2001;298:26–33. https://doi.org/10.1016/s0921-5093(00)01318-6.
[162] Gu D, Shi Q, Lin K, Xi L. Microstructure and performance evolution and underlying thermal mechanisms of Ni-based parts fabricated by selective laser melting. Addit Manuf 2018;22. https://doi.org/10.1016/j.addma.2018.05.019.
[163] Hunt JD. Steady state columnar and equiaxed growth of dendrites and eutectic. Mater Sci Eng 1984;65. https://doi.org/10.1016/0025-5416(84)90201-5.
[164] Gäumann M, Bezençon C, Canalis P, Kurz W. Single-crystal laser deposition of superalloys: Processing-microstructure maps. Acta Mater 2001;49:1051–62. https://doi.org/10.1016/S1359-6454(00)00367-0.
[165] Helmer H, Bauereiß A, Singer RF, Körner C. Grain structure evolution in Inconel 718 during selective electron beam melting. Mater Sci Eng A 2016;668:180–7. https://doi.org/10.1016/j.msea.2016.05.046.
[166] Murray SP, Pusch KM, Polonsky AT, Torbet CJ, Seward GGE, Zhou N, et al. A defect-resistant Co–Ni superalloy for 3D printing. Nat Commun 2020;11. https://doi.org/10.1038/s41467-020-18775-0.
[167] Zhang Z, Han Q, Yang S, Yin Y, Gao J. Laser powder bed fusion of advanced submicrometer TiB2

reinforced high-performance Ni-based composite. Mater Sci Eng A 2021;817:141416. https://doi.org/10.1016/j.msea.2021.141416.
[168] Chen L, Sun Y, Li L, Ren X. Microstructural evolution and mechanical properties of selective laser melted a nickel-based superalloy after post treatment. Mater Sci Eng A 2020;792. https://doi.org/10.1016/j.msea.2020.139649.
[169] Jiang R, Mostafaei A, Pauza J, Kantzos C, Rollett AD. Varied heat treatments and properties of laser powder bed printed Inconel 718. Mater Sci Eng A 2019;755:170–80. https://doi.org/10.1016/j.msea.2019.03.103.
[170] Trosch T, Strößner J, Völkl R, Glatzel U. Microstructure and mechanical properties of selective laser melted Inconel 718 compared to forging and casting. Mater Lett 2016;164:428–31. https://doi.org/10.1016/j.matlet.2015.10.136.
[171] Park JH, Bang GB, Lee KA, Son Y, Kim WR, Kim HG. Effect on microstructural and mechanical properties of Inconel 718 superalloy fabricated by selective laser melting with rescanning by low energy density. J Mater Res Technol 2021;10. https://doi.org/10.1016/j.jmrt.2020.12.053.
[172] Sunny S, Mathews R, Yu H, Malik A. Effects of microstructure and inherent stress on residual stress induced during powder bed fusion with roller burnishing. Int J Mech Sci 2022;219. https://doi.org/10.1016/j.ijmecsci.2022.107092.
[173] Popov V, Katz-Demyanetz A, Bamberger M. Heat transfer and phase formation through EBM 3D-printing of Ti-6Al-4V cylindrical parts. Defect Diffus. Forum, vol. 383, 2018. https://doi.org/10.4028/www.scientific.net/DDF.383.190.
[174] Tian Y, McAllister D, Colijn H, Mills M, Farson D, Nordin M, et al. Rationalization of microstructure heterogeneity in INCONEL 718 builds made by the direct laser additive manufacturing process. Metall Mater Trans A Phys Metall Mater Sci 2014. https://doi.org/10.1007/s11661-014-2370-6.
[175] Rielli VV, Piglione A, Pham M-S, Primig S. On the detailed morphological and chemical evolution of phases during laser powder bed fusion and common post-processing heat treatments of IN718. Addit Manuf 2022;50:102540. https://doi.org/10.1016/j.addma.2021.102540.
[176] Seah KHW, Hemanth J, Sharma SC. Effect of the cooling rate on the dendrite arm spacing and the ultimate tensile strength of cast iron. J Mater Sci 1998;33. https://doi.org/10.1023/A:1004321007806.
[177] Murr LE, Gaytan SM, Ramirez DA, Martinez E, Hernandez J, Amato KN, et al. Metal Fabrication by Additive Manufacturing Using Laser and Electron Beam Melting Technologies. J Mater Sci Technol 2012;28:1–14. https://doi.org/10.1016/S1005-0302(12)60016-4.
[178] Sames WJ, Unocic KA, Helmreich GW, Kirka MM, Medina F, Dehoff RR, et al. Feasibility of in situ controlled heat treatment (ISHT) of Inconel 718 during electron beam melting additive manufacturing. Addit Manuf 2017;13. https://doi.org/10.1016/j.addma.2016.09.001.
[179] Nandwana P, Kirka M, Okello A, Dehoff R. Electron beam melting of Inconel 718: effects of processing and post-processing. Mater Sci Technol (United Kingdom) 2018;34. https://doi.org/10.1080/02670836.2018.1424379.
[180] Divya VD, Muñoz-Moreno R, Messé OMDM, Barnard JS, Baker S, Illston T, et al. Microstructure of selective laser melted CM247LC nickel-based superalloy and its evolution through heat treatment. Mater Charact 2016;114:62–74. https://doi.org/10.1016/j.matchar.2016.02.004.
[181] Babu SS, Raghavan N, Raplee J, Foster SJ, Frederick C, Haines M, et al. Additive Manufacturing of Nickel Superalloys: Opportunities for Innovation and Challenges Related to Qualification. Metall Mater Trans A 2018;49:3764–80. https://doi.org/10.1007/s11661-018-4702-4.
[182] Zhong C, Gasser A, Kittel J, Wissenbach K, Poprawe R. Improvement of material performance of Inconel 718 formed by high deposition-rate laser metal deposition. Mater Des 2016;98. https://doi.org/10.1016/j.matdes.2016.03.006.
[183] Kuo YL, Kamigaichi A, Kakehi K. Characterization of Ni-Based Superalloy Built by Selective Laser Melting and Electron Beam Melting. Metall Mater Trans A Phys Metall Mater Sci 2018;49:3831–7. https://doi.org/10.1007/s11661-018-4769-y.
[184] Páramo-Kañetas P, Özturk U, Calvo J, Cabrera JM, Guerrero-Mata M. High-temperature deformation of delta-processed Inconel 718. J Mater Process Technol 2018;255:204–11. https://doi.org/10.1016/j.jmatprotec.2017.12.014.
[185] Pröbstle M, Neumeier S, Hopfenmüller J, Freund LP, Niendorf T, Schwarze D, et al. Superior creep strength of a nickel-based superalloy produced by selective laser melting. Mater Sci Eng A 2016;674:299–307. https://doi.org/10.1016/j.msea.2016.07.061.
[186] Chen L, Sun Y, Li L, Ren X. Microstructure evolution, mechanical properties, and strengthening mechanism of TiC reinforced Inconel 625 nanocomposites fabricated by selective laser melting. Mater Sci Eng A 2020;792. https://doi.org/10.1016/j.msea.2020.139655.
[187] Ghiaasiaan R, Ahmad N, Gradl PR, Shao S, Shamsaei N. Additively manufactured Haynes 282: effect of unimodal vs. bimodal γ′- microstructure on mechanical properties. Mater Sci Eng A 2022;831:142234.

https://doi.org/10.1016/j.msea.2021.142234.
[188] Wessman A, Cormier J, Hamon F, Rainey K, Tin S, Tiparti D, et al. Microstructure and Mechanical Properties of Additively Manufactured Rene 65. Miner. Met. Mater. Ser., 2020. https://doi.org/10.1007/978-3-030-51834-9_94.
[189] Ahmad N, Ghiaasiaan R, Gradl PR, Shao S, Shamsaei N. Revealing deformation mechanisms in additively manufactured Alloy 718: Cryogenic to elevated temperatures. Mater Sci Eng A 2022;849:143528. https://doi.org/10.1016/j.msea.2022.143528.
[190] Ghiaasiaan R, Muhammad M, Gradl PR, Shao S, Shamsaei N. Superior tensile properties of Hastelloy X enabled by additive manufacturing. Mater Res Lett 2021;9:308–14. https://doi.org/10.1080/21663831.2021.1911870.
[191] Wang S, Ning J, Zhu L, Yang Z, Yan W, Dun Y, et al. Role of porosity defects in metal 3D printing: Formation mechanisms, impacts on properties and mitigation strategies. Mater Today n.d.
[192] Yamashita Y, Murakami T, Mihara R, Okada M, Murakami Y. Defect analysis and fatigue design basis for Ni-based superalloy 718 manufactured by selective laser melting. Int J Fatigue 2018;117:485–95. https://doi.org/10.1016/j.ijfatigue.2018.08.002.
[193] Tang M, Pistorius PC, Beuth JL. Prediction of lack-of-fusion porosity for powder bed fusion. Addit Manuf 2017;14:39–48. https://doi.org/10.1016/j.addma.2016.12.001.
[194] Ning J, Sievers DE, Garmestani H, Liang SY. Analytical modeling of part porosity in metal additive manufacturing. Int J Mech Sci 2020;172:105428. https://doi.org/10.1016/j.ijmecsci.2020.105428.
[195] Ricker RE, Heigel JC, Lane BM, Zhirnov I, Levine LE. Topographic Measurement of Individual Laser Tracks in Alloy 625 Bare Plates. Integr Mater Manuf Innov 2019;8:521–36. https://doi.org/10.1007/s40192-019-00157-0.
[196] Scipioni U, Wolfer AJ, Matthews MJ, Delplanque JR, Schoenung JM. On the limitations of Volumetric Energy Density as a design parameter for Selective Laser Melting. JMADE 2017;113:331–40. https://doi.org/10.1016/j.matdes.2016.10.037.
[197] Hojjatzadeh SMH, Parab ND, Guo Q, Qu M, Xiong L, Zhao C, et al. Direct observation of pore formation mechanisms during LPBF additive manufacturing process and high energy density laser welding. Int J Mach Tools Manuf 2020:103555. https://doi.org/10.1016/j.ijmachtools.2020.103555.
[198] Panwisawas C, Gong Y, Tony Y, Reed RC, Shinjo J. Additive manufacturability of superalloys : Process-induced porosity , cooling rate and metal vapour. Addit Manuf 2021;47:102339. https://doi.org/10.1016/j.addma.2021.102339.
[199] Rabin BH, Smolik GR, Korth GE. Characterization of entrapped gases in rapidly solidified powders. Mater Sci Eng A 1990;124:1–7. https://doi.org/10.1016/0921-5093(90)90328-Z.
[200] Chen G, Zhao SY, Tan P, Wang J, Xiang CS, Tang HP. A comparative study of Ti-6Al-4V powders for additive manufacturing by gas atomization, plasma rotating electrode process and plasma atomization. Powder Technol 2018;333:38–46. https://doi.org/10.1016/j.powtec.2018.04.013.
[201] Qi H, Azer M, Ritter A. Studies of Standard Heat Treatment Effects on Microstructure and Mechanical Properties of Laser Net Shape Manufactured INCONEL 718 n.d. https://doi.org/10.1007/s11661-009-9949-3.
[202] Zhong C, Chen J, Linnenbrink S, Gasser A, Sui S, Poprawe R. A comparative study of Inconel 718 formed by High Deposition Rate Laser Metal Deposition with GA powder and PREP powder. Mater Des 2016;107:386–92. https://doi.org/https://doi.org/10.1016/j.matdes.2016.06.037.
[203] Denda T, Bretz PL, Tien JK. Inclusion size effect on the fatigue crack propagation mechanism and fracture mechanics of a superalloy. Metall Trans A 1992;23:519–26. https://doi.org/10.1007/BF02801169.
[204] Qiu C, Chen H, Liu Q, Yue S, Wang H. On the solidification behaviour and cracking origin of a nickel-based superalloy during selective laser melting. Mater Charact 2019;148:330–44. https://doi.org/10.1016/j.matchar.2018.12.032.
[205] Xu X, Ding J, Ganguly S, Williams S. Investigation of process factors affecting mechanical properties of INCONEL 718 superalloy in wire + arc additive manufacture process. J Mater Process Technol 2019;265:201–9. https://doi.org/10.1016/j.jmatprotec.2018.10.023.
[206] Marchese G, Basile G, Bassini E, Aversa A, Lombardi M, Ugues D, et al. Study of the microstructure and cracking mechanisms of hastelloy X produced by laser powder bed fusion. Materials (Basel) 2018;11. https://doi.org/10.3390/ma11010106.
[207] Zhang YN, Cao X, Wanjara P, Medraj M. Oxide films in laser additive manufactured Inconel 718. Acta Mater 2013;61:6562–76. https://doi.org/https://doi.org/10.1016/j.actamat.2013.07.039.
[208] Lee PD, Quested PN, McLean M. Modelling of Marangoni effects in electron beam melting. Philos Trans R Soc A Math Phys Eng Sci 1998;356. https://doi.org/10.1098/rsta.1998.0207.
[209] Liu Y, Kang M, Wu Y, Wang M, Gao H, Otsuka T, et al. Proceedings of the 9th International Symposium on Superalloy 718 & Derivatives: Energy, Aerospace, and Industrial Applications. 2018.
[210] Case Study 05: Powder degradation. LPW Technol n.d.

[211] Kakehi K, Banoth S, Kuo YL, Hayashi S. Effect of yttrium addition on creep properties of a Ni-base superalloy built up by selective laser melting. Scr Mater 2020;183:71–4. https://doi.org/10.1016/j.scriptamat.2020.03.014.
[212] Chen Z, Wei P, Zhang S, Lu B, Zhang L, Yang X, et al. Graphene reinforced nickel-based superalloy composites fabricated by additive manufacturing. Mater Sci Eng A 2020;769:138484. https://doi.org/10.1016/j.msea.2019.138484.
[213] Ho I-T, Hsu T-H, Chang Y-J, Li C-W, Chang K-C, Tin S, et al. Effects of CoAl2O4 inoculants on microstructure and mechanical properties of IN718 processed by selective laser melting. Addit Manuf 2020;35:101328. https://doi.org/https://doi.org/10.1016/j.addma.2020.101328.
[214] Han Q, Gu Y, Setchi R, Lacan F, Johnston R, Evans SL, et al. Additive manufacturing of high-strength crack-free Ni-based Hastelloy X superalloy. Addit Manuf 2019;30:100919. https://doi.org/10.1016/j.addma.2019.100919.
[215] Bokstein BS, Epishin AI, Link T, Esin VA, Rodin AO, Svetlov IL. Model for the porosity growth in single-crystal nickel-base superalloys during homogenization. Scr Mater 2007;57:801–4. https://doi.org/10.1016/j.scriptamat.2007.07.012.
[216] Tammas-Williams S, Withers PJ, Todd I, Prangnell PB. Porosity regrowth during heat treatment of hot isostatically pressed additively manufactured titanium components. Scr Mater 2016;122:72–6. https://doi.org/10.1016/j.scriptamat.2016.05.002.
[217] Zhang X, Chen H, Xu L, Xu J, Ren X, Chen X. Cracking mechanism and susceptibility of laser melting deposited Inconel 738 superalloy. Mater Des 2019;183:108105. https://doi.org/10.1016/j.matdes.2019.108105.
[218] Elsaß M, Frommherz M, Scholz A, Oechsner M. Interdiffusion in MCrAlY coated nickel-base superalloys. Surf Coatings Technol 2016;307:565–73. https://doi.org/10.1016/j.surfcoat.2016.09.049.
[219] N. Carter L, M. Attallah M, C. Reed R. Laser powder bed fabrication of nickel-base superalloys: influence of parameters; characterisation, quantification and mitigation of cracking. Superalloys 2012 2012:577--586.
[220] DuPont JN, Lippold JC, Kiser SD. Welding metallurgy and weldability of nickel-base alloys. John Wiley & Sons; 2009.
[221] Tang YT, Panwisawas C, Ghoussoub JN, Gong Y, Clark J, Németh A, et al. Alloys-By-Design: Application to New Superalloys for Additive Manufacturing. Acta Mater 2020. https://doi.org/10.1016/j.actamat.2020.09.023.
[222] Böllinghaus T, Herold H, Cross CE, Lippold JC. Hot cracking phenomena in welds II. 2008. https://doi.org/10.1007/978-3-540-78628-3.
[223] Han Q, Gu Y, Soe S, Lacan F, Setchi R. Effect of hot cracking on the mechanical properties of Hastelloy X superalloy fabricated by laser powder bed fusion additive manufacturing. Opt Laser Technol 2020;124:105984. https://doi.org/10.1016/j.optlastec.2019.105984.
[224] Chen Y, Zhang K, Huang J, Hosseini SRE, Li Z. Characterization of heat affected zone liquation cracking in laser additive manufacturing of Inconel 718. Mater Des 2016;90:586–94. https://doi.org/https://doi.org/10.1016/j.matdes.2015.10.155.
[225] MB H, D A, R L, M H, G. M. Nickel based superalloy welding practices for industrial gas turbine applications. Sci Technol Weld Join 2004;9:13.
[226] Ramirez AJ, Lippold JC. High temperature behavior of Ni-base weld metal Part II - Insight into the mechanism for ductility dip cracking. Mater Sci Eng A 2004;380:245–58. https://doi.org/10.1016/j.msea.2004.03.075.
[227] Young GA, Capobianco TE, Penik MA, Morris BW, McGee JJ. The mechanism of ductility dip cracking in nickel-chromium alloys. Weld J 2008;87.
[228] Schröder J, Evans A, Mishurova T, Ulbricht A, Sprengel M, Serrano-Munoz I, et al. Diffraction-Based Residual Stress Characterization in Laser Additive Manufacturing of Metals. Metals (Basel) 2021;11:1830. https://doi.org/10.3390/met11111830.
[229] Wang X, Chou K. The effects of stress relieving heat treatment on the microstructure and residual stress of Inconel 718 fabricated by laser metal powder bed fusion additive manufacturing process. J Manuf Process 2019;48:154–63. https://doi.org/10.1016/j.jmapro.2019.10.027.
[230] Schröder J, Mishurova T, Fritsch T, Serrano-Munoz I, Evans A, Sprengel M, et al. On the influence of heat treatment on microstructure and mechanical behavior of laser powder bed fused Inconel 718. Mater Sci Eng A 2021;805:140555. https://doi.org/10.1016/j.msea.2020.140555.
[231] Mishurova T, Cabeza S, Thiede T, Nadammal N, Kromm A, Klaus M, et al. The Influence of the Support Structure on Residual Stress and Distortion in SLM Inconel 718 Parts. Metall Mater Trans A 2018;49:3038–46. https://doi.org/10.1007/s11661-018-4653-9.
[232] Fritsch T, Sprengel M, Evans A, Farahbod-Sternahl L, Saliwan-Neumann R, Hofmann M, et al. On the determination of residual stresses in additively manufactured lattice structures. J Appl Crystallogr

2021;54:228–36. https://doi.org/10.1107/S1600576720015344.
[233] Yeung H, Lane B, Fox J. Part geometry and conduction-based laser power control for powder bed fusion additive manufacturing. Addit Manuf 2019;30:100844. https://doi.org/10.1016/j.addma.2019.100844.
[234] Onuike B, Bandyopadhyay A. Additive manufacturing of Inconel 718 – Ti6Al4V bimetallic structures. Addit Manuf 2018;22:844–51. https://doi.org/10.1016/j.addma.2018.06.025.
[235] Mukherjee T, Zhang W, DebRoy T. An improved prediction of residual stresses and distortion in additive manufacturing. Comput Mater Sci 2017;126:360–72. https://doi.org/10.1016/j.commatsci.2016.10.003.
[236] Serrano-Munoz I, Evans A, Mishurova T, Sprengel M, Pirling T, Kromm A, et al. The Importance of Subsurface Residual Stress in Laser Powder Bed Fusion IN718. Adv Eng Mater 2022;24:2100895. https://doi.org/10.1002/adem.202100895.
[237] Residual Stresses in Selective Laser Melted Samples of a Nickel Based Superalloy. Residual Stress. 2018, vol. 6, 2018. https://doi.org/10.21741/9781945291890-41.
[238] Mercelis P, Kruth JP. Residual stresses in selective laser sintering and selective laser melting. Rapid Prototyp J 2006;12:254–65. https://doi.org/10.1108/13552540610707013.
[239] Moat RJ, Pinkerton AJ, Li L, Withers PJ, Preuss M. Residual stresses in laser direct metal deposited Waspaloy. Mater Sci Eng A 2011;528:2288–98. https://doi.org/10.1016/j.msea.2010.12.010.
[240] Zhang T, Collins DM, Dunne FPE, Shollock BA. Crystal plasticity and high-resolution electron backscatter diffraction analysis of full-field polycrystal Ni superalloy strains and rotations under thermal loading. Acta Mater 2014;80. https://doi.org/10.1016/j.actamat.2014.07.036.
[241] Cabeza S, Özcan B, Cormier J, Pirling T, Polenz S, Marquardt F, et al. Strain Monitoring During Laser Metal Deposition of Inconel 718 by Neutron Diffraction, 2020, p. 1033–45. https://doi.org/10.1007/978-3-030-51834-9_101.
[242] Mukherjee T, Manvatkar V, De A, DebRoy T. Mitigation of thermal distortion during additive manufacturing. Scr Mater 2017;127:79–83. https://doi.org/10.1016/j.scriptamat.2016.09.001.
[243] Serrano-Munoz I, Ulbricht A, Fritsch T, Mishurova T, Kromm A, Hofmann M, et al. Scanning Manufacturing Parameters Determining the Residual Stress State in LPBF IN718 Small Parts. Adv Eng Mater 2021;23:2100158. https://doi.org/10.1002/adem.202100158.
[244] Nadammal N, Cabeza S, Mishurova T, Thiede T, Kromm A, Seyfert C, et al. Effect of hatch length on the development of microstructure, texture and residual stresses in selective laser melted superalloy Inconel 718. Mater Des 2017;134:139–50. https://doi.org/10.1016/j.matdes.2017.08.049.
[245] Nadammal N, Mishurova T, Fritsch T, Serrano-Munoz I, Kromm A, Haberland C, et al. Critical role of scan strategies on the development of microstructure, texture, and residual stresses during laser powder bed fusion additive manufacturing. Addit Manuf 2021;38:101792. https://doi.org/10.1016/j.addma.2020.101792.
[246] Serrano-Munoz I, Mishurova T, Thiede T, Sprengel M, Kromm A, Nadammal N, et al. The residual stress in as-built Laser Powder Bed Fusion IN718 alloy as a consequence of the scanning strategy induced microstructure. Sci Rep 2020;10:14645. https://doi.org/10.1038/s41598-020-71112-9.
[247] Wang Z, Denlinger E, Michaleris P, Stoica AD, Ma D, Beese AM. Residual stress mapping in Inconel 625 fabricated through additive manufacturing: Method for neutron diffraction measurements to validate thermomechanical model predictions. Mater Des 2017;113:169–77. https://doi.org/https://doi.org/10.1016/j.matdes.2016.10.003.
[248] Marchese G, Lorusso M, Parizia S, Bassini E, Lee JW, Calignano F, et al. Influence of heat treatments on microstructure evolution and mechanical properties of Inconel 625 processed by laser powder bed fusion. Mater Sci Eng A 2018;729:64–75. https://doi.org/10.1016/j.msea.2018.05.044.
[249] ASTM International. E1417/E1417M-16 Liquid Penetrant Testing. West Conshohocken, PA: ASTM International; 2016. https://doi.org/10.1520/E1417.
[250] ASTM International. E709-15 Standard Guide for Magnetic Particle Testing. West Conshohocken, PA: ASTM International; 2015. https://doi.org/https://doi.org/10.1520/E0709-15.
[251] Du W, Bai Q, Wang Y, Zhang B. Eddy current detection of subsurface defects for additive/subtractive hybrid manufacturing. Int J Adv Manuf Technol 2018;95:3185–95. https://doi.org/10.1007/s00170-017-1354-2.
[252] Lopez A, Bacelar R, Pires I, Santos TG, Sousa JP, Quintino L. Non-destructive testing application of radiography and ultrasound for wire and arc additive manufacturing. Addit Manuf 2018;21:298–306. https://doi.org/10.1016/j.addma.2018.03.020.
[253] Ye D, Hong GS, Zhang Y, Zhu K, Fuh JYH. Defect detection in selective laser melting technology by acoustic signals with deep belief networks. Int J Adv Manuf Technol 2018;96:2791–801. https://doi.org/10.1007/s00170-018-1728-0.
[254] Waller JM, Parker BH, Hodges KL, Burke ER, Walker JL. Nondestructive Evaluation of Additive Manufacturing State-of-the-Discipline Report. Nasa/Tm-2014-218560 2014:1–36. https://doi.org/10.13140/RG.2.1.1227.9844.

[255] Townsend A, Senin N, Blunt L, Leach RK, Taylor JS. Surface texture metrology for metal additive manufacturing: a review. Precis Eng 2016;46:34–47. https://doi.org/10.1016/j.precisioneng.2016.06.001.
[256] Todorov EI, Boulware P, Gaah K. Demonstration of array eddy current technology for real-time monitoring of laser powder bed fusion additive manufacturing process. In: Shull PJ, editor. Nondestruct. Charact. Monit. Adv. Mater. Aerospace, Civ. Infrastructure, Transp. XII, SPIE; 2018, p. 40. https://doi.org/10.1117/12.2297511.
[257] Yusa N, Chen W, Wang J, Hashizume H. Fabrication of imitative cracks by 3D printing for electromagnetic nondestructive testing and evaluations. Case Stud Nondestruct Test Eval 2016;5:9–14. https://doi.org/10.1016/j.csndt.2016.03.004.
[258] Mandache C, Krause TW, Clapham L. Investigation of Optimum Field Amplitude for Stress Dependence of Magnetic Barkhausen Noise. IEEE Trans Magn 2007;43:3976–83. https://doi.org/10.1109/TMAG.2007.904793.
[259] Lu QY, Wong CH. Additive manufacturing process monitoring and control by non-destructive testing techniques: challenges and in-process monitoring. Virtual Phys Prototyp 2018;13:39–48. https://doi.org/10.1080/17452759.2017.1351201.
[260] Ehlers H, Pelkner M, Thewes R. Heterodyne Eddy Current Testing Using Magnetoresistive Sensors for Additive Manufacturing Purposes. IEEE Sens J 2020;20:5793–800. https://doi.org/10.1109/JSEN.2020.2973547.
[261] Smith RJ, Hirsch M, Patel R, Li W, Clare AT, Sharples SD. Spatially resolved acoustic spectroscopy for selective laser melting. J Mater Process Technol 2016;236:93–102. https://doi.org/10.1016/j.jmatprotec.2016.05.005.
[262] Zió G, Chlebus E, Szymczyk P, Kurzac J. Application of X-ray CT method for discontinuity and porosity detection in 316L stainless steel parts produced with SLM technology. Arch Civ Mech Eng 2014;14:608–14. https://doi.org/10.1016/j.acme.2014.02.003.
[263] Kasperovich G, Haubrich J, Gussone J, Requena G. Correlation between porosity and processing parameters in TiAl6V4 produced by selective laser melting. Mater Des 2016;105:160–70. https://doi.org/10.1016/j.matdes.2016.05.070.
[264] Salarian M, Asgari H, Vlasea M. Pore space characteristics and corresponding effect on tensile properties of Inconel 625 fabricated via laser powder bed fusion. Mater Sci Eng A 2020;769:138525. https://doi.org/10.1016/j.msea.2019.138525.
[265] Carter LN, Martin C, Withers PJ, Attallah MM. The influence of the laser scan strategy on grain structure and cracking behaviour in SLM powder-bed fabricated nickel superalloy. J Alloys Compd 2014;615:338–47.
[266] Naragani D, Sangid MD, Shade PA, Schuren JC, Sharma H, Park JS, et al. Investigation of fatigue crack initiation from a non-metallic inclusion via high energy x-ray diffraction microscopy. Acta Mater 2017;137:71–84. https://doi.org/10.1016/j.actamat.2017.07.027.
[267] Karme A, Kallonen A, Matilainen VP, Piili H, Salminen A. Possibilities of CT Scanning as Analysis Method in Laser Additive Manufacturing. Phys Procedia 2015;78:347–56. https://doi.org/10.1016/j.phpro.2015.11.049.
[268] Gu D, Shi X, Poprawe R, Bourell DL, Setchi R, Zhu J. Material-structure-performance integrated laser-metal additive manufacturing. Science (80-) 2021;372. https://doi.org/10.1126/science.abg1487.
[269] Guo Q, Zhao C, Escano LI, Young Z, Xiong L, Fezzaa K, et al. Transient dynamics of powder spattering in laser powder bed fusion additive manufacturing process revealed by in-situ high-speed high-energy x-ray imaging. Acta Mater 2018;151:169–80. https://doi.org/10.1016/j.actamat.2018.03.036.
[270] Wang F, Mao H, Zhang D, Zhao X, Shen Y. Online study of cracks during laser cladding process based on acoustic emission technique and finite element analysis. Appl Surf Sci 2008;255:3267–75. https://doi.org/10.1016/j.apsusc.2008.09.039.
[271] Lott P, Schleifenbaum H, Meiners W, Wissenbach K, Hinke C, Bültmann J. Design of an optical system for the in situ process monitoring of Selective Laser Melting (SLM). Phys Procedia 2011;12:683–90. https://doi.org/10.1016/j.phpro.2011.03.085.
[272] Everton SK, Hirsch M, Stavroulakis PI, Leach RK, Clare AT. Review of in-situ process monitoring and in-situ metrology for metal additive manufacturing. Mater Des 2016;95:431–45. https://doi.org/10.1016/j.matdes.2016.01.099.
[273] Raplee J, Plotkowski A, Kirka MM, Dinwiddie R, Okello A, Dehoff RR, et al. Thermographic Microstructure Monitoring in Electron Beam Additive Manufacturing. Sci Rep 2017;7:1–16. https://doi.org/10.1038/srep43554.
[274] Mohr G, Altenburg SJ, Ulbricht A, Heinrich P, Baum D, Maierhofer C, et al. In-situ defect detection in laser powder bed fusion by using thermography and optical tomography—comparison to computed tomography. Metals (Basel) 2020;10. https://doi.org/10.3390/met10010103.
[275] Mireles J, Ridwan S, Morton PA, Hinojos A, Wicker RB. Analysis and correction of defects within parts

fabricated using powder bed fusion technology. Surf Topogr Metrol Prop 2015;3:034002. https://doi.org/10.1088/2051-672X/3/3/034002.
[276] Liu F, Lin X, Yang G, Song M, Chen J, Huang W. Microstructure and residual stress of laser rapid formed Inconel 718 nickel-base superalloy. Opt Laser Technol 2011;43:208–13. https://doi.org/10.1016/j.optlastec.2010.06.015.
[277] Choi JP, Shin GH, Yang S, Yang DY, Lee JS, Brochu M, et al. Densification and microstructural investigation of Inconel 718 parts fabricated by selective laser melting. Powder Technol 2017;310:60–6. https://doi.org/10.1016/j.powtec.2017.01.030.
[278] Nadammal N, Cabeza S, Mishurova T, Thiede T, Kromm A, Seyfert C, et al. Effect of hatch length on the development of microstructure, texture and residual stresses in selective laser melted superalloy Inconel 718. Mater Des 2017;134:139–50. https://doi.org/10.1016/j.matdes.2017.08.049.
[279] Terner M, Lee J, Marchese G, Biamino S, Hong HU. Electron backscattered diffraction to estimate residual stress levels of a superalloy produced by laser powder bed fusion and subsequent heat treatments. Materials (Basel) 2020;13:1–18. https://doi.org/10.3390/ma13204643.
[280] Qiao G, Zhang B, Bai Q, Dilnoza Y. Effect of Heat Treatment on Microstructure and Residual Stress of GH3536 Superalloy Fabricated by Selective Laser Melting. J Mater Eng Perform 2021;30. https://doi.org/10.1007/s11665-021-06094-4.
[281] Carlsson S, Larsson PL. On the determination of residual stress and strain fields by sharp indentation testing. Part II: Experimental investigation. Acta Mater 2001;49. https://doi.org/10.1016/S1359-6454(01)00123-9.
[282] Carlsson S, Larsson PL. On the determination of residual stress and strain fields by sharp indentation testing. Part I: Theoretical and numerical analysis. Acta Mater 2001;49. https://doi.org/10.1016/S1359-6454(01)00122-7.
[283] Schajer GS. Measurement of non-uniform residual stresses using the hole- drilling method. part i-stress calculation procedures. J Eng Mater Technol Trans ASME 1988;110. https://doi.org/10.1115/1.3226059.
[284] Pynn R. Neutron Scattering—A Non-destructive Microscope for Seeing Inside Matter, 2009. https://doi.org/10.1007/978-0-387-09416-8_2.
[285] Bartlett JL, Croom BP, Burdick J, Henkel D, Li X. Revealing mechanisms of residual stress development in additive manufacturing via digital image correlation. Addit Manuf 2018;22:1–12. https://doi.org/10.1016/j.addma.2018.04.025.
[286] Gouge M, Denlinger E, Irwin J, Li C, Michaleris P. Experimental validation of thermo-mechanical part-scale modeling for laser powder bed fusion processes. Addit Manuf 2019;29:100771. https://doi.org/https://doi.org/10.1016/j.addma.2019.06.022.
[287] Fitzpatrick ME, Fry AT, Holdway P, Kandil FA, Shackleton J, Suominen L. Determination of residual stresses by X-ray diffraction. Teddington, UK: National Physical Laboratory; 2005.
[288] Watkins T, Bilheux H, An K, Payzant A, Dehoff R, Duty C, et al. Neutron characterization for additive manufacturing. Adv Mater Process 2013;171:23–7.
[289] du Plessis A, Yadroitsev I, Yadroitsava I, Le Roux SG. X-Ray Microcomputed Tomography in Additive Manufacturing: A Review of the Current Technology and Applications. 3D Print Addit Manuf 2018;5:227–47. https://doi.org/10.1089/3dp.2018.0060.
[290] Schmeiser F, Krohmer E, Schell N, Uhlmann E, Reimers W. Experimental observation of stress formation during selective laser melting using in situ X-ray diffraction. Addit Manuf 2020;32:101028. https://doi.org/10.1016/j.addma.2019.101028.
[291] Schmeiser F, Krohmer E, Schell N, Uhlmann E, Reimers W. Internal Stress Evolution and Subsurface Phase Transformation in Titanium Parts Manufactured by Laser Powder Bed Fusion—An In Situ X-Ray Diffraction Study. Adv Eng Mater 2021;23:2001502. https://doi.org/10.1002/adem.202001502.
[292] Uhlmann E, Krohmer E, Schmeiser F, Schell N, Reimers W. A laser powder bed fusion system for in situ x-ray diffraction with high-energy synchrotron radiation. Rev Sci Instrum 2020;91:075104. https://doi.org/10.1063/1.5143766.
[293] Sangid MD, Book TA, Naragani D, Rotella J, Ravi P, Finch A, et al. Role of heat treatment and build orientation in the microstructure sensitive deformation characteristics of IN718 produced via SLM additive manufacturing. Addit Manuf 2018;22:479–96. https://doi.org/10.1016/j.addma.2018.04.032.
[294] Grasso M, Colosimo BM. Process defects and in situ monitoring methods in metal powder bed fusion: a review. Meas Sci Technol 2017;28:044005. https://doi.org/10.1088/1361-6501/aa5c4f.
[295] Boone N, Zhu C, Smith C, Todd I, Willmott JR. Thermal near infrared monitoring system for electron beam melting with emissivity tracking. Addit Manuf 2018;22:601–5. https://doi.org/10.1016/j.addma.2018.06.004.
[296] Tapia G, Elwany A. A Review on Process Monitoring and Control in Metal-Based Additive Manufacturing. J Manuf Sci Eng 2014;136. https://doi.org/10.1115/1.4028540.
[297] McNeil JL, Sisco K, Frederick C, Massey M, Carver K, List F, et al. In-Situ Monitoring for Defect

Identification in Nickel Alloy Complex Geometries Fabricated by L-PBF Additive Manufacturing. Metall Mater Trans A 2020;51:6528–45. https://doi.org/10.1007/s11661-020-06036-0.
[298] Bartlett JL, Heim FM, Murty Y V., Li X. In situ defect detection in selective laser melting via full-field infrared thermography. Addit Manuf 2018;24:595–605. https://doi.org/10.1016/j.addma.2018.10.045.
[299] Berumen S, Bechmann F, Lindner S, Kruth J-P, Craeghs T. Quality control of laser- and powder bed-based Additive Manufacturing (AM) technologies. Phys Procedia 2010;5:617–22. https://doi.org/10.1016/j.phpro.2010.08.089.
[300] Marziano V, Pugliese A, Merler S, Ajelli M. Detecting a Surprisingly Low Transmission Distance in the Early Phase of the 2009 Influenza Pandemic. Sci Rep 2017;7:12324. https://doi.org/10.1038/s41598-017-12415-2.
[301] Choo H, Sham K-L, Bohling J, Ngo A, Xiao X, Ren Y, et al. Effect of laser power on defect, texture, and microstructure of a laser powder bed fusion processed 316L stainless steel. Mater Des 2019;164:107534. https://doi.org/10.1016/j.matdes.2018.12.006.
[302] Lhuissier P, Bataillon X, Maestre C, Sijobert J, Cabrol E, Bertrand P, et al. In situ 3D X-ray microtomography of laser-based powder-bed fusion (L-PBF)—A feasibility study. Addit Manuf 2020;34:101271. https://doi.org/10.1016/j.addma.2020.101271.
[303] Zhao C, Fezzaa K, Cunningham RW, Wen H, De Carlo F, Chen L, et al. Real-time monitoring of laser powder bed fusion process using high-speed X-ray imaging and diffraction. Sci Rep 2017;7:1–11. https://doi.org/10.1038/s41598-017-03761-2.
[304] Kenel C, Grolimund D, Li X, Panepucci E, Samson VA, Sanchez DF, et al. In situ investigation of phase transformations in Ti-6Al-4V under additive manufacturing conditions combining laser melting and high-speed micro-X-ray diffraction. Sci Rep 2017;7:1–10. https://doi.org/10.1038/s41598-017-16760-0.
[305] Chen Y, Clark SJ, Collins DM, Marussi S, Hunt SA, Fenech DM, et al. Correlative Synchrotron X-ray Imaging and Diffraction of Directed Energy Deposition Additive Manufacturing. Acta Mater 2021;209:116777. https://doi.org/10.1016/j.actamat.2021.116777.
[306] Ghasemi-Tabasi H, de Formanoir C, Van Petegem S, Jhabvala J, Hocine S, Boillat E, et al. Direct observation of crack formation mechanisms with operando Laser Powder Bed Fusion X-ray imaging. Addit Manuf 2022;51:102619. https://doi.org/10.1016/j.addma.2022.102619.
[307] Al-Juboori LA, Niendorf T, Brenne F. On the Tensile Properties of Inconel 718 Fabricated by EBM for As-Built and Heat-Treated Components. Metall Mater Trans B 2018;49:2969–74. https://doi.org/10.1007/s11663-018-1407-4.
[308] Sun SH, Koizumi Y, Saito T, Yamanaka K, Li YP, Cui Y, et al. Electron beam additive manufacturing of Inconel 718 alloy rods: Impact of build direction on microstructure and high-temperature tensile properties. Addit Manuf 2018;23:457–70. https://doi.org/10.1016/j.addma.2018.08.017.
[309] Rickenbacher L, Etter T, Hövel S, Wegener K. High temperature material properties of IN738LC processed by selective laser melting (SLM) technology. Rapid Prototyp J 2013;19:282–90. https://doi.org/10.1108/13552541311323281.
[310] Marchese G, Parizia S, Rashidi M, Saboori A, Manfredi D, Ugues D, et al. The role of texturing and microstructure evolution on the tensile behavior of heat-treated Inconel 625 produced via laser powder bed fusion. Mater Sci Eng A 2020;769:138500. https://doi.org/10.1016/j.msea.2019.138500.
[311] Mostafaei A, Behnamian Y, Krimer YL, Stevens EL, Luo JL, Chmielus M. Effect of solutionizing and aging on the microstructure and mechanical properties of powder bed binder jet printed nickel-based superalloy 625. Mater Des 2016;111:482–91. https://doi.org/10.1016/j.matdes.2016.08.083.
[312] Haynes International. High-Temperature alloys n.d.
[313] Lewandowski JJ, Seifi M. Metal Additive Manufacturing: A Review of Mechanical Properties. Annu Rev Mater Res 2016;46:151–86. https://doi.org/10.1146/annurev-matsci-070115-032024.
[314] Sui S, Tan H, Chen J, Zhong C, Li Z, Fan W, et al. The influence of Laves phases on the room temperature tensile properties of Inconel 718 fabricated by powder feeding laser additive manufacturing. Acta Mater 2019;164:413–27. https://doi.org/10.1016/j.actamat.2018.10.032.
[315] Shaikh AS, Schulz F, Minet-Lallemand K, Hryha E. Microstructure and mechanical properties of Haynes 282 superalloy produced by laser powder bed fusion. Mater Today Commun 2021;26:102038. https://doi.org/10.1016/j.mtcomm.2021.102038.
[316] Boswell J, Jones J, Barnard N, Clark D, Whittaker M, Lancaster R. The effects of energy density and heat treatment on the microstructure and mechanical properties of laser additive manufactured Haynes 282. Mater Des 2021;205:109725. https://doi.org/10.1016/j.matdes.2021.109725.
[317] Montero-Sistiaga ML, Liu Z, Bautmans L, Nardone S, Ji G, Kruth J-P, et al. Effect of temperature on the microstructure and tensile properties of micro-crack free hastelloy X produced by selective laser melting. Addit Manuf 2020;31:100995. https://doi.org/10.1016/j.addma.2019.100995.
[318] Ramakrishnan A, Dinda GP. Direct laser metal deposition of Inconel 738. Mater Sci Eng A 2019;740–741:1–13. https://doi.org/10.1016/j.msea.2018.10.020.

[319] Risse J. Additive Manufacturing of Nickel-Base Superalloy IN738LC by Laser Powder Bed Fusion. r Rheinisch-Westfälischen Technischen Hochschule Aachen, 2019. https://doi.org/10.18154/RWTH-2 019-06822.
[320] Jena A, Atabay SE, Brochu M. Microstructure and mechanical properties of crack-free Inconel 738 fabricated by laser powder bed fusion. Mater Sci Eng A 2022;850:143524. https://doi.org/10.1016/j.msea.2022.143524.
[321] Xue L, Chen J-Y, Islam MU, Pritchard J, Manente D, Rush S. Laser consolidation of Ni-base IN-738 superalloy for repairing gas turbine blades. Int. Congr. Appl. Lasers Electro-Optics, Laser Institute of America; 2000, p. D30–9. https://doi.org/10.2351/1.5059473.
[322] Wang K, Sun Z, Liu Y, Lv Y. Investigation of Microstructure and Mechanical Performance of IN738LC Superalloy Thin Wall Produced by Pulsed Plasma Arc Additive Manufacturing. Materials (Basel) 2020;13:3924. https://doi.org/10.3390/ma13183924.
[323] J. Wilkes, K. Hoopes JH. Creep and Tensile Properties of Direct Metal Laser Sintered (DMLS) Inconel 738LC Coupons and Comparison to Cast Properties. 6th Int. Supercrit. CO2 Power Cycles Symp., Pittsburgh, Pennsylvania: n.d.
[324] Sotov A V., Agapovichev A V., Smelov VG, Kokareva V V., Dmitrieva MO, Melnikov AA, et al. Investigation of the IN-738 superalloy microstructure and mechanical properties for the manufacturing of gas turbine engine nozzle guide vane by selective laser melting. Int J Adv Manuf Technol 2020;107:2525–35. https://doi.org/10.1007/s00170-020-05197-x.
[325] Kim K-S, Kang T-H, Kassner ME, Son K-T, Lee K-A. High-temperature tensile and high cycle fatigue properties of inconel 625 alloy manufactured by laser powder bed fusion. Addit Manuf 2020;35:101377. https://doi.org/10.1016/j.addma.2020.101377.
[326] Hanynes International. Hanynes International n.d. haynesintl.com.
[327] Hosseini SA, Abbasi SM, Madar KZ, Yazdi HMK. The effect of boron and zirconium on wrought structure and γ-γ′ lattice misfit characterization in nickel-based superalloy ATI 718Plus. Mater Chem Phys 2018;211:302–11. https://doi.org/10.1016/j.matchemphys.2018.01.076.
[328] Sanchez-Mata O, Muñiz-Lerma JA, Wang X, Atabay SE, Attarian Shandiz M, Brochu M. Microstructure and mechanical properties at room and elevated temperature of crack-free Hastelloy X fabricated by laser powder bed fusion. Mater Sci Eng A 2020;780:139177. https://doi.org/10.1016/j.msea.2020.139177.
[329] Xu Z, Murray JW, Hyde CJ, Clare AT. Effect of post processing on the creep performance of laser powder bed fused Inconel 718. Addit Manuf 2018;24:486–97. https://doi.org/10.1016/j.addma.2018.10.027.
[330] Xu J, Gruber H, Deng D, Peng RL, Moverare JJ. Short-term creep behavior of an additive manufactured non-weldable Nickel-base superalloy evaluated by slow strain rate testing. Acta Mater 2019;179:142–57. https://doi.org/10.1016/j.actamat.2019.08.034.
[331] Brenne F, Taube A, Pröbstle M, Neumeier S, Schwarze D, Schaper M, et al. Microstructural design of Ni-base alloys for high-temperature applications: impact of heat treatment on microstructure and mechanical properties after selective laser melting. Prog Addit Manuf 2016;1:141–51. https://doi.org/10.1007/s40964-016-0013-8.
[332] Zhang Y, Li Z, Nie P, Wu Y. Effect of Cooling Rate on the Microstructure of Laser-Remelted INCONEL 718 Coating. Metall Mater Trans A 2013;44:5513–21. https://doi.org/10.1007/s11661-013-1903-8.
[333] Kuo YL, Horikawa S, Kakehi K. The effect of interdendritic δ phase on the mechanical properties of Alloy 718 built up by additive manufacturing. Mater Des 2017;116:411–8. https://doi.org/10.1016/j.matdes.2016.12.026.
[334] Cuddihy MA, Stapleton A, Williams S, Dunne FPE. On cold dwell facet fatigue in titanium alloy aero-engine components. Int J Fatigue 2017;97:177–89. https://doi.org/10.1016/j.ijfatigue.2016.11.034.
[335] Suresh S. Fatigue of Materials. Cambridge University Press; 1998. https://doi.org/10.1017/CBO9780511806575.
[336] Ralph I. Stephens, Ali Fatemi, Robert R. Stephens HOF. Metal Fatigue in Engineering, 2nd Edition. Wiley; 2000.
[337] Fatemi A, Shamsaei N. Multiaxial fatigue: An overview and some approximation models for life estimation. Int J Fatigue 2011;33:948–58. https://doi.org/10.1016/j.ijfatigue.2011.01.003.
[338] Yadollahi A, Shamsaei N. Additive manufacturing of fatigue resistant materials: Challenges and opportunities. Int J Fatigue 2017;98:14–31. https://doi.org/10.1016/j.ijfatigue.2017.01.001.
[339] Aydinöz ME, Brenne F, Schaper M, Schaak C, Tillmann W, Nellesen J, et al. On the microstructural and mechanical properties of post-treated additively manufactured Inconel 718 superalloy under quasi-static and cyclic loading. Mater Sci Eng A 2016;669:246–58. https://doi.org/10.1016/j.msea.2016.05.089.
[340] Theriault A, Xue L, Dryden JR. Fatigue behavior of laser consolidated IN-625 at room and elevated temperatures. Mater Sci Eng A 2009;516:217–25. https://doi.org/10.1016/j.msea.2009.03.056.
[341] Konečná R, Kunz L, Nicoletto G, Bača A. Long fatigue crack growth in Inconel 718 produced by selective laser melting. Int J Fatigue 2016;92:499–506. https://doi.org/10.1016/j.ijfatigue.2016.03.012.

[342] Gribbin S, Bicknell J, Jorgensen L, Tsukrov I, Knezevic M. Low cycle fatigue behavior of direct metal laser sintered Inconel alloy. Int J Fatigue 2016;93:156–67.
[343] Sui S, Chen J, Fan E, Yang H, Lin X, Huang W. The influence of Laves phases on the high-cycle fatigue behavior of laser additive manufactured Inconel 718. Mater Sci Eng A 2017;695:6–13. https://doi.org/10.1016/j.msea.2017.03.098.
[344] Poulin J-R, Brailovski V, Terriault P. Long fatigue crack propagation behavior of Inconel 625 processed by laser powder bed fusion: Influence of build orientation and post-processing conditions. Int J Fatigue 2018;116:634–47. https://doi.org/10.1016/j.ijfatigue.2018.07.008.
[345] Solberg K, Berto F. The effect of defects and notches in quasi-static and fatigue loading of Inconel 718 specimens produced by selective laser melting. Int J Fatigue 2020;137:105637. https://doi.org/10.1016/j.ijfatigue.2020.105637.
[346] Fatemi A, Molaei R, Simsiriwong J, Sanaei N, Pegues J, Torries B, et al. Fatigue behaviour of additive manufactured materials: An overview of some recent experimental studies on <scp>Ti-6Al-4V</scp> considering various processing and loading direction effects. Fatigue Fract Eng Mater Struct 2019;42:991–1009. https://doi.org/10.1111/ffe.13000.
[347] Wan HY, Luo YW, Zhang B, Song ZM, Wang LY, Zhou ZJ, et al. Effects of surface roughness and build thickness on fatigue properties of selective laser melted Inconel 718 at 650 °C. Int J Fatigue 2020;137:105654. https://doi.org/10.1016/j.ijfatigue.2020.105654.
[348] Komarasamy M, Shukla S, Williams S, Kandasamy K, Kelly S, Mishra RS. Microstructure, fatigue, and impact toughness properties of additively manufactured nickel alloy 718. Addit Manuf 2019;28:661–75. https://doi.org/10.1016/j.addma.2019.06.009.
[349] Kotzem D, Dumke P, Sepehri P, Tenkamp J, Walther F. Effect of miniaturization and surface roughness on the mechanical properties of the electron beam melted superalloy Inconel®718. Prog Addit Manuf 2020;5:267–76. https://doi.org/10.1007/s40964-019-00101-w.
[350] Witkin DB, Patel D, Albright T V., Bean GE, McLouth T. Influence of surface conditions and specimen orientation on high cycle fatigue properties of Inconel 718 prepared by laser powder bed fusion. Int J Fatigue 2020;132:105392. https://doi.org/10.1016/j.ijfatigue.2019.105392.
[351] Koutiri I, Pessard E, Peyre P, Amlou O, De Terris T. Influence of SLM process parameters on the surface finish, porosity rate and fatigue behavior of as-built Inconel 625 parts. J Mater Process Technol 2018;255:536–46. https://doi.org/10.1016/j.jmatprotec.2017.12.043.
[352] Mostafaei A, Neelapu SHVR, Kisailus C, Nath LM, Jacobs TDB, Chmielus M. Characterizing surface finish and fatigue behavior in binder-jet 3D-printed nickel-based superalloy 625. Addit Manuf 2018;24:200–9. https://doi.org/10.1016/j.addma.2018.09.012.
[353] Guo P, Lin X, Li J, Zhang Y, Song M, Huang W. Electrochemical behavior of Inconel 718 fabricated by laser solid forming on different sections. Corros Sci 2018;132:79–89. https://doi.org/10.1016/j.corsci.2017.12.021.
[354] Yadollahi A, Mahtabi MJ, Khalili A, Doude HR, Newman JC. Fatigue life prediction of additively manufactured material: Effects of surface roughness, defect size, and shape. Fatigue Fract Eng Mater Struct 2018;41:1602–14. https://doi.org/10.1111/ffe.12799.
[355] Lambert DM. EVALUATION OF THE EFFECT OF SURFACE FINISH ON HIGH-CYCLE FATIGUE OF SLM-IN718. NASAGOV 2016.
[356] Kristin Morgan and Douglas Wells. Overview of Fatigue and Damage Tolerance Performance of SLM Alloy 718 2016.
[357] Palmer Frye, Muztahid Muhammad, Jutima Simsiriwong and NS. VERY HIGH CYCLE FATIGUE BEHAVIOR OF LASER BEAM-POWDER BED FUSED INCONEL 718. Solid Free Fabr 2019 Proc 30th Annu Int Solid Free Fabr Symp – An Addit Manuf Conf Rev Pap 2019.
[358] Witkin DB, Albright T V., Patel DN. Empirical Approach to Understanding the Fatigue Behavior of Metals Made Using Additive Manufacturing. Metall Mater Trans A 2016;47:3823–36. https://doi.org/10.1007/s11661-016-3501-z.
[359] Kobryn PA, Semiatin SL. Mechanical Properties of Laser-Deposited Ti-6Al-4V, International Solid Freeform Fabrication Symposium; 2001. https://doi.org/10.26153/tsw/3261.
[360] Edwards P, Ramulu M. Fatigue performance evaluation of selective laser melted Ti-6Al-4V. Mater Sci Eng A 2014;598:327–37. https://doi.org/10.1016/j.msea.2014.01.041.
[361] Leuders S, Thöne M, Riemer A, Niendorf T, Tröster T, Richard HA, et al. On the mechanical behaviour of titanium alloy TiAl6V4 manufactured by selective laser melting: Fatigue resistance and crack growth performance. Int J Fatigue 2013;48:300–7. https://doi.org/10.1016/j.ijfatigue.2012.11.011.
[362] Leuders S, Lieneke T, Lammers S, Tröster T, Niendorf T. On the fatigue properties of metals manufactured by selective laser melting – The role of ductility. J Mater Res 2014;29:1911–9. https://doi.org/10.1557/jmr.2014.157.
[363] Cao F, Zhang T, Ryder MA, Lados DA. A Review of the Fatigue Properties of Additively Manufactured

Ti-6Al-4V. JOM 2018;70:349–57. https://doi.org/10.1007/s11837-017-2728-5.
[364] Nakatani M, Masuo H, Tanaka Y, Murakami Y. Effect of Surface Roughness on Fatigue Strength of Ti-6Al-4V Alloy Manufactured by Additive Manufacturing. Procedia Struct Integr 2019;19:294–301. https://doi.org/10.1016/j.prostr.2019.12.032.
[365] Shui X, Yamanaka K, Mori M, Nagata Y, Kurita K, Chiba A. Effects of post-processing on cyclic fatigue response of a titanium alloy additively manufactured by electron beam melting. Mater Sci Eng A 2017;680:239–48. https://doi.org/10.1016/j.msea.2016.10.059.
[366] Masuo H, Tanaka Y, Morokoshi S, Yagura H, Uchida T, Yamamoto Y, et al. Influence of defects, surface roughness and HIP on the fatigue strength of Ti-6Al-4V manufactured by additive manufacturing. Int J Fatigue 2018;117:163–79. https://doi.org/10.1016/j.ijfatigue.2018.07.020.
[367] Muhammad M, Frye P, Simsiriwong J, Shao S, Shamsaei N. An investigation into the effects of cyclic strain rate on the high cycle and very high cycle fatigue behaviors of wrought and additively manufactured Inconel 718. Int J Fatigue 2021;144:106038. https://doi.org/10.1016/j.ijfatigue.2020.106038.
[368] Nezhadfar PD, Johnson AS, Shamsaei N. Fatigue behavior and microstructural evolution of additively manufactured Inconel 718 under cyclic loading at elevated temperature. Int J Fatigue 2020;136:105598. https://doi.org/10.1016/j.ijfatigue.2020.105598.
[369] Kirka MM, Greeley DA, Hawkins C, Dehoff RR. Effect of anisotropy and texture on the low cycle fatigue behavior of Inconel 718 processed via electron beam melting. Int J Fatigue 2017;105:235–43. https://doi.org/10.1016/j.ijfatigue.2017.08.021.
[370] Gribbin S, Ghorbanpour S, Ferreri NC, Bicknell J, Tsukrov I, Knezevic M. Role of grain structure, grain boundaries, crystallographic texture, precipitates, and porosity on fatigue behavior of Inconel 718 at room and elevated temperatures. Mater Charact 2019;149:184–97. https://doi.org/10.1016/j.matchar.2019.01.028.
[371] Witkin DB, Adams P, Albright T. Microstructural evolution and mechanical behavior of nickel-based superalloy 625 made by selective laser melting. In: Helvajian H, Piqué A, Wegener M, Gu B, editors., 2015, p. 93530B. https://doi.org/10.1117/12.2083699.
[372] Maj P, Zdunek J, Mizera J, Kurzydlowski KJ, Sakowicz B, Kaminski M. Microstructure and strain-stress analysis of the dynamic strain aging in inconel 625 at high temperature. Met Mater Int 2017;23:54–67. https://doi.org/10.1007/s12540-017-6264-1.
[373] Tsuji H, Nakajima H. Effect of test temperature on tensile and fatigue properties of nickel-base heat-resistant alloys. J Nucl Mater 1987;151:1–9. https://doi.org/10.1016/0022-3115(87)90049-3.
[374] Sleeswyk A. Slow strain-hardening of ingot iron. Acta Metall 1958;6:598–603. https://doi.org/10.1016/0001-6160(58)90101-9.
[375] Armas AF, Bettin OR, Alvarez-Armas I, Rubiolo GH. Strain aging effects on the cyclic behavior of austenitic stainless steels. J Nucl Mater 1988;155–157:644–9. https://doi.org/10.1016/0022-3115(88)90388-1.
[376] H. Abdel-Raouf, A. Plumtree THT. Cyclic Stress–Strain Behavior—Analysis, Experimentation, and Failure Prediction. In: L.F. Coffin EK, editor. ASTM STP 519, ASTM STP 519; 1973, p. 28–57.
[377] SRINIVASAN V, SANDHYA R, BHANUSANKARARAO K, MANNAN S, RAGHAVAN K. Effects of temperature on the low cycle fatigue behaviour of nitrogen alloyed type 316L stainless steel. Int J Fatigue 1991;13:471–8. https://doi.org/10.1016/0142-1123(91)90482-E.
[378] Sankara Rao KB, Castelli MG, Allen GP, Ellis JR. A critical assessment of the mechanistic aspects in HAYNES 188 during low-cycle fatigue in the range 25 °C to 1000 °C. Metall Mater Trans A 1997;28:347–61. https://doi.org/10.1007/s11661-997-0137-z.
[379] Essmann U, Mughrabi H. Annihilation of dislocations during tensile and cyclic deformation and limits of dislocation densities. Philos Mag A 1979;40:731–56. https://doi.org/10.1080/01418617908234871.
[380] Shankar V, Kumar A, Mariappan K, Sandhya R, Laha K, Bhaduri AK, et al. Occurrence of dynamic strain aging in Alloy 617M under low cycle fatigue loading. Int J Fatigue 2017;100:12–20. https://doi.org/10.1016/j.ijfatigue.2017.03.001.
[381] Nilsson JO, Sandström R. Influence of temperature and microstructure on creep-fatigue of Alloy 800H. High Temp Technol 1988;6:181–6. https://doi.org/10.1080/02619180.1988.11753398.
[382] Fournier D, Pineau A. Low cycle fatigue behavior of inconel 718 at 298 K and 823 K. Metall Trans A 1977;8:1095–105. https://doi.org/10.1007/BF02667395.
[383] Barat K, Ghosh M, Sivaprasad S, Kar SK, Tarafder S. High-Temperature Low-Cycle Fatigue Behavior in HAYNES 282: Influence of Initial Microstructure. Metall Mater Trans A Phys Metall Mater Sci 2018;49:5211–26. https://doi.org/10.1007/s11661-018-4760-7.
[384] Antolovich SD. Microstructural aspects of fatigue in Ni-base superalloys. Philos Trans R Soc A Math Phys Eng Sci 2015;373:20140128. https://doi.org/10.1098/rsta.2014.0128.
[385] Lerch BA, Gerold V. Cyclic hardening mechanisms in NIMONIC 80A. Metall Trans A 1987;18:2135–41. https://doi.org/10.1007/bf02647085.

[386] Song Z, Gao W, Wang D, Wu Z, Yan M, Huang L, et al. Very-High-Cycle Fatigue Behavior of Inconel 718 Alloy Fabricated by Selective Laser Melting at Elevated Temperature. Materials (Basel) 2021;14:1001. https://doi.org/10.3390/ma14041001.
[387] Schmiedel A, Burkhardt C, Henkel S, Weidner A, Biermann H. Very High Cycle Fatigue Investigations on the Fatigue Strength of Additive Manufactured and Conventionally Wrought Inconel 718 at 873 K. Metals (Basel) 2021;11:1682. https://doi.org/10.3390/met11111682.
[388] KOBAYASHI K, YAMAGUCHI K, HAYAKAWA M, KIMURA M. High-temperature fatigue properties of austenitic superalloys 718, A286 and 304L. Int J Fatigue 2008;30:1978–84. https://doi.org/10.1016/j.ijfatigue.2008.01.004.
[389] Amanov A, Pyun Y-S, Kim J-H, Suh C-M, Cho I-S, Kim H-D, et al. Ultrasonic fatigue performance of high temperature structural material Inconel 718 alloys at high temperature after UNSM treatment. Fatigue Fract Eng Mater Struct 2015;38:1266–73. https://doi.org/10.1111/ffe.12330.
[390] Johnson AS, Shao S, Shamsaei N, Thompson SM, Bian L. Microstructure, Fatigue Behavior, and Failure Mechanisms of Direct Laser-Deposited Inconel 718. JOM 2017;69:597–603. https://doi.org/10.1007/s11837-016-2225-2.
[391] Balachandramurthi AR, Moverare J, Dixit N, Deng D, Pederson R. Microstructural influence on fatigue crack propagation during high cycle fatigue testing of additively manufactured Alloy 718. Mater Charact 2019;149:82–94. https://doi.org/10.1016/j.matchar.2019.01.018.
[392] Iliopoulos AP, Jones R, Michopoulos JG, Phan N, Rans C. Further Studies into Crack Growth in Additively Manufactured Materials. Materials (Basel) 2020;13:2223. https://doi.org/10.3390/ma13102223.
[393] Wei B, Liu Z, Nong B, Cao B, Lv X, Ren Y, et al. Microstructure, cracking behavior and mechanical properties of René 104 superalloy fabricated by selective laser melting. J Alloys Compd 2021;867:158377. https://doi.org/10.1016/j.jallcom.2020.158377.
[394] Sabelkin VP, Cobb GR, Doane BM, Kemnitz RA, O'Hara RP. Torsional behavior of additively manufactured nickel alloy 718 under monotonic loading and low cycle fatigue. Mater Today Commun 2020;24:101256. https://doi.org/10.1016/j.mtcomm.2020.101256.
[395] Nicoletto G. Smooth and notch fatigue behavior of selectively laser melted Inconel 718 with as-built surfaces. Int J Fatigue 2019;128:105211. https://doi.org/10.1016/j.ijfatigue.2019.105211.
[396] Jiao ZH, Lei LM, Yu HC, Xu F, Xu RD, Wu XR. Experimental evaluation on elevated temperature fatigue and tensile properties of one selective laser melted nickel based superalloy. Int J Fatigue 2019;121:172–80. https://doi.org/10.1016/j.ijfatigue.2018.12.024.
[397] Poulin J-R, Kreitcberg A, Terriault P, Brailovski V. Long fatigue crack propagation behavior of laser powder bed-fused inconel 625 with intentionally-seeded porosity. Int J Fatigue 2019;127:144–56. https://doi.org/10.1016/j.ijfatigue.2019.06.008.
[398] Yu X, Lin X, Tan H, Hu Y, Zhang S, Liu F, et al. Microstructure and fatigue crack growth behavior of Inconel 718 superalloy manufactured by laser directed energy deposition. Int J Fatigue 2021;143:106005. https://doi.org/10.1016/j.ijfatigue.2020.106005.
[399] Amato K. Comparison of Microstructures and Properties for a Ni-Base Superalloy (Alloy 625) Fabricated by Electron Beam Melting. J Mater Sci Res 2012;1. https://doi.org/10.5539/jmsr.v1n2p3.
[400] Clavel M, Pineau A. Fatigue behaviour of two nickel-base alloys I: Experimental results on low cycle fatigue, fatigue crack propagation and substructures. Mater Sci Eng 1982;55:157–71. https://doi.org/10.1016/0025-5416(82)90129-X.
[401] Li HY, Sun HL, Bowen P, Knott JF. Effects of compressive residual stress on short fatigue crack growth in a nickel-based superalloy. Int J Fatigue 2018;108:53–61. https://doi.org/10.1016/j.ijfatigue.2017.11.010.
[402] Mercer C, Soboyejo ABO, Soboyejo WO. Micromechanisms of fatigue crack growth in a forged Inconel 718 nickel-based superalloy. Mater Sci Eng A 1999;270:308–22. https://doi.org/10.1016/S0921-5093(99)00214-2.
[403] Osinkolu G., Onofrio G, Marchionni M. Fatigue crack growth in polycrystalline IN 718 superalloy. Mater Sci Eng A 2003;356:425–33. https://doi.org/10.1016/S0921-5093(03)00156-4.
[404] Dieter GE. Mechanical Metallurgy. 3rd ed. Boston, MA, MA: McGraw-Hill; 1986.
[405] Kumar P, Ramamurty U. Microstructural optimization through heat treatment for enhancing the fracture toughness and fatigue crack growth resistance of selective laser melted Ti 6Al 4V alloy. Acta Mater 2019;169:45–59. https://doi.org/10.1016/j.actamat.2019.03.003.
[406] Seifi M, Salem AA, Satko DP, Grylls R, Lewandowski JJ. Effects of Post-processing on Microstructure and Mechanical Properties of SLM-Processed IN-718, 2018, p. 515–26. https://doi.org/10.1007/978-3-319-89480-5_33.
[407] Gotterbarm MR, Seifi M, Melzer D, Džugan J, Salem AA, Liu ZH, et al. Small scale testing of IN718 single crystals manufactured by EB-PBF. Addit Manuf 2020;36:101449.

https://doi.org/10.1016/j.addma.2020.101449.
[408] Yu X, Lin X, Liu F, Wang L, Tang Y, Li J, et al. Influence of post-heat-treatment on the microstructure and fracture toughness properties of Inconel 718 fabricated with laser directed energy deposition additive manufacturing. Mater Sci Eng A 2020;798:140092. https://doi.org/10.1016/j.msea.2020.140092.
[409] L. James. Fatigue-crack growth in Inconel 718 weldments at elevated temperatures. Weld Res Supplliment 1978;57:17s-23s.
[410] Editor Committee of Chinese Aerospace Material Manual. Chinese Aerospace Material Manual: Deforming Superalloy and Casting Superalloy. second. Standards Press of China, Beijing, 2001, p. 355.; 2001.
[411] Sampath D, Akid R, Morana R. Estimation of crack initiation stress and local fracture toughness of Ni-alloys 945X (UNS N09946) and 718 (UNS N07718) under hydrogen environment via fracture surface topography analysis. Eng Fract Mech 2018;191:324–43. https://doi.org/10.1016/j.engfracmech.2017.12.010.
[412] Tobler RL. Low temperature effects on the fracture behaviour of a nickel base superalloy. Cryogenics (Guildf) 1976;16:669–74. https://doi.org/10.1016/0011-2275(76)90039-4.
[413] Xiao L, Chen D, Chaturvedi MC. Effect of Boron and Carbon on the Fracture Toughness of IN 718 Superalloy at Room Temperature and 650 °C. J Mater Eng Perform 2005;14:528–38. https://doi.org/10.1361/105994905X56106.
[414] C. Hautfenne, S. Nardone EDB. Influence of heat treatments and build orientation on the creep strength of additive manufactured IN718. 4th Int. ECCC Conf., Dusseldorf, Germany: n.d.
[415] Shassere B, Greeley D, Okello A, Kirka M, Nandwana P, Dehoff R. Correlation of Microstructure to Creep Response of Hot Isostatically Pressed and Aged Electron Beam Melted Inconel 718. Metall Mater Trans A 2018;49:5107–17. https://doi.org/10.1007/s11661-018-4812-z.
[416] Strondl A, Palm M, Gnauk J, Frommeyer G. Microstructure and mechanical properties of nickel based superalloy IN718 produced by rapid prototyping with electron beam melting (EBM). Mater Sci Technol 2011;27:876–83. https://doi.org/10.1179/026708309X12468927349451.
[417] Lass EA, Stoudt MR, Williams ME, Katz MB, Levine LE, Phan TQ, et al. Formation of the Ni3Nb δ-Phase in Stress-Relieved Inconel 625 Produced via Laser Powder-Bed Fusion Additive Manufacturing. Metall Mater Trans A 2017;48:5547–58. https://doi.org/10.1007/s11661-017-4304-6.
[418] Hilal H, Lancaster R, Jeffs S, Boswell J, Stapleton D, Baxter G. The Influence of Process Parameters and Build Orientation on the Creep Behaviour of a Laser Powder Bed Fused Ni-based Superalloy for Aerospace Applications. Materials (Basel) 2019;12:1390. https://doi.org/10.3390/ma12091390.
[419] Davies SJ, Jeffs SP, Coleman MP, Lancaster RJ. Effects of heat treatment on microstructure and creep properties of a laser powder bed fused nickel superalloy. Mater Des 2018;159:39–46. https://doi.org/10.1016/j.matdes.2018.08.039.
[420] Håkan Brodin, Olov Andersson SJ. Mechanical testing of a selective laser melted superalloy. 13th Int. Conf. Fract., Beijing, China: 2013.
[421] Kunze K, Etter T, Grässlin J, Shklover V. Texture, anisotropy in microstructure and mechanical properties of IN738LC alloy processed by selective laser melting (SLM). Mater Sci Eng A 2015;620:213–22. https://doi.org/10.1016/j.msea.2014.10.003.
[422] Tang HP, Yang GY, Jia WP, He WW, Lu SL, Qian M. Additive manufacturing of a high niobium-containing titanium aluminide alloy by selective electron beam melting. Mater Sci Eng A 2015;636:103–7. https://doi.org/10.1016/j.msea.2015.03.079.
[423] Yu S, Liu J, Wei M, Luo Y, Zhu X, Liu Y. Compressive property and energy absorption characteristic of open-cell ZA22 foams. Mater Des 2009;30:87–90. https://doi.org/10.1016/j.matdes.2008.04.041.
[424] McLouth TD, Witkin DB, Bean GE, Sitzman SD, Adams PM, Lohser JR, et al. Variations in ambient and elevated temperature mechanical behavior of IN718 manufactured by selective laser melting via process parameter control. Mater Sci Eng A 2020;780:139184. https://doi.org/10.1016/j.msea.2020.139184.
[425] Sanchez S, Gaspard G, Hyde CJ, Ashcroft IA, Ravi GA, Clare AT. The creep behaviour of nickel alloy 718 manufactured by laser powder bed fusion. Mater Des 2021;204. https://doi.org/10.1016/j.matdes.2021.109647.
[426] Witkin DB, Hayes RW, McLouth TD, Bean GE. Anomalous Notch Rupture Behavior of Nickel-Based Superalloy Inconel 718 Due to Fabrication by Additive Manufacturing. Metall Mater Trans A 2019;50:3458–65. https://doi.org/10.1007/s11661-019-05298-7.
[427] Wang LY, Wang YC, Zhou ZJ, Wan HY, Li CP, Chen GF, et al. Small punch creep performance of heterogeneous microstructure dominated Inconel 718 fabricated by selective laser melting. Mater Des 2020;195:109042. https://doi.org/10.1016/j.matdes.2020.109042.
[428] Zhang H, Gu D, Ma C, Guo M, Yang J, Zhang H, et al. Understanding tensile and creep properties of WC reinforced nickel-based composites fabricated by selective laser melting. Mater Sci Eng A 2021;802:140431. https://doi.org/10.1016/j.msea.2020.140431.

[429] Nagahari T, Nagoya T, Kakehi K, Sato N, Nakano S. Microstructure and Creep Properties of Ni-Base Superalloy IN718 Built up by Selective Laser Melting in a Vacuum Environment. Metals (Basel) 2020;10:362. https://doi.org/10.3390/met10030362.
[430] Xu Z, Hyde CJ, Tuck C, Clare AT. Creep behaviour of inconel 718 processed by laser powder bed fusion. J Mater Process Technol 2018;256:13–24. https://doi.org/10.1016/j.jmatprotec.2018.01.040.
[431] Popovich VA, Borisov E V., Heurtebise V, Riemslag T, Popovich AA, Sufiiarov VS. Creep and Thermomechanical Fatigue of Functionally Graded Inconel 718 Produced by Additive Manufacturing, 2018, p. 85–97. https://doi.org/10.1007/978-3-319-72526-0_9.
[432] Xu J, Gruber H, Boyd R, Jiang S, Peng RL, Moverare JJ. On the strengthening and embrittlement mechanisms of an additively manufactured Nickel-base superalloy. Materialia 2020;10:100657. https://doi.org/10.1016/j.mtla.2020.100657.
[433] Mostafa A, Shahriari D, Rubio IP, Brailovski V, Jahazi M, Medraj M. Hot compression behavior and microstructure of selectively laser-melted IN718 alloy. Int J Adv Manuf Technol 2018;96:371–85. https://doi.org/10.1007/s00170-017-1522-4.
[434] Hu X-A, Zhao G-L, Jiang Y, Ma X-F, Liu F-C, Huang J, et al. Experimental Investigation on the LCF Behavior Affected by Manufacturing Defects and Creep Damage of One Selective Laser Melting Nickel-Based Superalloy at 815 °C. Acta Metall Sin (English Lett 2020;33:514–27. https://doi.org/10.1007/s40195-019-00986-0.
[435] Qiu C, Chen H, Liu Q, Yue S, Wang H. On the solidification behaviour and cracking origin of a nickel-based superalloy during selective laser melting. Mater Charact 2019;148:330–44. https://doi.org/10.1016/j.matchar.2018.12.032.
[436] Schneider J, Lund B, Fullen M. Effect of heat treatment variations on the mechanical properties of Inconel 718 selective laser melted specimens. Addit Manuf 2018;21:248–54. https://doi.org/10.1016/j.addma.2018.03.005.
[437] Keiser DD, Brown HL. Review of the physical metallurgy of Alloy 718. Idaho National Engineering Lab., Idaho Falls (USA); 1976.
[438] Wang LY, Zhou ZJ, Li CP, Chen GF, Zhang GP. Comparative investigation of small punch creep resistance of Inconel 718 fabricated by selective laser melting. Mater Sci Eng A 2019;745:31–8. https://doi.org/10.1016/j.msea.2018.12.083.
[439] Kuo Y-L, Nagahari T, Kakehi K. The Effect of Post-Processes on the Microstructure and Creep Properties of Alloy718 Built Up by Selective Laser Melting. Materials (Basel) 2018;11:996. https://doi.org/10.3390/ma11060996.
[440] Cao M, Zhang D, Gao Y, Chen R, Huang G, Feng Z, et al. The effect of homogenization temperature on the microstructure and high temperature mechanical performance of SLM-fabricated IN718 alloy. Mater Sci Eng A 2021;801:140427. https://doi.org/10.1016/j.msea.2020.140427.
[441] Zhou L, Mehta A, McWilliams B, Cho K, Sohn Y. Microstructure, precipitates and mechanical properties of powder bed fused inconel 718 before and after heat treatment. J Mater Sci Technol 2019;35:1153–64. https://doi.org/10.1016/j.jmst.2018.12.006.
[442] Wang Y, Shi J. Microstructure and Tensile Properties of SLM Graphene Reinforced Inconel 718 Alloy After Post Heat Treatment. Vol. 2 Mater. Jt. MSEC-NAMRC-Manufacturing USA, American Society of Mechanical Engineers; 2018. https://doi.org/10.1115/MSEC2018-6694.
[443] Kuo YL, Horikawa S, Kakehi K. Effects of build direction and heat treatment on creep properties of Ni-base superalloy built up by additive manufacturing. Scr Mater 2017;129:74–8. https://doi.org/10.1016/j.scriptamat.2016.10.035.
[444] Wei HL, Mukherjee T, Zhang W, Zuback JS, Knapp GL, De A, et al. Mechanistic models for additive manufacturing of metallic components. Prog Mater Sci 2020:100703. https://doi.org/10.1016/j.pmatsci.2020.100703.
[445] Frazier WE. Metal additive manufacturing: A review. J Mater Eng Perform 2014;23:1917–28. https://doi.org/10.1007/s11665-014-0958-z.
[446] Klassen A, Bauereiß A, Körner C. Modelling of electron beam absorption in complex geometries. J Phys D Appl Phys 2014;47. https://doi.org/10.1088/0022-3727/47/6/065307.
[447] Everhart TE, Hoff PH. Determination of kilovolt electron energy dissipation vs penetration distance in solid materials. J Appl Phys 1971;42:5837–46.
[448] Lee YS, Zhang W. Modeling of heat transfer, fluid flow and solidification microstructure of nickel-base superalloy fabricated by laser powder bed fusion. Addit Manuf 2016;12:178–88. https://doi.org/https://doi.org/10.1016/j.addma.2016.05.003.
[449] Khairallah SA, Martin AA, Lee JRI, Guss G, Calta NP, Hammons JA, et al. Controlling interdependent meso-nanosecond dynamics and defect generation in metal 3D printing. Science (80-) 2020;368:660–5. https://doi.org/10.1126/science.aay7830.
[450] Manvatkar V, De A, Debroy T. Heat transfer and material flow during laser assisted multi-layer additive

manufacturing. J Appl Phys 2014;116. https://doi.org/10.1063/1.4896751.
[451] Messler Jr RW. Principles of welding: processes, physics, chemistry, and metallurgy. John Wiley & Sons; 2008.
[452] Khairallah SA, Anderson A. Mesoscopic simulation model of selective laser melting of stainless steel powder. J Mater Process Technol 2014;214:2627–36. https://doi.org/10.1016/j.jmatprotec.2014.06.001.
[453] Rai R, Elmer JW, Palmer TA, Debroy T. Heat transfer and fluid flow during keyhole mode laser welding of tantalum, Ti-6Al-4V, 304L stainless steel and vanadium. J Phys D Appl Phys 2007;40:5753–66. https://doi.org/10.1088/0022-3727/40/18/037.
[454] Eagar TW, Tsai NS. Temperature Fields Produced By Traveling Distributed Heat Sources. Weld J (Miami, Fla) 1983;62:346–55.
[455] Andreotta R, Ladani L, Brindley W. Finite element simulation of laser additive melting and solidification of Inconel 718 with experimentally tested thermal properties. Finite Elem Anal Des 2017;135:36–43. https://doi.org/10.1016/j.finel.2017.07.002.
[456] Knapp GL, Raghavan N, Plotkowski A, DebRoy T. Experiments and simulations on solidification microstructure for Inconel 718 in powder bed fusion electron beam additive manufacturing. Addit Manuf 2019;25:511–21. https://doi.org/10.1016/j.addma.2018.12.001.
[457] He X, Mazumder J. Transport phenomena during direct metal deposition. J Appl Phys 2007;101. https://doi.org/10.1063/1.2710780.
[458] Lee Y, Farson DF. Simulation of transport phenomena and melt pool shape for multiple layer additive manufacturing. J Laser Appl 2016;28:012006. https://doi.org/10.2351/1.4935711.
[459] Körner C, Helmer H, Bauereiß A, Singer RF. Tailoring the grain structure of IN718 during selective electron beam melting. MATEC Web Conf 2014;14. https://doi.org/10.1051/matecconf/20141408001.
[460] Gao X, Abreu Faria G, Zhang W, Wheeler KR. Numerical analysis of non-spherical particle effect on molten pool dynamics in laser-powder bed fusion additive manufacturing. Comput Mater Sci 2020;179:109648. https://doi.org/10.1016/j.commatsci.2020.109648.
[461] Lia F, Martukanitz RM, Park JZ, DebRoy T, Mukherjee T, Keist JS, et al. Process and microstructural validation of the laser-based directed energy deposition process for Ti-6Al-4V and Inconel 625 material. Mater Sci Technol 2015.
[462] Rosenthal D. The theory of moving sources of heat and its application of metal treatments. Trans ASME 1946;68:849–66.
[463] King WE, Barth HD, Castillo VM, Gallegos GF, Gibbs JW, Hahn DE, et al. Observation of keyhole-mode laser melting in laser powder-bed fusion additive manufacturing. J Mater Process Technol 2014;214:2915–25. https://doi.org/10.1016/j.jmatprotec.2014.06.005.
[464] Patel S, Vlasea M. Melting modes in laser powder bed fusion. Materialia 2020;9. https://doi.org/10.1016/j.mtla.2020.100591.
[465] Chen Q, Zhao Y, Strayer S, Zhao Y, Aoyagi K, Koizumi Y, et al. Elucidating the effect of preheating temperature on melt pool morphology variation in Inconel 718 laser powder bed fusion via simulation and experiment. Addit Manuf 2021;37:101642.
[466] Krol TA, Seidel C, Schilp J, Hofmann M, Gan W, Zaeh MF. Verification of structural simulation results of metal-based additive manufacturing by means of neutron diffraction. Phys Procedia 2013;41:849–57.
[467] Chen Q, Fu Y, To AC. Multiphysics modeling of particle spattering and induced defect formation mechanism in Inconel 718 laser powder bed fusion. Int J Adv Manuf Technol 2022;123:783–91. https://doi.org/10.1007/s00170-022-10201-7.
[468] Lee YS, Zhang W. Mesoscopic simulation of heat transfer and fluid flow in laser powder bed additive manufacturing. Solid Free. Fabr. Proc., 2015, p. 1154–65.
[469] Gusarov A V., Smurov I. Modeling the interaction of laser radiation with powder bed at selective laser melting. Phys Procedia 2010;5:381–94. https://doi.org/10.1016/j.phpro.2010.08.065.
[470] Körner C, Attar E, Heinl P. Mesoscopic simulation of selective beam melting processes. J Mater Process Technol 2011;211:978–87. https://doi.org/https://doi.org/10.1016/j.jmatprotec.2010.12.016.
[471] Rai A, Helmer H, Körner C. Simulation of grain structure evolution during powder bed based additive manufacturing. Addit Manuf 2017;13:124–34.
[472] Wang W, Lee PD, Mclean M. A model of solidification microstructures in nickel-based superalloys: predicting primary dendrite spacing selection. Acta Mater 2003;51:2971–87.
[473] Shin YC, Bailey N, Katinas C, Tan W. Predictive modeling capabilities from incident powder and laser to mechanical properties for laser directed energy deposition. Comput Mech 2018;61:617–36.
[474] Acharya R, Sharon JA, Staroselsky A. Prediction of microstructure in laser powder bed fusion process. Acta Mater 2017;124:360–71. https://doi.org/10.1016/j.actamat.2016.11.018.
[475] Rappaz M, Gandin C-A. Probabilistic modelling of microstructure formation in solidification processes. Acta Metall Mater 1993;41:345–60.
[476] Tourret D, Karma A. Multiscale dendritic needle network model of alloy solidification. Acta Mater

2013;61:6474–91.
[477] Tourret D, Karma A. Three-dimensional dendritic needle network model for alloy solidification. Acta Mater 2016;120:240–54.
[478] Tourret D, Francois MM, Clarke AJ. Multiscale dendritic needle network model of alloy solidification with fluid flow. Comput Mater Sci 2019;162:206–27.
[479] Wei L, Lin X, Wang M, Huang W. Low artificial anisotropy cellular automaton model and its applications to the cell-to-dendrite transition in directional solidification. Mater Discov 2016;3:17–28.
[480] Keller T, Lindwall G, Ghosh S, Ma L, Lane BM, Zhang F, et al. Application of finite element, phase-field, and CALPHAD-based methods to additive manufacturing of Ni-based superalloys. Acta Mater 2017;139:244–53. https://doi.org/10.1016/j.actamat.2017.05.003.
[481] Zinoviev A, Zinovieva O, Ploshikhin V, Romanova V, Balokhonov R. Evolution of grain structure during laser additive manufacturing. Simulation by a cellular automata method. Mater Des 2016;106:321–9.
[482] Tan W, Bailey NS, Shin YC. A novel integrated model combining Cellular Automata and Phase Field methods for microstructure evolution during solidification of multi-component and multi-phase alloys. Comput Mater Sci 2011. https://doi.org/10.1016/j.commatsci.2011.03.044.
[483] Wei HL, Knapp GL, Mukherjee T, DebRoy T. Three-dimensional grain growth during multi-layer printing of a nickel-based alloy Inconel 718. Addit Manuf 2019;25:448–59.
[484] Lian Y, Gan Z, Yu C, Kats D, Liu WK, Wagner GJ. A cellular automaton finite volume method for microstructure evolution during additive manufacturing. Mater Des 2019;169:107672.
[485] Rodgers TM, Madison JD, Tikare V, Maguire MC. Predicting mesoscale microstructural evolution in electron beam welding. Jom 2016;68:1419–26.
[486] Raabe D. Scaling Monte Carlo kinetics of the Potts model using rate theory. Acta Mater 2000;48:1617–28.
[487] Song J, Chew Y, Bi G, Yao X, Zhang B, Bai J, et al. Numerical and experimental study of laser aided additive manufacturing for melt-pool profile and grain orientation analysis. Mater Des 2018;137:286–97. https://doi.org/10.1016/j.matdes.2017.10.033.
[488] Walton D, Chalmers u B. The origin of the preferred orientation in the columnar zone of ingots. Trans Am Inst Min Metall Eng 1959;215:447–57.
[489] David SA, Babu SS, Vitek JM. Welding: Solidification and microstructure. Jom 2003;55:14–20.
[490] Wei HL, Mazumder J, DebRoy T. Evolution of solidification texture during additive manufacturing. Sci Rep 2015;5:1–7.
[491] Paul S, Liu J, Strayer ST, Zhao Y, Sridar S, Klecka MA, et al. A Discrete Dendrite Dynamics Model for Epitaxial Columnar Grain Growth in Metal Additive Manufacturing with Application to Inconel. Addit Manuf 2020;36:101611. https://doi.org/10.1016/j.addma.2020.101611.
[492] Ni M, Chen C, Wang X, Wang P, Li R, Zhang X, et al. Anisotropic tensile behavior of in situ precipitation strengthened Inconel 718 fabricated by additive manufacturing. Mater Sci Eng A 2017;701:344–51. https://doi.org/10.1016/j.msea.2017.06.098.
[493] Kundin J, Mushongera L, Emmerich H. Phase-field modeling of microstructure formation during rapid solidification in Inconel 718 superalloy. Acta Mater 2015;95:343–56.
[494] Wang X, Liu PW, Ji Y, Liu Y, Horstemeyer MH, Chen L. Investigation on microsegregation of IN718 alloy during additive manufacturing via integrated phase-field and finite-element modeling. J Mater Eng Perform 2019;28:657–65.
[495] Wang X, Chou K. Microstructure simulations of Inconel 718 during selective laser melting using a phase field model. Int J Adv Manuf Technol 2019;100:2147–62.
[496] Zhou N, Lv DC, Zhang HL, McAllister D, Zhang F, Mills MJ, et al. Computer simulation of phase transformation and plastic deformation in IN718 superalloy: Microstructural evolution during precipitation. Acta Mater 2014;65:270–86.
[497] Zhao Y, Li K, Gargani M, Xiong W. A comparative analysis of Inconel 718 made by additive manufacturing and suction casting: Microstructure evolution in homogenization. Addit Manuf 2020;36:101404. https://doi.org/10.1016/j.addma.2020.101404.
[498] Ghosh S, Ma L, Levine LE, Ricker RE, Stoudt MR, Heigel JC, et al. Single-track melt-pool measurements and microstructures in Inconel 625. Jom 2018;70:1011–6.
[499] Chen F, Cui Z, Ou H, Long H. Mesoscale modeling and simulation of microstructure evolution during dynamic recrystallization of a Ni-based superalloy. Appl Phys A 2016;122:1–13.
[500] Lass EA, Stoudt MR, Katz MB, Williams ME. Precipitation and dissolution of δ and γ ″during heat treatment of a laser powder-bed fusion produced Ni-based superalloy. Scr Mater 2018;154:83–6.
[501] Nie P, Ojo OA, Li Z. Numerical modeling of microstructure evolution during laser additive manufacturing of a nickel-based superalloy. Acta Mater 2014;77:85–95. https://doi.org/10.1016/j.actamat.2014.05.039.
[502] Amato KN, Gaytan SM, Murr LE, Martinez E, Shindo PW, Hernandez J, et al. Microstructures and mechanical behavior of Inconel 718 fabricated by selective laser melting. Acta Mater 2012;60:2229–39.

https://doi.org/10.1016/j.actamat.2011.12.032.
[503] Zhang F, Levine LE, Allen AJ, Stoudt MR, Lindwall G, Lass EA, et al. Effect of heat treatment on the microstructural evolution of a nickel-based superalloy additive-manufactured by laser powder bed fusion. Acta Mater 2018;152:200–14. https://doi.org/10.1016/j.actamat.2018.03.017.
[504] Kumara C, Deng D, Hanning F, Raanes M, Moverare J, Nylén P. Predicting the Microstructural Evolution of Electron Beam Melting of Alloy 718 with Phase-Field Modeling. Metall Mater Trans A 2019;50:2527–37. https://doi.org/10.1007/s11661-019-05163-7.
[505] Ramsperger M, Singer RF, Körner C. Microstructure of the Nickel-Base Superalloy CMSX-4 Fabricated by Selective Electron Beam Melting. Metall Mater Trans A 2016;47:1469–80. https://doi.org/10.1007/s11661-015-3300-y.
[506] Mukherjee T, DebRoy T. Mitigation of lack of fusion defects in powder bed fusion additive manufacturing. J Manuf Process 2018;36:442–9. https://doi.org/10.1016/j.jmapro.2018.10.028.
[507] Martin AA, Calta NP, Hammons JA, Khairallah SA, Nielsen MH, Shuttlesworth RM, et al. Ultrafast dynamics of laser-metal interactions in additive manufacturing alloys captured by in situ X-ray imaging. Mater Today Adv 2019;1:100002. https://doi.org/10.1016/j.mtadv.2019.01.001.
[508] Svensson M, Ackelid U, Ab A. Titanium alloys manufactured with electron beam melting mechanical and chemical properties. Proc. Mater. Process. Med. devices Conf., ASM International; 2010, p. 189–94.
[509] Bayat M, Mohanty S, Hattel JH. Multiphysics modelling of lack-of-fusion voids formation and evolution in IN718 made by multi-track/multi-layer L-PBF. Int J Heat Mass Transf 2019;139:95–114. https://doi.org/https://doi.org/10.1016/j.ijheatmasstransfer.2019.05.003.
[510] Mercelis P, Kruth J. Residual stresses in selective laser sintering and selective laser melting. Rapid Prototyp J 2006.
[511] Gnäupel-Herold T, Slotwinski J, Moylan S. Neutron measurements of stresses in a test artifact produced by laser-based additive manufacturing. AIP Conf. Proc., vol. 1581, American Institute of Physics; 2014, p. 1205–12.
[512] Rangaswamy P, Holden TM, Rogge RB, Griffith ML. Residual stresses in components formed by the laserengineered net shaping (LENS®) process. J Strain Anal Eng Des 2003;38:519–27.
[513] Sochalski-Kolbus LM, Payzant EA, Cornwell PA, Watkins TR, Babu SS, Dehoff RR, et al. Comparison of Residual Stresses in Inconel 718 Simple Parts Made by Electron Beam Melting and Direct Laser Metal Sintering. Metall Mater Trans A Phys Metall Mater Sci 2015;46:1419–32. https://doi.org/10.1007/s11661-014-2722-2.
[514] Wu A, LeBlanc MM, Kumar M, Gallegos GF, Brown DW, King WE. Effect of laser scanning pattern and build direction in additive manufacturing on anisotropy, porosity and residual stress. 2014 TMS Annu. Meet. Exhib. San Diego, CA, 2014.
[515] Prabhakar P, Sames WJ, Dehoff R, Babu SS. Computational modeling of residual stress formation during the electron beam melting process for Inconel 718. Addit Manuf 2015;7:83–91.
[516] Cheng B, Shrestha S, Chou K. Stress and deformation evaluations of scanning strategy effect in selective laser melting. Addit Manuf 2016;12:240–51. https://doi.org/10.1016/j.addma.2016.05.007.
[517] Cheng B, Price S, Lydon J, Cooper K, Chou K. On Process Temperature in Powder-Bed Electron Beam Additive Manufacturing: Model Development and Validation. J Manuf Sci Eng Trans ASME 2014;136:1–12. https://doi.org/10.1115/1.4028484.
[518] Pant P, Proper S, Luzin V, Sjöström S, Simonsson K, Moverare J, et al. Mapping of residual stresses in as-built Inconel 718 fabricated by laser powder bed fusion: A neutron diffraction study of build orientation influence on residual stresses. Addit Manuf 2020;36:101501.
[519] Deng D, Peng RL, Brodin H, Moverare J. Microstructure and mechanical properties of Inconel 718 produced by selective laser melting: Sample orientation dependence and effects of post heat treatments. Mater Sci Eng A 2018;713:294–306.
[520] Fu CH, Guo YB. Three-dimensional temperature gradient mechanism in selective laser melting of Ti-6Al-4V. J Manuf Sci Eng 2014;136.
[521] Dai K, Shaw L. Thermal and stress modeling of multi-material laser processing. Acta Mater 2001;49:4171–81.
[522] Peng H, Go DB, Billo R, Gong S, Shankar MR, Gatrell BA, et al. Part-scale model for fast prediction of thermal distortion in DMLS additive manufacturing; Part 2: a quasi-static thermo-mechanical model. Solid Free. Fabr. Symp., 2016, p. 382–97.
[523] Zaeh MF, Branner G. Investigations on residual stresses and deformations in selective laser melting. Prod Eng 2010;4:35–45. https://doi.org/10.1007/s11740-009-0192-y.
[524] Li C, Fu CH, Guo YB, Fang FZ. A multiscale modeling approach for fast prediction of part distortion in selective laser melting. J Mater Process Technol 2016;229:703–12.
[525] Li C, Liu ZY, Fang XY, Guo YB. On the simulation scalability of predicting residual stress and distortion in selective laser melting. J Manuf Sci Eng 2018;140.

[526] Ueda Y, Fukuda K, Nakacho K, Endo S. A new measuring method of residual stresses with the aid of finite element method and reliability of estimated values. J Soc Nav Archit Japan 1975;1975:499–507.
[527] Chen Q, Liang X, Hayduke D, Liu J, Cheng L, Oskin J, et al. An inherent strain based multiscale modeling framework for simulating part-scale residual deformation for direct metal laser sintering. Addit Manuf 2019;28:406–18. https://doi.org/https://doi.org/10.1016/j.addma.2019.05.021.
[528] Liang X, Chen Q, Cheng L, Yang Q, To A. A modified inherent strain method for fast prediction of residual deformation in additive manufacturing of metal parts. Proc. Solid Free. Fabr. Conf., 2017.
[529] Schoinochoritis B, Chantzis D, Salonitis K. Simulation of metallic powder bed additive manufacturing processes with the finite element method: A critical review. Proc Inst Mech Eng Part B J Eng Manuf 2017;231:96–117. https://doi.org/10.1177/0954405414567522.
[530] Wen S, Dong A, Lu Y, Zhu G, Shu D, Sun B. Finite Element Simulation of the Temperature Field and Residual Stress in GH536 Superalloy Treated by Selective Laser Melting. Jinshu Xuebao/Acta Metall Sin 2018;54:393–403. https://doi.org/10.11900/0412.1961.2017.00284.
[531] Yang YP, Jamshidinia M, Boulware P, Kelly SM. Prediction of microstructure, residual stress, and deformation in laser powder bed fusion process. Comput Mech 2018;61:599–615. https://doi.org/10.1007/s00466-017-1528-7.
[532] Prabhakar P, Sames WJ, Dehoff R, Babu SS. Computational modeling of residual stress formation during the electron beam melting process for Inconel 718. Addit Manuf 2015;7:83–91. https://doi.org/10.1016/j.addma.2015.03.003.
[533] Ghorbanpour S, Zecevic M, Kumar A, Jahedi M, Bicknell J, Jorgensen L, et al. A crystal plasticity model incorporating the effects of precipitates in superalloys: application to tensile, compressive, and cyclic deformation of Inconel 718. Int J Plast 2017;99:162–85.
[534] Keshavarz S, Ghosh S. A crystal plasticity finite element model for flow stress anomalies in Ni 3 Al single crystals. Philos Mag 2015;95:2639–60. https://doi.org/10.1080/14786435.2015.1073858.
[535] Dao M, Asaro RJ. Non-Schmid effects and localized plastic flow in intermetallic alloys. Mater Sci Eng A 1993;170:143–60. https://doi.org/10.1016/0921-5093(93)90376-P.
[536] Ardeljan M, Beyerlein IJ, Knezevic M. A dislocation density based crystal plasticity finite element model: application to a two-phase polycrystalline HCP/BCC composites. J Mech Phys Solids 2014;66:16–31.
[537] Ghorbanpour S, Alam ME, Ferreri NC, Kumar A, McWilliams BA, Vogel SC, et al. Experimental characterization and crystal plasticity modeling of anisotropy, tension-compression asymmetry, and texture evolution of additively manufactured Inconel 718 at room and elevated temperatures. Int J Plast 2020;125:63–79.
[538] Bidron G, Doghri A, Malot T, Fournier-dit-Chabert F, Thomas M, Peyre P. Reduction of the hot cracking sensitivity of CM-247LC superalloy processed by laser cladding using induction preheating. J Mater Process Technol 2020;277. https://doi.org/10.1016/j.jmatprotec.2019.116461.
[539] Dye D, Hunziker O, Reed RC. Numerical analysis of the weldability of superalloys. Acta Mater 2001;49. https://doi.org/10.1016/S1359-6454(00)00361-X.
[540] Han Q, Mertens R, Montero-Sistiaga ML, Yang S, Setchi R, Vanmeensel K, et al. Laser powder bed fusion of Hastelloy X: Effects of hot isostatic pressing and the hot cracking mechanism. Mater Sci Eng A 2018;732:228–39. https://doi.org/10.1016/j.msea.2018.07.008.
[541] Mazur M, Benoit M, Easton M, Brandt M. Selective laser melting of Inconel 625 alloy with reduced defect formation. J Laser Appl 2020;32:022058. https://doi.org/10.2351/7.0000093.
[542] Hu YL, Lin X, Yu XB, Xu JJ, Lei M, Huang WD. Effect of Ti addition on cracking and microhardness of Inconel 625 during the laser solid forming processing. J Alloys Compd 2017;711:267–77. https://doi.org/10.1016/j.jallcom.2017.03.355.
[543] Griffiths S, Tabasi HG, Ivas T, Maeder X, Luca A De, Zweiacker K, et al. Combining Alloy and Process Modification for Micro-crack Mitigation in an Additively Manufactured Ni-base Superalloy. Addit Manuf 2020:104743. https://doi.org/10.1016/j.addma.2020.101443.
[544] Attallah M, Terasaki H, Moat R, Bray S, Komizo Y, Preuss M. In-Situ observation of primary melting in Ni-base superalloy using confocal laser scanning microscopy. Mater Charact 2011;62:760.
[545] Zhong M, Sun H, Liu W, Zhu X, He J. Boundary liquation and interface cracking characterization in laser deposition of Inconel 738 on directionally solidified Ni-based superalloy 2005;53:159–64. https://doi.org/10.1016/j.scriptamat.2005.03.047.
[546] Ruttert B, Ramsperger M, Mujica Roncery L, Lopez-Galilea I, Körner C, Theisen W. Impact of hot isostatic pressing on microstructures of CMSX-4 Ni-base superalloy fabricated by selective electron beam melting. Mater Des 2016;110:720–7. https://doi.org/10.1016/j.matdes.2016.08.041.
[547] Peng H, Shi Y, Gong S, Guo H, Chen B. Microstructure, mechanical properties and cracking behaviour in a γ′-precipitation strengthened nickel-base superalloy fabricated by electron beam melting. Mater Des 2018;159:155–69. https://doi.org/10.1016/j.matdes.2018.08.054.
[548] Boswell JH, Clark D, Li W, Attallah MM. Cracking during thermal post-processing of laser powder bed

fabricated CM247LC Ni-superalloy. Mater Des 2019;174:107793. https://doi.org/10.1016/j.matdes.2019.107793.
[549] Sreeramagiri P, Bhagavatam A, Ramakrishnan A, Alrehaili H, Dinda GP. Design and development of a high-performance Ni-based superalloy WSU 150 for additive manufacturing. J Mater Sci Technol 2020;47. https://doi.org/10.1016/j.jmst.2020.01.041.
[550] Zhou N, Dicus AD, Forsik SAJ, Wang T, Colombo GA, Epler ME. Development of a New Alumina-Forming Crack-Resistant High-γ′ Fraction Ni-Base Superalloy for Additive Manufacturing. Miner. Met. Mater. Ser., 2020. https://doi.org/10.1007/978-3-030-51834-9_102.
[551] Shukla A, Sarkar S, Durga A, Adharapurapu R, Dial L, Sondhi SK. Computational Design of Additively Printable Nickel Superalloys. Miner. Met. Mater. Ser., 2020. https://doi.org/10.1007/978-3-030-51834-9_104.
[552] Tomus D, Rometsch PA, Heilmaier M, Wu X. Effect of minor alloying elements on crack-formation characteristics of Hastelloy-X manufactured by selective laser melting. Addit Manuf 2017;16:65–72. https://doi.org/10.1016/j.addma.2017.05.006.
[553] Cloots M, Kunze K, Uggowitzer PJ, Wegener K. Microstructural characteristics of the nickel-based alloy IN738LC and the cobalt-based alloy Mar-M509 produced by selective laser melting. Mater Sci Eng A 2016;658:68–76. https://doi.org/10.1016/j.msea.2016.01.058.
[554] Tang L, Liang J, Cui C, Li J, Zhou Y, Sun X, et al. Influence of Co content on the microstructures and mechanical properties of a Ni–Co base superalloy made by specific additive manufacturing process. Mater Sci Eng A 2020;786. https://doi.org/10.1016/j.msea.2020.139438.
[555] Coniglio N, Cross CE. Initiation and growth mechanisms for weld solidification cracking. Int Mater Rev 2013;58. https://doi.org/10.1179/1743280413Y.0000000020.
[556] Wang X, Carter LN, Pang B, Attallah MM, Loretto MH. Microstructure and yield strength of SLM-fabricated CM247LC Ni-Superalloy. Acta Mater 2017;128:87–95. https://doi.org/10.1016/j.actamat.2017.02.007.
[557] Bermingham MJ, StJohn DH, Krynen J, Tedman-Jones S, Dargusch MS. Promoting the columnar to equiaxed transition and grain refinement of titanium alloys during additive manufacturing. Acta Mater 2019;168:261–74. https://doi.org/10.1016/j.actamat.2019.02.020.
[558] Polonsky AT, Raghavan N, Echlin MP, Kirka MM, Dehoff RR, Pollock TM. 3D Characterization of the Columnar-to-Equiaxed Transition in Additively Manufactured Inconel 718, 2020, p. 990–1002. https://doi.org/10.1007/978-3-030-51834-9_97.
[559] Xi L, Wang P, Prashanth KG, Li H, Prykhodko H V., Scudino S, et al. Effect of TiB2 particles on microstructure and crystallographic texture of Al-12Si fabricated by selective laser melting. J Alloys Compd 2019;786:551–6. https://doi.org/10.1016/j.jallcom.2019.01.327.
[560] Villaret V, Deschaux-Beaume F, Bordreuil C. A solidification model for the columnar to equiaxed transition in welding of a Cr-Mo ferritic stainless steel with Ti as inoculant. J Mater Process Technol 2016;233:115–24. https://doi.org/10.1016/j.jmatprotec.2016.02.017.
[561] Bramfitt BL. The effect of carbide and nitride additions on the heterogeneous nucleation behavior of liquid iron. Metall Trans 1970;1. https://doi.org/10.1007/BF02642799.
[562] Xia TD, Chen X, Li QL, Zhao WJ. Grain refining efficiency and mechanism of pure nickel. Rare Met 2015;34. https://doi.org/10.1007/s12598-013-0125-y.
[563] Kelly PM, Zhang M-X. Edge-to-edge matching—The fundamentals. Metall Mater Trans A 2006;37. https://doi.org/10.1007/s11661-006-1003-0.
[564] Yang W, Qu P, Liu L, Jie Z, Huang T, Wang F, et al. Nucleation Crystallography of Ni Grains on CrFeNb Inoculants Investigated by Edge-to-Edge Matching Model in an IN718 Superalloy. Adv Eng Mater 2018;20:1–6. https://doi.org/10.1002/adem.201700568.
[565] Porter DA, Easterling KE. Phase Transformations in Metals and Alloys. 1992. https://doi.org/10.1007/978-1-4899-3051-4.
[566] Prasad A, Yuan L, Lee P, Patel M, Qiu D, Easton M, et al. Towards understanding grain nucleation under Additive Manufacturing solidification conditions. Acta Mater 2020;195. https://doi.org/10.1016/j.actamat.2020.05.012.
[567] Binczyk F, Śleziona J, Gradoń P. Modification of Macrostructure of Nickel Superalloys With Cobalt Nanoparticles. Kompozyty 2011;11:49–54.
[568] Matysiak H, Zagorska M, Balkowiec A, Adamczyk-Cieslak B, Dobkowski K, Koralnik M, et al. The Influence of the Melt-Pouring Temperature and Inoculant Content on the Macro and Microstructure of the IN713C Ni-Based Superalloy. Jom 2016;68:185–97. https://doi.org/10.1007/s11837-015-1672-5.
[569] Ho I-T, Hsu T-H, Chang Y-J, Li C-W, Chang K-C, Tin S, et al. Effects of CoAl<inf>2</inf>O<inf>4</inf> inoculants on microstructure and mechanical properties of IN718 processed by selective laser melting. Addit Manuf 2020;35. https://doi.org/10.1016/j.addma.2020.101328.
[570] XIAO W han, LU S qiang, WANG Y chao, SHI J. Mechanical and tribological behaviors of

graphene/Inconel 718 composites. Trans Nonferrous Met Soc China (English Ed 2018;28. https://doi.org/10.1016/S1003-6326(18)64841-1.
[571] Gu D, Zhang H, Dai D, Xia M, Hong C, Poprawe R. Laser additive manufacturing of nano-TiC reinforced Ni-based nanocomposites with tailored microstructure and performance. Compos Part B Eng 2019;163. https://doi.org/10.1016/j.compositesb.2018.12.146.
[572] Han Q, Gu Y, Huang J, Wang L, Low KWQ, Feng Q, et al. Selective laser melting of Hastelloy X nanocomposite: Effects of TiC reinforcement on crack elimination and strength improvement. Compos Part B Eng 2020;202. https://doi.org/10.1016/j.compositesb.2020.108442.
[573] Rong T, Gu D, Shi Q, Cao S, Xia M. Effects of tailored gradient interface on wear properties of WC/Inconel 718 composites using selective laser melting. Surf Coatings Technol 2016;307. https://doi.org/10.1016/j.surfcoat.2016.09.011.
[574] Kenel C, Luca A De, Joglekar SS, Leinenbach C, Dunand C. Evolution of Y2O3 dispersoids during laser powder bed fusion of oxide dispersion strengthened Ni-Cr-Al-Ti γ / γ ' superalloy. Addit Manuf 2021;47:102224. https://doi.org/10.1016/j.addma.2021.102224.
[575] Ho I-T, Chen Y-T, Yeh A-C, Chen C-P, Jen K-K. Microstructure evolution induced by inoculants during the selective laser melting of IN718. Addit Manuf 2018;21. https://doi.org/10.1016/j.addma.2018.02.018.
[576] Rong T, Gu D. Formation of novel graded interface and its function on mechanical properties of WC1-x reinforced Inconel 718 composites processed by selective laser melting. J Alloys Compd 2016;680. https://doi.org/10.1016/j.jallcom.2016.04.107.
[577] Hsu T-H, Chang K-C, Chang Y-J, Ho I-T, Tin S, Li C-W, et al. Effect of Carbide Inoculants Additions in IN718 Fabricated by Selective Laser Melting Process, 2020, p. 982–9. https://doi.org/10.1007/978-3-030-51834-9_96.
[578] Hong C, Gu D, Dai D, Gasser A, Weisheit A, Kelbassa I, et al. Laser metal deposition of TiC/Inconel 718 composites with tailored interfacial microstructures. Opt Laser Technol 2013;54. https://doi.org/10.1016/j.optlastec.2013.05.011.
[579] Zhang B, Bi G, Nai S, Sun CN, Wei J. Microhardness and microstructure evolution of TiB2 reinforced Inconel 625/TiB2 composite produced by selective laser melting. Opt Laser Technol 2016;80:186–95. https://doi.org/10.1016/j.optlastec.2016.01.010.
[580] Yang S, Han Q, Yin Y, Gao J, Zhang Z, Gu Y, et al. Effects of micrometer-sized TiB2 on crack mitigation, mechanical and electrochemical performance of a Ni-based alloy fabricated by selective laser melting. Opt Laser Technol 2021;142. https://doi.org/10.1016/j.optlastec.2021.107240.
[581] Chang K-C, Lee M-Y, Hsu T-H, Chang Y-J, Lo K-C, Kim HS, et al. An Effective Strengthening Strategy of Nano Carbide Precipitation and Cellular Microstructure Refinement in a Superalloy Fabricated by Selective Laser Melting Process. Metals (Basel) 2021;11. https://doi.org/10.3390/met11111691.
[582] Ma C, Chen L, Cao C, Li X. Nanoparticle-induced unusual melting and solidification behaviours of metals. Nat Commun 2017;8:1–7. https://doi.org/10.1038/ncomms14178.
[583] Gu D, Shen Y. Balling phenomena during direct laser sintering of multi-component Cu-based metal powder. J Alloys Compd 2007;432:163–6. https://doi.org/10.1016/j.jallcom.2006.06.011.
[584] Yuan P, Gu D, Dai D. Particulate migration behavior and its mechanism during selective laser melting of TiC reinforced Al matrix nanocomposites. Mater Des 2015;82:46–55. https://doi.org/10.1016/j.matdes.2015.05.041.
[585] Tucho WM, Cuvillier P, Sjolyst-Kverneland A, Hansen V. Microstructure and hardness studies of Inconel 718 manufactured by selective laser melting before and after solution heat treatment. Mater Sci Eng A 2017;689:220–32. https://doi.org/10.1016/j.msea.2017.02.062.
[586] Kirka MM, Unocic KA, Raghavan N, Medina F, Dehoff RR, Babu SS. Microstructure Development in Electron Beam-Melted Inconel 718 and Associated Tensile Properties. Jom 2016;68:1012–20. https://doi.org/10.1007/s11837-016-1812-6.
[587] Deng D, Peng RL, Brodin H, Moverare J. Microstructure and mechanical properties of Inconel 718 produced by selective laser melting: Sample orientation dependence and effects of post heat treatments. Mater Sci Eng A 2018;713:294–306. https://doi.org/10.1016/j.msea.2017.12.043.
[588] Muñoz-Moreno R, Divya VD, Driver SL, Messé OMDM, Illston T, Baker S, et al. Effect of heat treatment on the microstructure, texture and elastic anisotropy of the nickel-based superalloy CM247LC processed by selective laser melting. Mater Sci Eng A 2016;674:529–39. https://doi.org/10.1016/j.msea.2016.06.075.
[589] Yu C-H, Peng RL, Calmunger M, Luzin V, Brodin H, Moverare J. Anisotropic Deformation and Fracture Mechanisms of an Additively Manufactured Ni-Based Superalloy, 2020, p. 1003–13. https://doi.org/10.1007/978-3-030-51834-9_98.
[590] Chlebus E, Gruber K, Kuźnicka B, Kurzac J, Kurzynowski T. Effect of heat treatment on the microstructure and mechanical properties of Inconel 718 processed by selective laser melting. Mater Sci Eng A 2015;639:647–55. https://doi.org/10.1016/j.msea.2015.05.035.
[591] Kirka MM, Fernandez-Zelaia P, Lee Y, Nandwana P, Yoder S, Acevedo O, et al. Mechanical Performance

of a Non-weldable Ni-Base Superalloy: Inconel 738 Fabricated by Electron Beam Melting. Miner. Met. Mater. Ser., 2020. https://doi.org/10.1007/978-3-030-51834-9_105.
[592] Li X, Shi JJ, Wang CH, Cao GH, Russell AM, Zhou ZJ, et al. Effect of heat treatment on microstructure evolution of Inconel 718 alloy fabricated by selective laser melting. J Alloys Compd 2018;764:639–49. https://doi.org/10.1016/j.jallcom.2018.06.112.
[593] Idell Y, Levine LE, Allen AJ, Zhang F, Campbell CE, Olson GB, et al. Unexpected δ-Phase Formation in Additive-Manufactured Ni-Based Superalloy. JOM 2016;68. https://doi.org/10.1007/s11837-015-1772-2.
[594] Zhou N, Lv DC, Zhang HL, McAllister D, Zhang F, Mills MJ, et al. Computer simulation of phase transformation and plastic deformation in IN718 superalloy: Microstructural evolution during precipitation. Acta Mater 2014;65. https://doi.org/10.1016/j.actamat.2013.10.069.
[595] Mahadevan S, Nalawade S, Singh JB, Verma A, Paul B, Ramaswamy K. Evolution of δ phase microstructure in alloy 718. 7th Int. Symp. Superalloy 718 Deriv. 2010, vol. 2, 2010. https://doi.org/10.1002/9781118495223.ch57.
[596] Strößner J, Terock M, Glatzel U. Mechanical and Microstructural Investigation of Nickel-Based Superalloy IN718 Manufactured by Selective Laser Melting (SLM). Adv Eng Mater 2015;17:1099–105. https://doi.org/10.1002/adem.201500158.
[597] Lass EA, Stoudt MR, Williams ME, Katz MB, Levine LE, Phan TQ, et al. Formation of the Ni3Nb δ-Phase in Stress-Relieved Inconel 625 Produced via Laser Powder-Bed Fusion Additive Manufacturing. Metall Mater Trans A Phys Metall Mater Sci 2017;48. https://doi.org/10.1007/s11661-017-4304-6.
[598] Beaubois V, Huez J, Coste S, Brucelle O, Lacaze J. Short term precipitation kinetics of delta phase in strain free Inconel* 718 alloy. Mater Sci Technol 2004;20:1019–26. https://doi.org/10.1179/026708304225019830.
[599] Du J, Lv X, Deng Q, Luo Y. Effect of Solution Treatment on the Microstructure and Mechanical Properties of IN718 Alloy. Xiyou Jinshu Cailiao Yu Gongcheng/Rare Met Mater Eng 2017;46:2359–65. https://doi.org/10.1016/s1875-5372(17)30197-2.
[600] Zhao X, Lin X, Chen J, Xue L, Huang W. The effect of hot isostatic pressing on crack healing, microstructure, mechanical properties of Rene88DT superalloy prepared by laser solid forming. Mater Sci Eng A 2009;504. https://doi.org/10.1016/j.msea.2008.12.024.
[601] Wang F. Mechanical property study on rapid additive layer manufacture Hastelloy® X alloy by selective laser melting technology. Int J Adv Manuf Technol 2012;58:545–51. https://doi.org/10.1007/s00170-011-3423-2.
[602] Ding X, Koizumi Y, Wei D, Chiba A. Effect of process parameters on melt pool geometry and microstructure development for electron beam melting of IN718: A systematic single bead analysis study. Addit Manuf 2019;26:215–26. https://doi.org/10.1016/j.addma.2018.12.018.
[603] Stjohn DH, Qian M, Easton MA, Cao P. The Interdependence Theory: The relationship between grain formation and nucleant selection. Acta Mater 2011;59:4907–21. https://doi.org/10.1016/j.actamat.2011.04.035.
[604] Raghavan N, Dehoff R, Pannala S, Simunovic S, Kirka M, Turner J, et al. Numerical modeling of heat-transfer and the influence of process parameters on tailoring the grain morphology of IN718 in electron beam additive manufacturing. Acta Mater 2016;112:303–14. https://doi.org/10.1016/j.actamat.2016.03.063.
[605] Wei HL, Elmer JW, DebRoy T. Three-dimensional modeling of grain structure evolution during welding of an aluminum alloy. Acta Mater 2017;126. https://doi.org/10.1016/j.actamat.2016.12.073.
[606] Lei Y, Aoyagi K, Chiba A. A method to manipulate non-steady-state columnar-to-equiaxed transition in powder bed fusion additive manufacturing using an electron beam. Acta Mater 2022;227:117717. https://doi.org/10.1016/j.actamat.2022.117717.
[607] Geiger F, Kunze K, Etter T. Tailoring the texture of IN738LC processed by selective laser melting (SLM) by specific scanning strategies. Mater Sci Eng A 2016;661:240–6. https://doi.org/10.1016/j.msea.2016.03.036.
[608] Liu F, Lin X, Huang C, Song M, Yang G, Chen J, et al. The effect of laser scanning path on microstructures and mechanical properties of laser solid formed nickel-base superalloy Inconel 718. J Alloys Compd 2011;509. https://doi.org/10.1016/j.jallcom.2010.11.176.
[609] Plotkowski A, Kirka MM, Babu SS. Verification and validation of a rapid heat transfer calculation methodology for transient melt pool solidification conditions in powder bed metal additive manufacturing. Addit Manuf 2017;18:256–68. https://doi.org/10.1016/j.addma.2017.10.017.
[610] Chauvet E, Tassin C, Blandin JJ, Dendievel R, Martin G. Producing Ni-base superalloys single crystal by selective electron beam melting. Scr Mater 2018;152:15–9.
[611] Collins PC, Brice DA, Samimi P, Ghamarian I, Fraser HL. Microstructural Control of Additively Manufactured Metallic Materials. Annu Rev Mater Res 2016;46:63–91. https://doi.org/10.1146/annurev-matsci-070115-031816.

[612] Seidel A, Degener L, Schneider J, Brueckner F, Beyer E, Leyens C. Novel Approach for Suppressing of Hot Cracking Via Magneto-fluid Dynamic Modification of the Laser-Induced Marangoni Convection. Miner. Met. Mater. Ser., 2020. https://doi.org/10.1007/978-3-030-51834-9_95.
[613] Mumtaz KA, Erasenthiran P, Hopkinson N. High density selective laser melting of Waspaloy®. J Mater Process Technol 2008;195:77–87. https://doi.org/10.1016/j.jmatprotec.2007.04.117.
[614] Xia M, Gu D, Yu G, Dai D, Chen H, Shi Q. Influence of hatch spacing on heat and mass transfer, thermodynamics and laser processability during additive manufacturing of Inconel 718 alloy. Int J Mach Tools Manuf 2016;109:147–57. https://doi.org/10.1016/j.ijmachtools.2016.07.010.
[615] Zhang Y, Wang H, Song X, Nie Z. Preparation and Performance of Spherical Ni Powder for SLM Processing. Jinshu Xuebao/Acta Metall Sin 2018;54. https://doi.org/10.11900/0412.1961.2018.00153.
[616] Nguyen QB, Luu DN, Nai SML, Zhu Z, Chen Z, Wei J. The role of powder layer thickness on the quality of SLM printed parts. Arch Civ Mech Eng 2018;18:948–55. https://doi.org/10.1016/j.acme.2018.01.015.
[617] Craeghs T, Clijsters S, Yasa E, Bechmann F, Berumen S, Kruth J-P. Determination of geometrical factors in Layerwise Laser Melting using optical process monitoring. Opt Lasers Eng 2011;49:1440–6. https://doi.org/10.1016/j.optlaseng.2011.06.016.
[618] Yasa E, Poyraz O, Solakoglu EU, Akbulut G, Oren S. A Study on the Stair Stepping Effect in Direct Metal Laser Sintering of a Nickel-based Superalloy. Procedia CIRP 2016;45:175–8. https://doi.org/10.1016/j.procir.2016.02.068.
[619] Fox JC, Moylan SP, Lane BM. Effect of Process Parameters on the Surface Roughness of Overhanging Structures in Laser Powder Bed Fusion Additive Manufacturing. Procedia CIRP 2016;45:131–4. https://doi.org/10.1016/j.procir.2016.02.347.
[620] Covarrubias EE, Eshraghi M. Effect of Build Angle on Surface Properties of Nickel Superalloys Processed by Selective Laser Melting. JOM 2018;70:336–42. https://doi.org/10.1007/s11837-017-2706-y.
[621] Maleki E, Bagherifard S, Bandini M, Guagliano M. Surface post-treatments for metal additive manufacturing: Progress, challenges, and opportunities. Addit Manuf 2020;37:101619. https://doi.org/10.1016/j.addma.2020.101619.
[622] Kaynak Y, Tascioglu E. Post-processing effects on the surface characteristics of Inconel 718 alloy fabricated by selective laser melting additive manufacturing. Prog Addit Manuf 2020;5:221–34. https://doi.org/10.1007/s40964-019-00099-1.
[623] Palma T, Munther M, Sharma M, Hackel L, Beheshti A, Davami K. Nanomechanical Characterization of Laser Peened Additively Manufactured Inconel 718 Superalloy. Adv Eng Mater 2019;21:1900499. https://doi.org/10.1002/adem.201900499.
[624] Zhihao F, Libin L, Longfei C, Yingchun G. Laser Polishing of Additive Manufactured Superalloy. Procedia CIRP 2018;71:150–4. https://doi.org/10.1016/j.procir.2018.05.088.
[625] Mohammadian N, Turenne S, Brailovski V. Surface finish control of additively-manufactured Inconel 625 components using combined chemical-abrasive flow polishing. J Mater Process Technol 2018;252:728–38. https://doi.org/10.1016/j.jmatprotec.2017.10.020.
[626] Enrique PD, Marzbanrad E, Mahmoodkhani Y, Jiao Z, Toyserkani E, Zhou NY. Surface modification of binder-jet additive manufactured Inconel 625 via electrospark deposition. Surf Coatings Technol 2019;362:141–9.
[627] Yao S, Wang T. Improved surface of additive manufactured products by coating. J Manuf Process 2016;24:212–6. https://doi.org/10.1016/j.jmapro.2016.09.007.
[628] Dunbar AJ, Denlinger ER, Gouge MF, Simpson TW, Michaleris P. Comparisons of laser powder bed fusion additive manufacturing builds through experimental in situ distortion and temperature measurements. Addit Manuf 2017;15:57–65. https://doi.org/10.1016/j.addma.2017.03.003.
[629] Gao M, Wang Z, Li X, Zeng X. The effect of deposition patterns on the deformation of substrates during direct laser fabrication. J Eng Mater Technol Trans ASME 2013;135. https://doi.org/10.1115/1.4024195.
[630] Lu Y, Wu S, Gan Y, Huang T, Yang C, Junjie L, et al. Study on the microstructure, mechanical property and residual stress of SLM Inconel-718 alloy manufactured by differing island scanning strategy. Opt Laser Technol 2015;75:197–206. https://doi.org/10.1016/j.optlastec.2015.07.009.
[631] Cheng B, Shrestha S, Chou YK. Stress and deformation evaluations of scanning strategy effect in selective laser melting. ASME 2016 11th Int Manuf Sci Eng Conf MSEC 2016 2016;3:240–51. https://doi.org/10.1115/MSEC20168819.
[632] Kalentics N, Boillat E, Peyre P, Ćirić-Kostić S, Bogojević N, Logé RE. Tailoring residual stress profile of Selective Laser Melted parts by Laser Shock Peening. Addit Manuf 2017;16. https://doi.org/10.1016/j.addma.2017.05.008.
[633] Donoghue J, Antonysamy AA, Martina F, Colegrove PA, Williams SW, Prangnell PB. The effectiveness of combining rolling deformation with Wire-Arc Additive Manufacture on β-grain refinement and texture modification in Ti-6Al-4V. Mater Charact 2016;114. https://doi.org/10.1016/j.matchar.2016.02.001.
[634] Cheng Y, Xiao Z, Zhu H, Zeng X, Wang G. Influence of substrate characteristics on residual stress of

SLMed Inconel 718. Rapid Prototyp J 2019;25:792–9. https://doi.org/10.1108/RPJ-09-2018-0238.

Biography

Dr. Amir Mostafaei is an Assistant Professor in the Department of Materials, Mechanical and Aerospace Engineering at the Illinois Institute of Technology, Chicago, since January 2020, with a Ph.D. in Materials Science and Engineering from the University of Pittsburgh, PA, USA, a post-doc research fellow at the Manufacturing Futures Initiatives (MFI) Center at Carnegie Mellon University between September 2018 and December 2019 and an M.Sc. degree in Corrosion and Materials Protection (Sahand University of Technology, Iran). His Ph.D. research was primary on binder jet 3D printing of structural, bio-compatible, metal matrix composites and magnetic shape memory alloys. Effects of print processing optimization during binder jetting as well as post-processing development including sintering and surface treatment of the 3D printed parts were investigated on the microstructural evolution, phase formation, and resulting properties of binder jetted parts. Additionally, he has been working on laser powder bed fusion of metallic materials and evaluation of the processing parameters on the microstructure, porosity distribution, mechanical properties, and corrosion behavior of various additive manufactured parts from titanium, aluminum, stainless steel, and nickel-based alloys. Dr. Mostafaei has published literature in high-temperature corrosion and failure analysis of stainless steels and nickel-based superalloys used in petroleum and nuclear power plants, multi-functional organic coatings, welding metallurgy, and nanomaterials fabrication. Finally, Dr. Mostafaei's research mainly focuses on applying fundamental aspects of materials science and engineering to address the demands of various manufacturing industries via additive manufacturing.

Dr. Reza Ghiaasiaan is currently with the Department of Mechanical Engineering at Auburn University, as Assistant Research Professor working at the National Center for Additive Manufacturing Excellence. NCAME is a NASA and NIST funded research center focused on advancing the additive manufacturing (AM) technology. NCAME is also one of the two U.S.-based founding partners of the ASTM International Additive Manufacturing Center of Excellence (AM CoE). Prior to his appointment at NCAME, Dr. Ghiaasiaan has obtained a wealth of engineering experience through many years in industry, including leadership and R&D engineering positions, specializing in thermofluid, solidification/casting and physical/mechanical metallurgy of metallic alloying systems. Dr. Ghiaasiaan then took his skillset to McMaster University, where he received his Ph.D. in 2015 in Mechanical Engineering focused on microscopic characterization and materials properties using various processing methodologies such as innovative casting and additive manufacturing processes. The focus of his research was on the physical metallurgy and various processing methods of metallic alloying systems including additive manufacturing, which is his continued primary area of interest at Auburn University. Dr. Ghiaasiaan received his Professional Engineer (P.Eng.) licensure in 2018 as he obtained his full membership to the Professional Engineering Ontario (PEO) Association, designated as P.Eng. in Canada.

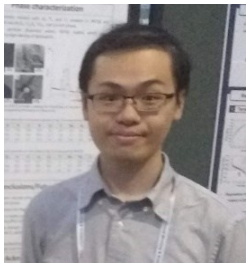

I-Ting Ho is a Ph.D. candidate under the supervision of Prof. Sammy Tin in Department of Mechanical, Materials, and Aerospace Engineering at Illinois Institute of Technology, Chicago, since May 2019, with a M.S. degree in Department of Materials Science and Engineering at National Tsing Hua University, Taiwan. I-Ting leads his efforts on optimization of miscellaneous properties of Ni-base and Ni-Fe-base superalloys processed by laser powder bed fusion (L-PBF) using fundamental knowledge of materials science since 2016. I-Ting also participated the project on mitigation of processibility of Ni-base superalloys via alloy design led by National Chung-Shen Institute of Science and technology (NCSIST), Taiwan. His PhD research mainly focuses on applying various inoculant particles including oxides, borides, and intermetallic as nucleation agents to reduce anisotropy and crystallographic texture present within superalloys processed by L-PBF, and he currently works on the microstructural analysis using EPMA, EBSD, and XRD in Department of Materials Science and Engineering at the University of Arizona.

Seth Strayer is a NASA Space Technology Graduate Research Fellow pursuing his Ph.D. in mechanical engineering in the Department of Mechanical Engineering and Materials Science at the University of Pittsburgh, Pittsburgh, PA, USA, since September 2020. Before his fellowship award, Strayer spent his first year of graduate school focusing on mesoscale process modeling of Ni-based superalloys, including laser-powder interactions, melt pool geometry and heat transfer, solidification, porosity, and thermal stress analysis for Inconel 718. Strayer graduated summa cum laude from the University of Pittsburgh in August 2019, obtaining his BSME with a minor in mathematics and holding relevant positions such as a mechanical engineering co-op with Curtiss-Wright EMD, undergraduate research assistant, mathematics tutor, and student grader. His current research focuses on coupling mesoscale process modeling with machine learning to address the fundamental lack of understanding between the additive manufacturing process and the final part quality.

Dr. Kai-Chun Chang earned his Ph.D. degree in the Department of Material Science and Engineering at National Tsing-Hua university, Taiwan, studying under the guidance of Professor An-Chou Yeh. He received his Bachelor's degree in the Department of Material Science and Engineering at National Tsing-Hua university, Taiwan, in 2014. Kai-Chun's research focuses on the microstructure evolution of hard metal and Ni-based superalloy fabricated by laser powder bed fusion. His research interests include powder metallurgy, high entropy alloy, superalloy and powder bed laser fusion.

Dr. Nima Shamsaei is currently the Philpott-WestPoint Stevens Distinguished Professor in the Department of Mechanical Engineering at Auburn University, where he is also the founding director of the National Center for Additive Manufacturing Excellence (NCAME), a NASA and NIST funded research center focused on advancing the additive manufacturing (AM) technology. NCAME is also one of the two U.S.-based founding partners of the ASTM International Additive Manufacturing Center of Excellence (AM CoE) with the aim to guide multi-disciplinary research and foster effective collaborations amongst industry, government, academia, and non-profit organizations for ensuring a coordinated, global effort for rapidly closing standards and workforce development gaps in advanced manufacturing. Prior to joining academia, Dr. Shamsaei spent many years in industry, including in leadership positions, specializing in fatigue analysis and durability test development. Dr. Shamsaei then took his skillset to Mississippi State University in 2013 and initiated a university level AM research track. The focus of his research was on the structural integrity of AM metallic materials, which is his continued primary area of interest at Auburn University. His research work has resulted so far in publishing over 220 peer-reviewed journal articles and conference proceedings as well as 90+ technical presentations including 50+ invited talks or keynote/plenary speeches in the areas of fatigue, fracture, mechanics of materials, and AM material/part qualification, certification and standardization. Several government agencies and private companies sponsor many of his research projects in order to advance AM technology for faster industrial adoption. He has served as the guest editor for the International Journal of Fatigue 1st, 2nd, and 3rd special issues on Additive Manufacturing in 2017, 2019, and 2021, as well as the Journal of Materials Processing Technology's special issue on AM process qualification in 2021. Dr. Shamsaei also organizes multiple AM-related symposia and conferences in ASTM, TMS, and ASME.

Dr. Shuai Shao is currently an associate professor of Mechanical Engineering at Auburn University. He has published over 50 peer reviewed journal articles and book chapters and has given 20+ invited/regular presentations. His expertise is multiscale materials modeling, materials characterization, and fatigue applied to additively manufactured materials. Dr. Shao has served as PI/Co-PI in multiple research projects from federal agencies, including the Department of Energy, the National Aeronautics and Space Administration, and the National Institute of Standards and Technology. Dr. Shao is serving as referee for prestigious journals as well as organizing symposia in prominent international conferences. He has also received numerous awards, including the "2019 LSU Mechanical Engineering Outstanding Teacher Award", "2019 LSU Alumni Association Rising Faculty Research Award", "2018 LSU Summer Research Stipend", and "2015 TMS Hysitron Presentation Silver Medal Award". One of his research articles made the cover of the Jan 2016 issue of JOM.

Dr. Santanu Paul is a Post-Doctoral Associate at the Department of Mechanical Engineering, University of Pittsburgh, USA since October 2018. He completed his Ph.D in 2018 from the Indian Institute of Technology Bombay and Monash University, Australia. His doctoral research focused on corelating the thermal, metallurgical and mechanical interactions to predict the in-process temperature, metallurgical phase and stress evolution, and mitigate build failure in metal Additive Manufacturing (AM). He was awarded the *NAMRI/SME Outstanding Paper Award* in 2016 by the *Society of Manufacturing Engineers* for describing the process mechanics in AM. At the University of Pittsburgh, Dr. Paul's research focuses on establishing relationship between process, microstructure and properties of AM processed Nickel superalloys using crystal plasticity finite element (CPFE) method. He has developed the Discrete Dendrite Dynamics (DDD) model for predicting the grain microstructure of the entire AM build, using powder bed fusion (PBF) and wire-arc AM (WAAM).

Dr. An-Chou Yeh is a full Professor at the Materials Science and Engineering department, National Tsing Hua University, Taiwan. He received a First-Class degree honor in Aerospace Materials Engineering from Imperial College, UK; a PhD in Materials Science and Metallurgy from Cambridge University, UK. His research interests include alloys design, microstructure engineering, additive manufacturing, single crystal casting, superalloys, high entropy alloys. He has been awarded Marcus A. Grossmann Young Author Award by ASM International, Excellent Young Engineer Award by CSME, Mercator Fellow Award by German DFG, Excellent Young Academic Researcher Award by MRS-T.

Dr. Sammy Tin is currently the Department Head and Professor of Materials Science and Engineering at the University of Arizona. Formerly, he was the Charles and Lee Finkl Professor of Materials Engineering and the Director of the Thermal Processing Technology Center at the Illinois Institute of Technology. He received a B.S. in Materials Engineering from Cal Poly – San Luis Obispo, M.S. in Materials Science and Engineering from Carnegie Mellon University and a PhD in Materials Science and Engineering from the University of Michigan. For over 20 years, Professor Tin has led research programs on a variety of polycrystalline and single crystal Ni-base superalloys. Professor Tin serves on the Editorial Committee for Metallurgical and Materials Transactions A, Materials Science and Engineering A, and was the recipient of the 2004 Rolls-Royce Mark Shipton Patent Award, the 2006 IOM3 Cook/Ablett Award and the 2007 ASM Marcus A Grossmann Award. Professor Tin is a Fellow of ASM International and has authored over 100 manuscripts in referred journals and conference proceedings.

Dr. Albert To is currently William Kepler Whiteford Professor in the Department of Mechanical Engineering and Materials Science at University of Pittsburgh, where he also serves as the Director of the ANSYS Additive Manufacturing Research Laboratory. Dr. To obtained his Ph.D. from U.C. Berkeley in 2005 and conducted postdoctoral research at Northwestern University from 2005-2008. He joined University of Pittsburgh as Assistant Professor in 2008 and was promoted to Associate Professor in 2014 and to Endowed Professor in 2019. His current research interests lie in design optimization, fast process modeling, and process-microstructure-property relationship for metal additive manufacturing. The computational methods his group developed for AM have been adopted and commercialized by engineering simulation software companies such as ANSYS. Dr. To has over 100 peer-reviewed journal and he is currently an associate editor for Additive Manufacturing in charge of modeling and simulation.